2008

Dynamic Shear Bands in Metals under High Strain Rates

Amin Hisham Almasri
Louisiana State University and Agricultural and Mechanical College, aalmas1@lsu.edu

DYNAMIC SHEAR BANDS IN METALS UNDER HIGH STRAIN RATES

A Dissertation
Submitted to the Graduate Faculty of the
Louisiana State University and
Agricultural and Mechanical College
in partial fulfillment of the
requirements for the degree of
Doctor of Philosophy

in

The Department of Civil & Environmental Engineering

by
Amin Hisham Almasri
B.S., Jordan University of Science and Technology, Irbid, Jordan, 2001
M.S., Jordan University of Science and Technology, Irbid, Jordan, 2004
May, 2008

TO MY LOVING PARENTS

MAY ALLAH BLESS YOU IN THIS LIFE AND IN THE HEREAFTER

ACKNOWLEDGEMENTS

I would like to express my gratitude to Almighty Allah for providing me the blessings to complete this work. The writing of this dissertation was not possible without his guidance and help.

I would also like to acknowledge the personal and practical support of numerous people. My sincere gratitude goes to my parents for their love, support, and patience over the last few years.

I wish to express my thanks to my advisor Boyd Professor George Z. Voyiadjis for his guidance and support, both scientifically and financially. He never hesitated to provide me with support and motivation in every step of the way.

I would like to thank my committee members: Professors Suresh Moorthy, Steve Cai, Su-Seng Pang, Wen J. Meng, and David P. Young. Thank you for your patience in reading this dissertation and for the many constructive comments.

I would like to express my personal gratitude to my colleagues in the Advanced Computational Solid Mechanics Laboratory (CSM Lab) particularly Ziad, Adam, and P.J. My graduate studies would not have been the same without their friendship. Exceptional thanks to Dr. Farid H. Abed (CSM Lab colleague) for his valuable instructions in using the finite element code ABAQUS.

TABLE OF CONTENTS

ABSTRACT

Adiabatic shear bands have been observed for a long time to occur under different conditions in many applications. Analysis of these localizations highly depends on the selection of the constitutive model. Hence, two constitutive models that take temperature and strain rate effect into account are proposed. The first model is a physically based model that depends on basic physical quantities, such as dislocation densities, Burgers vector, and activation energy. The second model is a simple empirical power model with a softening term. The empirical constitutive law is seen to be more successful in capturing the mechanical behavior of steel alloy under different temperatures and strain rates, and therefore is used in the finite element analysis.

Generally in finite element analysis, a finer mesh will yield results that are more accurate, but on the other hand will increase the computational cost. One way to handle this issue is through using a nonlocal gradient theory that is associated with a material length scale. Experimental procedure is utilized to obtain the length scale for steel alloys. To capture the rate sensitivity of the length scale, two models are proposed for the material dynamic hardness; a simple power law model, and a physically based model. The power law is chosen to be implemented in a finite element subroutine to be used to simulate adiabatic shear banding.

Explicit finite element analysis is used to solve different problems of adiabatic shear banding. Three examples include adiabatic shear bands due to material inhomogeneities as well as due to deformation gradients are presented. The simulation results of the steel penetration problem are seen to be in a very good agreement with available experimental data. It is also noticed that deformation mode changes significantly in the steel beam impact problem at different impact velocities.

CHAPTER 1: INTRODUCTION TO SHEAR BANDS

1.1 Introduction

One of the earliest pioneering works on shear bands was reported by Tresca (1878). After applying a blow with a steam hammer to a platinum bar during hot forging process, Tresca observed formation of hot lines crossing in X-shape. To monitor the pattern of these hot lines, metals were coated with wax. Using these patterns Tresca estimated the amount of plastic work converted to heat to be around 73% in iron and about 94% in copper. These hot lines are what are termed nowadays the Adiabatic Shear Bands (ASB). An ASB is a narrow region, usually in the order of tens of micrometers wide, undergoing very high shearing due to high strain rate dynamic loading. These regions are of intense plastic deformation that forms after softening of the material due to the fact that the heat generated by plastic work overcomes the hardening effects. In other words the deformation rate is higher than the heat flow of this region, which results in a high localized temperature that causes material softening in that area. The continuity of the two sides of the shear band is maintained despite the relatively high parallel displacement that occurs between these two sides. As shown in Figure 1.1, this movement is very similar to mode II crack or what is called sliding crack, and usually is in the order of millimeters, which is considered relatively high compared to the width of the band.

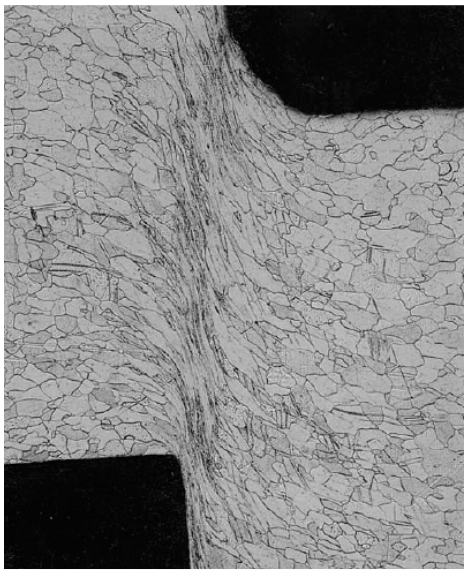

Figure 1.1: Typical localized deformation (shear band) in Remco iron (Mason and Worswick, 2001).

Microscopic photos of shear bands indicated that there are two types of ASBs: deformed shear bands and transformed shear bands. The transformed shear bands (which also called white shear bands) are bands that undergo a

phase transformation of the crystal structure of the material as shown in Figure 1.2.a, which explains the white color of the band under the microscope. The deformed shear bands are bands with high shearing that did not reach the phase transformation point as shown in Figure 1.2.b. The deformed shear band occurs as a first stage of localization as illustrated in Figure 1.3, and the white shear band is a consequence of further development of the deformed shear band. It is clear from the figures that unlike the deformed shear bands, the transformed shear bands have distinct boundaries and a well-defined width. The transformed shear bands in steel go through a martensitic transformation. Martensite, named after the German metallurgist Adolf Martens (1850-1914), is one class of hard minerals occurring as plate-shaped crystals. Sometimes these crystals are described wrongfully as needle-shaped because they look like that when viewed in a cross-section. It most commonly refers to a form of iron and carbon found in very hard steels used for example in springs. The crystallographic structure for martensite is body-centered tetragonal (BCT) symmetry, and results from the rapid cooling of austenite during quenching. After itching the martensite looks like a white band, which is why transformed shear bands are sometimes called “white bands”.

Figure 1.4 shows a typical microhardness profile of shear bands of several kinds of steel. It can be seen that the center of the shear bands has the higher hardness compared to its neighbor material. This also indicates a possible change in other material properties such the hardening and the ultimate strength.

On the other hand, Austenite, named after Sir William Chandler Roberts-Austen (1843-1902), is a non-magnetic metallic solid solution of carbon and iron that exists in steel above the critical temperature of 1333°F (about 723°C). It has a face-centered cubic (FCC) structure which allows it to hold a high proportion of carbon in solution. When austenite cools down, it breaks down into two forms of phases: the first is a mixture of ferrite (also called α-iron) and cementite (which is iron carbide; Fe_3C, also known as cohenite and has orthorhombic crystal structure). This mixture mostly exists in two special forms of arrangements between ferrite and cementite which are pearlite and bainite. The second form is the martensitic transformation where small distortion occurs to the lattice. The proportions of these forms of structures, which reflect the mechanical properties of the steel, are related directly to the rate of cooling of the material. Martensite has a lower density than ferrite, so that the transformation between phases often results in a relative change of volume. In addition the martensite structure is highly brittle and susceptible to formation of voids and cracks as shown in Figure 1.5. These different phases of Iron alloy phases can be more easily demonstrated through the phase diagram in Figure 1.6, which shows the equilibrium diagram for combinations of carbon in a solid solution of iron.

Adiabatic shear bands have been observed for a long time to occur under different conditions in many applications. Although shear bands are usually seen in a metal that is subjected to high strain rates (greater than 10^2 sec^{-1}), these

bands take place also in lower strain rates. Most material failures at high strain rate are usually preceded by adiabatic shear band formation. Some examples of adiabatic shear band failure mechanism include:

1. Penetration and perforation of steel shells by ballistic impact (see for example Raftenberg and Krause, 1999).
2. Fragmentation of steel casement after explosion.
3. High-speed machining with large strain, high strain rate and heat concentration. ASBs have been observed in the serrated chips of some difficult-to-machining materials (Burns and Davies, 2002).
4. Metal forming.

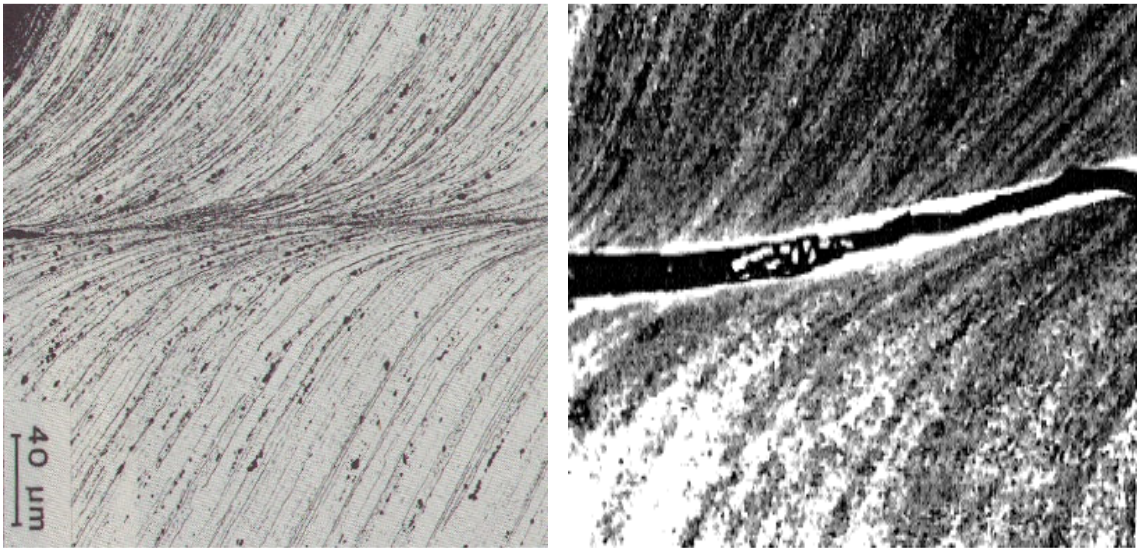

(a) (b)

Figure 1.2: (a) Deformed shear band (Wingrove, 1973), and (b) Transformed shear band (Kalthoff, 2000).

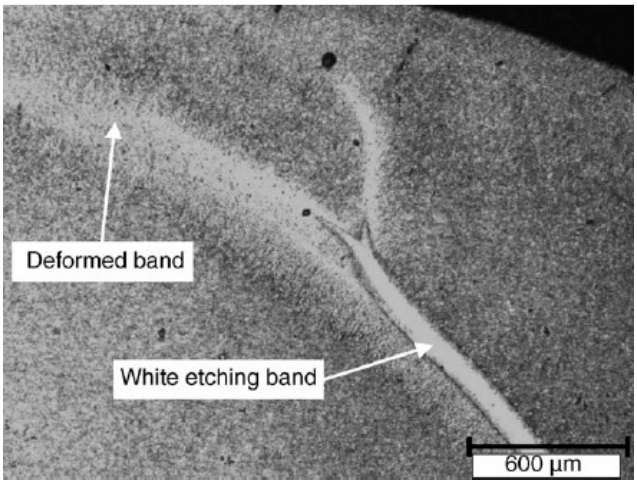

Figure 1.3: Transformed band and deformed band of a steel sample after impact (Odeshi et al., 2005).

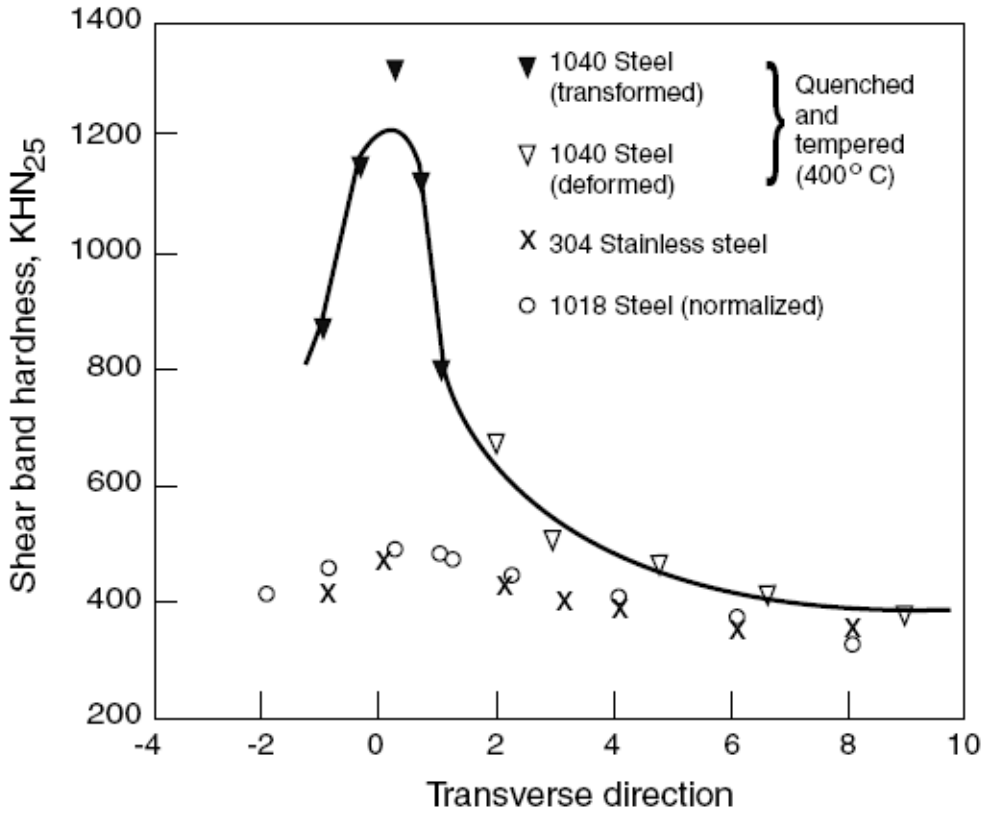

Figure 1.4: Microhardness profiles across shear bands in different kinds of steel (Rogers and Shastry, 1981).

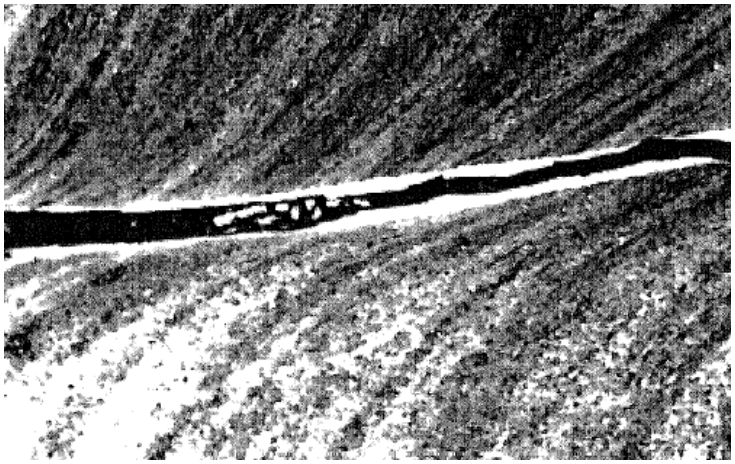

Figure 1.5: Void formation in a transformed shear band in steel 42 CrMo 4 (Kalthoff, 2000).

The formation of the adiabatic shear bands can generally be described by the following mechanism. When a material is subjected to high shearing strain due to high rate of the applied loading, the external work will initiate plastic deformation in the material, and most of this external work – especially for material with

considerable heat diffusion – will be dissipated as heat. This process increases the temperature of the material. But since material is never pure, inhomogeneities in material will form concentration areas of plastic deformation, and because of the high rate of loading and the high rate of deformation, the heat generated at these areas is more than the dissipated heat, which will raise the local temperature of these areas. This high local temperature has a weakening effect on this localized area (reduction in yield stress, etc.) and will result in significant reduction in its performance against more plastic deformation. This localized degradation in material will allow more deformation in that area which means more heat generated, and again more localized softening. This instability cycle of localized softening will continue as the high deformation localizes to a very narrow region. Finally, cracks and voids start to appear in these shear bands until eventually results in material failure where material can no longer sustain the applied load. It is worth to mention that in addition to material inhomogeneities, geometrical discontinuities can be the cause of the formation of the shear bands.

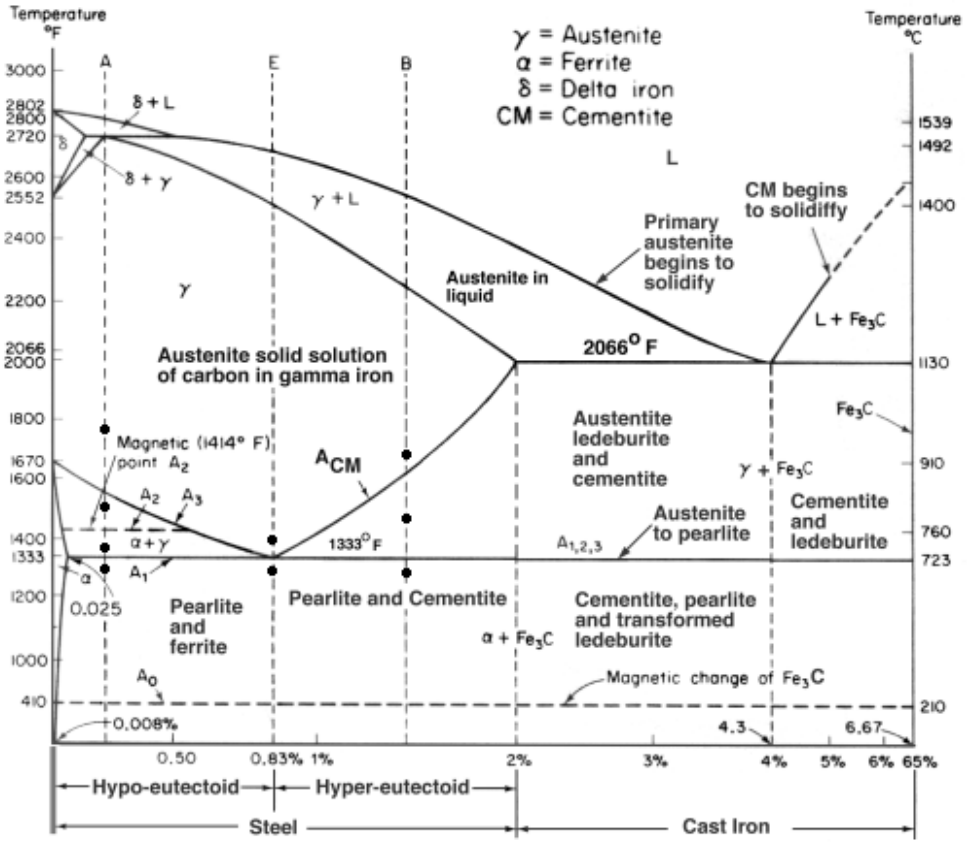

Figure 1.6: Phase Diagram of carbon and iron combinations (Pollack, 1988).

1.2 Literature Survey

As it was previously mentioned, one of the earliest observations of shear bands was that of Tresca in 1878. During his study of a platinum bar subjected to a blow with a steam hammer Tresca observed some hot lines that have an X-shape in the bar. The metals were coated with wax to monitor the pattern of these hot lines. Using these patterns Tresca estimated the amount of plastic work converted to heat to be around 73% in iron and about 94% in copper. Later on in 1921, Massey also reported the formation of heat lines during hot forging of metals. The first use of the term adiabatic shear band is believed to be by Zener and Hollomon (1944). They tried to explain the physics of the formation of the adiabatic stress strain relationship of low carbon steel tensile specimens. It was seen that while strain rate has a slight effect on the isothermal stress strain relation, a high increase in strain rate can cause the deformation to change from isothermal to adiabatic one, which showed initial instabilities in the stress strain diagram. To study these instabilities, a standard type die was used to form a punching in a steel plate. A 1/800" white band (martensite) was reported with 1/8" relative movement of the two sides of the band. They proposed that, when the material undergoes a deformation the stress is raised by the strain hardening and lowered by the associated rise in temperature (or what is called thermal softening). When the thermal softening overcomes the strain hardening, the behavior changes from isothermal to adiabatic deformation. Backman and Finnegan (1973) experimentally investigated metals and alloys subjected to ballistic impacts and explosive loadings. They tested hollow cylinders made of SAE 4130 steel, SAE 1020 steel, and 2024-T4 aluminum alloy. Four microstructures of SAE 4130 steel were used: lamellar pearlite, ferrite, tempered martensite and lower bainite. They found that either a deformed or a transformed band will form in a specific microstructure. For the lamellar pearlite and ferrite, a deformed band formed, while for the tempered martensite and lower bainite, a transformed band existed. In addition, specific patterns of cracks and fractures were observed to follow the formation of the shear bands in the specimen. The authors stated in the conclusion that the variety of forms of fracture that accompany the adiabatic shear band behavior tends to indicate that adiabatic shear and fractures are two separate phenomena. The pictures of the SAE 1020 steel showed that shear bands could initiate at flaws, pits, scratches, and inhomogeneities in the material that is capable of intensifying local stresses and strains. The width of the shear zones of the different materials was measured to be in the range 3–10 μm, and this width appeared to depend more on the type of material than on the loading conditions.

Lee et al. (1998) investigated the microstructural development of the ASBs due to ballistic impact in WELDALITE 049 alloy. The microstructure was examined under microscopes, and fine dynamic recrystallization of the grains was observed accompanied by high dislocation density. Winter (1975) studied the adiabatic shear bands in titanium and polymethylmethacrylate (PMMA). Flat ended steel cylindrical rods (D = 4 mm, L = 20 mm) were accelerated using a gas

gun to speeds up to 330 m/s. The targets were titanium rods (D = 16 mm, L = 25 mm) and PMMA blocks (L = 40 mm, W = 60 mm, t = 2.54 mm). Transmission Electron Microscope (TEM) was used to obtain images for the shear bands. For the titanium, a shear band of a V-shape pattern was observed, and spherical cavities were reported to occur in the band. Cavities and cracks were also seen in shear bands in the PMMA. Rogers and Shastry (1980) used cylindrical steel projectiles (D = 0.6", L = 4") to impact plates of different materials with thickness ranges from 1/4" to 5/16". The plates were made of AISI 1040 steel, AISI 1018 steel, and AISI 1075 steel. Microhardness tests were made across the shear bands. Mircohardness profiles show that the central zone of the shear band has the highest hardness. Microscopic images indicated that the deformed band preceded the formation of the transformed band. Ballistic impact experiments of 9.5 mm thick 7039-T6 aluminium and 6 mm thick titanium plates were conducted by Woodward et al. (1984). They showed that both materials fail by plugging by shear bands.

Bourne et al. (1984) used hollow cylinders (D = 40, L = 70 mm, t = 1.8 mm) of iron, copper, aluminum, and steel under explosive loads. Three phenomena were observed in the formed fragments under high strain loading, namely twinning, recrystallization, and shear bands. Twinning happens at normal rates of strain by a dislocation movement mechanism and occurs at low temperatures. Recrystallization occurs if the deformation is sufficiently large and rapid to heat the fragments above their recrystallization temperature, which usually leads to grain sizes smaller than those in the original material. When the heat generated by the plastic deformations does not have sufficient time to dissipate, shear bands occur. Initiation and propagation characteristics of dynamic shear bands in single edge notched specimens made of C300 maraging steel (which is known for possessing superior strength without losing malleability) were studied experimentally by Gudure et al. (2001). They employed a two dimensional high speed infrared camera to measure the evolution of the temperature field during the formation of the shear band. Infrared images showed the transition of crack tip plastic zone into a shear band. In addition, hot spots distributed along the length of a well developed shear band were observed.

Affourad et al. (1984) investigated four martensitic steel (20CND8, Z50CDV, 35 NCDV16, and 4340) cylinder specimens (D = 6 mm, L = 6 mm). The standard compression split Hopkinson bar was used to test the cylinders. The microscopic images showed that fracture is accompanied by the development of shear bands which lead to the formation of cracks, and that fracture always forms on shear surfaces inclined at about 45º. Lee et al. (2004) conducted high velocity impact experiments through a wide range of strain rates (10^{-3} to 7.5×10^{3} sec^{-1}) on 304L stainless steel gas tungsten arc welded joints, using compressive split Hopkinson bar. The impact properties of the tested weldments showed a high dependency on the applied strain rate. As the strain rate increases, the flow stress increased and the fracture strain decreased. The main fracture mechanism was adiabatic shearing.

Ballistic experiments on titanium Ti-6%Al-4%V were done by Timothy and Hutchinson (1985). They reported that the shear bands consist of regions of very intense shear deformation of the same original microstructure modified by the effect of elevated temperature. They performed microhardness tests on these bands and showed that the smaller the width of the shear bands, the higher the hardness of that band. Spherical cavities were sometimes observed in the shear bands. Grebe et al. (1985) conducted ballistic impact experiments on 12.5 mm thick plates. Commercial purity titanium and Ti-6%-Al-4%V alloy were used with stepped front portion steel cylinder projectiles. Microscopic images showed spherical and elliptical voids along the shear bands. Microindentation hardness tests were carried out on the shear bands region, but the results showed only slight differences between the band's hardness values and adjacent region's hardness values. Duan et al. (2003) studied two kinds of steel target plates, medium (0.45%) carbon steel and 30CrMnMo steel, under projectile loading. It was seen that the medium carbon steel did not easily form ASBs, while the 30CrMnMo steel with higher strength and hardness formed two kinds of ASBs as illustrated in Figure 1.7. The first kind of ASBs in 30CrMnMo steel was 45º with respect to the penetration direction, and cracks were found along the ASBs. The width of the ASB was about 20 μm. The second kind of ASBs was 45º with respect to the opposite direction of penetration, and their width is around 10 μm, and there were small cracks observed in them. Both of the two kinds of ASBs originated from the perforation surface.

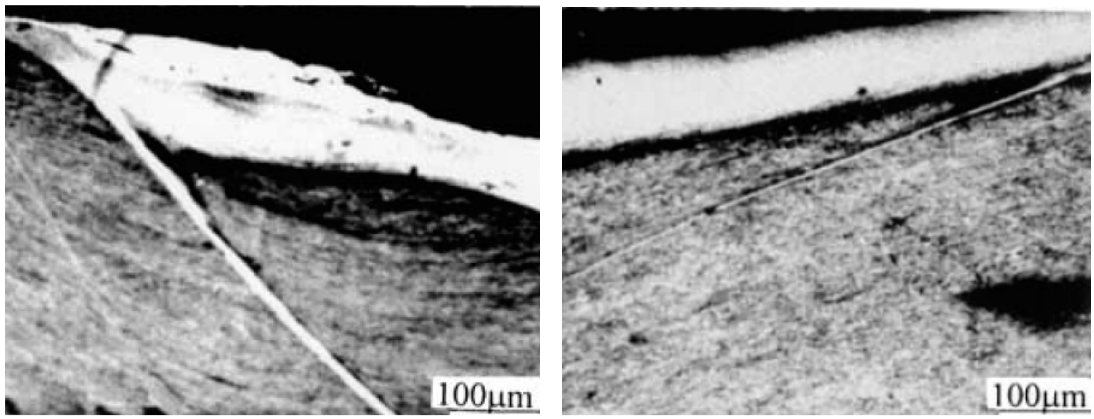

(a) (b)

Figure 1.7: In 30CrMnMo steel, (a) the first kind of ASBs oriented about 45º with respect to the penetration direction, (b) the second kind of ASB oriented about 45◦ with respect to the opposite direction of penetration (Duan et al., 2003).

The summary by Shockey (1988) of a series of experiments showed that material fails by nucleation, growth, and coalescence of voids under dynamic tensile loading. Contrary to what was believed at that time, the metallographic observations of contained exploding cylinders showed that microstructural features are not important to shear bands. They reported that in 4340 steels shear band initiation was apparently unaffected by microstructural features. This

was justified by the assumption that the shear band paths do not seem to deviate from the surfaces of maximum shear strain even when inclusions existed nearby. Giovanola (1988a, 1988b) experimented on hollow 4340 steel cylinders and used the Hopkinson torsion bar. He reported that three features were clear in the shear band fracture surfaces: smeared material, pattern of microvoids, and smeared knobby material. Xu et al. (2001) studied microstructural evolution in localized shear deformation in an 8090 Al–Li alloy at ambient temperature and 77 K. Both types of ASBs were seen in the alloy. They found that the deformed shear bands in tests at 77 K are not as well defined as those developed at ambient temperature. Adiabatic shearing and its effect on fracture behavior of AISI 4340 steel at high compressive strain-rate of about 1.9×10^{3} s^{-1} was investigated by Odeshi et al. (2005). They noted that cracking was initiated by formation of micropores during adiabatic heating and thermal softening along the shear bands. As adiabatic shearing proceeded, the pores coalesced to form clusters of pores. These clusters are responsible for microcrack initiation, which precedes the shear failure along the adiabatic shear bands. Duan and Wang (2005) studied the fine microstructure of the ASBs in the serrated chips of low alloy steel $30CrNi_3MoV$ subjected to orthogonal cutting conditions. The results show that the structure between the center of the ASB and matrix is different, and the average microhardness values in the shear band (which consisted mainly of martensite, χ-Fe_5C_2, F_3C and austenite) exceeded quenched martensite hardness. Zhang and Clifton (2003) reported results for pressure-shear plate impact experiments designed to study the competition between dynamic shear fracture and dynamic shear band formation for a crack subjected to plane wave loading in Mode III fracture. Propagation of a shear band ahead of the main crack was analyzed. The predicted speed of propagation of the tip of the band is found to be substantially less than that corresponding to the measured extension of the shear band in the experiments. Reduced shearing resistance in the shear band, presumably due to thermal softening, is viewed as the likely explanation for the relatively long shear bands observed. Kalthoff (2000) in his pioneering work of loading edge cracks by edge impact, used three different types of materials, namely, Araldite B epoxy resin, high strength maraging X2 NiCoMo 1895 steel and aluminum alloy Al 7075. The epoxy resin failure was by tensile cracks in the whole range of the applied strain rate. The high strength steel showed tensile cracks failure at low rate of applied loading, but above certain limit of loading rate adiabatic shear bands was found to form. In aluminum material the failure was in the form of adiabatic shear bands in low rates of loading as well as in high rates of loading. ASBs were even found in aluminum specimens at quasi static conditions. He also reported a significant increase in microhardness inside the ASB region, which agrees with many of the results of other researches.

Besides the experimental work, several theoretical models have been developed during the last decades that can be found in the literature. Also a considerable amount of simulation work has been done, especially by using finite element method. Li et al. (2002) carried out two and three dimensional mesh free

Galerkin simulation of adiabatic shear bands in pre-notched plate under impact load. They were able to capture the details of the adiabatic shear band to a point where the periodic temperature profile inside shear band at the microscale can clearly be seen. The simulation also showed an intense high strain rate region in front of the shear band tip, which they believe is caused by wave trapping at the shear band tip. They suggested that this might be the main reason of damage and stress collapse inside the shear band and provides a key link for self-sustained instability. Baucom and Zikry (1999) conducted a perturbation analysis on material instabilities and adiabatic shear bands under high strain rate load conditions. They were able to characterize the material instabilities beyond the initial instability point, and then it was possible to monitor the strength of this material instability throughout the deformation history to distinguish between material instabilities and shear strain localization. Zhu and Batra (1990) studied the problem of plain strain thermomechanical deformations in viscoplastic body that contains a rigid ellipsoidal inclusion at the center, subjected to high strain rate. The rigid inclusion can acts as a second phase particle such as oxides or carbides in steel, and can act as a nucleus for the shear band. The results showed that the shear band initiates near the tip of the inclusion and propagates along a line inclined 45º with respect to the horizontal axis. The effective stress near the inclusion tip drops noticeably near the tip of the inclusion and as the band propagates along the 45° direction the shear stress drops also. This was followed somewhat later by a sharp increase in the maximum principal logarithmic strain at the same point. Brun et al. (2003) utilized the boundary element method to analyze the incremental elastic deformations resulting from a given homogeneous strain. Shear bands are analyzed as special case of bifurcations of elastic structures. This special case where shear bands may occur as the first possible bifurcation is the so-called "van Hove condition", in which the solid is subject to prescribed displacements over the entire boundary and the current state (deformation and stress) is homogeneous. Batra and Wang (1994) studied finite dynamic plane strain thermomechanical deformations of a thermally softening viscoplastic body of square cross-section subjected to combined compression and shear at high strain-rate. Different ratios of the compressive to shear loadings were applied. A material thermal defect in the body was entered into the analysis by adding a temperature bump centered at the centroid of the cross-section, while the rest of the body is under uniform initial temperature distribution. This higher temperature at the centroid softens the material there and causes more deformation at that area. These higher deformations around the centroid of the cross-section heat it up more and the temperature there rises faster than the rest of the body, and eventually instability initiates at the centroid and propagates to one edge in the direction of maximum shearing.

Kim and Batra (1992) also investigated thermomechanical deformations of a thermally softening viscoplastic block undergoing overall adiabatic simple shearing deformations. The analysis accounted for the dependence of the specific heat, thermal conductivity and shear modulus of the material on the temperature. To ensure the formation of an ASB, a geometric defect in the form

of smoothly variable thickness was suggested. It was found that due to a higher initial temperature in the specimen, a delay in the initiation of the shear bands occurred, and the width of the bands was wider. Another numerical approach for studying thermo-visco-plastic deformation was developed by Zhou et al. (2006). They were able to simulate fully localized plastic flow with high resolution and good efficiency. This was applied to ASBs where the interactions between a single shear band and its surroundings and between shear bands themselves was taken into account. The study showed that a shear band may grow intermittently because of the interactions with other bands. They suggest that this method is specifically adequate for investigating the self-organized multiple ASBs. Edwards et al. (2005) developed a model for quantifying shear band propagation in bulk metallic glasses. The stress, temperature, and band propagation speed were implemented in the model. The model quantifies the shear-band length, width, and speed, as well as the direction of propagation and the magnitude of displacement across the band. Feng and Bassim (1999) modeled the formation of ASB in AISI 4340 steel using the finite element method. Both strain hardening and thermal softening were considered in the modeling during initialization and growth of the shear band. The obtained results show that the ASB could initialize at material defects. The stress evolution for the ASB was roughly divided into three stages. In the first stage, the stress resistance stays constant which indicates the absence of any plastic deformation. It then increases to some extent due to strain hardening effect. Finally a significant decrease occurs where thermal softening dominates. The growth of the ASB was affected by the strain hardening, thermal softening and thermal conduction. They state that “without thermal conduction, it appears impossible to increase the width of the ASB.”

Voyiadjis and Dorgan (2004), in order to predict the observed characteristic width of shear bands in plastic materials, used internal length scales by the incorporation of higher-order gradients into the constitutive equations. Voyiadjis and Abed (2007) utilized physically based yield functions for body-centered cubic (bcc) and face-centered cubic (fcc) types of metal structures in investigating necking and dynamic shear localizations over a wide range of temperatures and strain rates. The Consistency model was employed in determining the increment of the viscoplastic multiplier and consequently a proper definition for the continuum elasto-viscoplastic tangent modulus is derived. Mesh-independent results were obtained using the finite element analysis in investigating the localization behavior for tantalum, vanadium, and niobium for bcc metals and OFHC copper for fcc metals. Voyiadjis and Abu Al-Rub (2007) and Abu Al-Rub and Voyiadjis (2007) presented within the finite element context the numerical algorithms for the integration of the thermodynamically consistent formulation of geometrically nonlinear gradient-enhanced model. Model capabilities were preliminarily illustrated for the dynamic localization of inelastic flow in adiabatic shear bands and the perforation of a 12mm thick Weldox 460E steel plates by deformable blunt projectiles at various

impact speeds. The simulated shear band results well illustrated the potential of the proposed model in dealing with the well-known mesh sensitivity problem.

Bronkhorst et al. (2006) conducted an experimental and numerical study on hat-shaped samples to investigate the shear localization growth. The hat-shaped specimen is an axisymmetric sample with an upper ‘‘hat’’ portion and a lower ‘‘brim’’ portion with the shear zone located between the hat and the brim. This geometry has been widely used to study the initiation and propagation of the shear bands. The shear zone length was 870–890 μm with deformation imposed through a split-Hopkinson pressure bar system at maximum top-to-bottom velocity in the range of 8–25 m/s. Two materials were used, tantalum and 316L stainless steel samples. The tantalum samples did not show shear bands but the stainless steel sample formed a late stage shear band. Experimental results were compared to finite element analysis using both conductive and adiabatic continuum models, and the models gave good prediction of the experimental data. The models suggested that for an initial temperature of 298º K, a temperature in the neighborhood of 900º K was recorded within the shear band. The numerical results for stainless steel suggest that melting temperature was reached throughout the shear band shortly after peak load. In addition to the shear stress, a significant normal stress relative to the shear zone basis line existed. Mason and Worswick (2001) studied adiabatic shear localization in three ferrous metals: annealed Armco and as-received Remco iron, both of which are high purity alpha iron; shock-hardened Remco iron; and 4340 steel quenched and tempered to a range of hardness levels. Punching-shear experiments were performed using a compressive split-Hopkinson bar at different initial temperatures. Experimental evidence from microscopical images showed that the tempered 4340 steels were susceptible to localization through adiabatic shear banding; but on the other hand, as-received and shock-hardened Remco iron and annealed Armco iron were not. Finite element simulations were also performed to simulate the experiments using two adiabatic shear failure criteria, namely maximum shear stress with a minimum critical shear strain rate, and the second is flow localization. The onset of instability was successfully predicted by both criteria, but the deformation which follows the instability was not well predicted.

1.3 Objectives and Methodology of Study

The main objective of this study is to develop a better understanding for the behavior of shear bands and shear localization during deformation of metals under high strain rates and impact loading. Many factors that affect this phenomenon should be accounted for in this work, such as strain rate dependence, initial temperature, and the degree of strain hardening of the material. This will be done through developing a constitutive model for metals that can capture the effect of the factors mentioned before. Moreover, this constitutive model should also be able to capture the softening effects associated

with high strain rate inelastic deformations, which are attributed mainly to the localized high rise in temperature.

The key technical ingredients of simulating dynamic shear band propagation are two: (1) identifying micromechanical characterization of the material such as a length scale that can help in regularizing the adiabatic shear band problem, and (2) constitutive modeling in post-bifurcation phase, i.e., how to simulate the threshold of stress collapse inside the shear band.

It is known that in such problems the finite element solution usually suffers from mesh size dependence and mesh alignment sensitivity. The classical rate-independent plasticity theory does not possess any intrinsic length scale. Hence, it is incapable of regularizing the state variables during the analysis, which leads to numerical instabilities in the simulation of strain localization. To overcome this sensitivity, a gradient formulation in conjunction with rate dependence that will be incorporated into the different terms in the constitutive model that will be associated with a material intrinsic length scale.

Several regularization mechanisms have been introduced in constitutive modeling. They include: viscoplastic models (Needleman, 1988, 1989); thermal dissipation models (LeMonds and Needleman, 1986a, 1986b; Oliver, 1989; and Voyiadjis and Abed, 2007); non-local inelastic models (Bazant et al., 1984; Bazant and Pijaudier-Cabot, 1988; and Cabot and Bazant, 1987); strain gradient models (Aifantis, 1992; Zbib and Aifantis, 1992; de Borst and Sluys, 1991; de Borst and Pamin, 1996; Voyiadjis et al., 2001; and Voyiadjis and Dorgan, 2004); and others.

In the current study, both gradient theory and viscoplasticity will be used as regularization approaches to overcome the numerical instabilities that would appear during the simulation of shear localizations. Viscoplasticity imposes an implicit length scale. However, gradient theory will introduce an explicit length scale; that is a mechanical viscous length scale. Sometimes, a thermal length scale can also be introduced. It was reported by Li et al. (2002) that usually, the thermal length scale is about 100 μm while the mechanical viscous length scale is only around 1 μm. Zhu and Zbib (1995) showed that the deformation length scale for typical steel is about two orders of magnitude larger than the thermal length scale. This contradiction may be attributed to some other factors that affect the determination of these length scales such as the higher sensitivity of the thermal length scale on the strain rate. This will be addressed in the present study through the introduction of strain dependency in the length scale formulation. Also it has been shown that the effect of including thermal gradients on the shear band characteristics is less than that of material strain gradients. Hence, the thermal gradient will not be considered here. On the other hand, Batra (1987) noted that although there are several length scales in strain-rate gradient-dependent materials, their effect on the ASBs is not clear.

The mechanical viscous length scale is the one that will be associated with the viscoplasticity as a material rate dependent property, and since the problem under investigation here is a dynamic problem, a dynamic length scale should be also used in this gradient theory. One way to obtain such a length scale is through experimental results of dynamic instrumented indentation. The indentation tests are usually used to measure one of the basic material characteristics which is the hardness of metals. These tests can be described simply as forcing a hard indenter into a relatively softer material and the load on the indenter is measured versus the indentation depth. Micro- and nano-indentation tests have shown that the material hardness increases with decreasing indentation size (McElhaney et al., 1998; Lim and Chaudhri, 1999; Elmustafa and Stone, 2003; Abu Al-Rub and Voyiadjis, 2004; and Voyiadjis and Abu Al-Rub, 2002). However, the current available testing equipment can run dynamic hardness tests at only macro scales, and other machines can run nano-indentaion tests at static loads, and there is no equipment that can do dynamic nano-indentation tests. For this reason, nano–indentation tests will be carried out in this study only at static rates to find static material length scale. The dynamic effect will be taken into account through a proposed simple model that will be verified from hardness tests.

Many researchers have tried to address the indentation size effect problem through a number of gradient enhanced theories that incorporate an intrinsic length scale in the constitutive equations which are originally based on the classical continuum approach. A typical gradient theory includes a higher order derivative term in the constitutive equation along with coefficients that represent length scale measures of the deformed material in the microscopic level. The gradient plasticity theories have shown good agreement with the aforementioned material size dependence that was observed in instrumented hardness experiments (Shu and Fleck, 1998; Nix and Gao, 1998; and Huang et al., 2000). Gradients are introduced in the constitutive relationships to account for the microstructural interaction where the material behavior at any point is assumed to depend not only on the state of that point but also on the state of its neighboring region.

Finally, the proposed model will be implemented in Abaqus/Explicit user subroutine to analyze and solve different two- and three-dimensional finite element models of shear localization problems under different conditions. Using explicit finite element will ensure taking the effect of mass inertia into consideration. The stresses, strains, strain energies, viscous dissipation, and load-displacement curves will be obtained and compared to available experimental data in order to verify the proposed model and approach.

CHAPTER 2: PLASTICITY AND VISCOPLASTICITY THEORY

2.1 Introduction

The material will deform plastically with irreversible deformation if it is loaded beyond a given stress threshold. A brittle material such as concrete, glass, or rock has only elastic deformation under tension before it fractures. On the other hand, rocks and concrete under high confining pressure can undergo substantial plastic deformation before failure and exhibit ductile material properties. Metals generally show considerable amount of plasticity even in the absence of confining pressure.

The theory of plasticity is an area in mechanics of materials that deals with the plastic deformation and the limit load carrying capacity of materials and structures. Plasticity describes the theories and methods of yield initiation of materials under complex stress state and calculation of stresses and strains in a deformed structure after part or the whole structure has yielded. As in the case of elasticity, it is necessary to establish equations of equilibrium and compatibility and to determine the relations between stress and strain in the form of evolution equations. In addition, some conditions of yield initiation are needed, which is usually referred to as the yield criterion or yield function.

In 1864, two notes were presented by Tresca (1864) dealing with the experimental investigations on plastic flow of metals under great pressure. He first postulated a yield condition for the continuum problem that became the well-known Tresca yield criterion. Saint-Venant (1870) was the first to set up the fundamental equations of plasticity and to use them to solve several practical problems. The following assumptions are introduced in the formulation of the fundamental equations of plasticity:

1. The volume of the material does not change during plastic deformation; i.e. the Poisson's ratio equals half.
2. The directions of principal strains coincide with the directions of principal stresses for isotropic materials;
3. The maximum shearing stress at initiation of plasticity is equal to a specific constant. This means that the Tresca criterion was used as a yield condition. Sometimes, it is referred to as the maximum shear stress criterion or single-shear criterion.

Using these hypotheses, Saint-Venant solved several problems related to plasticity such as torsion of circular shafts, pure bending of rectangular prismatic bars, and the deformation of hollow circular cylinders under the internal pressure. In fact, Saint-Venant initiated the study of a complete new field of solid mechanics. Saint- Venant called the new subject Plasticodynamics. Since that time, plasticity has been the object of considerable research.

The theory of plasticity was originally developed for the description of the behavior of metallic materials. From the microscopic point of view, the

deformational mechanisms of metal are quite different from those of concrete, rock and soils. While the later is due to the initiation and nucleation of microcracks at the aggregate-mortar interface as well as through the mortar, air or cracks, the former is due to the arrangement of dislocations of polycrystals.

2.2 Yield Strength and Yield Criteria

A yield criterion is a function of stress state and material parameters. The suitability of any proposed yield criterion must be examined by experiment results. A great many experiments and investigations on yield criteria of metallic materials were conducted by Hancock (1908), Smith (1909), Taylor and Quinney (1931), Winstone (1984), and many others. The reasonable choice of a yield criterion is very important for calculation and applications.

After the comparison of the shear yield strength and tensile yield strength among 30 different materials, Kishkin and Ratner (see Ratner, 1949) divided the metals into four kinds according to the ratio of the shear yield strength to tensile yield strength τ_s/σ_s as follows:

1. $\tau_s/\sigma_s \cong 0.50$ (0.48 – 0.53, five materials), which fits the single-shear yield criterion (Tresca yield criterion).
2. $\tau_s/\sigma_s \cong 0.58$ (0.54 – 0.62, nine materials), which fits the Huber-von Mises yield criterion.
3. $\tau_s/\sigma_s \cong 0.68$ (0.67 – 0.71, eight materials), which agrees with the twin-shear yield criterion.
4. $\tau_s/\sigma_s < 0.4$ (0.31 – 0.41, eight materials), which gives a nonconvex result that does not agree with existing criteria at that time.

With regard to the ratio of shear strength to tensile strength of metals, the values in the literature are generally in the range 0.52 – 0.63 for carbon steel and 0.65 – 0.78 for alloy steel.

Generally, the ratio of shear yield stress τ_y to the tensile yield stress σ_s is different for different materials. According to the convexity of yield surface, the shear yield strengths are in the range of $\tau_s = (0.5 - 0.667)\sigma_s$ for those metallic materials that have the same strength in tension and compression. Yield stresses of metallic materials are higher than $\tau_s/\sigma_s = 0.5$. Many yield stresses of high-strength steel, high-strength alloys, and non-metallic materials are higher than $\tau_s = 0.667\sigma_s$. These materials might be of the kind that has different strengths in tension and in compression.

2.3 Elasto-Plastic Constitutive Relations for the Uniaxial Case

The post-yielding and loading-and-unloading behaviors of the materials are related to the stress-strain relation for plastically deformed solids, namely the constitutive relations for plastic deformation of engineering materials. Classical plasticity theory postulates plastic flow rules such as the Levy-Mises and Prandtl-Reuss equations, Drucker's stability concept, isotropic, kinematic and combined

hardening rules, and derives general stress-strain relations for plastic deformation of different materials.

For a stress-strain curve shown in Figure 2.1 of an elasto-plastic material, the behavior can be characterized by an elastic region with an elastic modulus E until yielding commences at the axial yield stress σ_y, and a plastic region with a continually varying local tangent E_T to the curve. E_T is called the elasto-plastic tangent modulus. In the elastic region, the stress-strain relation is usually assumed to be a linear form such as:

$$\sigma = E\varepsilon \tag{2.1}$$

where σ is the uniaxial stress, ε is the uniaxial strain, and E is the elastic modulus. In the case of small strains, the total strain increment $d\varepsilon$ in the uniaxial stress state is the sum of the elastic strain increment $d\varepsilon^e$ and the plastic strain increment $d\varepsilon^p$, i.e.:

$$d\varepsilon = d\varepsilon^e + d\varepsilon^p \tag{2.2}$$

The stress increment can be related linearly to the elastic strain increment in the plastic region as follows:

$$d\sigma = Ed\varepsilon^e = E(d\varepsilon - d\varepsilon^p) \tag{2.3}$$

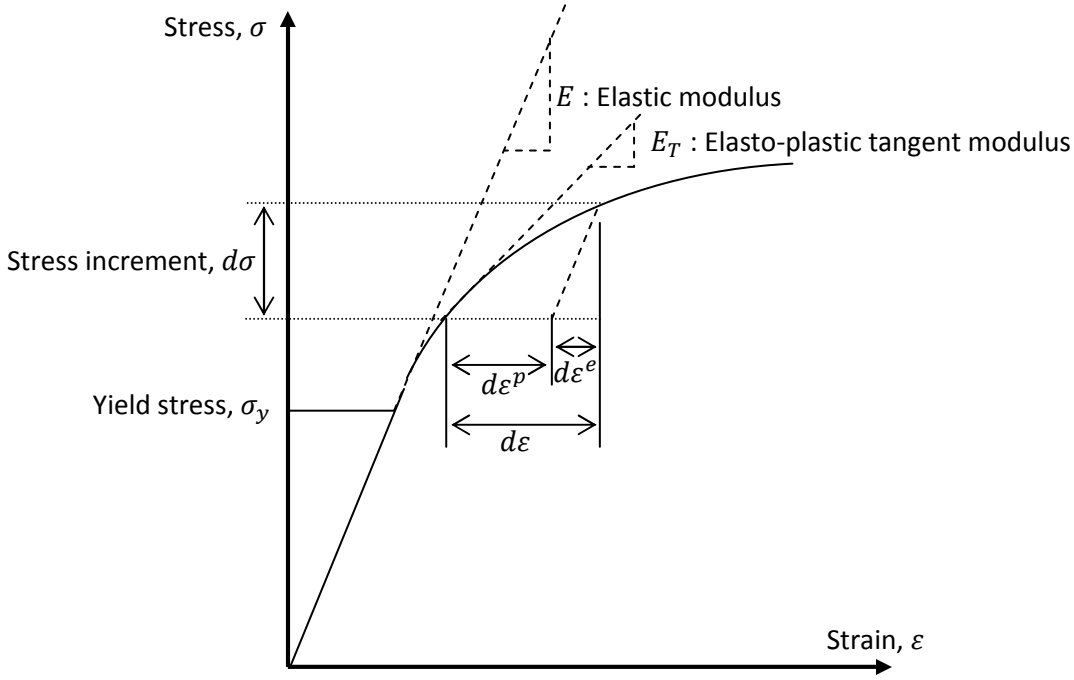

Figure 2.1: Uniaxial elasto-plastic stress strain curve.

The initial yield point σ_y differentiates between the elastic and plastic regions. The stress in the plastic region can be determined by a hardening rule:

$$\sigma = \sigma(\kappa) \tag{2.4}$$

where κ is the hardening parameter. In the uniaxial stress state, the plastic strain ε^p is usually used on the hardening parameter, i.e. $\kappa = \varepsilon^p$. The plastic strain ε^p is history or path dependent, and can be calculated by:

$$\varepsilon^p = \int d\varepsilon^p \tag{2.5}$$

Using the strain increment decomposition, the plastic strain increment can be expressed as:

$$d\varepsilon^p = d\varepsilon - d\varepsilon^e = \frac{d\sigma}{E_T} - \frac{d\sigma}{E} = \left(\frac{1}{E_T} - \frac{1}{E}\right) d\sigma \tag{2.6}$$

where the elasto-plastic tangent modulus E_T is a function of both the stress and plastic strain:

$$E_T = E_T(\sigma, \varepsilon^p) \tag{2.7}$$

which should be determined experimentally from a simple uniaxial yield test. Based on Equations (2.6) and (2.7), an incremental constitutive relation of the material can be obtained. In fact, the resulting constitutive relation differs for plastic loading and elastic loading or unloading. It is necessary to identify whether the process is in the plastic loading or elastic unloading region. Loading and unloading represents a deformation process starting from a plastic state and continues to deform plastically and then returns to the elastic region. A previous plastic state is always implied. The loading and unloading criterion in the uniaxial stress state can be represented as:

$$\sigma d\sigma \geq 0 \text{ for loading} \tag{2.8}$$

$$\sigma d\sigma < 0 \text{ for unloading} \tag{2.9}$$

It is seen that the fundamental elements of the plastic deformation includes initial yielding of the material, strain hardening and subsequent yielding, incremental constitutive equation and loading and unloading criteria, etc. For the three-dimensional case, the constitutive equations can be represented in tensor notation, which will be discussed in the following sections.

2.4 Stress-Strain Relations for Three Dimensional Case

The extension of one-dimensional plasticity into a multi-dimensional plasticity provides an even greater challenge both experimentally and theoretically. In the early development, two major schools of thought were

developed; the flow theory and the deformation theory. The deformation theory was proposed by Hencky in 1924 and the approach was used thereafter by Russian researchers. The Hencky equation is an elastic stress-strain relationship in the three-dimensional case that has the following form:

$$\varepsilon_{ij} = \frac{\sigma_{ij}}{2G} - \frac{3\nu}{E}\sigma_m\delta_{ij} \tag{2.10}$$

where ε_{ij} is the total strain tensor, σ_{ij} is the stress tensor, δ_{ij} is the Kronecker delta, G is the shear modulus, ν is the Poisson's ratio, and σ_m is the mean stress (and sometimes called the hydrostatic pressure) and equals $\sigma_{kk}/3$. The material constants are related by the equation:

$$G = \frac{E}{2(1+\nu)} \tag{2.11}$$

The elastic and shear modulii become the elasto-plastic tangent modulii in the plastic regime. Equation (2.10) may now be rewritten as the following form:

$$\varepsilon_{ij} = \frac{1}{E}\left[(1+\nu)\sigma_{ij} - 3\nu\sigma_m\delta_{ij}\right] = \frac{1}{E}\left[(1+\nu)\delta_{ik}\delta_{jl} - \nu\delta_{ij}\delta_{kl}\right]\sigma_{kl} \tag{2.12}$$

The elastic stress tensor can then be obtained to be:

$$\sigma_{ij} = \frac{E}{1+\nu}\left[\varepsilon_{ij} + \frac{3\nu}{1-2\nu}\varepsilon_m\delta_{ij}\right] = \frac{E}{1+\nu}\left[\delta_{ik}\delta_{jl} + \frac{\nu}{1-2\nu}\delta_{ij}\delta_{kl}\right]\varepsilon_{kl} \tag{2.13}$$

where $\varepsilon_m = \varepsilon_{kk}/3$ is the mean strain. One can note that the total strain ε_{ij} rather than the strain increment $d\varepsilon_{ij}$ is derived and, therefore, this deformation theory is also known as the total strain theory. On the other hand, the flow theory emphasizing the strain increment is also known as the incremental theory. The deformation theory is convenient for use, due to its mathematical simplicity, in solving problems with proportional loading. The final state of strain is determined by the final state of stress. However, it is known that the equations of deformation theory are not suitable for nonproportional loading conditions and hence the deformation theory will not be further pursued here. However, one can express the stress strain relation in incremental form from these equations as follows:

$$d\varepsilon_{ij} = S_{ijkl}d\sigma_{kl} \tag{2.14}$$

or

$$d\sigma_{ij} = C_{ijkl}d\varepsilon_{kl} \tag{2.15}$$

where

$$S_{ijkl} = \frac{1}{E}\left[(1+\nu)\delta_{ik}\delta_{jl} - \nu\delta_{ij}\delta_{kl}\right] \tag{2.16}$$

and

$$C_{ijkl} = \frac{E}{1+\nu}\left[\delta_{ik}\delta_{jl} + \frac{\nu}{1-2\nu}\delta_{ij}\delta_{kl}\right] \tag{2.17}$$

in which S_{ijkl} is the compliance tensor, and C_{ijkl} is the stiffness tensor. The stiffness tensor has 21 independent constants for anisotropic material, and reduces to only two independent constants for isotropic materials.

2.5 Yield Surface and Strain Hardening

For various engineering materials, a yield criterion indicating the stress level at which plastic flow commences must be postulated. A relationship between stress and strain must be developed for post-yield behavior, i.e. when the deformation is made up of both elastic and plastic components. The yield surface separates the plastic region from the elastic region. The change of the stress state from the yield surface toward its interior will cause elastic unloading. Plastic loading will occur only if the increment of the stress is directed toward the outside of the yield surface.

The deviatoric stress s_{ij} can be written as:

$$s_{ij} = \begin{bmatrix} \sigma_{11} - \sigma_m & \sigma_{12} & \sigma_{13} \\ \sigma_{21} & \sigma_{22} - \sigma_m & \sigma_{23} \\ \sigma_{31} & \sigma_{32} & \sigma_{33} - \sigma_m \end{bmatrix} \tag{2.18}$$

then the yield function can be represented by:

$$F(s_{ij}, k^2) = 0 \quad \text{or} \quad f(s_{ij}) = k^2 \tag{2.19}$$

where k is a material parameter which may be determined experimentally. It can be a function of a number of material strength coefficients, or a constant for an elastic-perfect-plastic material. The parameter k represents the radius of the yield surface and, when it increases, the yield surface expands in size. The term k can be defined as a function of a hardening parameter, κ, thus the yield function can be extended to describe post-yield of the material, or $k = k(\kappa)$.

For isotropic material, the yield function is independent of the orientation of the coordinate system employed, therefore, it is usually presented by a function of the three deviatoric stress invariants, i.e.:

$$F(J_1, J_2, J_3, k^2) = 0 \tag{2.20}$$

where J_1, J_2 and J_3 are respectively the first, second and the third deviatoric stress invariants of the deviatoric stress tensor:

$$J_1 = s_{11} + s_{22} + s_{33} = 0 \tag{2.21}$$

$$J_2 = \frac{1}{2} s_{ij} s_{ij} \tag{2.22}$$

$$J_3 = |s_{ij}| \tag{2.23}$$

For the elasto-perfect-plastic material, the parameter k in the yield function is a constant. It means that the yield surface is independent of the plastic strain, thus the geometry and the size of the yield surface will not change with the successive deformation of the material. The post-yielding surface is exactly the initial one. The stress point remains on the yield surface during plastic loading condition, and the stress point moves in inside the yield surface during unloading. For a plastic hardening material, k can be defined by a work-hardening or strain-hardening parameter κ. The post-yielding surface is thus different from the initial yielding surface. The use of only the second invariant J_2 in the yield function leads to satisfactory results for most metals. In this case, the yield function is expressed as:

$$f(J_2) = k^2 \tag{2.24}$$

Equation (2.24) is known as the Huber-von Mises yield criterion (or simply Mises yield criterion) and is widely used in applications for metals. A physical interpretation of the Huber-von Mises yield criterion is that yielding begins when the elastic distortion energy reaches a critical value. This interpretation is reasonable for isotropic materials.

The total strain increments (Equation (2.2)) in three-dimensional case can be generalized as:

$$d\varepsilon_{ij} = d\varepsilon_{ij}^{e} + d\varepsilon_{ij}^{p} \tag{2.25}$$

where $d\varepsilon_{ij}^{e}$ is the elastic strain increment tensor, and $d\varepsilon_{ij}^{p}$ is the plastic strain increment tensor. The decomposition is correct for cases of infinitesimal strain only. In the case of finite strain, there will be geometrical elasto-plastic coupling between the elastic and plastic strain measures so that Equation (2.25) will lose its conventional physical meaning. However, CR-1018 steel which is the main material that will be studied here will be mainly used within the confines of small strain theory, and the additive decomposition can still be assumed to be valid.

After initial yielding, the stress level at which further plastic deformation occurs may be dependent on the current degree of plastic straining. Such a phenomenon is termed work hardening or strain hardening. Thus the yield surface will vary at each stage of the plastic deformation, with the subsequent yield surfaces being dependent on the plastic strains in some way. Due to its dissipation feature of the plastic deformation process it is history or path

dependent. In other words, there will not be a one-to-one correspondence between stress-strain during plastic deformation. Some alternative models which describe strain hardening in a material are illustrated in Figure 2.2. A perfect plastic material means that the yield stress level does not depend in any way on the degree of plastic deformation. If the subsequent yield surfaces are a uniform expansion of the original yield curve, without translation, the strain hardening model is termed isotropic. On the other hand if the subsequent yield surfaces preserve their shape and orientation but translate in the stress space as a rigid body, kinematic hardening is said to take place. Such a hardening model gives rise to the experimentally observed Bauschinger effect during cyclic loading. However, the Bauschinger effect is not considered in the isotropic hardening. Generally, the adiabatic shear band problem is not susceptible to cyclic loading, and therefore the use of isotropic hardening rule should be adequate in analyzing such a problem.

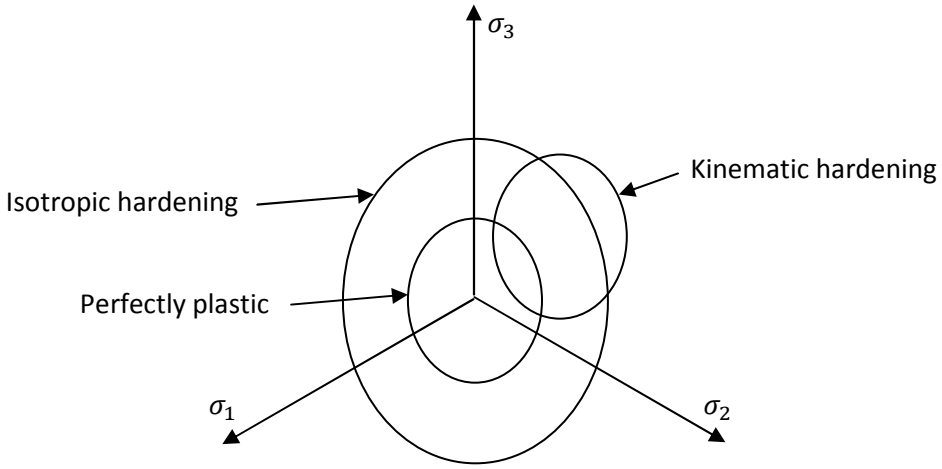

Figure 2.2: Yield surface of different strain hardening behaviors.

The progressive development of the yield surface can be defined by relating the yield stress f to the plastic deformation by means of the hardening parameter κ. This can be postulated to be a function of the total plastic work W_p, only. Plastic deformation can also be associated with the dissipation of energy so that it is irreversible. One now obtains:

$$\kappa = W_p \tag{2.26}$$

where

$$W_p = \int \sigma_{ij} d\varepsilon_{ij}^p \tag{2.27}$$

Alternatively, κ can be related to a measure of the total plastic deformation termed the effective, generalized or equivalent plastic strain which is defined incrementally as:

$$d\bar{\varepsilon}_p = \sqrt{\frac{2}{3} d\varepsilon_{ij}^p d\varepsilon_{ij}^p} \tag{2.28}$$

The hardening parameter κ is assumed to be defined as:

$$\kappa = \bar{\varepsilon}_p \tag{2.29}$$

where $\bar{\varepsilon}_p$ is the result of integrating $d\bar{\varepsilon}_p$ over the strain path. This behavior is known as strain hardening.
Strain state for which $f = k$ represent plastic state, while elastic behavior is characterized by $f < k$. At a plastic state $f = k$, the incremental change in the yield function due to an incremental stress change is:

$$df = \frac{\partial f}{\partial \sigma_{ij}} d\sigma_{ij} \tag{2.30}$$

Consequently one obtains:

$df < 0$ represents the case where elastic unloading occurs and the stress point returns inside the yield surface.

$df = 0$ represents the case where neutral loading occurs and the stress point remains on the yield surface.

$df > 0$ represents the case where plastic loading occurs for strain hardening material.

2.6 Plastic Flow Rule

The general mathematical treatment of the constitutive equation for plastic deformation or flow was proposed by Huber-von Mises in 1928. In elastic theory the strain tensor was related to the stress tensor through an elastic potential function, the complementary strain energy U such that:

$$\varepsilon_{ij} = \frac{\partial U}{\partial \sigma_{ij}} \tag{2.31}$$

By extending this idea to plasticity theory, Mises proposed that there exists a plastic potential function $Q(\sigma_{ij})$ related to the plastic strain increments $d\varepsilon_{ij}^p$ as follows:

$$d\varepsilon_{ij}^p = d\lambda \frac{\partial Q}{\partial \sigma_{ij}} \tag{2.32}$$

where $d\lambda$ is a proportional positive scalar factor called the Lagrangian multiplier. The plastic flow rule shown in Equation (2.32) is the so called plastic potential theory. The plastic potential $Q(\sigma_{ij}) = C$, or a constant, represents a surface in the six-dimensional stress space, and the plastic strain $d\varepsilon_{ij}^{p}$ can be represented by a vector that is perpendicular to the surface $Q(\sigma_{ij}) = C$.

A common approach in metal plasticity theory, is the use of associative plasticity that is to assume that the plastic potential function $Q(\sigma_{ij})$ is the same as the yield function $F(\sigma_{ij})$:

$$Q(\sigma_{ij}) = F(\sigma_{ij}) \tag{2.33}$$

then Equation (2.32) can be written as:

$$d\varepsilon_{ij}^{p} = d\lambda \frac{\partial F}{\partial \sigma_{ij}} \tag{2.34}$$

which indicates that the plastic flow vector is normal to the yield surface. This is called the associated flow rule. On the other hand, if $Q \neq F$, the flow rule is called nonassociated. Therefore in order to determine $d\lambda$, in associative plasticity, the yield function needs to be first defined.

The association of Q with F is based on an assumption whose validity can be verified empirically. Experimental observations show that the plastic deformation of metals can be characterized quite well by the associated flow rule, but for some porous materials such as rocks, concrete, and soils, the nonassociated flow rule may provide a better representation of their plastic deformation. Mathematically it can be shown using Drucker's stability postulate that for a material to be stable then it must satisfy Drucker's postulate, and the flow vector must be associated. Drucker (1951) proposed a unified approach based on his stability postulate to establish the general plastic stress-strain relations. One major consequence of Drucker's posulate is that it can be proved that the yield surface must be convex

Applying the Huber-von Mises yield criterion yields:

$$\frac{\partial J_2}{\partial \sigma_{ij}} = s_{ij} \tag{2.35}$$

where s_{ij} is the deviatoric part of stress tensor. Equation (2.34) then yields:

$$d\varepsilon_{ij}^{p} = d\lambda \frac{\partial F}{\partial \sigma_{ij}} = d\lambda s_{ij} \tag{2.36}$$

which is the Prandtl-Reuss equation, or the Levy-Mises equation if the elastic strain rate is ignored. Thus, within the general framework of the plastic potential

theory, the Prandtl-Reuss or the Levy-Mises equation implies the Huber-von Mises yield function and the associated flow rule.

2.7 Viscoplasticity

Metallic materials are generally strain-rate sensitive at high temperature, but not equally sensitive at room temperature. There are exceptions such as AISI Type 304 stainless steel and others. The 304 stainless steel is strain rate sensitive at room temperature even at the low strain-rate range of 10^{-6} to 10^{-3} s^{-1}; on the other hand, materials such as aluminum alloys are not strain-rate sensitive in this range. Metals are generally strain-rate sensitive under dynamic loading. The stress–strain curve for a higher strain-rate lies above that for a lower strain-rate. In other words, the material loaded at higher strain rate exhibits higher strength.

Due to low strain-rate sensitivity of most metals at room temperature in the strain-rate range of 10^{-6} to 10^{-3} s^{-1} (or quasi-static), the permanent deformation of metals has been classified as plastic deformation or rate-independent plastic deformation. This is an approximation, because in reality the metals are more or less strain-rate dependent. However, it is a reasonable approximation and it enables the development of theories of plasticity. The strain-rate sensitive plasticity is also known as viscoplasticity. Most theories of viscoplasticity are formulated by adding the strain-rate sensitivity to a theory of plasticity. Even within the quasi-static strain-rate range, the presence of strain rate effect leads to creep and stress relaxation. However, the strain-rate effect is especially significant under dynamic loading.

The mathematical structure underlying classical (rate dependent) viscoplasticity is motivated by examining the response of the mechanical device arranged as illustrated in Figure 2.3. The device possesses unit length and unit area, and consists of a dashpot with constant η that represents damping property of material, which is connected in parallel with a coulombic frictional device with constant σ_y that simulates initiation of plastic deformation, and a spring with elastic constant E as the material stiffness.

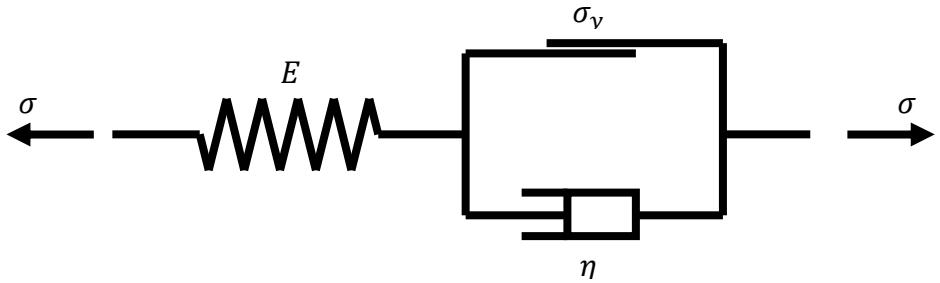

Figure 2.3: One dimensional rheological model illustrating the response of a one dimensional viscoplastic model.

Let σ be the applied stress on the device, and let ε be the total strain, then the additive decomposition of the total strain will be:

$$\varepsilon = \varepsilon^e + \varepsilon^{vp} \tag{2.37}$$

where ε^e is the strain in the spring. Hence:

$$\sigma = E\varepsilon^e = E(\varepsilon - \varepsilon^{vp}) \tag{2.38}$$

Next, two possibilities are examined. First, let the applied stress be less than the yield stress. This means the dashpot will not move and no instantaneous change should take place in the viscoplastic strain, i.e.:

$$\dot{\varepsilon}^{vp} = 0 \qquad \text{if} \qquad f(\sigma) = \sigma^2 - \sigma_y^2 < 0 \tag{2.39}$$

The second possibility is that the applied stress exceeds the yield stress. In this case the stress in the frictional device is σ_y and the stress on the dashpot, called the extra stress and denoted by σ_{ex}, is given as:

$$\sigma_{ex} = \sigma^2 - \sigma_y^2 \qquad \text{if} \qquad f(\sigma) = \sigma^2 - \sigma_y^2 \geq 0 \tag{2.40}$$

Using the fact that the stress σ_{ex} on the dashpot is connected to the strain through the viscous relationship:

$$\sigma_{ex} = \eta\dot{\varepsilon}^{vp} \tag{2.41}$$

one obtains:

$$\dot{\varepsilon}^{vp} = \frac{1}{\eta} f(\sigma) \qquad \text{if} \qquad f(\sigma) = \sigma^2 - \sigma_y^2 \geq 0 \tag{2.42}$$

if the ramp function (McCauly brackets) is denoted by:

$$\langle x \rangle = \frac{x + |x|}{2} \tag{2.43}$$

then the flow rule can be written as:

$$\dot{\varepsilon}^{vp} = \frac{\langle \phi \rangle}{\eta} \frac{\partial f}{\partial \sigma_{ij}} \tag{2.44}$$

This relation is usually referred to as a viscoplastic constitutive equation of the Perzyna type. The term $\gamma\langle\phi\rangle$ can be assumed to be the yield function normalized by the viscosity coefficient. However, in practice the term instead is expressed as a power law it in terms of the effective stress σ_e and the yield stress σ_y, so that:

$$\phi = \left(\frac{\sigma_e}{\sigma_y} - 1\right)^N \tag{2.45}$$

where N is a calibration variable. The yield stress σ_y can be a function of strain or any hardening parameter. The rate-independent elastic-plastic model is recovered if η approaches its minimum value η_o, which represents the value at which the viscosity is negligible.

Localization in material usually causes high deformation rates, which are reduced and distributed in the finite element mesh by means of the viscosity, which is the basic idea behind the rate-dependent behavior. The main disadvantage of the viscoplasticity theory is the necessity of adding an artificial feature, the viscosity, to the material behavior when it displays rate dependence. Its main advantage is that it does not need any additional global discretizations, since it requires only supplementary operations at the local level (constitutive law), whose implementation in common non-linear finite element packages is very simple.

The finite element package that will be used in this work, Abaqus/Explicit, already contains one form of viscoplasticity which is the bulk viscosity. Bulk viscosity introduces damping associated with the volumetric straining. Its purpose is to improve the modeling of high-speed dynamic events. There are two forms of bulk viscosity in Abaqus/Explicit. The first is found in all elements and is introduced to damp the "ringing" in the highest element frequency. This damping is sometimes referred to as truncation frequency damping. It generates a bulk viscosity pressure, which is linear in the volumetric strain:

$$p_{bv1} = b_1 \rho c_d L_e \dot{\varepsilon}_{vol} \tag{2.46}$$

where b_1 is a damping coefficient (default is 0.06), ρ is the current material density, c_d is the current dilatational wave speed, L_e is an element characteristic length, and $\dot{\varepsilon}_{vol}$ is the volumetric strain rate. The second form of the bulk viscosity pressure is found only in solid continuum elements. This form is quadratic in the volumetric strain rate:

$$p_{bv2} = \rho(b_2 L_e \dot{\varepsilon}_{vol})^2 \tag{2.47}$$

where b_2 is a damping coefficient (default is 1.2). The quadratic bulk viscosity is applied only if the volumetric strain rate is compressive.

CHAPTER 3: MATERIAL CONSTITUTIVE MODELING*

3.1 Introduction

The primary goal of developing any constitutive law is to have a tool that can describe material behavior. One of the most important relationships that describe the material performance of a structure when it is subjected to loading is the stress–strain curve. In order for a constitutive model to be widely applicable, it has to have the ability to account for any changes in temperature and strain rate which covers a very wide range of applications, ranging from regular static loading to high speed machining, high velocity impact, penetration mechanics and shear localization problems. In addition it is vital for the same model to be applicable at low temperatures in frigid conditions to very high temperatures such as in the case of the space shuttle.

Material behavior that includes strain rate and temperature dependence has been of great interest to researchers. The developed constitutive equations fall broadly into two groups:

a) Empirical constitutive equations (also called phenomenological models) that incorporate work-hardening, thermal softening, and strain-rate hardening terms. Work-hardening is usually expressed by a power hardening term that includes a work-hardening coefficient. The strain rate sensitivity is usually represented by a number of coefficients. The effect of temperature on the flow stress is represented by exponential or power-law functions. Examples of these constitutive models are the equations presented by Littonski (1977), Klopp et al. (1985), and Johnson and Cook (1983).

b) Microstructurally-based constitutive equations (also called physically based constitutive models) are based on the micromechanics of plastic deformation and are rooted in the thermally-activated motion of dislocations. The separation of short- and long-range barriers as well as their shape yields the strain, strain-rate, and temperature dependence of the flow stress. The models developed by Kocks et al. (1975), Zerilli and Armstrong (1987), Voyiadjis and Abed (2005) and Klepaczko (1988) integrate such an approach.

The objective of this chapter is to develop two different material models that can replicate the real behavior of metal alloys. The first model is a physically based model that depends on basic physical quantities, such as dislocation densities, Burgers vector, and activation energy. The second model is a simple empirical power model. Both models take into account the strain rate and temperature change in the material. The model that predicts a more realistic behavior of metal alloys will be used in the forthcoming finite element analysis. Finally, the models will be tested against dynamic hardness, which represents a multi stress state.

---

*Portions of this chapter are reprinted by permissions of ASCE.

3.2 Physically Based Model

The steel metal alloys consist mainly of iron which is a body-centered cubic (bcc) crystal structure, in addition to other different materials such as carbon (content between 0.02% and 1.7 or 2.0% by weight), manganese, tungsten, and nickel. Some of these additives have different crystal structure than iron; for example nickel has faced-centered cubic (fcc) crystal structure. For that reason one would expect that the behavior of bcc metals should be the major contribution to the behavior of steel alloys with a minor effect of the other additives. Body-centered cubic metals, such as iron, exhibit high strain rate and temperature sensitivity, and their mechanical properties such as yield and flow stresses are strongly affected by these factors.

Flow stress expressions are used to indicate the resistance to plastic flow of the material at any instant under any strain rate and temperature. Yield and flow stress are sensitive to variations of high strain rates. This sensitivity is observed in plots of yield stress or flow stress versus the logarithm of the strain rate for various strain values. Increasing the strain rate tends generally to increase the flow stress of the material and shift the entire stress-strain curve to higher stress levels. On the other hand, temperature has a more complicated effect on the yield and flow stress of metals. Temperature dependence of yield and flow stress of metals has been studied extensively by researchers, and based on experimental observations; the thermal behavior of yield stress can be approximated by this curve illustrated in Figure 3.1. Four main regions can be identified on the curve. The first region is at very low temperatures where the behavior would follow any pattern depending on the type of material. Although theoretically yield stress at these low temperatures should be decreasing, the yield stress would increase, decrease or stay constant with increasing temperature. At higher temperatures (the second region) yield stress decreases with increasing temperatures until it reaches the third region where temperature has no effect on yield stress. At very high temperatures stresses will start decreasing again with increasing temperature. In pure fcc metals the lattice friction stress is always low and the initial yield stress remains low even at low temperatures. For bcc metals, on the other hand, the lattice friction stress is significantly below a rough value of $0.2T_m$, (where T_m is the melting point in Kelvin) and it increases with decreasing temperature. The effect of increasing lattice friction is to increase the initial yield strength. Thus, for bcc metals below a roughly $0.2T_m$, the effect of decreasing temperature or increasing strain rate is to raise the overall level of the stress/strain curve. A practical consequence of this is that the increased strain rate may tend to decrease the range of stable elongation at room temperature for the stretch-forming operations in bcc metals. In fact, it is not necessary for all metals to have the whole four regions. For some metals the behavior may be limited to just one or two parts of the full range of the curve as it will be seen later for different metals.

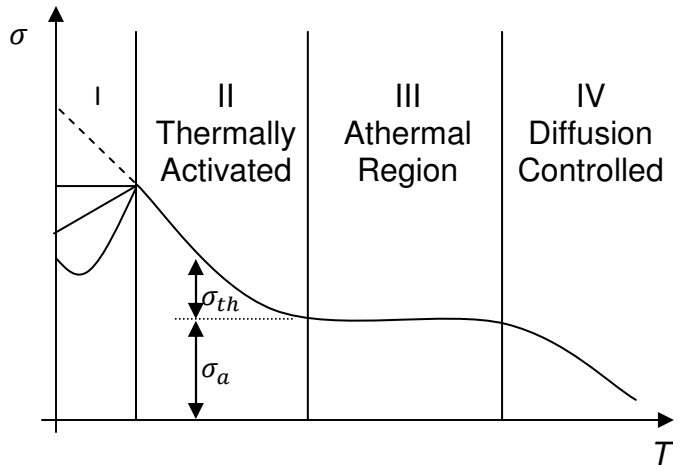

Figure 3.1: Schematic behavior of yield stress versus temperature of metals.

Crystal bcc and fcc structures show distinct differences between them in the mode of hardening and dependence on the strain rate and temperature. In bcc metals, the thermal yield stress, due to the Peierls barriers, shows strong dependence on the strain rate and temperature while the plastic strain hardening is independent of them which represent the athermal stress. For the case of fcc metals the thermal stresses is strongly dependent on the plastic strain due to the domination of the dislocation intersections on the mechanisms behavior of the thermal activation analysis.

Large plastic deformations often lead to failure by localized deformation and shear bands in ductile metals. This process is strain, strain rate, and temperature dependent. The sensitivity of bcc metals to high-temperature and strain-rate and their mechanical properties are attributed to the rate-controlling mechanism of the thermal component of the flow stress. While the activation volume has been shown to decrease with plastic strain for fcc metals, it is seen to be constant for bcc metals. Therefore an increase in strain rate should only produce a constant increase for the whole stress-strain curve for bcc metals. In addition, the activation volume for bcc metals is much smaller than for fcc metals, yielding a much higher temperature and strain-rate sensitivity. While a large number of studies have probed the mechanical behavior of a broad spectrum of metals, the details of the underlying deformation mechanisms remain poorly understood and in some cases controversial, (Hoge and Mukherjee, 1977; and Gourdin and Lassila, 1995).

Screw dislocations in bcc metals have non-planar dislocation cores (non-screw dislocations—including kinks—are relatively mobile), and so dislocation slip in bcc metals is generally controlled by the high Peierls stress (Duesbury and Vitek, 1998). Thermal activation aids dislocation glide by effectively

decreasing the intrinsic lattice friction (lowering the additional energy required to slip), which lowers the flow stress of the material. Thermal activation plays a considerable role in the double kink motion of screw dislocations; a small segment of a screw dislocation advances past an energy barrier forming short lengths of positive and negative edge character which rapidly run out of the crystal, pulling ahead the rest of the screw dislocation in the process. The yield stress in most bcc metals is strongly temperature-dependent, and one also expects strong rate dependency of the flow stress. One main important issue here is the coupled rate- and temperature-dependence of the mechanical behavior, motivated in particular by applications in high-strain-rate loading. Strain hardening is primarily accomplished through long-range barriers (Kocks et al., 1975) such as dislocation pile-up at grain boundaries. Since the long-range barriers are relatively temperature insensitive, increasing temperature tends to have a relatively small effect on the strain hardening. Sensitivity to impurities, especially at elevated temperatures, is also attributable to the open nature of the lattice which allows solute atoms to readily diffuse into the strain fields of dislocations, thus pinning them to the lattice. Excellent reviews of plastic deformation in bcc metals in general are provided by Christian (1983) and Taylor (1992).

Johnson and Cook (1983) developed a phenomenological model that is widely used in finite element codes in analysis for static and dynamic problems in order to predict the behavior of the material flow stress at different strain rates and temperatures. One main advantage of this model is that it is relatively easy to obtain its material parameters with simple experimental procedures by obtaining the stress–strain curves at different strain rates and temperatures. Most metals show that strain rate sensitivity is temperature dependent and hence strain rate and temperature is expected to be coupled in any suggested constitutive model. However, the strain rate and temperature in the Johnson-Cook model are uncoupled. In addition the model does not discriminate between the different crystal structures of metals. It is a phenomenologically based model.

Zerilli and Armstrong (1987) suggested a dislocation mechanism concept based on thermal activation analysis to develop a constitutive model for metals that takes into account the strain rate and temperature dependence in a coupled manner. The model is developed for two kinds of microstructures, body centered cubic and face centered cubic. The rational for the differences in the two forms mainly depends on the dislocation characteristics for each particular structure. Yield stress in fcc metals shows dependence on strain hardening mainly, while in bcc metals shows stronger dependence of the yield stress on temperature and strain rate. In other words, the cutting of dislocation forests is the principal mechanism in fcc metals, while in bcc metals; the overcoming of Peierls–Nabarro barriers is the principal mechanism. This model has been widely used in many computer codes from which its material parameters are physically interpreted.

Zerilli–Armstrong (Z-A) model, which is physically based one, has been shown to be slightly in better agreement with experimental results as compared to the Johnson–Cook model; however, both models are not very accurate in capturing the behavior of metals at very large strains (Johnson and Holmquist, 1988). The Z-A model uses mathematical approximations that allows their model to give reasonable results only for the case of small strains (Voyiadjis and Abed, 2005).

Voyiadjis and Abed (2005) used the concept of thermal activation energy along with the dislocation interactions mechanism in modeling the flow stress for both bcc and fcc metals under different strain rates and temperatures. They considered the mobile dislocation density evolution to capture the behavior of the plastic deformation for both bcc and fcc metals. Their model, showed good agreement with experimental results for several bcc and fcc metals (Ta, Mo, Nb, V and OFHC Cu). They also addressed some inconsistencies of the Z-A model.

3.2.1 Mathematical Formulation

Macroscopic plasticity in metals is primarily the result of dislocations moving through the crystal lattice. The interaction of these dislocations with the lattice and with the various obstacles encountered within the lattice determines the flow strength of the material. The motion of a dislocation through the lattice or past an obstacle requires the surmounting of an energy barrier by a combination of applied stress and ‘‘thermal activation’’ (Ashby and Frost, 1975). The result is that the effective shear stress required to generate an overall plastic strain rate is intimately tied to the temperature at which the deformation occurs (this discussion is limited to strain rate regimes which are below those dominated by phonon drag and other ‘‘viscous’’ lattice interactions). The form of the macroscopic plastic response is thus determined, at the microscopic level, by the mechanisms associated with dislocation motion and dislocation multiplication, by the statistics of mobile dislocation populations, by the nature of the obstacles and the statistics of obstacle distributions, and by the relationship between the externally imposed plastic strain rate and the dislocation kinetics.

The free energy for activation of material (or Gibbs free energy), U, is chosen to be the thermodynamic state function such that the stress, σ, and absolute temperature, T, are the independent state variables, i.e. $U = U(\sigma, T)$. This state function is related to the activation enthalpy, ΔH, through the isothermal relationship:

$$U = \Delta H - T\Delta S \tag{3.1}$$

where the activation entropy, ΔS, can be expressed as follows:

$$\Delta S = -\frac{\partial U}{\partial T}\Big|_{\sigma} \tag{3.2}$$

Combining equations (3.1) and (3.2) results in the following relationship (Kocks et al., 1975):

$$Q_T \equiv \Delta H = \frac{\partial(U/T)}{\partial(1/T)}\Big|_{\sigma} \tag{3.3}$$

where Q_T is the activation energy. This is a useful relationship because it provides a means whereby functional forms for the free energy can be determined from experimental data. Many forms of the activation energy can be found in the literature as a function of stress or temperature or even constant. In the present work the free energy is assumed to be additively decomposed into a thermal part, namely Q_{th}, and a stress dependent part, Q_s, as follows:

$$Q = Q_s + Q_{th} \tag{3.4}$$

Many authors use a linear relationship for temperature dependence of the thermal activation energy as an approximation of the experimental data (Freed et al., 1991). However, the experimental results are not linear and a better approximation can be obtained using the following power-exponential equation:

$$Q_{th} = Q_c \left(\frac{T}{T_t}\right)^2 e^{A\left(1-\frac{T}{T_t}\right)} \tag{3.5}$$

where T_t is the transition temperature beyond which the thermal activation energy maintains a constant value, Q_c is the thermal activation energy at T_t, and A is a constant. It appears to be no theoretical bases for the temperature-dependent activation energy; and its motivation is rather phenomenological (Miller, 1976). On the other hand, the stress dependent activation energy was observed to depend linearly on the applied stress as follows (Freed et al., 1991):

$$Q_s = \Delta H \left(1 - \frac{\sigma_{th}}{\hat{\sigma}}\right) \tag{3.6}$$

where σ_{th} is the applied stress associated with the thermal activation mechanism, and $\hat{\sigma}$ is the stress threshold. A free energy of this form is a characteristic of obstacle-controlled dislocation glide, where a uniform distribution of rectangular obstacles is assumed. Substituting equations (3.5) and (3.6) into equation (3.3) and performing the integration, one can obtain the thermal and stress dependent expressions of the Gibbs free energy of activation respectively:

$$U_{th} = \frac{Q_c T}{A T_t} e^{A\left(1-\frac{T}{T_t}\right)} \tag{3.7}$$

and

$$U_s = Q_s \left(1 - \frac{\sigma_{th}}{\hat{\sigma}}\right) \tag{3.8}$$

where Q_s is the activation energy at zero stress.

Several equations were proposed by researchers describing the dislocation density evolution. One evolution equation suggested by Klepaczko (1987) is as follows:

$$\frac{d\rho}{d\gamma_p} = M(\dot{\gamma}_p) - k(\dot{\gamma}_p, T)(\rho - \rho_o) \tag{3.9}$$

where ρ is the average total dislocation density, ρ_o is the initial average total dislocation density, M is the multiplication factor that is function of plastic shear strain rate $\dot{\gamma}_p$, and k is the annihilation factor that is dependent on the shear strain rate and temperature. While this relation expresses the evolution of the total dislocation density in one differential equation, Bammann (2001) proposed an evolution equation for statistically stored dislocations in terms of both statistically stored (ρ_{ss}) and geometrically necessary (ρ_{gn}) dislocation densities as follows:

$$\dot{\rho}_{ss} = c_1(\rho_{gn} + \sqrt{\rho_{ss}})\dot{\gamma}_p - c_2\rho_{ss}\dot{\gamma}_p \tag{3.10}$$

where c_1 and c_2 are constants. Kubin and Estrin (1990) proposed the following equation to describe the mobile dislocation density evolution:

$$\dot{\rho}_m = \left(\frac{\lambda_1}{b^2} - \lambda_2\rho_m - \frac{\lambda_3\sqrt{\rho_f}}{b}\right)\dot{\varepsilon}_p \tag{3.11}$$

where $\dot{\varepsilon}_p$ is the equivalent plastic strain rate, b is the Burgers vector, ρ_m is the average mobile dislocation density, ρ_f is the average forest dislocation density, λ_1 is a constant coefficient related to the multiplication of mobile dislocations, λ_2 is a constant coefficient related to the mobile dislocations mutual annihilation and trapping, and λ_3 is a constant coefficient related to the mobile dislocation immobilization through interaction with forest dislocations. Microscopically, slip is realized by the motion of line defects in the crystal structure, termed dislocations. While moving through a crystal, dislocations cause plastic strains ε_p.

The average dislocation velocity v can be determined through thermal activation by overcoming local obstacles to dislocation motion. The following general expression of the plastic strain rate which will be used in this work is postulated by Bammann and Aifantis (1982):

$$\dot{\varepsilon}_p = x_1 v + x_2\dot{\rho}_m = (\partial\gamma_p/\partial l)v + (\partial\gamma_p/\partial\rho)\dot{\rho}_m \tag{3.12}$$

where, after making use of Orowans equation, the scalar coefficient ($x_1 \sim b\rho_m$) is related to the magnitude of the Burgers vector and the mobile dislocation density and consequently, one can relate the coefficient ($x_2 \sim bl$) to the same

microstructural physical components with the dislocation distance instead of the mobile dislocation density. Equation (3.12) can then be expressed as follows:

$$\dot{\varepsilon}_p = \tilde{m} b \rho_m v + \tilde{m} b \dot{\rho}_m l \tag{3.13}$$

where $\tilde{m}$ is the Schmidt orientation tensor which has a maximum value of 0.5, and l is the dislocation moving distance. This equation reduces to the Orowan equation if a constant mobile dislocation density is assumed. Substituting equation (3.11) in (3.13) to eliminate $\dot{\rho}_m$ one obtains the equation for the dislocation velocity:

$$v = \frac{\dot{\varepsilon}_p}{\tilde{m} b \rho_m} \left(1 - \tilde{m} l \left(\frac{\lambda_1}{b} - \lambda_2 b \rho_m - \lambda_3 \sqrt{\rho_f}\right)\right) \tag{3.14}$$

Several models have been proposed for the velocity of dislocations in studies associated with viscoplastic behavior. For example, a power law relationship between the dislocation glide speed v and the applied shear stress τ has been assumed by Stein and Low (1960):

$$v = \left(\frac{\tau}{\tau_o}\right)^q \tag{3.15}$$

where τ_o is the shear stress at $v = 1 cm/sec$, and q is a constant. Different forms of this equation including power law and exponential relationships have been used by different authors (Gillis and Gilman, 1965; Kelly and Gillis, 1974; and Bammann and Aifantis, 1982). However, the following power law will be used in this work:

$$v = v_o \left(\frac{-U}{KT}\right)^q \tag{3.16}$$

where U is the energy of activation which will be shown to depend on the strain rate, K is Boltzmanns constant, T is the absolute temperature, and $v_o = d \,/\, t_w$ is the reference dislocation velocity. In the previous relation, d is the average distance the dislocation moves between the obstacles, and t_w is the time that a dislocation waits at an obstacle. Let $m = 1 \,/\, q$ and by substituting equation (3.14) into relation (3.16) one obtains:

$$U = -KT \left[\frac{v_o \tilde{m} b \rho_m}{1 - \tilde{m} l \left(\frac{\lambda_1}{b} - \lambda_2 b \rho_m - \lambda_3 \sqrt{\rho_f}\right)} \dot{\varepsilon}_p\right]^m \tag{3.17}$$

This relation suggests that a part of the energy of activation is dependent on the coupled strain rate and temperature. Assuming an additive decomposition for the free activation energy:

$$U = U_{th} + U_s \tag{3.18}$$

and using equations (3.7), (3.8) and (3.17) in equation (3.18) with rearranging the terms one obtains the following relation:

$$\sigma_{th} = \hat{\sigma}\left(1 + \frac{KT}{Q_s}\left[\frac{v_o \tilde{m} b \rho_m}{1-\tilde{m}l\left(\frac{\lambda_1}{b}-\lambda_2 b\rho_m-\lambda_3\sqrt{\rho_f}\right)}\dot{\varepsilon}_p\right]^m + \frac{Q_c T}{AT_t Q_s} e^{A\left(1-\frac{T}{T_t}\right)}\right) \tag{3.19}$$

The variables in this equation are T and $\dot{\varepsilon}_p$, which indicate that σ_{th} is the thermal part of the stress. It was found that the equivalent flow stress (which can be expressed as $\sigma = \left(3\sigma_{ij}\sigma_{ij}/2\right)^{1/2}$ for materials that follow von Mises) can be assumed to be additively decomposed into the equivalent thermal stress σ_{th} and the equivalent athermal stress σ_a (see Figure 3.1):

$$\sigma = \sigma_{th} + \sigma_a \tag{3.20}$$

The athermal stress σ_a is the part of the flow stress that is non-thermally activated which arises from interactions between moving dislocations and barriers having long range stress fields, while σ_{th} is the part the can be activated by thermal energy which arises from interactions with barriers having localized stress fields. This additional decomposition has been verified experimentally and is used widely in the literature (see for example, Zerilli and Armstrong, 1987).

In bcc metals it was found that the thermal stress and the thermal activation are almost independent of the plastic strain hardening. However, the athermal stress part is known to depend on the plastic strain and the initial yield threshold stress. Therefore, the athermal stress will be constant:

$$\sigma_a = B\varepsilon_p^n + Y_a \tag{3.21}$$

where ε_p is the equivalent plastic strain, B and n are plastic hardening constants, and Y_a is the athermal part of yield stress that is temperature independent. In fcc metals it was found that the thermal stress and the thermal activation depends highly on the plastic strain hardening. However, the athermal stress is independent of the plastic strain and will be attributed only to the initial yield stress. Therefore, the athermal stress will be constant:

$$\sigma_a = Y_a \tag{3.22}$$

The thermal stress can then be expressed as:

$$\sigma_{th} = \hat{\sigma}\left(1 + B_1 T\left[\dot{\varepsilon}_p\right]^m + B_2 T e^{A\left(1-\frac{T}{T_t}\right)}\right) \tag{3.23}$$

where

$$B_1 = \frac{K}{Q_s}\left[\frac{v_o \tilde{m} b \rho_m}{1-\tilde{m} l\left(\frac{\lambda_1}{b}-\lambda_2 b\rho_m-\lambda_3\sqrt{\rho_f}\right)}\right]^m \tag{3.24}$$

and

$$B_2 = \frac{Q_c}{AT_t Q_s} \tag{3.25}$$

The resulting constitutive relation for bcc metals is given as follows:

$$\sigma = \hat{\sigma}\left(1 + B_1 T\left[\dot{\varepsilon}_p\right]^m + B_2 T e^{A\left(1-\frac{T}{T_t}\right)}\right) + B\varepsilon_p^n + Y_a \tag{3.26}$$

As temperature decreases to the absolute zero, the thermal stress will reduce to the threshold yield stress which agrees with the physical interpretation of the thermal stress. Furthermore, when temperature rises to high values the thermal stress decreases and approaches zero. At that stage the total stress will be dominated by the athermal part of the stress, and the thermal stress will not have any significant effect.

For the fcc case, several authors (see for example Zerilli and Armstrong, 1987) approximately related $\hat{\sigma}$ to the strain using the following relation:

$$\hat{\sigma} \cong B\varepsilon_p^n \tag{3.27}$$

The resulting constitutive relation for fcc metals will be as follows:

$$\sigma = B\varepsilon_p^n\left(1 + B_1 T\left[\dot{\varepsilon}_p\right]^m + B_2 T e^{A\left(1-\frac{T}{T_t}\right)}\right) + Y_a \tag{3.28}$$

The temperature independent stress Y_a is to be independent of the plastic strain or strain rate, and hence at zero plastic strain the flow stress equals to the temperature independent stress. This results in the different stress-strain curves for different temperatures and different strain rates to initiate from the same point (i.e. temperature independent stress Y_a). This behavior is not completely true for all fcc metals where slight dependence of Y_a on the strain rate and temperature is observed. This can be corrected by introducing this dependence in Y_a, however it is beyond the scope of this work.

The constitutive model developed by Voyiadjis and Abed (2005) for fcc and bcc metals follows a similar approach to the one used here. However, one main difference in the proposed work is that the stress is related to the strain rate through a power term, while in the previous formulation (Voyiadjis and Abed, 2005) the stress is dependent on the logarithm of the strain rate. For the dependence of the strain rate upon applied stress several functions can be found in the literature. Nevertheless, the explicit function $\dot{\varepsilon}(\sigma, T)$ or $\sigma(\dot{\varepsilon}, T)$ is still the

subject of some controversy. The power function, the exponent and the hyperbolic sine are the most common forms that have been suggested and widely used. The power law proposed here is similar to many power law models that show a power dependence of the strain rate on the stress. In addition, even though some metals show a linear relationship between the stress and the logarithm of strain rate, most metals show this linear behavior only at very low strain rates (i.e. $10^{-1}/sec$), and as the strain rate increases the flow stress tends to increase dramatically in a nonlinear form. The power law is more suitable to describe this nonlinearity than the logarithmic term for a wider range of strain rates.

3.2.2 Application to Pure Iron

Iron is chosen here to test the applicability of the proposed model because it is one of the most commonly used metals in structural engineering applications, having a basic structure (bcc); furthermore, there is enough data for iron in the literature on the mechanical behavior at different strain rates and temperatures. Iron-based alloys are some of the most widely used metals in the world. These alloys are usually used in structural applications. Iron alloys containing some carbon and manganese are called steels, those with excess carbon are called cast iron, and pure iron is called ingot iron. The proposed model is used here to capture the mechanical behavior of annealed pure iron. For bcc metals one do not expect to have a significant effect of grain size on the strain hardening (Jia et al., 2003), and hence it will be neglected in this study.

True stress-strain curves of annealed ingot iron at temperatures ranging from 77ºK to 373ºK were obtained by Geil and Carwile (1950). These curves will be used here in order to obtain the different constants needed for the constitutive modeling of iron. These parameters will be obtained through a three steps procedure. The first step is to obtain the initial threshold stress Y_a. This can be done by plotting the change in yield stress with changing temperature. The yield stress will decrease with increasing temperature up to a point where it becomes almost constant, which is going to be the initial threshold stress Y_a. Figure 3.2 shows the temperature dependence of the annealed ingot iron. It is clear that the athermal stress portion Y_a is about 30 MPa and the thermal part of the stress vanishes after a temperature of 350ºK. Next step is to use a stress-strain curve at a temperature higher than 350ºK (where there is no thermal stress) to find the plastic strain constants B and n. This is illustrated in Figure 3.3 where the true stress is plotted versus the true plastic strain at a temperature of 373ºK (Geil and Carwile, 1950), and the plastic hardening constants are determined by regular curve fitting and found to be $B = 520MPa$ and $n = 0.35$. The last step in determining the constants will include determining the values of the rest of them, namely $\hat{\sigma}$, B_1, B_2, m, A, and T_t altogether. Two intercepting curves are used at the same time for this purpose; the first is the change in flow stress versus strain rate at a constant temperature (room temperature here) and the second is the change in flow stress versus temperature at static strain rate, as shown in Figure

3.4. The two curves of the flow stress are obtained at 0.1 plastic strain and they are fitted simultaneously to the model. The model parameters are listed in Table 3.1.

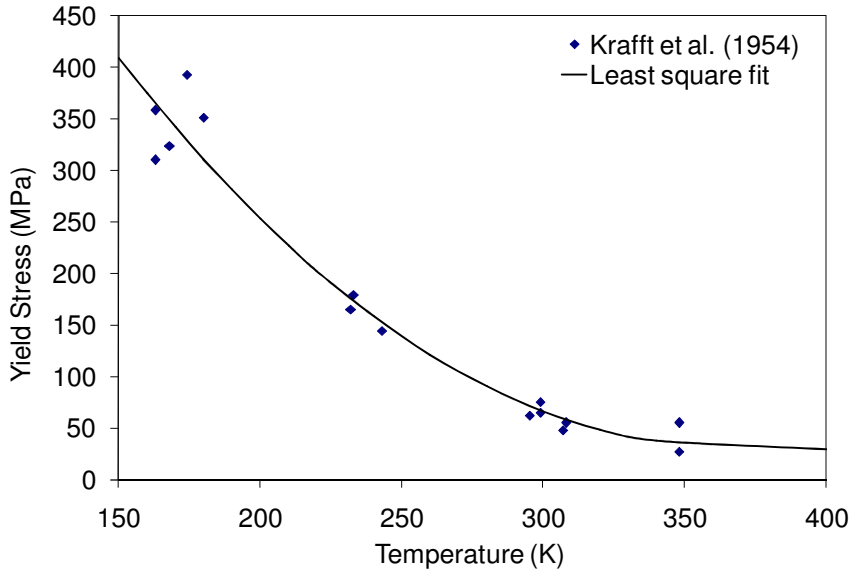

Figure 3.2: Temperature dependence of yield stress for annealed ingot iron.

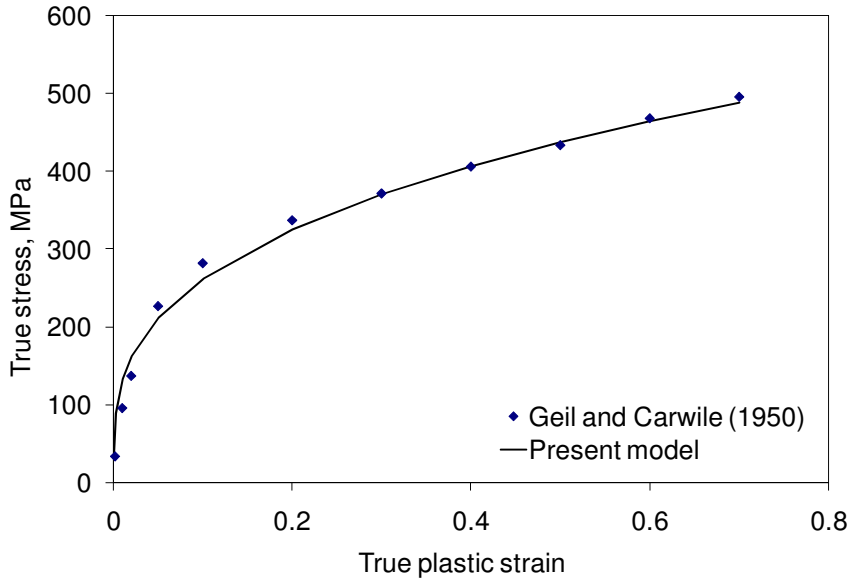

Figure 3.3: True stress versus true plastic strain of annealed ingot iron at 300ºK.

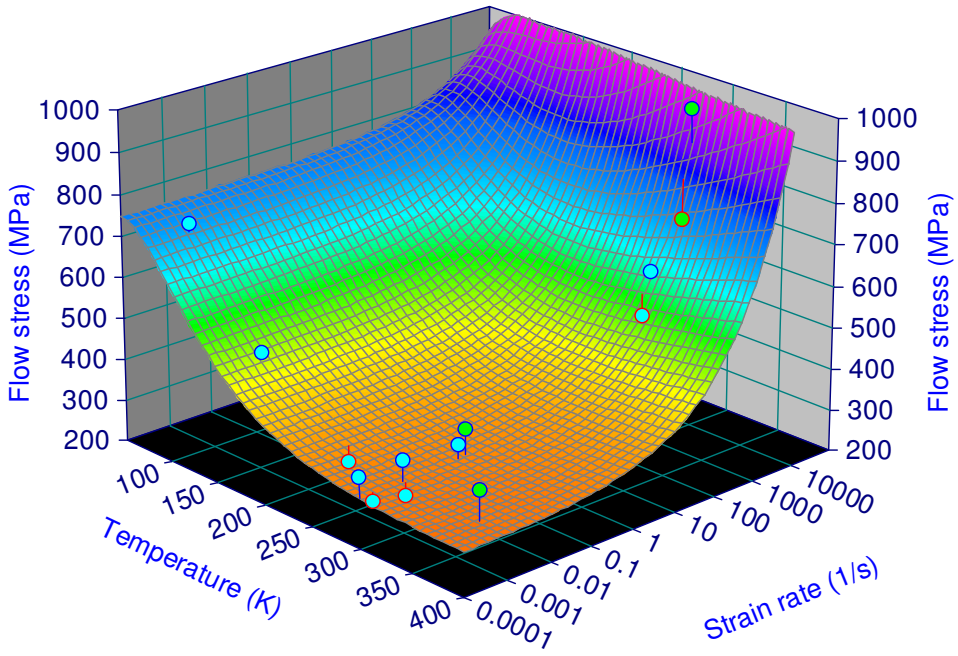

Figure 3.4: Flow stress versus strain rate and temperature for annealed ingot iron at 0.1 strain (Data by Rittel et al., 2006; and Geil and Carwile, 1950).

Table 3.1: Parameters for the annealed ingot iron for the proposed model.

Model parameters	Numerical value
Y_a	30 MPa
B	520 MPa
n	0.35
$\hat{\sigma}$	6.3
B_1	0.02
B_2	0.01
m	0.3
A	6
T_t	350ºK

True stress-strain diagram is plotted for a wide range of temperatures at static strain rates of $10^{-4}/sec$ along with experimental data obtained from Geil and Carwile (1950) in Figure 3.5. The stress-strain curve decreases smoothly with increasing temperature and reaches a value independent of temperature at about 300ºK. Deformation at low temperatures (i.e. room temperature and lower) take places mainly by twinning, where atoms slide layer by layer to bring deformed material into mirror-image lattice orientation relative to the undeformed material. Twins usually form at low temperatures and under rapid deformation. The model shows very good capabilities in capturing the effect of the change in temperature on the stress-strain diagram. At small strain values of about 0.02 the model overestimates experimental data but gives excellent prediction of flow stress at higher strains. In bcc metals a high lattice friction to the movement of a

dislocation may arise from the dissociation of a dislocation on several planes. If such dissociation occurs, it will be necessary to constrict the dislocation before it can glide in any one of the slip planes. This constriction will be more difficult to make as the temperature is lowered so that the large temperature dependence of the yield stress in bcc metals may be partly due to this effect. Another factor that plays an important role here is that the high Peierls–Nabarro stress, which is associated with materials with narrow dislocations, gives rise to a short-range barrier to dislocation motion. Such barriers are effective only over an atomic spacing, and hence thermal activation is able to aid the applied stress in overcoming them. Thermal activation helps a portion of the dislocation to cross the barrier after which the glide then proceeds by the sideways movement of kinks. Hence, because iron is a bcc material with narrow dislocations it exhibits a significant temperature-sensitivity; intrinsically hard materials rapidly lose their strength with increasing temperature. It should be noted that some of the experimental engineering stress-strain data include a peak load and softening behavior, but it does not appear on a true stress-strain diagram. Several investigators (see for example MacGregor, 1944a, 1944b; and Hollomon, 1944) have reported a linear relationship between the true stress and true strain from the point representing maximum load to fracture of the specimen. This softening region is also captured very well by the model although fewer points are available after maximum load. As the temperature increases above 150ºK the strain aging becomes a more influencing factor in increasing the total work hardening rates. Mechanism of deformation also plays an important role in the change of work hardening rate with increasing temperature. Below 150ºK the main mechanism that controls the deformation is crystal twinning (Neumann bands), but no evidence on this was found at temperatures higher than that (Geil and Carwil, 1950).

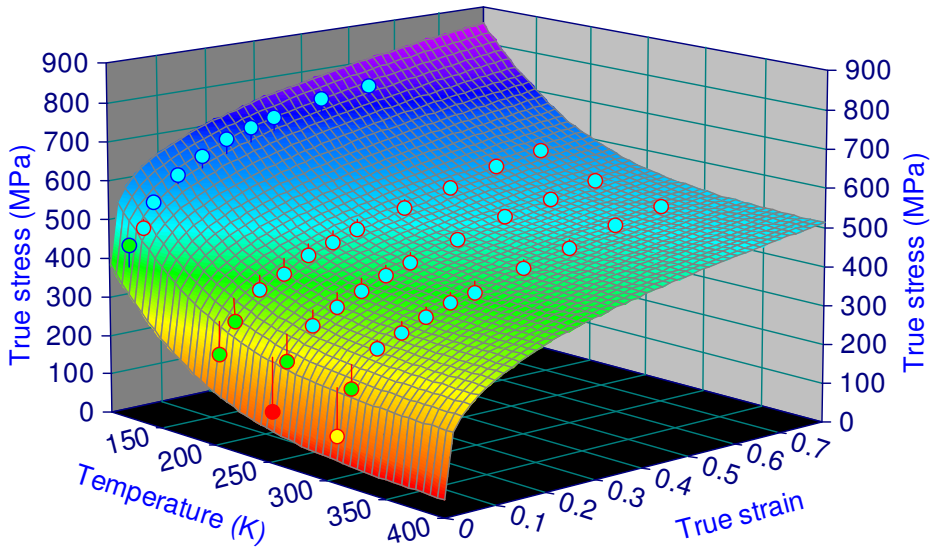

Figure 3.5: Static true stress and true plastic strain for annealed ingot iron for a wide range of temperatures (Data by Geil and Carwile, 1950).

In addition, the true stress-strain curves are plotted in Figure 3.6 for strain rates ranging from $10^{-3}/sec$ as quasi static condition to $10^{4}/sec$ representing the dynamic regime. The experimental results (Rittel et al., 2006) at high strain rates show high disturbance in stress-strain diagrams which is a common phenomenon at this range of rates. These curves were smoothed here in order to be comparable to the model. Both the yield and flow stresses increase with the increase in strain rate but the rate of increase in yield stress is higher than that of the rate in the flow stress. Furthermore, the difference between stress-strain curves at low and high strains remains nearly constant. In other words, the initial difference in the yield stress is around the same when computed at strains of 0.15 and 0.3. One can therefore surmise that strain hardening is independent of strain rate for bcc iron, as is observed in general for bcc metals. The proposed model again tends to over predict experimental results at very low strains for both low and high rates. The strain rate sensitivity appears at rates higher than about $1/sec$, while the stress-strain curve stays unchanged below that.

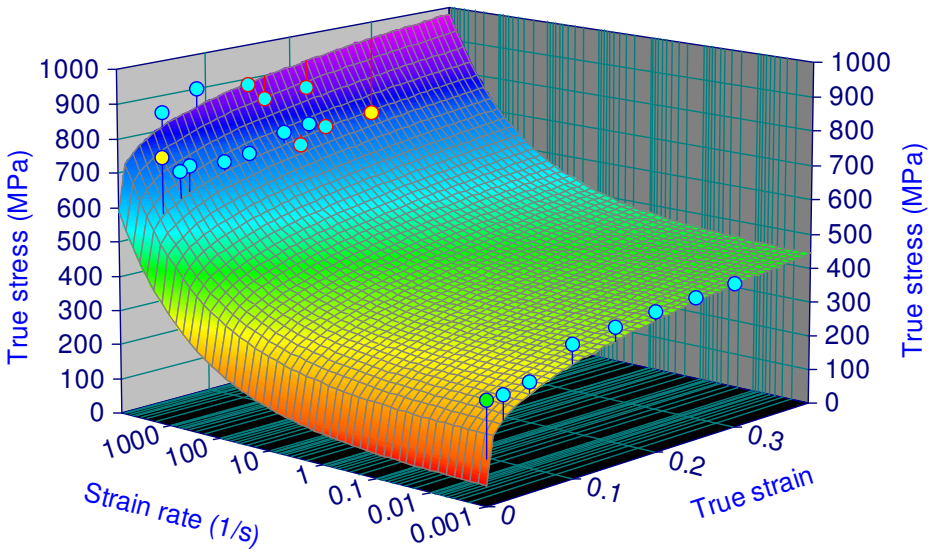

Figure 3.6: True stress-true plastic strain of annealed iron for a wide range of strain rates at 300ºK (Data by Rittel et al., 2006).

3.2.3 Application to OFHC Copper

Copper is widely used as a conductor of electricity. Copper is an fcc metal and has a high thermal and electrical conductivity in addition to its high ductility. The proposed model is used here to capture the mechanical behavior of Oxygen Free High Conductivity (OFHC) copper. It has been seen in experimental results (see for example Tanner and McDowell, 1999 and Lennon and Ramesh, 2004) that OFHC Copper does not have athermal stress component. A simple plot of the flow stress versus temperature, in Figure 3.7, shows that the flow stress keeps decreasing with increasing temperature. Even at very high temperatures of

about 1100ºK the flow stress does not reach a steady state mainly because the melting point of OFHC copper is about 1356ºK. This imposes Y_a to equal to zero.

The plastic hardening constants B and n can be determined indirectly through the flow dependence on temperature since the plastic strain here is coupled with the temperature and the strain rate. First the flow stress is plotted versus temperature as shown in Figure 3.8 for different values of the plastic strain. The intercepts of these constant slope lines represent hypothetically the flow stress at zero temperature, and using the least square fitting of these intercepts versus stress one obtains B and n as illustrated in Figure 3.9. The constants are obtained to be 600 MPa for B and 0.42 for n. For the transition temperature T_t the value of 610ºK given by Freed et al. (1991) is used. Finally, the rest of the constants of the model B_1 , B_2 , A and m are determined simultaneously. Three curves are used for this purpose, simultaneously; two of them are for the change in flow stress versus temperature at a constant low strain rate and the other at a constant high strain rate value as shown in Figure 3.10. The third curve is for flow stress versus strain rate at a constant temperature. The model parameters for copper are listed in Table 3.2.

The stress-strain diagram is plotted on a wide range of strain rates at a temperature of 293ºK along with experimental data obtained from Nemat-Nasser and Li (1998) in Figure 3.11. The yield stress is almost independent of the strain rate, and only the rate of hardening varies with the increasing strain rate which agrees well with the behavior of fcc metals. The proposed model tends to over predict experimental results at very low strain rates but on the other hand it shows better agreement with laboratory data at higher strain rates. In addition for low strain rates the model coincides with the experimental data in case of low strains and diverges at high strains of about 0.5. The stress-strain curve stays unchanged below a strain rate of $10^2/sec$, and starts increasing rapidly at higher rates, which indicates a low sensitivity of the model for low rates. The temperature effect on the stress-strain curves is shown in Figure 3.12. The model is plotted for a wide range of temperatures and also compared with the experimental results by Nemat-Nasser and Li (1998). At low temperatures, i.e. at 100ºK, the model underestimates the experimental data significantly in the case of high strains, while for temperatures higher than 700º the model predicts somehow higher flow stresses than the experimental obtained values. In other words flow stress in the proposed model is seen to be less sensitive toward temperature than the real behavior of OFHC copper. Nevertheless, except for very low temperatures the model generally can be considered to be in good agreement with the experimental data.

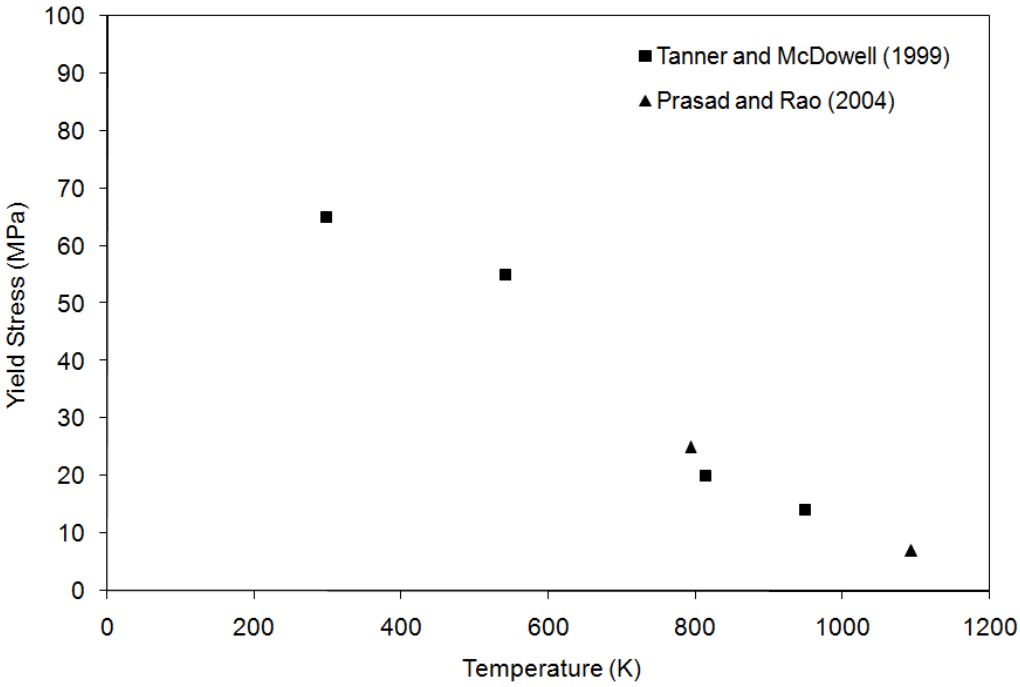

Figure 3.7: Temperature dependence of yield stress for annealed OFHC Copper.

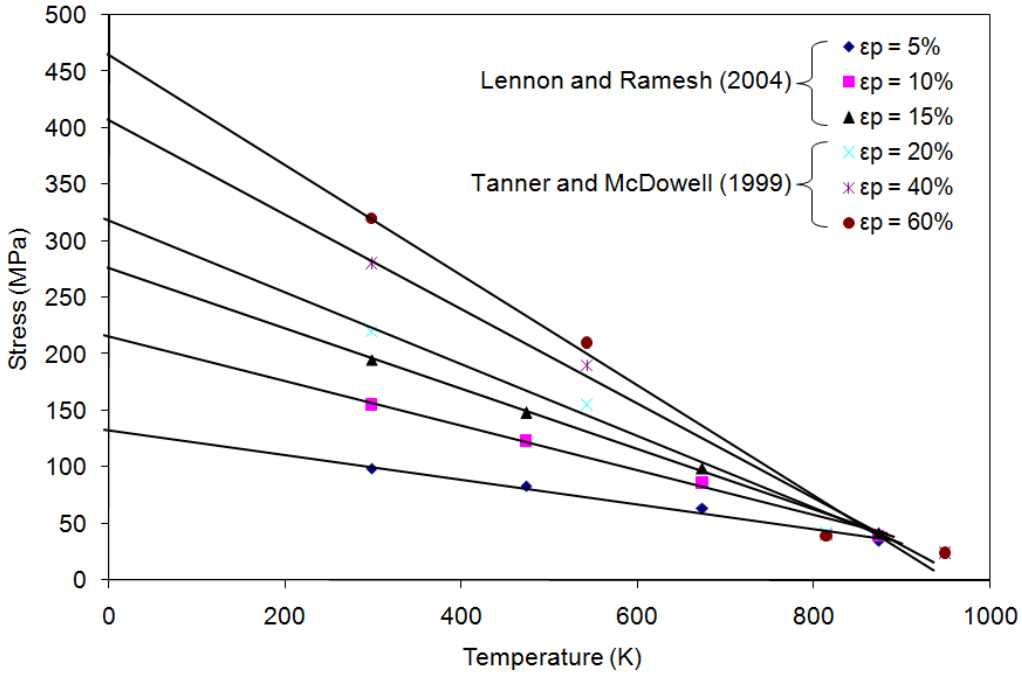

Figure 3.8: Flow stress versus temperature at different plastic strains for annealed OFHC Copper.

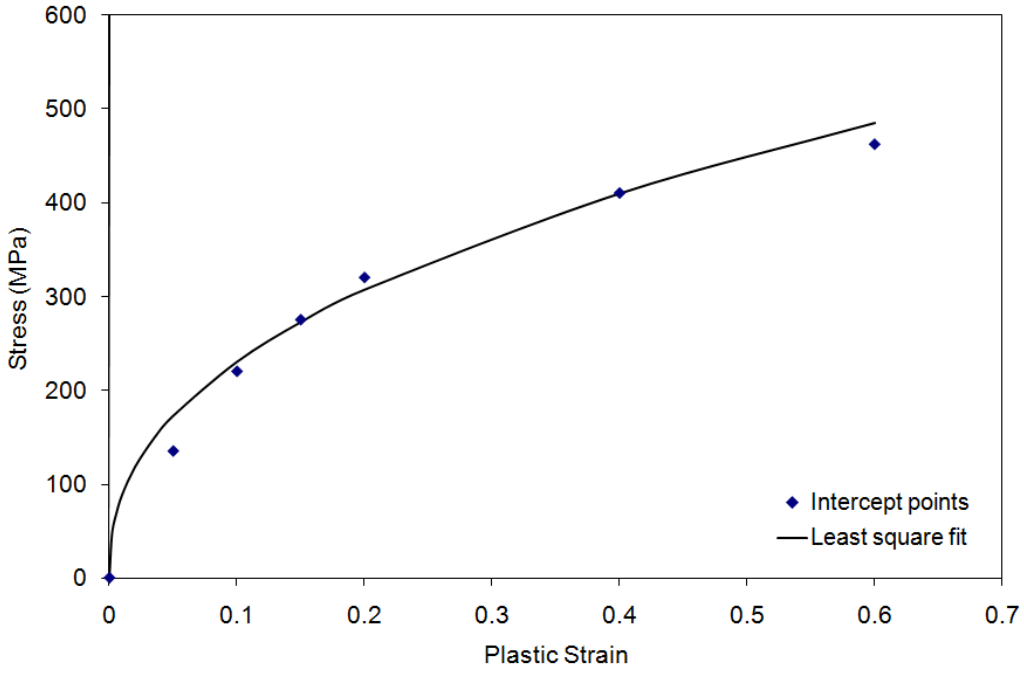

Figure 3.9: Least square fitting of stress versus plastic strain at 0ºK temperature to obtain hardening constant of annealed OFHC Copper.

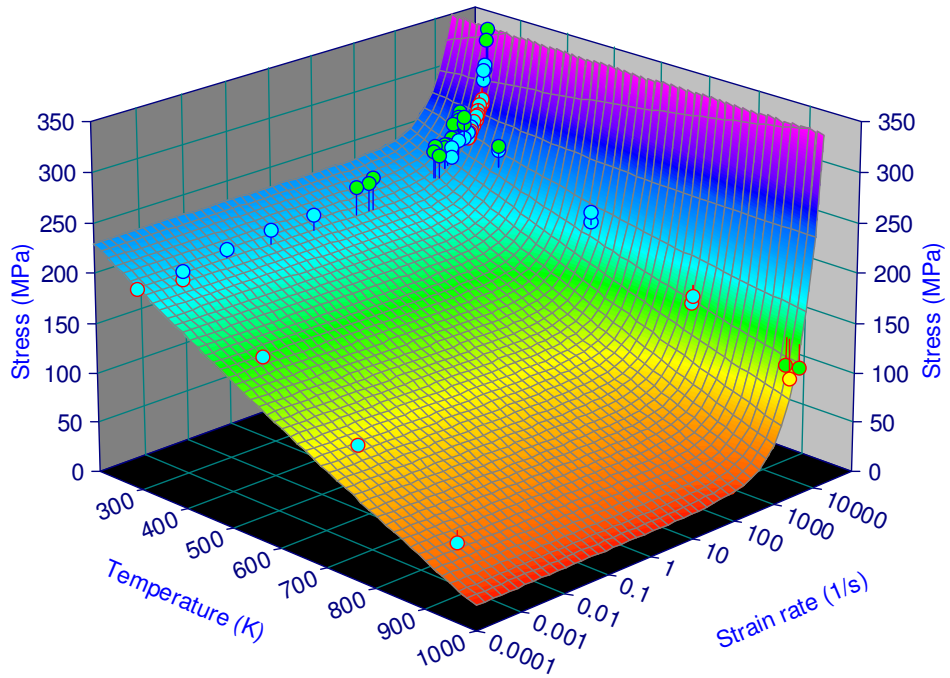

Figure 3.10: Flow stress versus strain rate and temperature of OFHC copper at a strain of 15% (Data by Regazzoni and Montheillet, 1984; and Follansbee et al., 1984)

Table 3.2: Parameters of OFHC copper for the proposed model.

Model parameters	Numerical value	Model parameters	Numerical value
Y_a	0 MPa	B_2	0.001
B	600 MPa	m	1.15
n	0.42	A	0.001
B_1	4×10^{-7}	T_t	610ºK

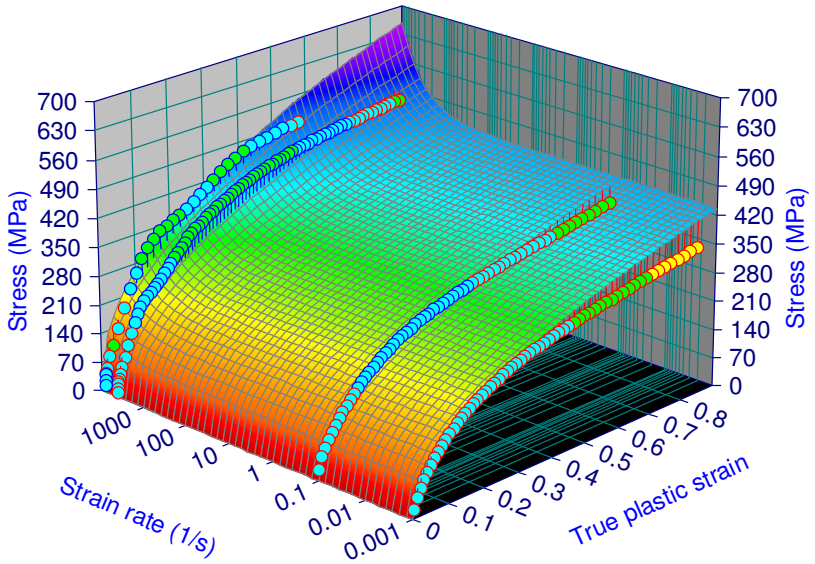

Figure 3.11: Stress-strain diagram of OFHC copper for a wide range of strain rates at a temperature of 293ºK. (Data by Nemat-Nasser and Li, 1998)

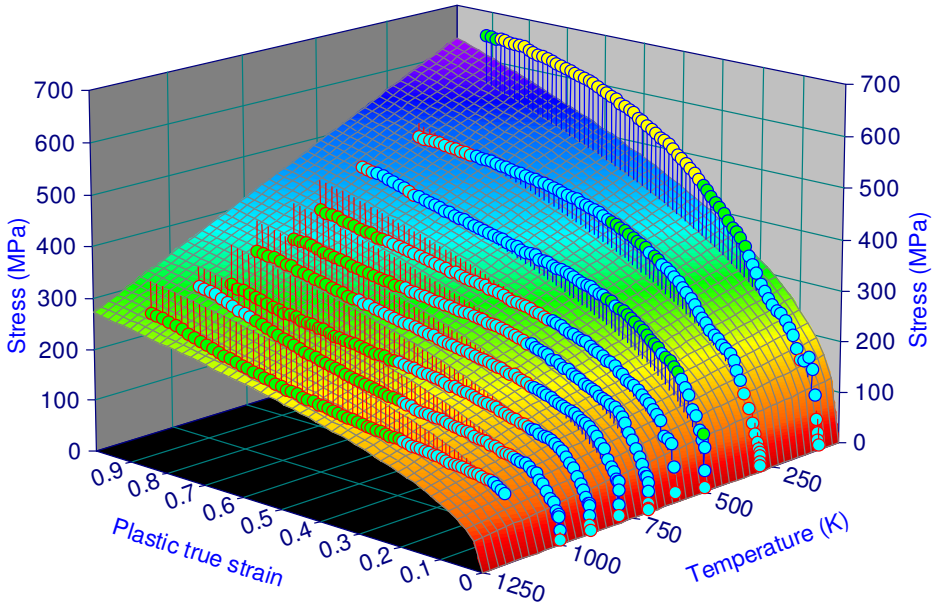

Figure 3.12: Stress-strain diagram of OFHC copper for a wide range of temperatures at a strain rate of $4 \times 10^3/sec$. (Data by Nemat-Nasser and Li, 1998)

3.2.4 Application to Dynamic Hardness

Hardness can be defined as the resistance of the material to indentation. The indentation test in metals although simple to conduct includes some complicated phenomena such as multi-axial plastic behavior. This test is quite important in defining the behavior of metals and therefore hardness is considered one of the most important properties of metals. Since plastic behavior of material can be rate sensitive, it is expected that one of the most important factors to affect material hardness is the strain rate effect.

Hardness obtained through low rates of loading, termed static hardness here, has been studied extensively both experimentally and theoretically through different theories and approaches (for example Ludwik, 1908; and Atkins and Tabor, 1965). However, less work has been carried out studying the hardness behavior for strain rate dependent materials under high strain rates of loading (see for example Koeppel and Subhash, 1999; and Lu et al., 2003). Tabor (1951) defined the dynamic hardness as the resistance of the metal to local indentation when the indentation is produced by a rapidly moving indenter. He discussed dynamic hardness mainly due to a falling indenter under gravity on the metal surface and defined the dynamic hardness number as the energy of impact over the volume of indentation. Researchers found that the volume of indentation is directly proportional to the kinetic energy of the indenter which implies that the metal offers an average pressure of resistance to the indenter. In a different approach the energy of rebound was taken as a measure of dynamic hardness. Regardless of the method used to measure the dynamic hardness, it was found that the dynamic hardness of a material is mostly higher than the static or quasi-static hardness, or in other words hardness value increases with increasing applied load rate or generally with increasing strain rate of loading (see for example Lu et al., 2003; Anton and Subhash, 2000; Sundararajan and Tirupataiah, 2006a, 2006b; and Andrews et al., 2002).

In indentation tests, the yield stress for work hardened materials was found to vary around the indenter. Using the slip line plasticity theory for indentation of a rigid sphere in a work hardened material it has been earlier stated by many researchers such as Prandtl (1920) and Tabor (1951) that the mean yield pressure P_m of plastic indentation is related directly to the representative yield stress σ_{yr} as follows:

$$P_m = c\sigma_{yr} \tag{3.29}$$

where c is nearly a constant and ranges from a value of 2.4 to 3. This suggests that for fully work hardened materials the yield pressure is essentially independent of the load and the size of the indentation.

The static hardness H_o is defined as the total load applied on the indenter divided by the projected area of the indentation, or equivalently the mean pressure the material will support. Accordingly, equation (3.29) gives:

$$H_o = c\sigma_{yr} \tag{3.30}$$

Tabor (1951), based on the mapping of the hardness-indentation depth curve ($H_o - h$ curve) to the tensile stress-plastic strain curve ($\sigma - P$), assumed that c is always a constant regardless of the work-hardening degree of the material and is usually taken between 2.4 to 3. It is worthwhile to mention that the assumption that c is a universal constant was doubted by some researchers where they found that the flow stress around the spherical indentation of different radii did not show any systematic correlation with the flow stress values at the indentation edge. This is because the plastic strains around the indentation are widely distributed. It is therefore important to emphasize at this stage the conditions under which equation (3.30) is based. Firstly, the target solid material is assumed to be isotropic, which implies that, in practice, the metal must be polycrystalline without any preferred orientation, or the indenter must be big enough relative to the microstructure of the material. Secondly, it is assumed that it is fully work-hardened and has a constant yield stress σ_{yr} under static loading, i.e. there is no difference between yield stress and flow stress. In practice this means that if the material work-hardens appreciably or shows an upper yield point, some other approach must be used. Lastly, it is assumed that the elastic deformation is unimportant. Except for very hard steels, the last assumption is generally valid for most metals

It is also important to note that for a material that tends to work-harden the indentation process itself will work-harden the material under the indenter which produces an increase in the flow stress. With the Vickers pyramidal indenter the plastic strains produced will vary from point to point under the indentation and hence the flow stress will also vary from point to point. A detailed analytical solution of the problem is not possible but one may provide a very simple analysis in the following way (Tabor, 1951). One can assume that there is a representative value of the flow stress which is related to the observed Vickers hardness by the relation given in equation (3.30), where c again has the value between 2.4 and 3. Using an empirical method it is found that the indentation produces a representative strain (also can be looked at as an average strain) ε_r equivalent to an 8% tensile strain. Hence, if for a given tensile stress-strain curve of the metal one determines the flow stress for an additional 8% strain, the Vickers hardness value will be three times this value (Tabor, 1951). It turned out that this additional strain is the same regardless of the size of the indentation as long as it is macro indentation (not micro- or nano-indentation). This is due to the principle of geometric similarity. It was also observed that the additional strain is roughly constant and independent of the initial state of work-hardening in the specimen. The most common value of this representative strain is about 8%, although Atkins and Tabor (1965) showed that this representative strain is a

function of the cone angle for the indentations conducted using the Vicker's indenter. They also found that this value of the effective strain for the 136º Vicker indenter can be taken as 0.11. More recently, Dao et al. (2001) proposed a systematic methodology for extracting various material parameters and as well as the representative strain from sharp indentation experiments. They suggested the representative strain to be 0.033 rather than 0.08 as has been proposed in the past literature (Dao et al., 2001). However, the value of 8% obtained by Tabor is still widely used in this field.

Koeppel and Subhash (1999) showed experimentally that equation (3.30) can be applied to dynamic hardness with the same constant c used for the static case. This means that the increase in the yield stress due to the application of a higher rate of strain is accompanied by an increase of the same order in the hardness:

$$H_d = c\sigma_{yr,d} \tag{3.31}$$

where H_d is the dynamic hardness and $\sigma_{yr,d}$ is the flow stress at 8% strain under high strain loading. The dynamic flow stress for bcc metals can be obtained in terms of the plastic strain, strain rate and temperature from equation (3.26) and the dynamic hardness is now expressed as:

$$H_d = c\left[\hat{\sigma}\left(1 + B_1 T\left[\dot{\varepsilon}_p\right]^m + B_2 T e^{A\left(1-\frac{T}{T_t}\right)}\right) + B\varepsilon_p^n + Y_a\right] \tag{3.32}$$

Using equation (3.28) for fcc metals, the dynamic hardness is given by:

$$H_d = c\left[B\varepsilon_p^n\left(1 + B_1 T\left[\dot{\varepsilon}_p\right]^m + B_2 T e^{A\left(1-\frac{T}{T_t}\right)}\right) + Y_a\right] \tag{3.33}$$

Equations (3.32) and (3.33) relate the hardness directly to the plastic strain, strain rate, and temperature. Equation (3.32) is plotted along with experimental data (Sundararajan and Tirupataiah, 2006a) of the indentation tests for annealed iron under the static and dynamic conditions at different levels of true plastic strain in Figure 3.13 with a constraint factor of 2.6. The estimation of strain rate of these experimental results highly depends on the used formula. Sundararajan and Tirupataiah (2006a) related the dynamic hardness to the mass of the impacting ball, the impacting velocity and the unrelaxed volume of the dynamic indentation formed. They estimated the strain rate to be of the order of $10^4/sec$ which can be considered quite high. However, in the present model the strain rate represents an equivalent value of the strain rate and is found to agree better with the experimental results at $2 \times 10^3/sec$. At low static strain rates the hardness from experimental results at 8% strain is about 670MPa of hardness while the model predicts a value of 770MPa, which is 15% more. This overestimation of the experimental data by the model decreases with increasing the average true

strain and disappears at 0.16 strain. For the dynamic results the model shows good prediction of the experimental results at low strains up to about 0.1 strain. In fact the hardness shows some kind of softening beyond 0.1 average strain, and diverges from the model which does not predict any softening behavior. Many metals show some strain softening behavior under high strain rate tests when it is drawn on an engineering stress-strain diagram, but not on a true stress-strain diagram. However, this was justified by a localization mechanism. It was suggested that the localization of plastic flow under dynamic indentation conditions is more severe at larger strains and hence it is responsible for the clear softening behavior. On the other hand the piling-up effect is expected to be negligible here as it is well known that for annealed materials, such as for iron used here, the piling-up of the displaced material at the sides of the indenter is much less than that in the case of a work-hardening material.

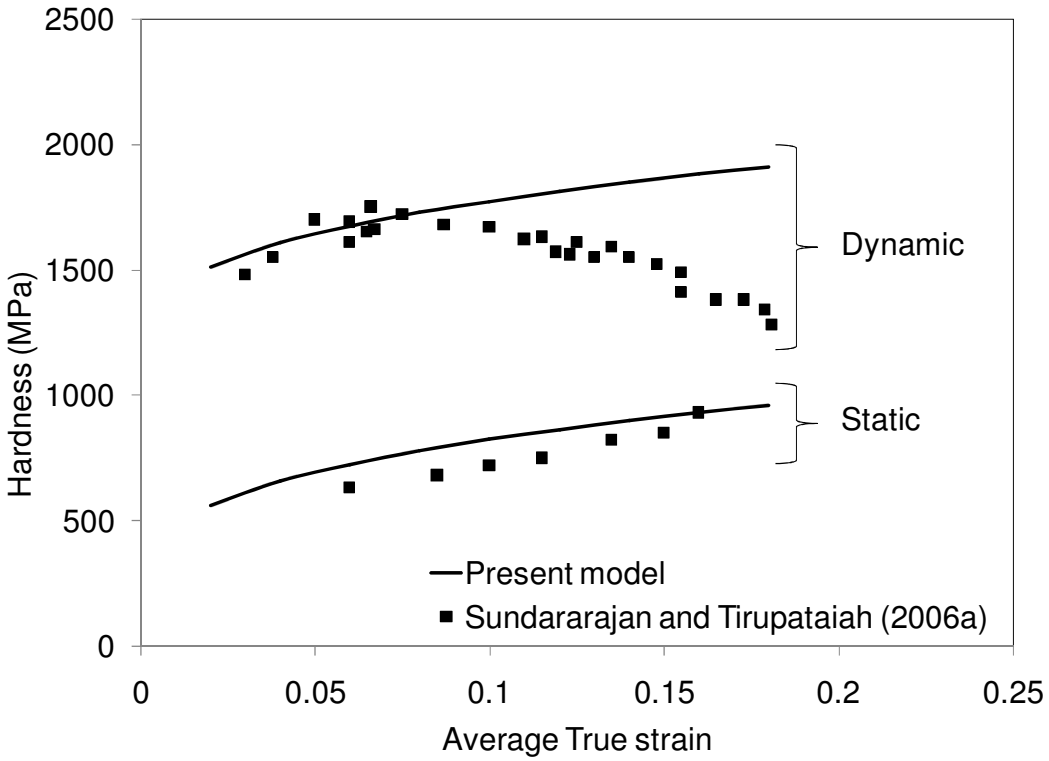

Figure 3.13: Hardness versus average true plastic strain under static and dynamic conditions for pure iron at room temperature.

Equation (3.33) is compared with experimental data (Sundararajan and Tirupataiah (2006a)) from indentation tests at different levels of true plastic strain in Figure 3.14 with a constraint factor of 2.6. The dynamic tests data is conducted at the same previous strain rate of the order of $10^4/sec$. At low plastic strains the equation coincides with the experimental results of the indentation tests at both static and dynamic tests but it diverges from the experimental data for higher plastic strains. It gives relatively good prediction up to plastic strains of 11%, and as the average plastic strain increases the equation underestimates static

hardness as well as dynamic hardness. One explanation for this may be attributed to the fact that most metals usually exhibit strain hardening in their plastic response where the flow stress increases with plastic strain. Since hardness is a strong function of flow stress and the material work hardens with strain, the hardness should then be expected to be greater when higher plastic strains are observed. The indentation process itself work hardens the material, and hence at higher plastic strains higher strain hardness is obtained experimentally. However, this effect is not accounted for in the constitutive model.

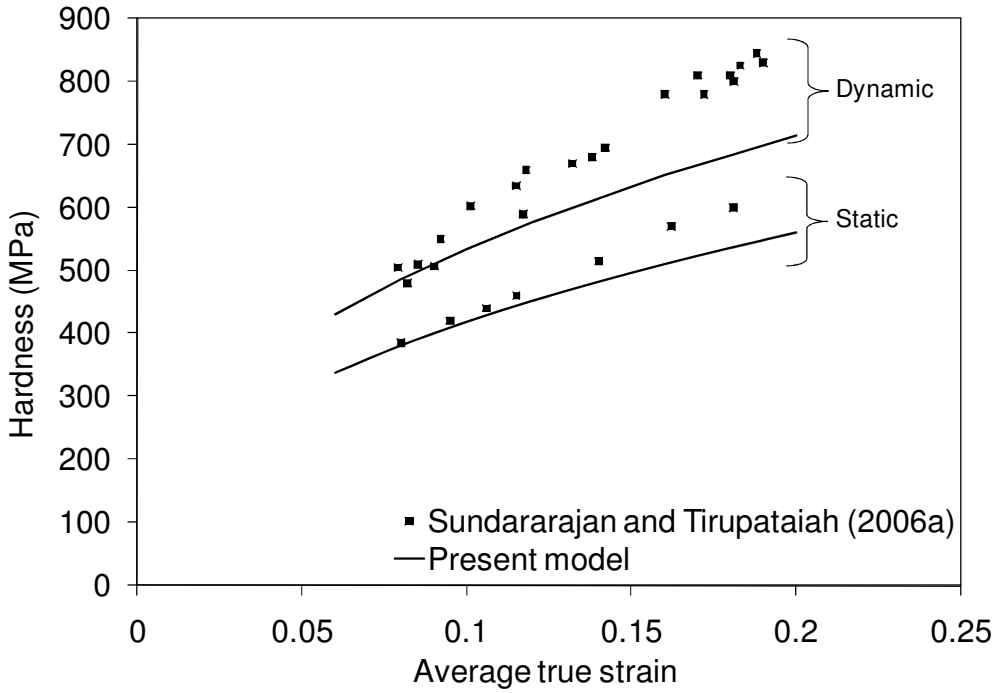

Figure 3.14: Hardness versus average true plastic strain under static and dynamic conditions of OFHC copper.

3.2.5 Metal Alloys Constitutive Model

Both bcc and fcc models can be utilized here in modeling the plastic deformation behavior of metal alloys that contain different percentages of bcc and fcc metals under low and high strain rates and temperatures. Such an alloy is AL-6XN stainless steel, where in addition to iron (bcc), the microstructure is composed mainly of 23.84% of nickel (Ni) (fcc metal) and 20.56% and 6.21% of chromium (Cr) and molybdenum (Mo) (bcc metals), respectively. Therefore, a combination of the aforementioned two physically based models is going to be used in order to characterize the plastic deformation of such materials.

The experimental results of steel alloys reveal some characteristics that need to be addressed in the constitutive modeling. The first one is that both the

hardening and the yield stress depend on the temperature and the strain rate and their corresponding history, which is not the case if one have either a bcc or fcc metal structure. Second characteristic is that the microstructure of the material evolves mainly with the temperature history. Third characteristic is that the long-range obstacles are related to the plastic strain as well as to the initial yield stress. Finally, the dynamic strain aging takes place when the temperature reaches some critical values (around 600–1000 K), and becomes weaker when the temperature exceeds that range. Dynamic strain aging also increases with increasing strain. However, the dynamic strain aging effects are not included in the present model since the plastic flow is considered in the range of temperatures and strain rates where diffusion and creep are not significant, and the plastic deformation is attributed mainly to the motion of dislocations.

In most metals, the temperature variation of the flow stress at certain strain and strain rate shows that the flow stress decreases as the temperature increases until a point where no further decreasing occurs and the stress becomes constant. This point represents the athermal stress value on the stress axis and the critical temperature value, T_{cr}, on the temperature axis. The critical temperature changes with strain rate while the athermal stress is independent of strain rate. In general, the athermal component of fcc metals consists of one component that is independent of strain (Y_a in Equation (3.21)), whereas, an additional strain-dependent component exists in bcc metals ($B\varepsilon^n$ in Equation (3.21)). The physical interpretation of the athermal stress component was investigated by many authors. Zerilli and Armstrong (1987) attributed the strain-independent component of the athermal stress to the influence of the solute and the initial dislocation density (originated in the material) on the yield stress. They defined the athermal stress component as the product of the microstructural stress intensity and the inverse square root of the average grain diameter. All this will lead to the following definition of the athermal component of the flow stress:

$$\sigma_a = B_1 \varepsilon_p^{n_1} + Y_a \tag{3.34}$$

where B_1 and n_1 represent the athermal hardening parameters.

The thermal activation of steel alloys containing fcc and bcc constituents under different strain rates shows a behavior that is between that of the bcc and fcc metals. The mechanism of bcc metals is defined as the overcoming of the short range barriers (Peierls–Nabarro barriers) through the movement of the initial dislocations (original dislocations), that is, the thermal stress contributes to the yield stress and does not depend on the accumulation of the dislocation densities through the plastic deformation. On the other hand, the cutting of dislocations forests which is attributed to the evolution and the accumulation of the mobile dislocations during the plastic deformation is the principle mechanism in fcc metals, This implies that the thermal stress in fcc is strongly dependent on the plastic strain. Therefore, the thermally activated flow stress of such alloys is additively decomposed here into two parts as follows (Abed and Voyiadjis, 2005):

$$\sigma_{th} = Y_{th} + H_{th} \tag{3.35}$$

where both the thermal yield stress Y_{th} and thermal hardening H_{th} are defined as follows:

$$Y_{th} = \hat{\sigma}\left(1 + B_1^Y T\left[\dot{\varepsilon}_p\right]^m + B_2^Y T e^{A\left(1-\frac{T}{T_t}\right)}\right) \tag{3.36}$$

$$H_{th} = B_2 \varepsilon_p^{n_2}\left(1 + B_1^H T\left[\dot{\varepsilon}_p\right]^m + B_2^H T e^{A\left(1-\frac{T}{T_t}\right)}\right) \tag{3.37}$$

Here B_2 and n_2 represent the thermal hardening parameters and their numerical values and are not necessarily the same as those in Equation (3.34). However, the parameters B_1^Y and B_2^Y are the same as those defined in Equation (3.26) and the parameters B_1^H and B_2^H are the same as those defined in Equation (3.28). Utilizing Equations (3.34), (3.35), (3.36), and (3.37), the final expression of the flow stress for steel alloys composed of fcc and bcc metals is given as follows:

$$\begin{aligned}\sigma = B_1 \varepsilon_p^{n_1} + Y_a + \hat{\sigma}\left(1 + B_1^Y T\left[\dot{\varepsilon}_p\right]^m + B_2^Y T e^{A\left(1-\frac{T}{T_t}\right)}\right) \\ + B_2 \varepsilon_p^{n_2}\left(1 + B_1^H T\left[\dot{\varepsilon}_p\right]^m + B_2^H T e^{A\left(1-\frac{T}{T_t}\right)}\right)\end{aligned} \tag{3.38}$$

The above relation is used to obtain the total flow stress for steel alloys at different strain rates and temperatures. It should be noted here, that the thermal component of the flow stress is non-negative. Thus, the thermal yield stress calculated using Equation (3.36) should be set equal to zero when it becomes negative which indicates that the temperature has exceeded its critical value. The critical temperature, however, is strain rate-dependent and it increases with the increase of the strain rate.

3.2.6 Application to Cold Rolled 1018 Steel

Cold rolled (CR) 1018 steel is one of the most widely used forms of structural steels. This type of steel has been known to be susceptible to shear band formation, and hence will be used here to test the proposed constitutive model. The chemical composition is 0.18% carbon, 0.7% manganese, maximum of 0.04% phosohorus, and maximum of 0.05% sulfur, with iron to balance the composition. Its microstructure will thus be essentially ferrite (α) with a small volume fraction of carbide (Fe_3C) often present as the α/Fe_3C eutectoid (pearlite). Although it is clear that this steel is made of mainly bcc metal (iron) with very small percentages of non metals, the existence of the brittle iron carbide particles can seriously affect the dislocation mechanism of bcc materials. For this reason,

the developed model in equation (3.26) for bcc metals should be tested against the mechanical behavior of CR-1018 steel.

Different stress-strain curves were obtained by Costin et al. (1980) for CR-1018 steel for temperature ranging from 116ºK to 380ºK and for two shear strain rates: $5 \times 10^{-4}/sec$ and $5 \times 10^{2}/sec$. The change in yield stress with increasing temperature is plotted in Figure 3.15 at the static rate in order to obtain the initial threshold stress Y_a. The yield stress decreases with increasing temperature until it becomes almost constant, which is around 400 MPa. That is going to be the initial threshold stress Y_a. It is clear that the thermal part of the stress vanishes after a temperature of 450ºK. Next step is to use a stress-strain curve at high temperature (where thermal stress is neglected) in order to find the hardening constants B and n. Figure 3.16 shows stress-strain curve at a temperature of 380ºK where the plastic hardening constants are determined to be $B = 150MPa$ and $n = 0.1$. The remaining constants $\hat{\sigma}$, B_1, B_2, m, A, and T_t are fitted simultaneously to three intercepting sets of experimental data at the same time; the first is the change in yield stress versus strain rate at a constant temperature of 295ºK (Steidel and Makerov, 1960) and the other two sets are for yield stress change versus temperature at shear strain rates of $5 \times 10^{-4}/sec$ and $5 \times 10^{2}/sec$ (Costin et al., 1980), as shown in Figure 3.17. The resulting model parameters are listed in Table 3.3.

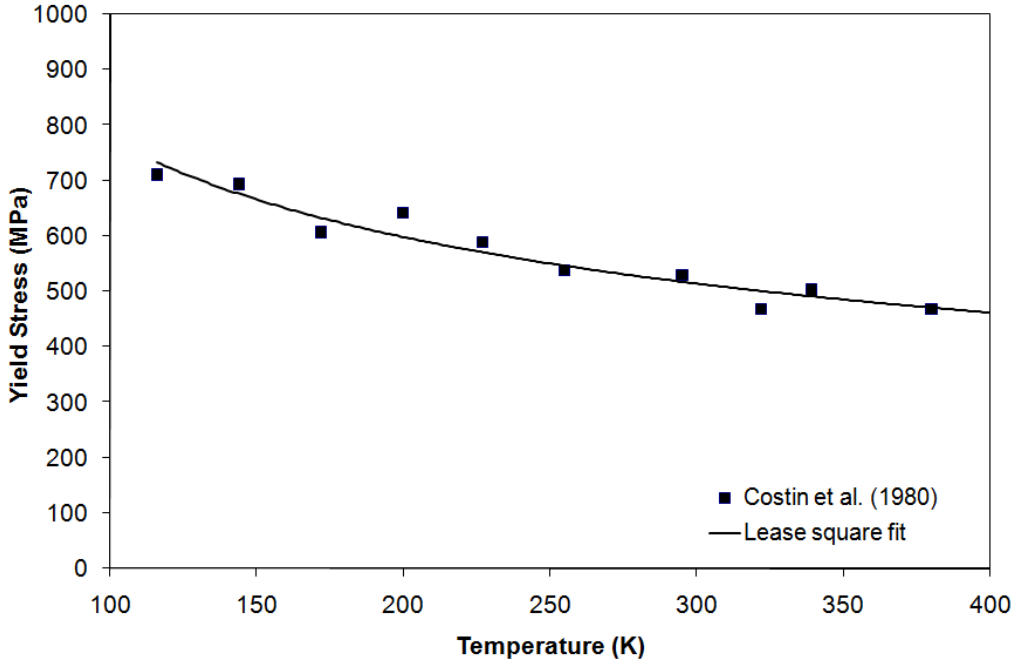

Figure 3.15: Dependence of yield stress on temperature for CR-1018 steel under static loading.

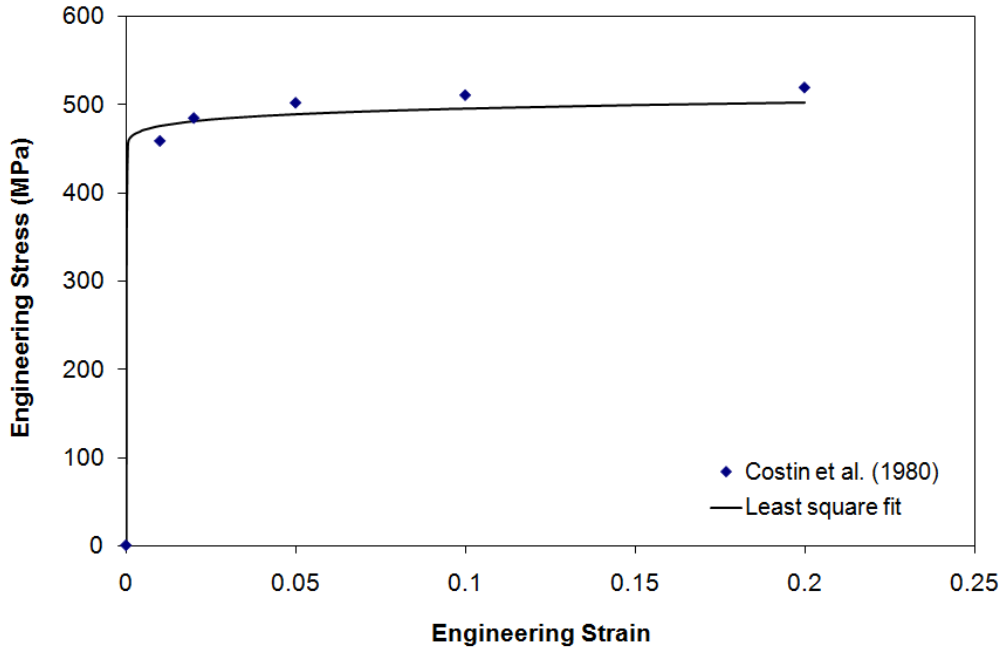

Figure 3.16: Stress-strain diagram of CR-1018 steel at 380ºK

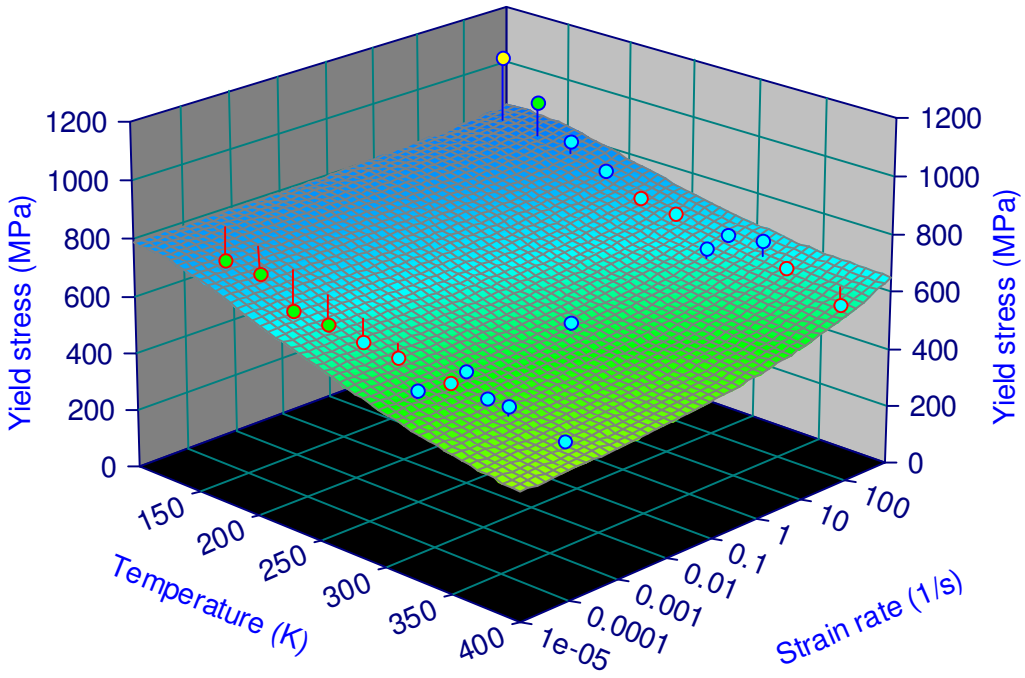

Figure 3.17: Yield stress versus strain rate and temperature for CR-1018 steel. (Data by Costin et al., 1980; and Steidel and Makerov, 1960).

Table 3.3: Parameters for the CR-1018 steel for the proposed model.

Model parameters	Numerical value
Y_a	400 MPa
B	150 MPa
n	0.1
$\hat{\sigma}$	25
B_1	0.01
B_2	0.004
m	0.15
A	5
T_t	500ºK

Stress-strain diagram for a wide range of temperatures is plotted at a static shear strain rate of $5 \times 10^{-4}/sec$ along with experimental data obtained from Costin et al. (1980) in Figure 3.18. The plot shows clearly how the stress-strain curve decreases with increasing temperature and is in good agreement with the experimental results except at very low temperatures. The model tends to underestimate the experimental data at temperature of 116ºK. The model is capable of capturing the effect of the change in temperature on the stress-strain diagram at both low and high strains when static rate loading is applied. On the other hand, under dynamic conditions with shear strain rate of $5 \times 10^{2}/sec$ the model is unable to capture the stress-strain curve as seen in Figure 3.19, especially at temperatures lower than 200ºK. In addition, the figure depicts softening behavior in CR-1018 steel that becomes clearer at lower temperatures, but still exists at high temperatures around 400ºK. At low temperatures of less than 200ºK with high rate of loading the material loses its ductility gradually with decreasing temperature and eventually its behavior becomes closer to brittle behavior rather than the ductile one.

The softening behavior that has been encountered in CR-1018 steel was not accounted for in the proposed physical model. Shear band problems are known to suffer softening behavior during the propagation stage. The physically based constitutive model that was developed previously does not describe any softening characteristics in CR-1018 steel, and hence another model needs to be developed for this case. For this reason, a phenomenological constitutive model will be proposed and tested in the following section in an effort to characterize the softening behavior of steel metal alloys as well as the strain rate and temperature dependency.

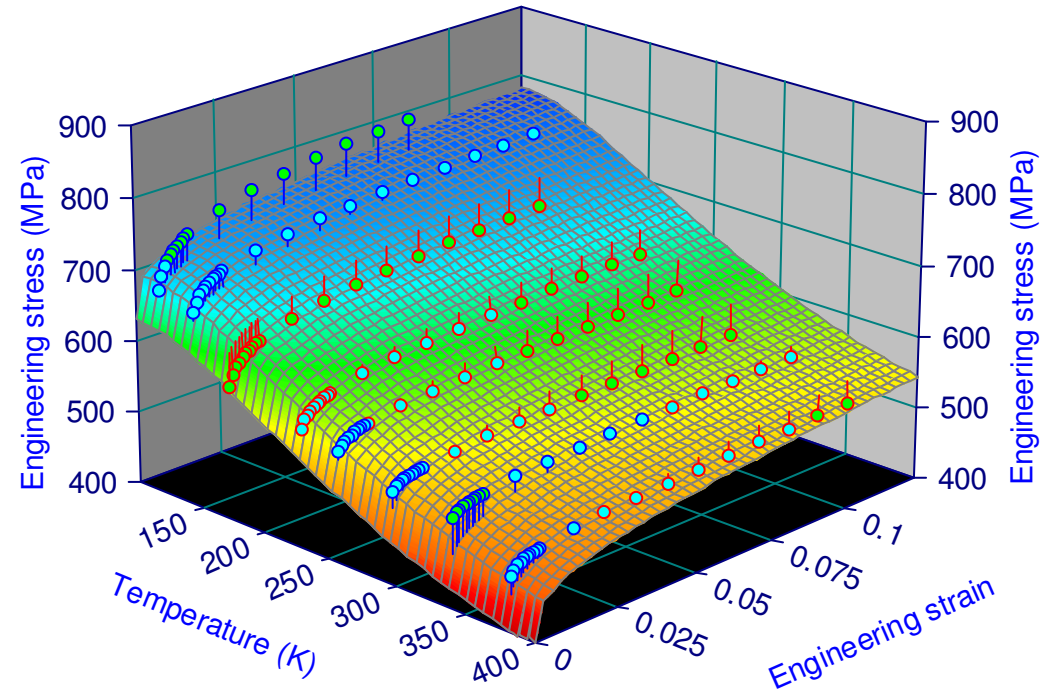

Figure 3.18: Stress-strain diagram for a wide range of temperatures at static loading. (Data by Costin et al., 1980)

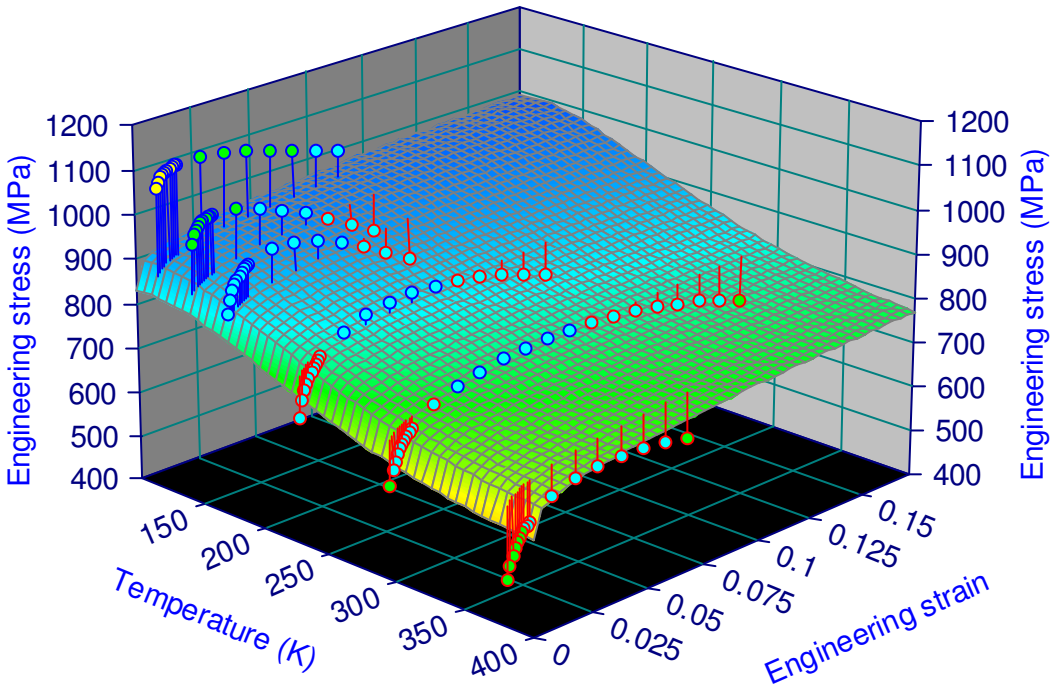

Figure 3.19: Stress-strain diagram for a wide range of temperatures at shear strain rate of $5 \times 10^2/sec$. (Data by Costin et al., 1980).

3.3 Phenomenological Model

Many forms of phenomenological or empirical models have been suggested by authors to describe the different characteristics of metals. Most have made no distinction between the constitutive function for the rate of work hardening and the rate of plastic flow. However, it has been common to combine both into a single function, the so called dynamic flow stress $\sigma = \hat{\sigma}(\varepsilon, \dot{\varepsilon}, T)$. Physical models of this dynamic flow stress are based on arguments from more or less elementary dislocation dynamics and then calibrated by choosing unknown parameters so as to fit selected data. On the other side empirical models are intended to capture the dominant effects of strain rate and temperature over a limited range of variables. In either case, the usual practice at the present involves a considerable amount of empiricism, and at least to some extent, it is always necessary to fit the analytical expressions to experimental data by choosing unknown constants for the best fit.

One of the most frequently used relationships between stress and strain is a simple power law proposed by Ludwik (1909):

$$\sigma = B\varepsilon^n \tag{3.39}$$

where σ and ε are the true stress and strain, respectively, n is the strain hardening exponent that varies between 0 and 1, and B is the hardening coefficient. This type of equations is very helpful in studying problems that include large plastic deformations such as shear banding and metal forming where non-uniform strain fields exist. As written, the flow stress exhibits no definite yield point, but with a small hardening exponent (i.e. n less than 0.1) the stress-strain curve shows a sharp knee that can be considered as the yield limit. This formula was originally proposed for unidirectional tensile straining, and it is understood that for the case of multi state stresses the strain will be the equivalent plastic strain.

Other models that can be found in the literature include Molinari and Clifton (1987) model, Litonski (1977) model, and Johnson and Cook (1983) model. All these models are explicit functions of strain, strain rate and temperature (i.e. $\sigma = \hat{\sigma}(\varepsilon, \dot{\varepsilon}, T)$). The dependence of stress on strain has always been in a power form, while the temperature function can be an inverse power or inversely linear. The strain rate dependence varies between a power term and a logarithmic form. The hardening and softening coefficients and exponents in these models are assumed constants and do not change with neither strain rate nor temperatures. This however is not quite accurate where these constants have been found to change with temperature and strain rate.

Bodner and Partom (1975) formulated a set of constitutive equations to represent elaso-viscoplastic strain hardening material behavior for large deformations and arbitrary loading histories. An essential feature of the

formulation is that the total deformation rate is considered to be separable into elastic and inelastic components which are functions of state variables at all stages of loading and unloading. Their calculations were based on material constants chosen to represent commercially pure titanium, in which they found that the temperature dependence of the material can be described by taking the strain rate power parameter to be a function of temperature. Naka et al. (2001) for example investigated the forming of aluminum-magnesium alloy sheets at different temperatures and rates. They showed that for the constitutive model of the Backofen type ($\sigma = C\varepsilon^n\dot{\varepsilon}^m$) at room temperature the strain hardening coefficient n increases slightly with increasing strain rate. On the other hand, the coefficient was found to decrease significantly from around 0.25 to less than 0.05 with increasing temperatures from 293ºK to 573ºK under static conditions. These researches raise serious questions about the use of constant coefficients in the flow stress function. Hence, instead of using an explicit strain rate and temperature variables in the constitutive model, one can propose the same simple power law (Ludwik, 1909) with the coefficients as linear functions of strain rate and temperature as follows:

$$\sigma = B_1\varepsilon^{n_1} \tag{3.40}$$

where

$$B_1 = a_1 + a_2T + a_3\dot{\varepsilon} + a_4T\dot{\varepsilon} \tag{3.41}$$

and

$$n_1 = a_5 + a_6T \tag{3.42}$$

where a_1 to a_6 are constants. Some of these constants are expected to be negative constants such as a_2 and a_6 that indicate thermal softening behavior. The forth term on the left side of Equation (3.41) ensures coupling behavior in materials between temperature and strain rate.

The strain softening phenomena is usually explained by the dislocation absorption on the grain boundaries, where dislocations delocalize and annihilate followed by a relaxation in lattice distortion. This effect of grain boundaries can reveal itself in grain boundary sliding where a decrease in dislocation density in the course of plastic deformation is noticed. This is a result of dislocation climb and multiple cross-slip that can lead to the formation and growth of subgrains. This decrease in dislocation density is known as the dynamic recovery. The rate of dynamic recovery depends on the deformation rate and the temperature and is greater than that of the corresponding static recovery. Strain hardening dominates material deformation at the early stages until softening due to dynamic recovery becomes significant, where at the late stage strain softening totally dominates the deformation. Hence, one can propose a simple term into the

constitutive equation similar to the strain hardening part that can represent the strain softening as follows:

$$\sigma = B_1 \varepsilon^{n_1} - B_2 \varepsilon^{n_2} \tag{3.43}$$

such that

$$B_2 = a_7 + a_8 T + a_9 \dot{\varepsilon} + a_{10} T \dot{\varepsilon} \tag{3.44}$$

and

$$n_2 = a_{11} + a_{12} T \tag{3.45}$$

where a_7 to a_{12} are constants. The negative sign indicates that the softening term works against the hardening one. Strain softening starts to dominate the plastic deformation at high strains and hence it would be expected that the strain softening exponent n_2 will have a value greater than unity so that the whole term will be negligible at low strains. The high value of the exponent n_2 ensures that the softening term will have the major effect on the plastic deformation at high strains.

3.3.1 Application to Cold Rolled 1018 Steel

In order to obtain the model constants for CR-1018 steel, stress-strain curves at different temperatures and strain rates obtained by Costin et al. (1980) are used (Figures 3.20 and 3.21). Firstly, every stress-strain curve at a specified temperature and strain rate is fitted to Equation (3.43) in order to obtain B_1, n_1, B_2, and n_2. It can be seen that there is no softening in the strain at the static strain rate, which results in a very small values in B_2. Next, these values are fitted into Equations (3.41), (3.42), (3.44), and (3.45) and plotted in Figures 3.22 to 3.25.

The hardening coefficient B_1 decreases with increasing temperature as illustrated in Figure 3.22, which agrees with the general behavior of metals where the strain hardening rate decreases with increasing temperature even when there is no softening behavior. With increasing strain rate the hardening coefficient increases linearly. This increase appears to be significantly above the strain rate of $100/sec$ on the logarithmic scale. The thermal sensitivity of B_1 is almost the same for low and high strain rates, which would indicate that the coupling between strain rate and temperature is week. On the other hand, the behavior of the softening coefficient looks different (Figure 3.23). At low strain rates where CR-1018 steel does not show any softening behavior, the B_2 coefficient has a very small value that is independent of temperature. With increasing strain rate the coefficient starts to acquire a value that is in the order of GPa's to compensate for the hardening part at high strains. Unlike the hardening coefficient, the softening one increases with increasing temperature at high rates of loading since metals have more softening when the temperature is raised.

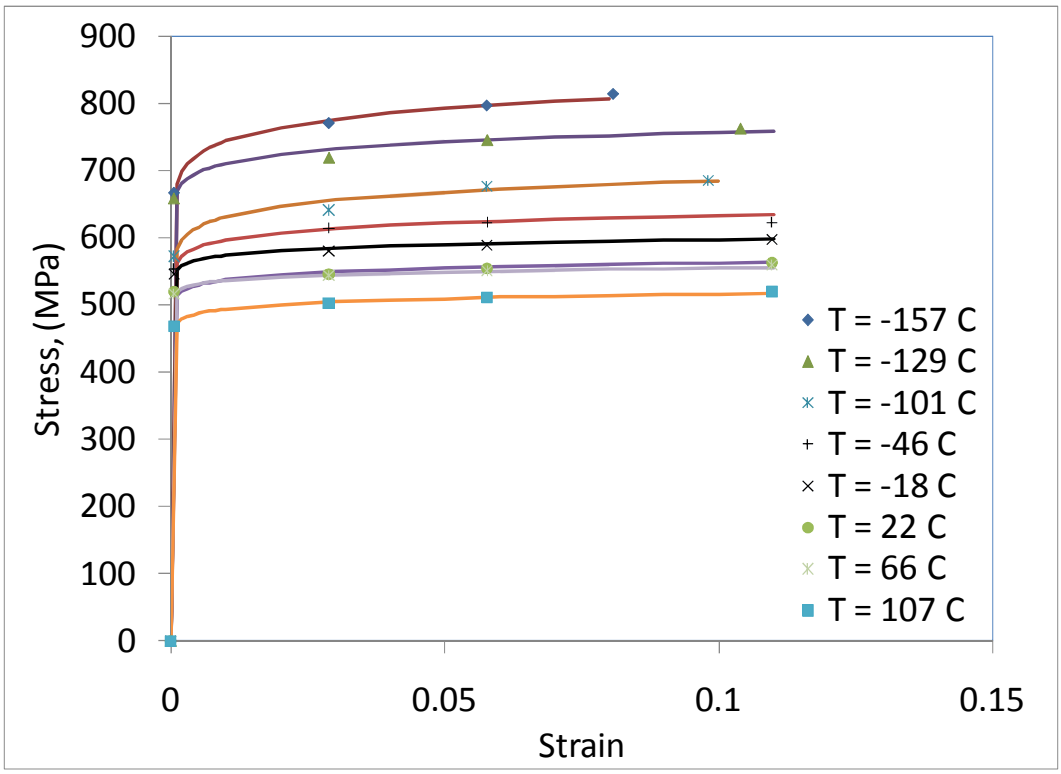

Figure 3.20: Stress-strain curves of CR-1018 steel for a wide range of temperatures at a shear strain rate of $5 \times 10^{-4}/sec.$ (Data by Costin et al., 1980).

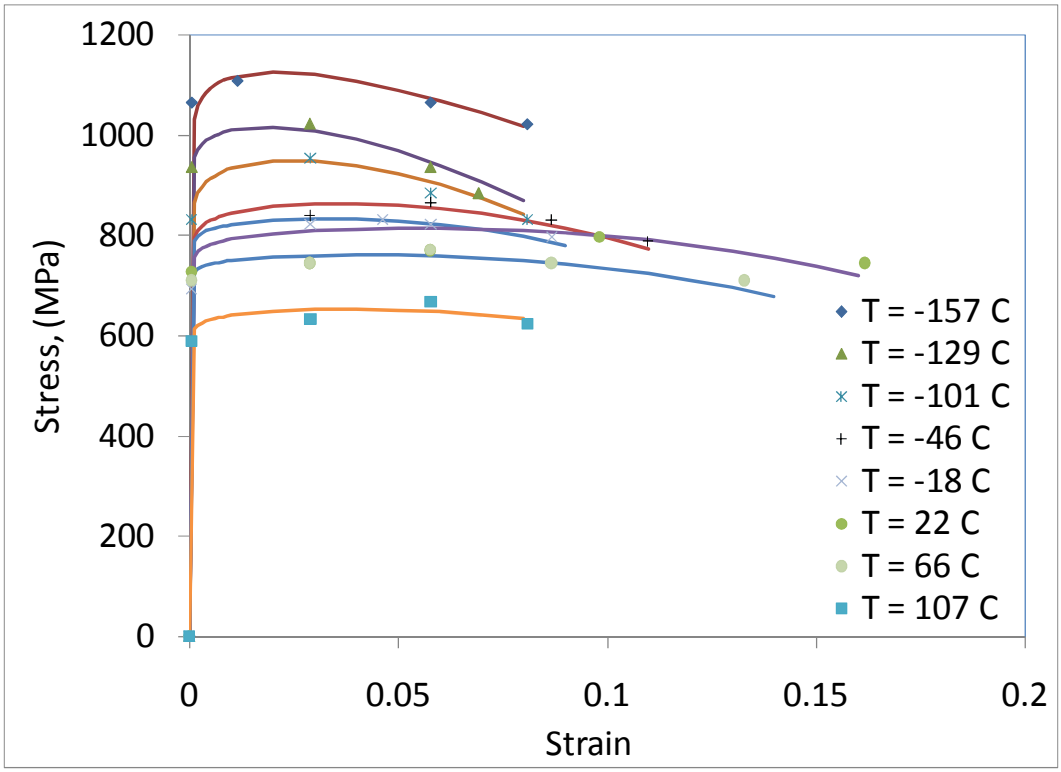

Figure 3.21: Stress-strain curves of CR-1018 steel for a wide range of temperatures at a shear strain rate of $5 \times 10^{2}/sec.$ (Data by Costin et al., 1980)

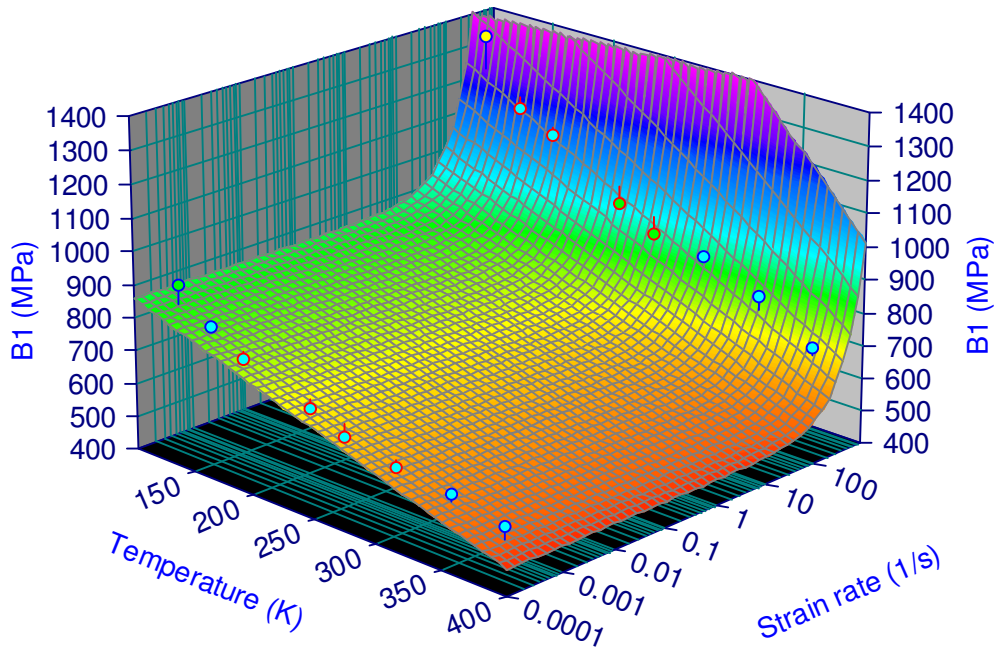

Figure 3.22: Change of hardening coefficient B_1 versus temperature and strain rate.

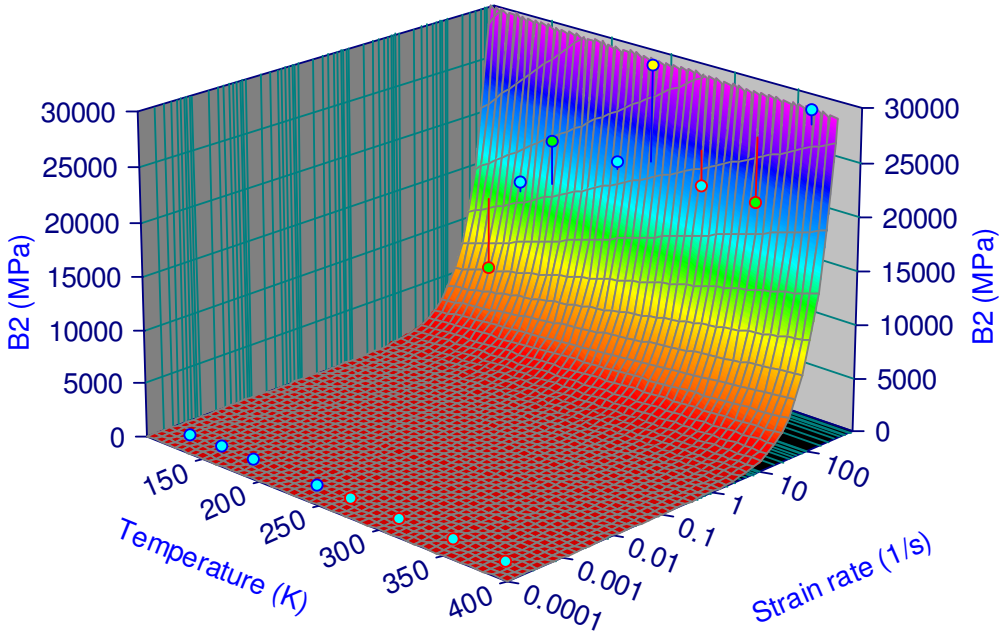

Figure 3.23: Change of softening coefficient B_2 versus temperature and strain rate.

Figure 3.24 shows the change of the hardening exponent n_1 with temperature and strain rate. The exponent is independent of the strain rate and only changes with temperature. As the temperature increases n_1 decreases which simulates a more ductile flattened stress-strain curve. The thermal sensitivity of the hardening exponent is about -0.01/100ºK. On the other hand the

softening exponent n_2 has a much larger value than n_1, which enables the constitutive equation to account for softening only at high strains. Generally the softening exponent should be greater than unity and can have a value of 3 or more as illustrated in Figure 3.25. Since n_2 is similar to n_1 in that both are independent of the strain rate, the softening exponent tends to increases with raising temperature indicating more thermal softening in the material. The softening exponent has a thermal sensitivity of about 0.5/100ºK. The model constants a_1 to a_{12} are listed in Table 3.4

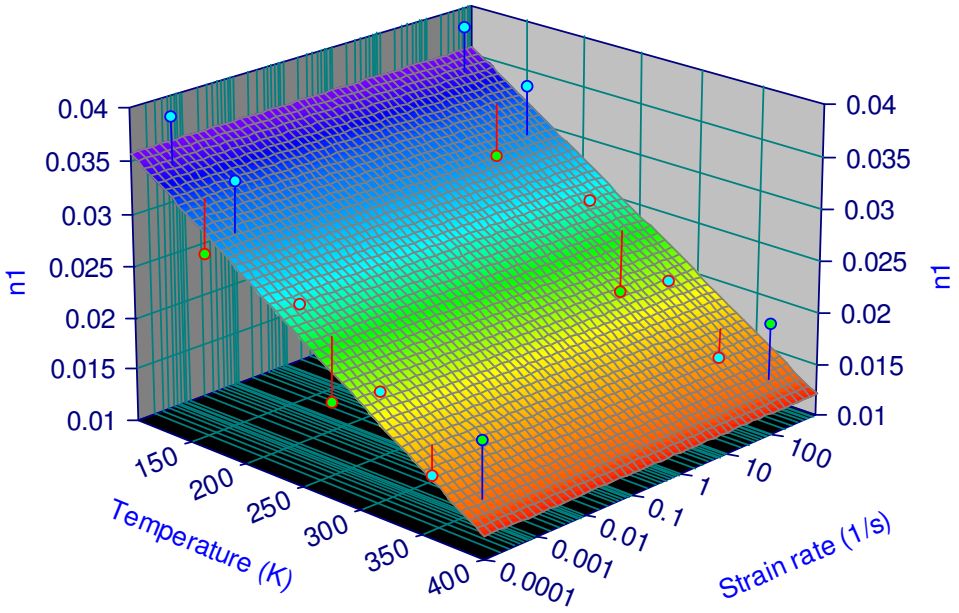

Figure 3.24: Change of hardening exponent n_1 versus temperature and strain rate.

Now with the entire model constants determined, the stress-strain diagrams can be plotted. Figure 3.26 describes the stress-strain curve for a full range of temperatures at a shear strain rate of $5 \times 10^{-4}/sec$. The model coincides with the experimental results at both low and high strains, and also captures the thermal softening with high precision. At high strain rates illustrated in Figure 3.27, the model also shows a very good agreement with the laboratory data at low and high strains where it captures the softening behavior of CR-1018 steel with good accuracy. The softening behavior is captured better at lower temperatures where steel acts closer to brittle material than ductile material. Finally, Figure 3.28 shows the stress-strain diagram for a wide range of strain rates at a temperature of 295ºK. It is clear that as strain rate increases, the softening characteristics become more obvious even at normal room temperature.

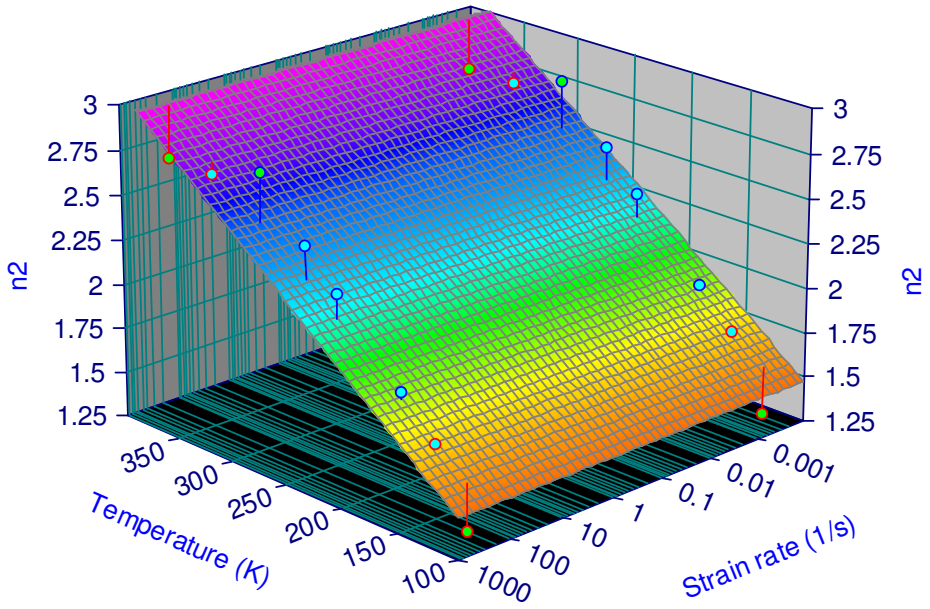

Figure 3.25: Change of softening exponent n_2 versus temperature and strain rate.

In this chapter two constitutive models were developed. The first is based on the physics of the dislocations dynamics, while the other is phenomenologically based model. The physically based model showed to be able to describe material behavior for pure bcc and fcc metals, but not the steel alloys. This is attributed to the more complex behavior of dislocations in alloys. The empirical constitutive law was more successful in capturing the mechanical behavior of CR-1018 steel alloy under different temperatures and strain rates. For this reason the empirical model will be the one to be used in studying the adiabatic shear bands and will be implemented in the viscoplastic finite element code under ABAQUS/Explicit program.

Table 3.4: Parameters of the constitutive model for the CR-1018 steel.

Model parameters	Numerical value	Model parameters	Numerical value
a_1	982.3	a_7	0.9945
a_2	-1.260	a_8	-0.00006053
a_3	1.785	a_9	17.96
a_4	-0.003136	a_{10}	0.2135
a_5	0.04364	a_{11}	0.9344
a_6	-0.00007879	a_{12}	0.005407

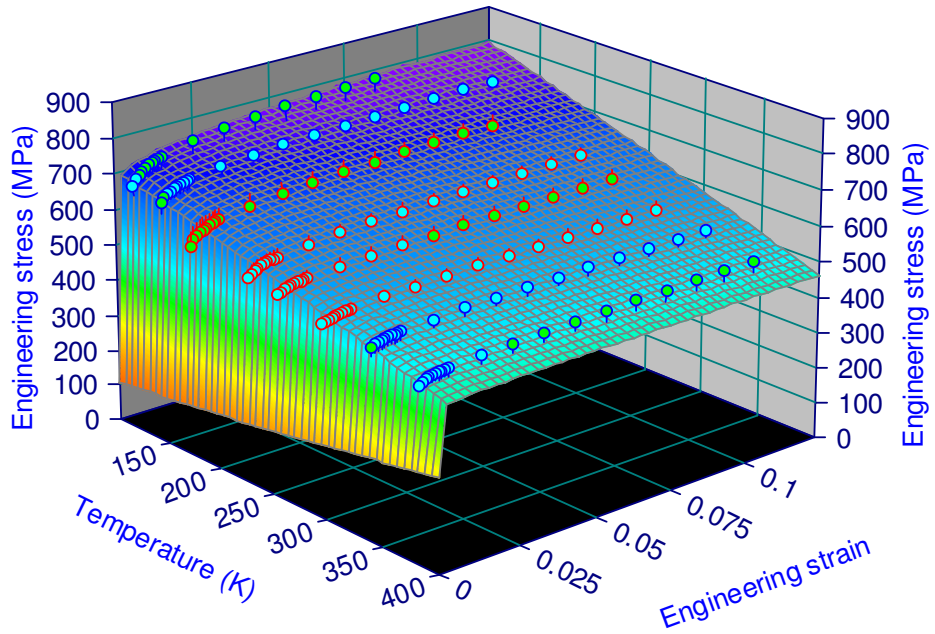

Figure 3.26: Stress-strain diagram for a wide range of temperatures at a shear strain rate of $5 \times 10^{-4}/sec$. (Data by Costin et al., 1980).

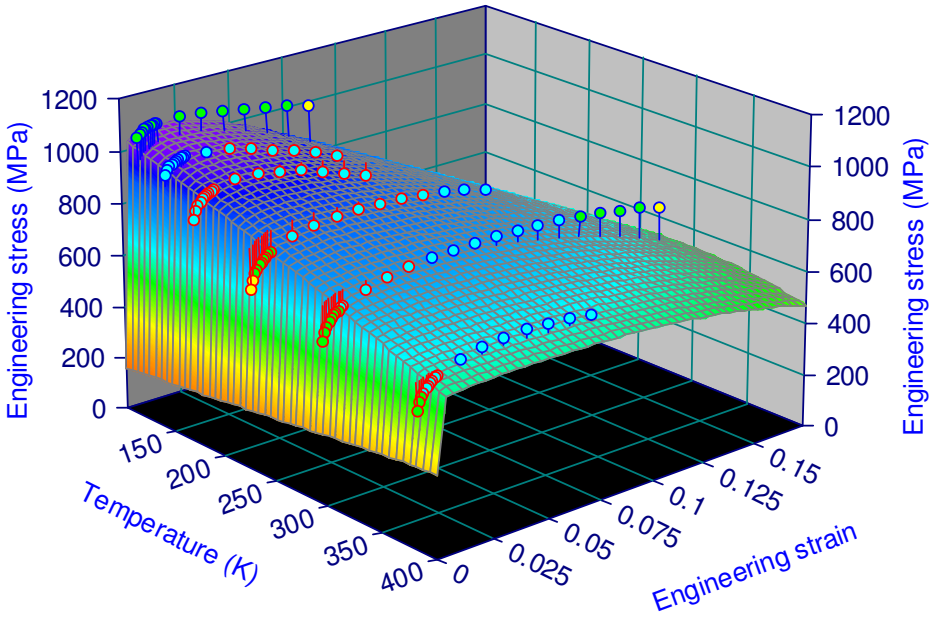

Figure 3.27: Stress-strain diagram for a wide range of temperatures at a shear strain rate of $5 \times 10^{2}/sec$. (Data by Costin et al., 1980).

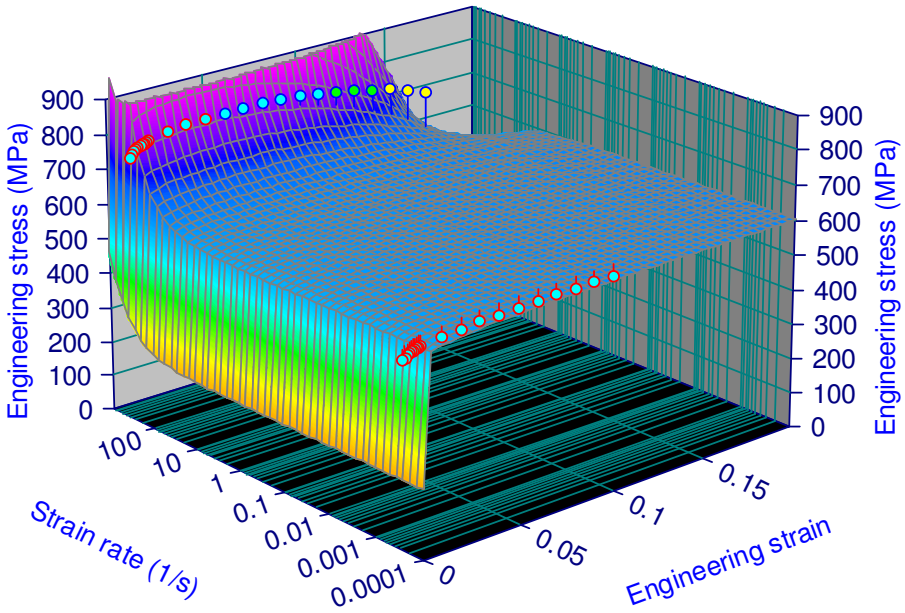

Figure 3.28: Stress-strain diagram for a wide range of strain rates at a temperature of 295ºK. (Data by Costin et al., 1980)

CHAPTER 4: ADIABATIC SHEAR BANDS

4.1 Shear Band Instability

Although adiabatic shear bands are very narrow, they are still generally considered a macroscopic mode of deformation. In continuum mechanics the occurrence of adiabatic shear bands signals a transition from homogeneous deformation to a localized one. For this reason the occurrence of adiabatic shear bands can be studied straightforwardly if the process of banding itself is not considered.

The basic idea of banding is physically simple. For normal plastic deformation, a positive increasing work increment is needed to cause deformation in material. When deformation in material starts to form with decreasing work imposed to the system, a transition in deformation modes will take place in the deforming system. This idea was proposed by Drucker (1951), establishing his well known hypothesis concerning stable and unstable deformation in plasticity theory. The concept is that plastic strain may occur at decreasing stresses beyond a maximum stress, satisfying a clear unstable deformation mode (see Figure 4.1).

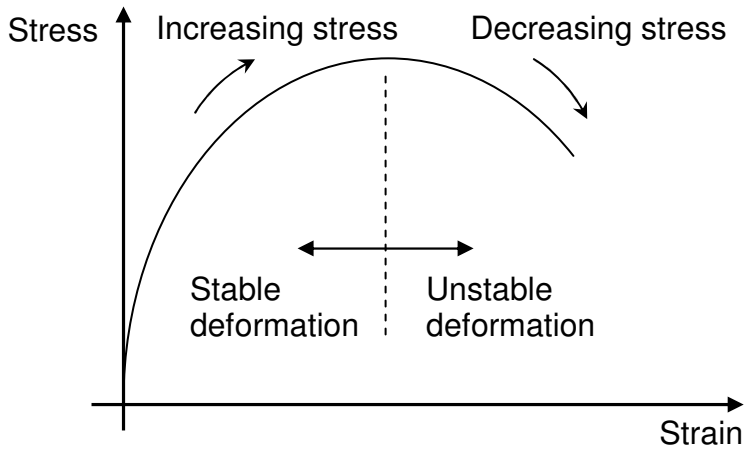

Figure 4.1: Stable and unstable plastic behavior of material.

Historically, the concept of instability occurring at a peak in the load or stress can be traced back to Considere (1885) who provided a geometrical construction to define the maximum load condition for necking in simple tension. Following the maximum load conditions in tension, Recht (1964), Culver (1973) and other investigators proposed empirical criteria for the onset of adiabatic shearing in accordance with the idea of a maximum shear stress criterion. Because there is no change in cross sectional area in simple shear, it is considered in many ways to be a simpler configuration than the tension test.

However, other factors, such as adiabatic shear localization, can make simple shear tests of real materials to be quite complex. If elastic deformations, history effects (including strain rate and temperature history effects) and phase transformations are neglected in the tested material, then the shear stress can be written as a function of shear strain γ, shear strain rate $\dot{\gamma}$, and temperature T as follows:

$$\tau = f(\gamma, \dot{\gamma}, T) \tag{4.1}$$

The corresponding incremental shear stress can be written as:

$$d\tau = \left(\frac{\partial \tau}{\partial \gamma}\right)_{\dot{\gamma},T} d\gamma + \left(\frac{\partial \tau}{\partial \dot{\gamma}}\right)_{\gamma,T} d\dot{\gamma} + \left(\frac{\partial \tau}{\partial T}\right)_{\gamma,\dot{\gamma}} dT \tag{4.2}$$

The three partial differential terms are of great importance in the discussion of the occurrence of adiabatic shear banding. They can be interpreted physically as follows:

$\left(\frac{\partial \tau}{\partial \gamma}\right)_{\dot{\gamma},T}$ is the shear strain hardening rate at instantaneous strain rate and temperature.

$\left(\frac{\partial \tau}{\partial \dot{\gamma}}\right)_{\gamma,T}$ is the shear strain rate hardening rate at instantaneous strain and temperature.

$\left(-\frac{\partial \tau}{\partial T}\right)_{\gamma,\dot{\gamma}}$ is the thermal softening rate at instantaneous strain and strain rate.

The maximum shear stress criterion requires that $d\tau = 0$, which implies that the point in the process where thermal softening just begins to outweigh strain and strain rate hardening is the starting point for instability. Strain rate hardening is generally appreciable only at very high strain rates and is usually much smaller than strain hardening for most engineering applications. Therefore, strain rate hardening may be neglected, and the criterion $d\tau = 0$ will correspond to:

$$\left(\frac{\partial \tau}{\partial \gamma}\right)_{\dot{\gamma},T} + \left(\frac{\partial \tau}{\partial T}\right)_{\gamma,\dot{\gamma}} \left(\frac{dT}{d\gamma}\right) = 0 \tag{4.3}$$

For adiabatic deformation, the increase in temperature due to the plastic work is:

$$dT = \frac{\beta \tau}{\rho c} d\gamma \tag{4.4}$$

where ρ is the material density, c is the specific heat, and β is the fraction of plastic work converted into heat. This factor is of big importance in studying adiabatic shear bands and has been studied decades ago. Some of the earliest

research on this subject is by Farren and Taylor (1925) and Taylor and Quinney (1934). Farren and Taylor (1925) studied tensile specimens of mild steel and copper using thermocouple measurements. They found that 86.5% of the plastic work done on the specimens converted into heat, while the percentage was 90.5% for copper. It was thought that the energy retained in the metals during distortion should be a definite fraction of the work done. The fractional energy appeared to be a constant for various amounts of distortion, with some variation from one metal to another. Therefore, a value between 85% and 95% is generally accepted in engineering applications for the amount of plastic work converted into heat. The effect of cold work on fractional energy was investigated later on by Taylor and Quinney (1934) with a series of torsion tests. The results showed that the ratio of the retained latent energy to the plastic work done on the specimen remains in the range of 5-10%. The ratio was not constant during the whole test, where beyond a certain amount of distortion the retained latent energy tends to decrease with further distortion and approaches a saturated value. Therefore, it is only an approximation that a fixed fraction of plastic work is assumed to convert into heat. However, this approximation is still accepted in engineering practices. Furthermore, sometimes it is more practical to just assume that the whole plastic work converts into heat and take $\beta = 1$.

For adiabatic tension tests, a uniaxial stress function σ of the following form is used:

$$\sigma = f(\varepsilon, \dot{\varepsilon}, T) \tag{4.5}$$

One can write the incremental uniaxial stress as follows:

$$d\sigma = \left(\frac{\partial \sigma}{\partial \varepsilon}\right)_{\dot{\varepsilon},T} d\varepsilon + \left(\frac{\partial \sigma}{\partial \dot{\varepsilon}}\right)_{\varepsilon,T} d\dot{\varepsilon} + \left(\frac{\partial \sigma}{\partial T}\right)_{\varepsilon,\dot{\varepsilon}} dT \tag{4.6}$$

where $\left(\frac{\partial \sigma}{\partial \varepsilon}\right)$ is the uniaxial strain hardening rate, $\left(\frac{\partial \sigma}{\partial \dot{\varepsilon}}\right)$ is the uniaxial strain rate hardening rate, and $\left(-\frac{\partial \sigma}{\partial T}\right)$ is the uniaxial thermal softening rate. In this case the instability occurs at maximum axial load where $dP = 0$, which leads to:

$$Ad\sigma + \sigma dA = 0 \tag{4.7}$$

Assuming that the material is incompressible during plastic deformation, the increment in the uniaxial tensile strain is:

$$d\varepsilon = -dA/A \tag{4.8}$$

where A is the current cross sectional area. Substituting Equation (4.8) in Equation (4.7) results:

$$d\sigma = \sigma d\varepsilon \tag{4.9}$$

Noting that the increase in temperature due to the plastic work becomes:

$$dT = \frac{\beta\sigma}{\rho c} d\varepsilon \tag{4.10}$$

Now substituting Equation (4.9) and (4.10) in Equation (4.6) and rearranging:

$$\frac{\left\{\frac{\beta}{\rho c}\left(-\frac{\partial\sigma}{\partial T}\right)+1\right\}}{\left\{\frac{1}{\sigma}\right\}\left(\frac{\partial\sigma}{\partial\varepsilon}\right)} = 1 \tag{4.11}$$

Using the constitutive equation of the material in Equation (3.40), the above criterion can be written in the form of a characteristic or instability strain ε_i as follows:

$$-\frac{\beta}{\rho c}\left\{[(a_2 + a_4\dot{\varepsilon}) + a_6(a_1 + a_2 T + a_3\dot{\varepsilon} + a_4 T\dot{\varepsilon})\ln\varepsilon_i]\varepsilon_i^{(a_5+a_6T+1)}\right\} + \varepsilon_i = a_5 + a_6 T \tag{4.12}$$

An explicit form of the instability strain cannot be found, and the equation has to be solved numerically. In addition, a similar yet more complex equation can be obtained for the full constitutive model of Equation (3.43).

In most steels, $\rho \approx 7800 kg/m^3$ and $c \approx 450 J/kgK$, which requires around 0.8 strain increment to rise the temperature about 100ºK. This might not be enough to soften the material thermally, and therefore a strain softening term in the hardening equation is required to soften the material. This indicates that Equation (3.40) is not adequate to calculate the instability strain, and the full equation (3.43) should be used instead. A small comparison (Figure 4.2) between the thermal softening $\frac{\partial\sigma}{\partial T}$ calculated from Equations (3.40) and (3.43) at a strain rate of $10^3/sec$ shows that the thermal softening predicted with Equation (3.40) is in the order of $\mathcal{O}(1)$/ºK, knowing that the rise in temperature due to the plastic deformation is around 100ºK. This means the decrease in the flow stress due to the thermal softening is in the order of $\mathcal{O}(100)$ and is small with respect to the strain hardening that is in the order of $\mathcal{O}(1000)$. Using Equation (3.43) with strain softening, on the other hand, shows much higher thermal softening that can overcome the strain hardening at late stages. Therefore, Equation (3.40) is not enough to simulate shear bands, and Equation (3.43) shall be used here.

The strain hardening rate, strain rate hardening rate, and the thermal softening rate can be found for Equation (3.43), respectively, to be as follows:

$$\frac{\partial\sigma}{\partial\varepsilon} = B_1 n_1 \varepsilon^{n_1-1} - B_2 n_2 \varepsilon^{n_2-1} = (a_1 + a_2 T + a_3\dot{\varepsilon} + a_4 T\dot{\varepsilon})(a_5 + a_6 T)\varepsilon^{(a_5+a_6T-1)} - (a_7 + a_8 T + a_9\dot{\varepsilon} + a_{10} T\dot{\varepsilon})(a_{11} + a_{12} T)\varepsilon^{(a_{11}+a_{12}T-1)} \tag{4.13}$$

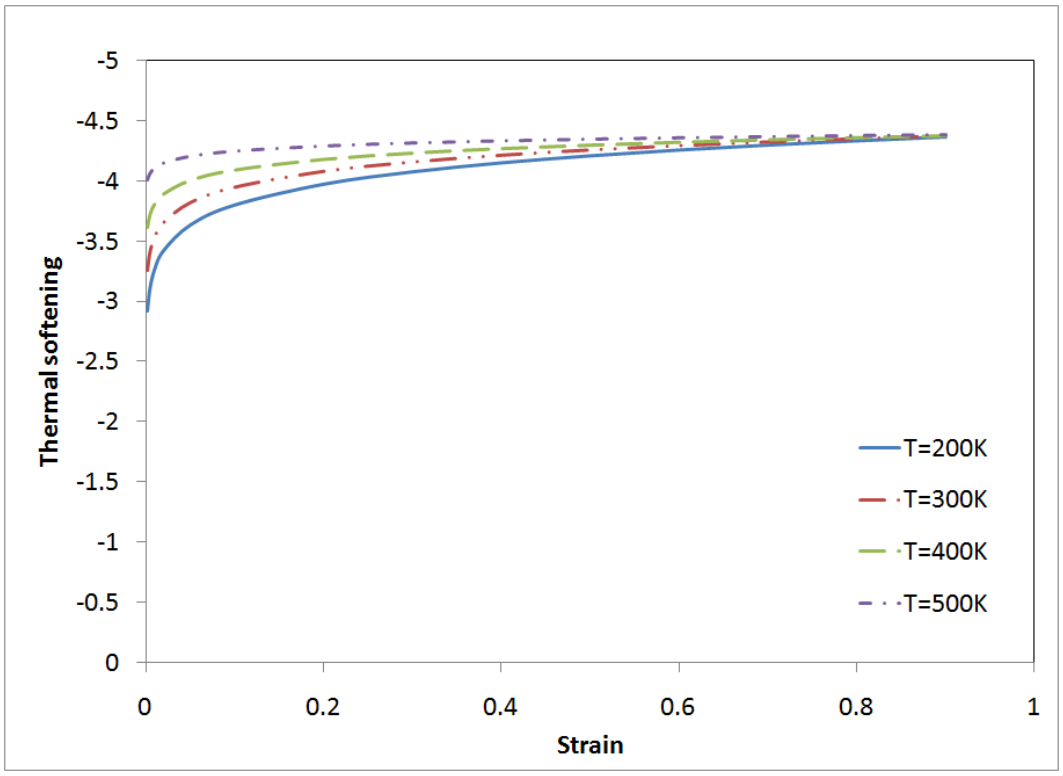

(a)

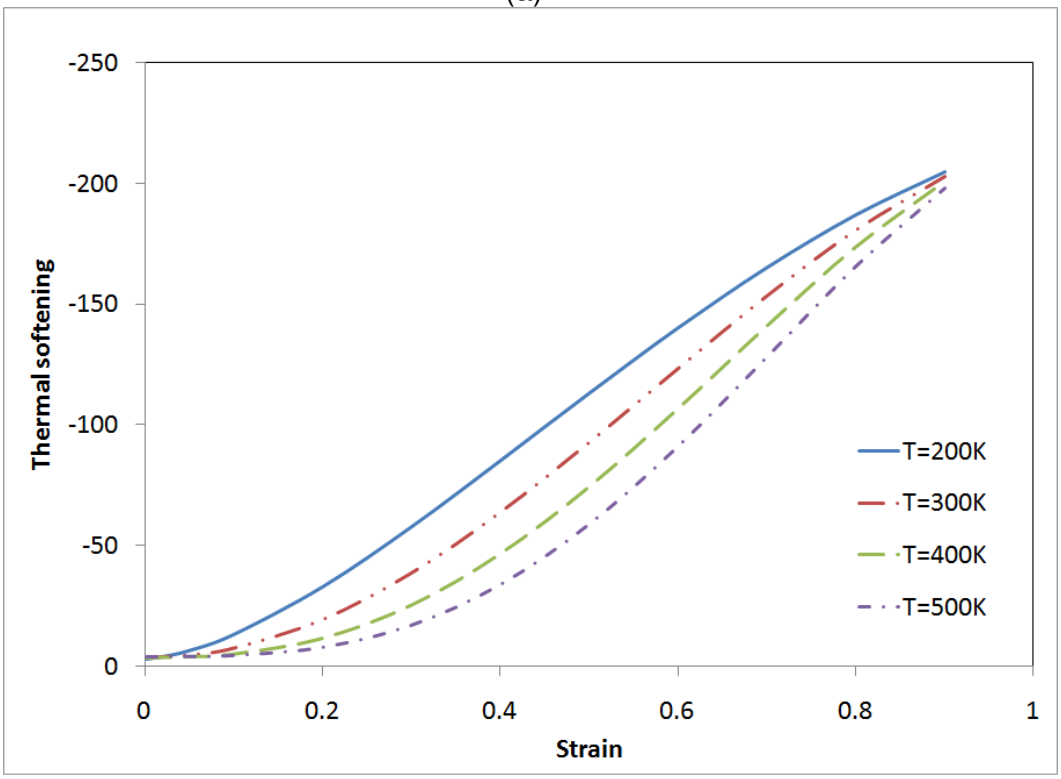

(b)

Figure 4.2: Thermal softening using (a) Equation(3.40), and (b) Equation (3.43)

$$\frac{\partial \sigma}{\partial \dot{\varepsilon}} = \frac{dB_1}{d\dot{\varepsilon}}\varepsilon^{n_1} - \frac{dB_2}{d\dot{\varepsilon}}\varepsilon^{n_2} = (a_3 + a_4 T)\varepsilon^{(a_5 + a_6 T)} - (a_9 + a_{10} T)\varepsilon^{(a_{11} + a_{12} T)} \quad (4.14)$$

$$\frac{\partial \sigma}{\partial T} = \frac{dB_1}{dT}\varepsilon^{n_1} + B_1 \frac{dn_1}{dT}\varepsilon^{n_1}\ln\varepsilon - \frac{dB_2}{dT}\varepsilon^{n_2} - B_2 \frac{dn_2}{dT}\varepsilon^{n_2}\ln\varepsilon = \{(a_2 + a_4\dot{\varepsilon}) + a_6(a_1 + a_2 T + a_3\dot{\varepsilon} + a_4 T\dot{\varepsilon})\ln\varepsilon\}\varepsilon^{(a_5 + a_6 T)} - \{(a_8 + a_{10}\dot{\varepsilon}) + a_{12}(a_7 + a_8 T + a_9\dot{\varepsilon} + a_{10} T\dot{\varepsilon})\ln\varepsilon\}\varepsilon^{(a_{11} + a_{12} T)} \quad (4.15)$$

Equation (4.13) is illustrated in Figure 4.3. The strain hardening rate decreases for both cases of low and high strain rates. In the case of the low strain rate, the hardening rate decreases until it reaches a very small stable yet positive value, while it keeps decreasing below zero for high strain rate, which indicates softening behavior. The hardening rate is higher at high strain rates and also the softening rate is higher compared to the low strain rate where the softening is missing. Rising temperatures cause the material to soften considerably. This thermal effect is stronger for high strain rates compared to the low ones. At high temperatures the effect of strain rate falls significantly since material starts acting more like a fluid. For example at a temperature of 500ºK, the strain hardening rate for low strain rate is very close to that of high strain rate.
Figure 4.4 shows how the strain hardening rate versus strain changes for different strain rates. At low strains the strain rate effect is negligible and becomes significant as the strain rises. Increasing the strain rate causes the material to start softening faster and at lower strain. This behavior has been seen in many metals where material starts acting more like a brittle material at high rates.

Strain rate hardening rate in Equation (4.14) is represented in Figure 4.5. It is clear from the equation that the strain rate hardening rate does not depend on the strain rate itself, and depends only on the strain and temperature. This hardening rate starts with a very small positive value and changes its sign (i.e. becomes softening) at a strain of 0.1. However, the value of strain rate hardening (or softening) is still small compared to the strain hardening and thermal softening, which is the main reason why it is usually neglected in the analysis of adiabatic shear bands. Temperature effect is not substantial here and noticeable only at strains higher than 0.7.

Thermal softening obtained in Equation (4.15) is plotted in Figure 4.6 for different temperatures at low and high strain rates. Thermal softening is very negligible at low strain rates compared to the high strain rate case, and temperature itself does not affect it significantly. At high strain rates the thermal softening reaches around 200 MPa/ºK at a strain of 0.9 where it is around 1.2 MPa/ºK at low strain rate. In addition, thermal softening increases with increasing temperature at low strain rate, but changes its behavior and decreases with increasing temperature at high strain rate. Thermal softening is also plotted versus strain for different strain rates in Figure 4.7. The thermal softening becomes crucial only at strain rates higher than $100/sec$, and can be neglected below that value.

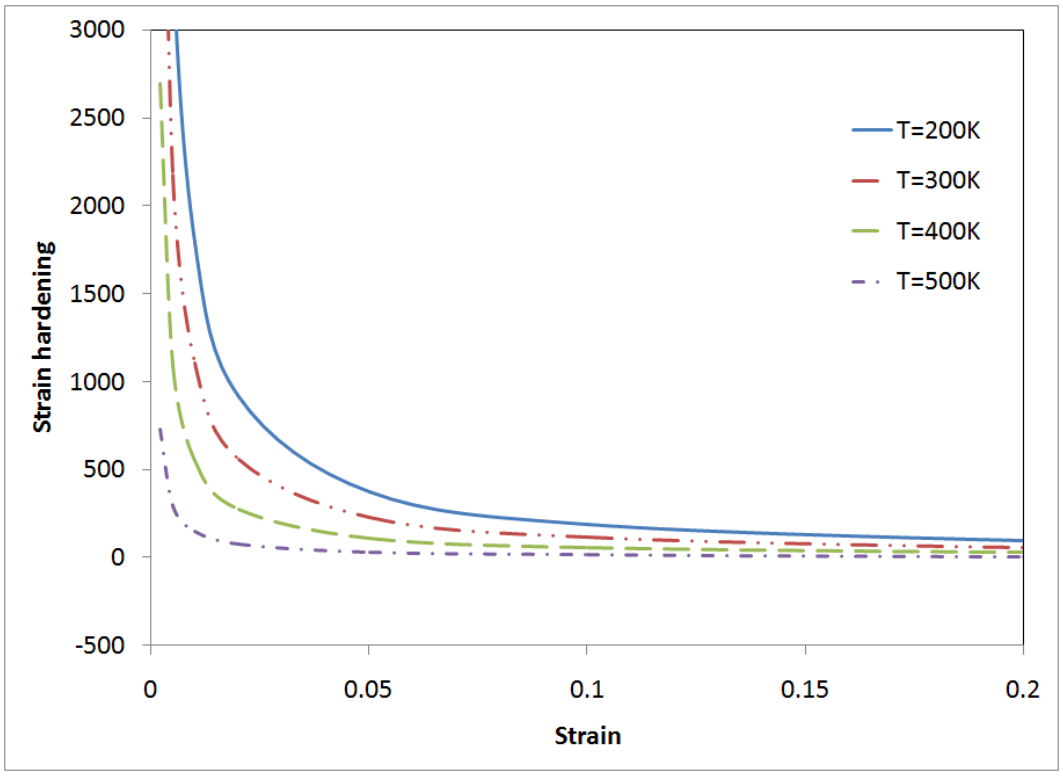

(a)

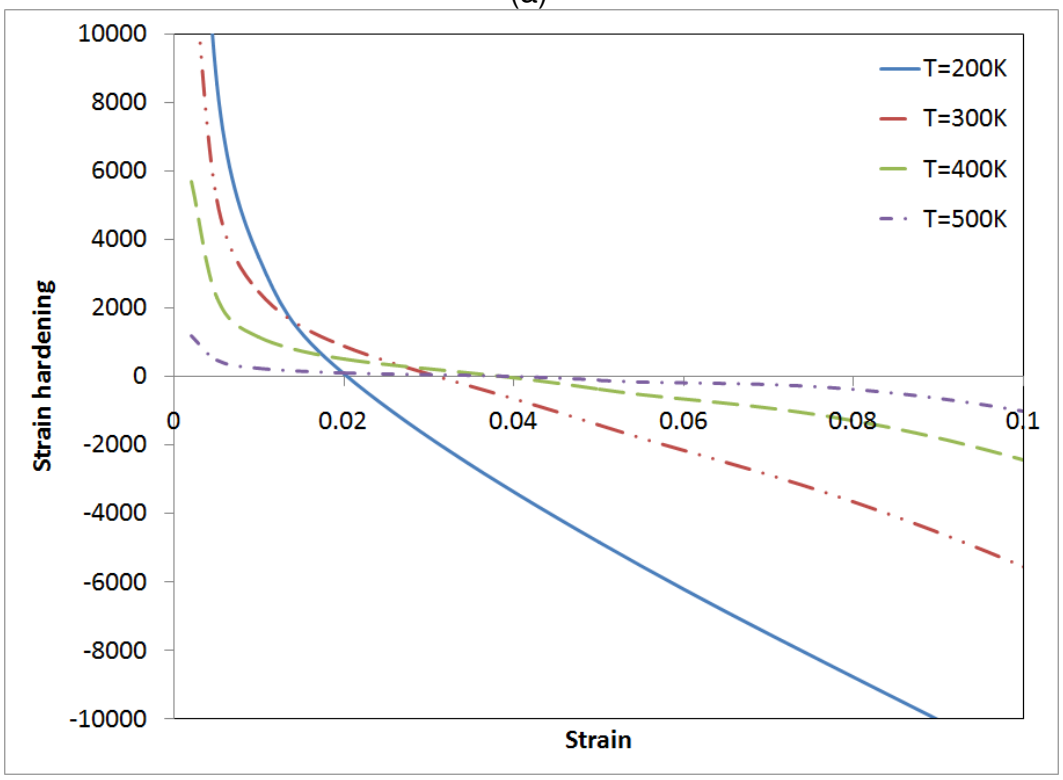

(b)

Figure 4.3: Change of strain hardening versus strain of CR-1018 steel for different temperatures at strain rates of (a) $0.001/sec$, and (b) $1000/sec$.

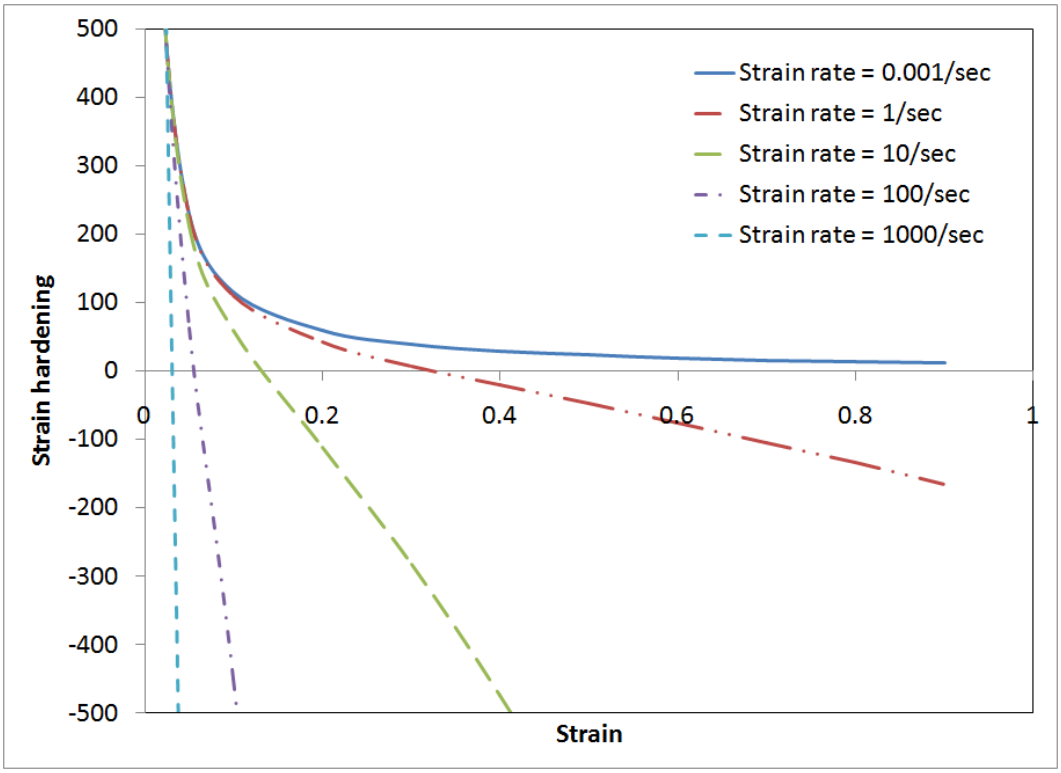

(a)

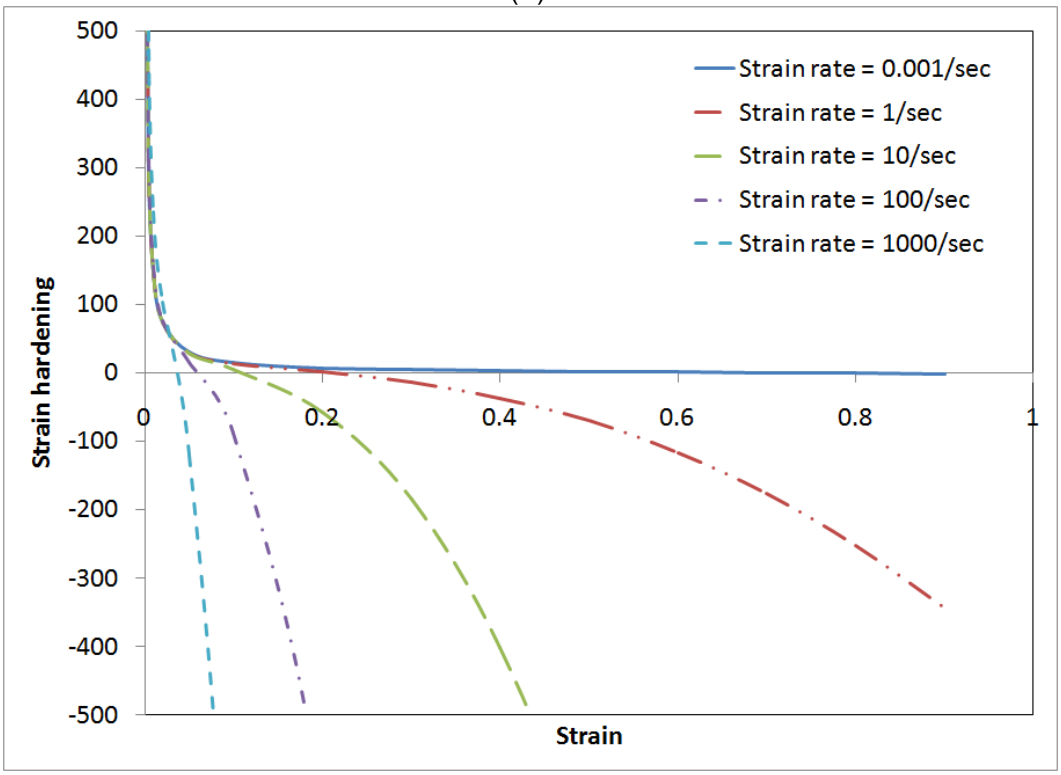

(b)

Figure 4.4: Change of strain hardening versus strain of CR-1018 steel for different strain rates at temperatures of (a) 300ºK, and (b) 500ºK.

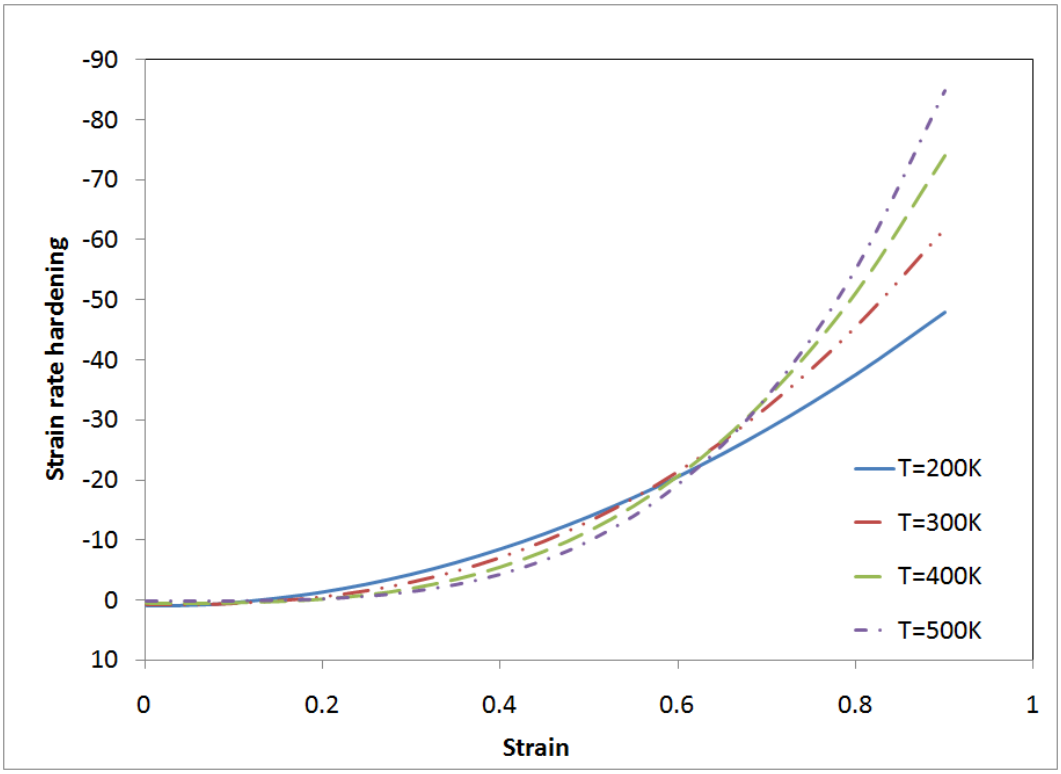

Figure 4.5: Change of strain hardening versus strain of CR-1018 steel for different temperatures.

The instability strain is finally calculated numerically using Equation (4.11). Figure 4.8 shows the change in instability strain with respect to temperature. Instability strain is seen to decrease with increasing temperature. This decline is almost linear at low strain rate and shows some curvature at high strain rate. The effect of strain rate is clearly high at room temperature and diminishes at higher temperature. The instability strain is also plotted against strain rate in Figure 4.9. The curve shape of the change of instability strain versus strain rate is the reverse of the flow stress curve versus the strain rate. The instability strain starts decreasing significantly at a strain rate higher than $100/sec$ in a logarithmic form. This strain rate sensitivity drops substantially at a temperature of 500ºK. This agrees with the results obtained by Batra and Wei (2007) where they showed that the instability strain for HY-100 steel decreases linearly on the strain rate range $10^3 - 10^6/sec$ in the logarithmic scale. As indicated before, the effect of temperature change is small here and hence it is expected to have only small influence on the initiation and propagation of adiabatic shear localization, which will be discussed next.

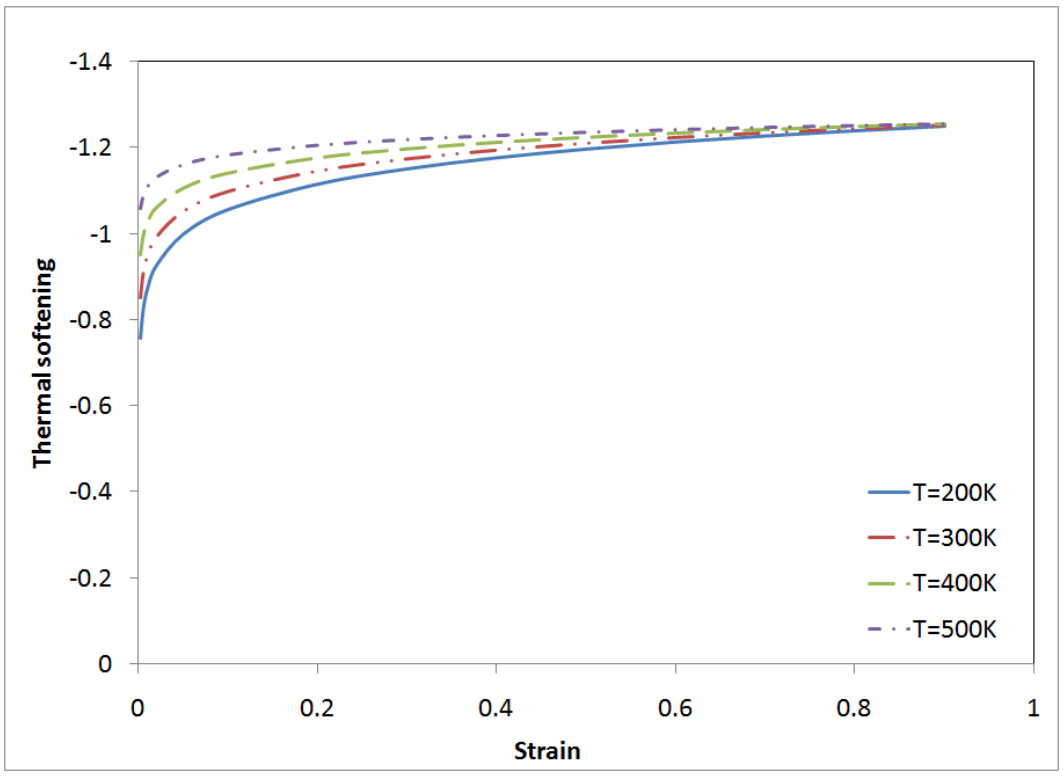

(a)

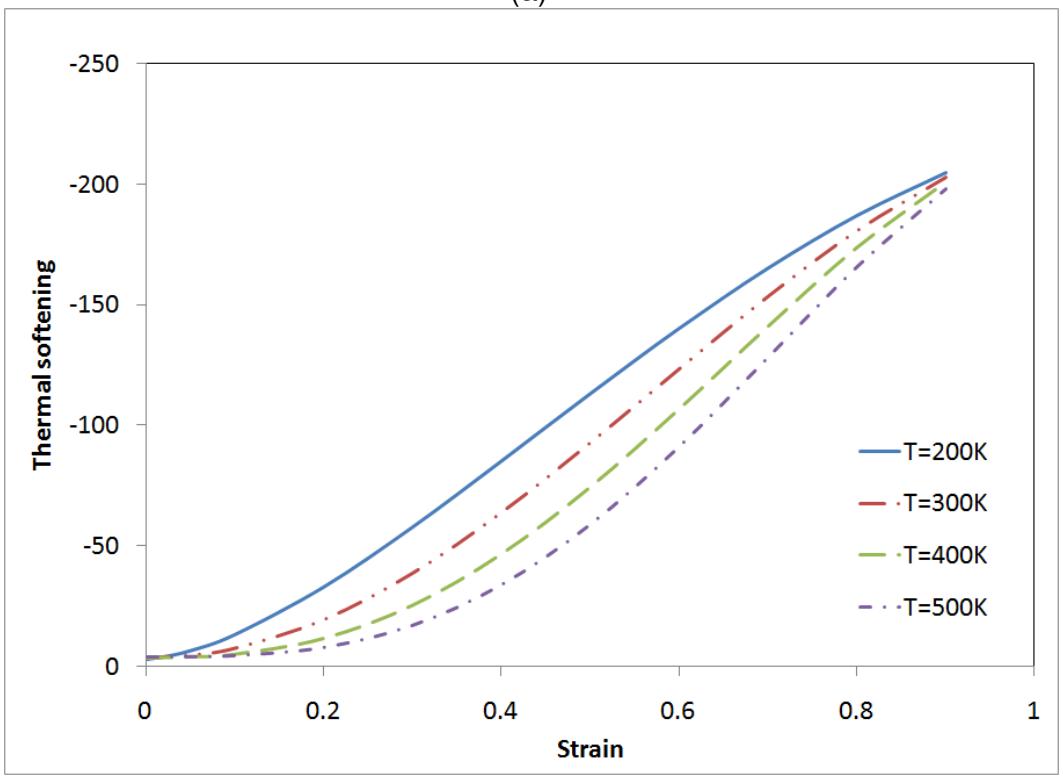

(b)

Figure 4.6: Change of thermal softening versus strain of CR-1018 steel for different temperatures at strain rates of (a) $0.001/sec$, and (b) $1000/sec$.

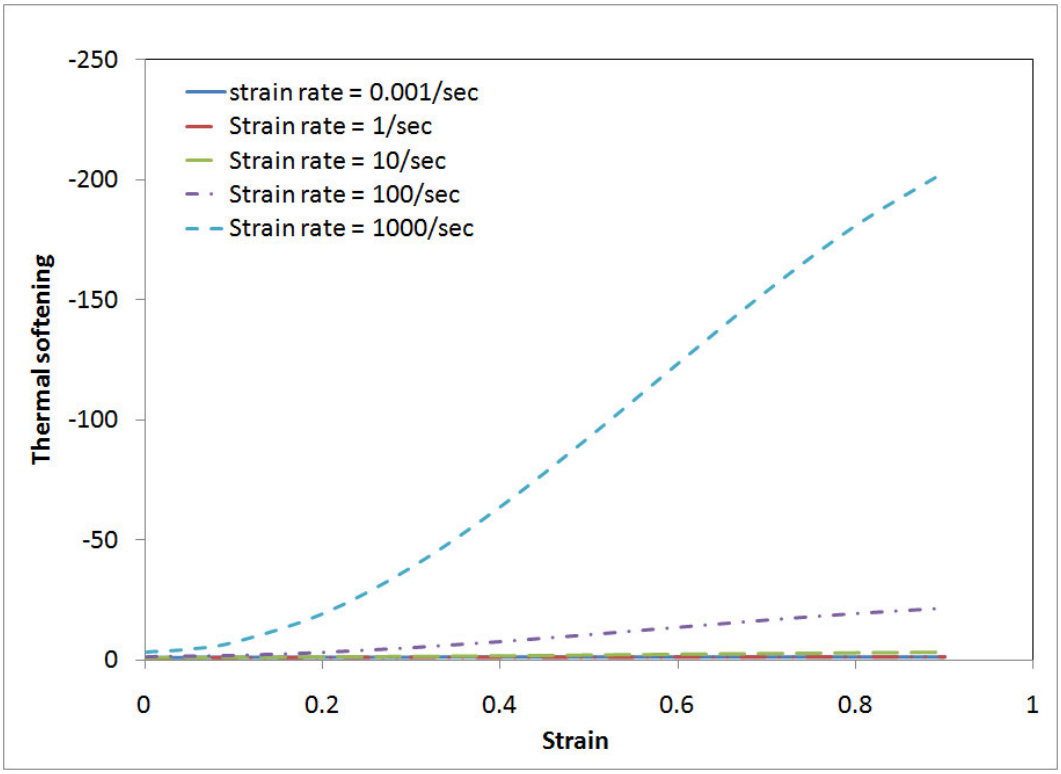

(a)

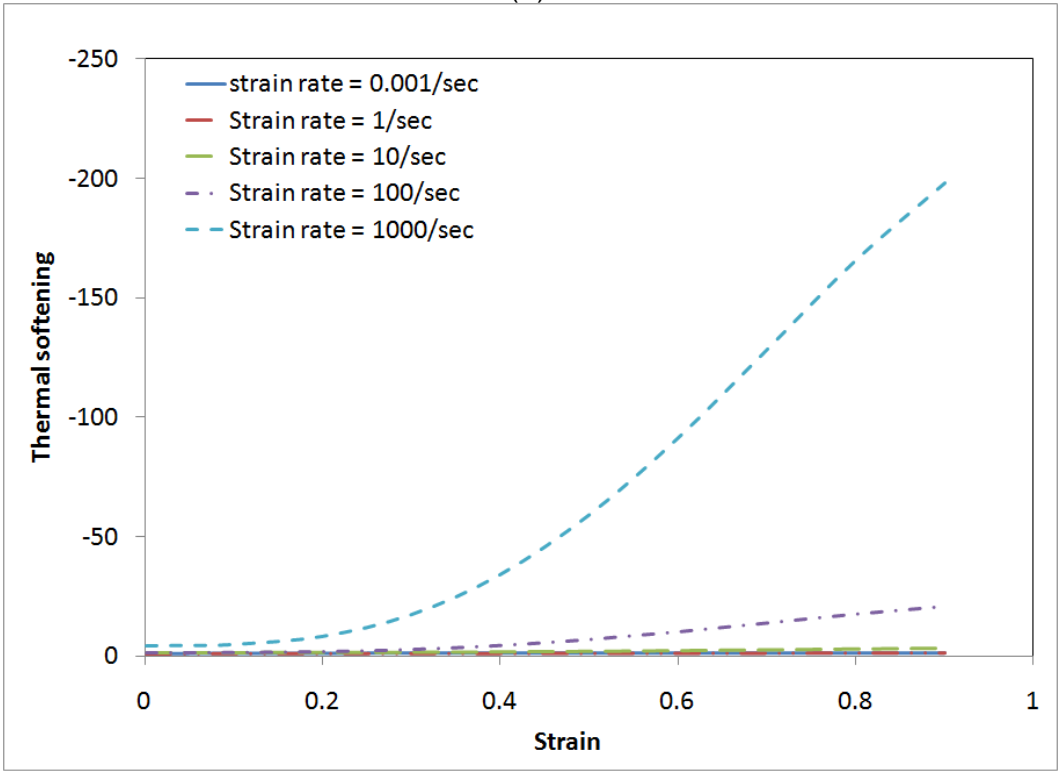

(b)

Figure 4.7: Change of thermal softening versus strain of CR-1018 steel for different strain rates at temperatures of (a) 300ºK, and (b) 500ºK.

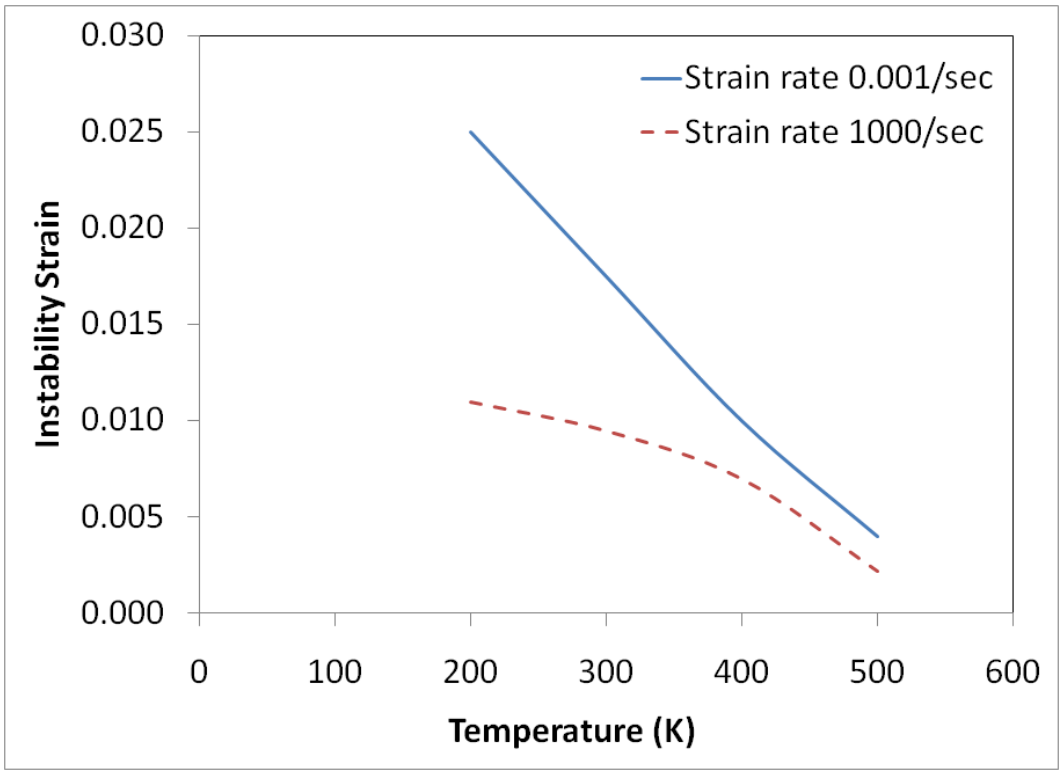

Figure 4.8: Occurrence of instability strain versus temperature for CR-1018 steel.

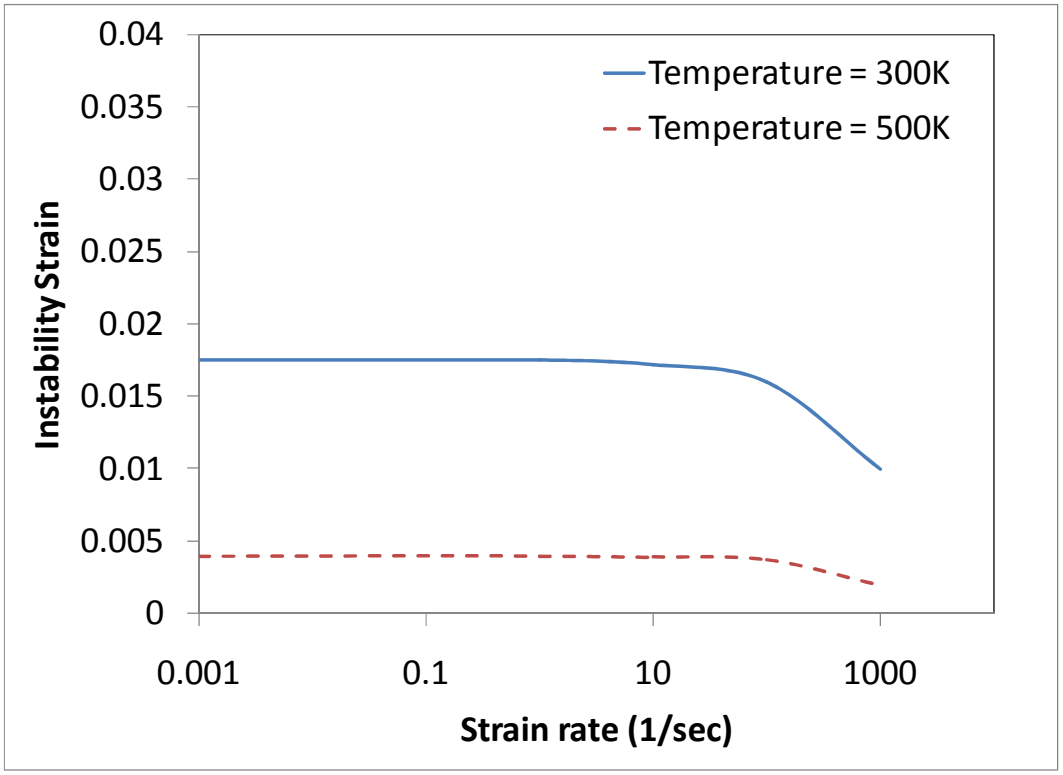

Figure 4.9: Occurrence of instability strain versus strain rate for CR-1018 steel.

4.2 Localization of Shear Bands

The principle of maximum shear stress described in the preceding section does not describe the shear localization itself, and hence a different approach is needed. One way of introducing the concept of localization is as follows. The deformation is assumed to occur in a defect containing inhomogeneous band within a uniformly deforming region. The inhomogenieties are defined as $d\varepsilon$ and $d\dot{\varepsilon}$, where d denotes the special difference between uniform and localized deformation. Since there is no change in the area during shear localization, Equation (4.7) can be written as:

$$\frac{d\sigma}{\sigma} = 0 = d\ln\sigma \tag{4.16}$$

Using the logarithmic expansion and retaining only the first term ($\ln(1+x) \approx x$ for $|x| < 1$), the constitutive model in Equation (3.43) is expressed in logarithmic form as follows:

$$\ln\sigma = \ln B_1 + n_1 \ln\varepsilon - \frac{B_2}{B_1}\varepsilon^{n_2-n_1} \tag{4.17}$$

In incremental form, the right hand side of Equation (4.16) can be written as:

$$d\ln\sigma = \frac{\partial\ln\sigma}{\partial\varepsilon}d\varepsilon + \frac{\partial\ln\sigma}{\partial\dot{\varepsilon}}d\dot{\varepsilon} + \frac{\partial\ln\sigma}{\partial T}dT \tag{4.18}$$

The temperature rise, dT, can be calculated from the fraction of the heat that is generated by plastic work, expressed in terms of stress and strain as shown in Equation (4.10). Using Equation (4.10) the temperature term in Equation (4.18) can be expressed as:

$$\frac{\partial\ln\sigma}{\partial T}dT = \frac{\partial\sigma}{\partial T}\frac{\beta}{\rho c}d\varepsilon \tag{4.19}$$

Substituting Equations (3.43) and (4.13) in (4.11), one can obtain the following expression for the change in stress with respect to temperature:

$$\frac{\partial\sigma}{\partial T} = \frac{\rho c}{\beta}\left\{1 - \frac{B_1 n_1 \varepsilon_i^{n_1-1} - B_2 n_2 \varepsilon_i^{n_2-1}}{B_1\varepsilon_i^{n_1} - B_2\varepsilon_i^{n_2}}\right\} \tag{4.20}$$

Deriving Equation (4.17) with respect to strain and strain rate and substituting that in Equation (4.18) along with Equations (4.16), (4.19) and (4.20), the strain rate increment is obtained as follows:

$$d\dot{\varepsilon} = -\frac{C_1 + C_2}{\frac{1}{B_1}\frac{dB_1}{d\dot{\varepsilon}} - \frac{B_1\frac{dB_2}{d\dot{\varepsilon}} - B_2\frac{dB_1}{d\dot{\varepsilon}}}{B_1^2}\varepsilon^{n_2-n_1}} d\varepsilon \tag{4.21}$$

where

$$C_1 = \left(\frac{n_1}{\varepsilon} - \frac{B_2}{B_1}(n_2 - n_1)\varepsilon^{n_2-n_1-1}\right) \tag{4.22}$$

and

$$C_2 = \left(1 - \frac{B_1 n_1 \varepsilon_i^{n_1-1} - B_2 n_2 \varepsilon_i^{n_2-1}}{B_1\varepsilon_i^{n_1} - B_2\varepsilon_i^{n_2}}\right) \tag{4.23}$$

This Equation represents an evolution equation for the strain rate during deformation. As long as C_1 is less than C_2, the growth rate of the strain rate gradient is slow. However, once C_1 outweighs C_2, rapid localization will occur. The instability strain obtained in Equation (4.11) can be used in Equation (4.23) along with Equation (4.22) to find the strain at which the localization initiates. The plot of change in localization strain is shown in Figure 4.10 versus temperature. Compared to the values of the instability strain, it is clear that the localization strain is higher at static strain rate. On the other hand, adiabatic shear bands occur usually at high strain rates, where the difference between localization strain and instability strain is not big. This fact offers us a hint, that the omission of the strain rate effect in the instability analysis still gives a reasonable prediction of the occurrence of the adiabatic shear bands. At high strain rate, the localization strain decreases with increasing temperature until it almost vanishes at 500ºK, which could mean that material will not suffer localization when the temperature is higher than that. It should be mentioned that even though localization may start at early stages, the rest of the material will still deform, but not as much as the in the shear band area.

As in the case of the instability strain, the localization strain decreases with increasing strain rate as illustrated in Figure 4.11. The effect of strain rate is more observed at high temperatures than at room temperature. Again, it is seen that the localization disappears at temperatures higher than 500ºK with high strain rates. At strain rates of $1000/sec$, the effect of changing temperature diminishes significantly. This would suggest that the effect of initial temperature can be neglected when studying adiabatic shear bands in CR-1018 steel.

4.3 Effect of Hydrostatic Pressure

Large hydrostatic pressures are experienced in many dynamic applications involving adiabatic shear band formation such as ballistic penetration, impact, and machining. Although the relationship between hydrostatic pressure and adiabatic shear band development remains an open question, its importance has been often noted. One explanation of the hydrostatic

pressure effect is through the formation of geometrical imperfections (voids). Effect of hydrostatic pressure on the formation and growth of voids has been explored extensively by researchers. This approach can help explain how hydrostatic pressure affects the behavior of adiabatic shear bands through the growth of voids in these bands.

Considering the incompressibility property of plastic deformation and the spherical symmetry, and assuming large stress triaxiality (i.e. the contribution of void shape change is neglected), Rice and Tracey (1969) express the void expansion rate in terms of initial void radius R_o as follows:

$$\dot{R}_o = 0.283 R_o e^{\left(\frac{3\sigma_m}{2\sigma_y}\right)} d\varepsilon_{eq} \tag{4.24}$$

where σ_m is the hydrostatic mean stress, σ_y is the yield stress, and $d\varepsilon_{eq}$ is the incremental equivalent strain. The RT model allows the calculation of the growth of a single spherical void in an infinite rigid–perfectly plastic material, which can be applied to CR-1018 steel as it behaves as a perfectly plastic material. This model has been developed for materials that obey von Mises plasticity, and should be modified appropriately for materials following other plasticity models such as Tresca materials. Integration of the preceding equation gives the relationship between the void radius R, the equivalent strain, and the hydrostatic pressure:

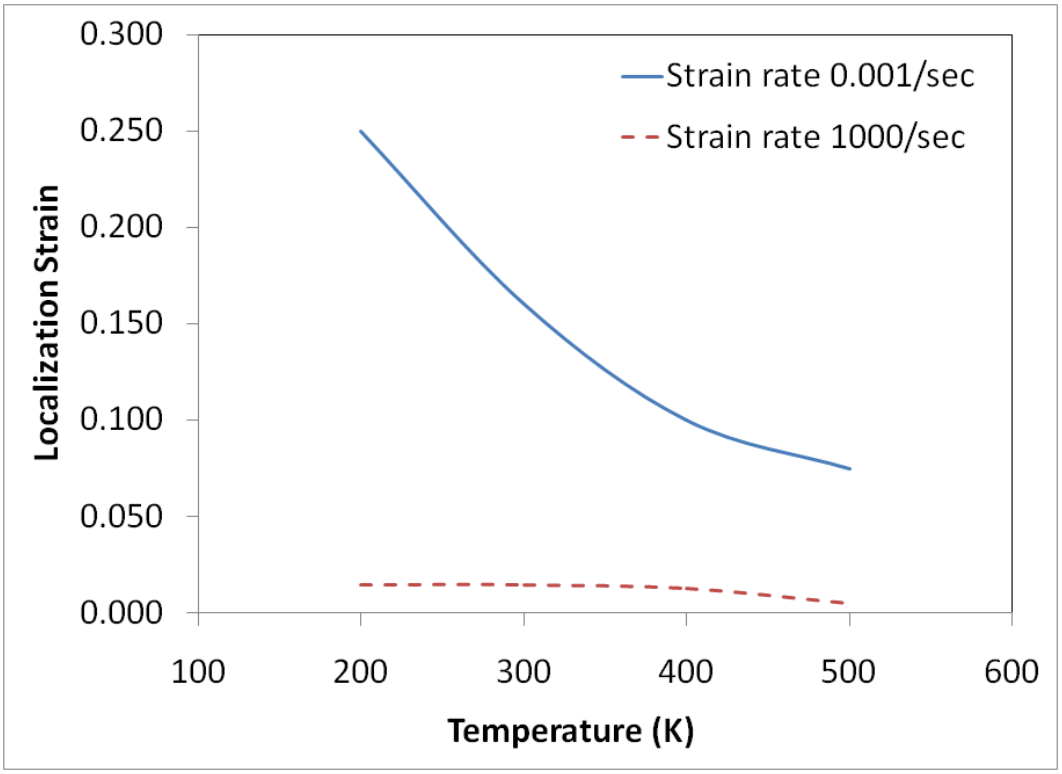

Figure 4.10: Occurrence of localization strain versus temperature for CR-1018 steel.

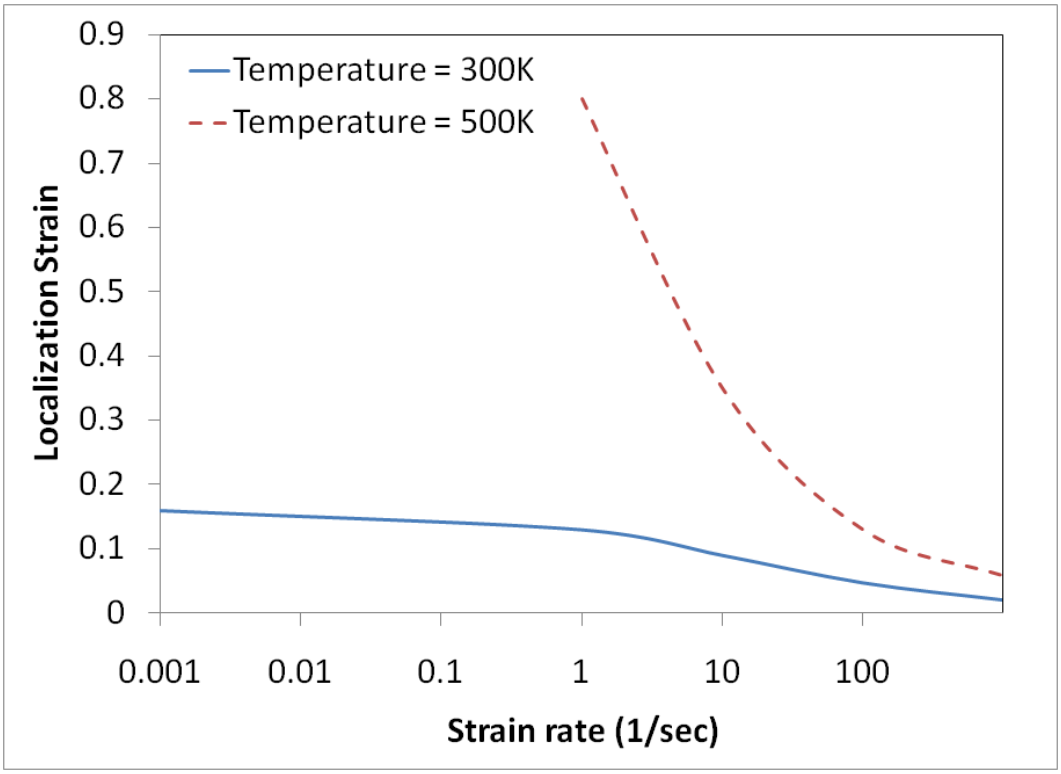

Figure 4.11: Occurrence of localization strain versus strain rate for CR-1018 steel.

$$R = 0.283R_o e^{\left(\frac{3\sigma_m}{2\sigma_y}\right)}\left(\varepsilon_{eq} - \varepsilon_{eq,o}\right) \tag{4.25}$$

where $\varepsilon_{eq,o}$ is the threshold equivalent strain for void nucleation. Using the maximum shear criterion, one can write:

$$dF = d\{\sigma(l-R)\} = (l-R)d\sigma - \sigma dR = 0 \tag{4.26}$$

where l is the gauge length of the specimen. Using Equation (4.26) and assuming that there are negligible changes in the strain rate and that deformation is adiabatic the criterion in Equation (4.6) becomes:

$$\frac{dR}{d\varepsilon}/(l-R) = \frac{1}{\sigma}\left(\frac{\partial\sigma}{\partial\varepsilon}\right) + \frac{\beta}{\rho c}\left(\frac{\partial\sigma}{\partial T}\right) \tag{4.27}$$

Substitution of the void growth rate, the expression for the void length together with the constitutive model in Equation (3.43) gives a critical strain for the initiation of shear bands subjected to hydrostatic pressure as follows:

$$\frac{1}{\sigma}\left(\frac{\partial\sigma}{\partial\varepsilon}\right) + \frac{\beta}{\rho c}\left(\frac{\partial\sigma}{\partial T}\right) = \frac{0.283R_o}{l-R} e^{\left(\frac{3\sigma_m}{2\sigma_y}\right)} \tag{4.28}$$

This equation has to be solved numerically to show the effect of hydrostatic pressure on the critical strain. To show this for CR-1018 steel graphically, the following values are used: $R_o = 1mm$, $R = 0.9mm$, $l = 10mm$ along with the material constants obtained previously. Figure 4.12 shows the change of instability strain versus hydrostatic pressure at different temperature. The hydrostatic pressure seems to increase the instability strain and retards the initiation of the adiabatic shear band. For example the instability strain at room temperature increases from 0.0095 in the absence of pressure to about 0.012 under pressure of 600 MPa. The dependence of the instability strain on the hydrostatic pressure is very close to a linear relation. This implies that the use of linear dependence of the void growth on hydrostatic pressure such as those by Gurson (1977) and Voyiadjis (1988) can also be used to describe such relations.

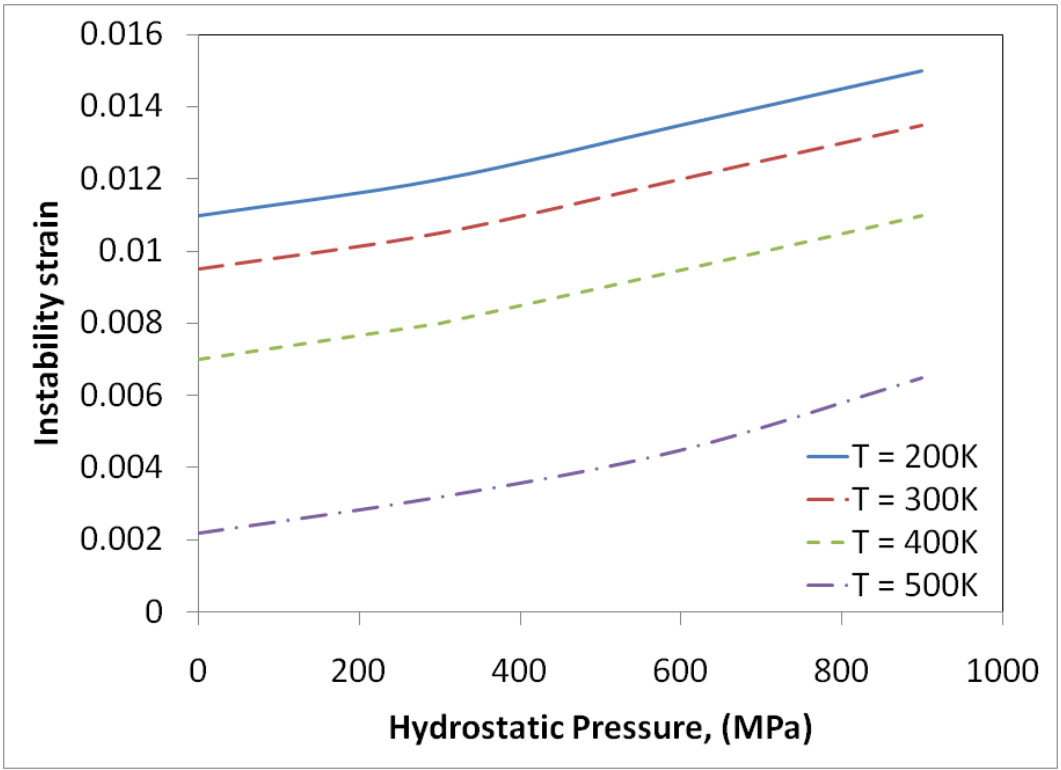

Figure 4.12: Instability strain versus hydrostatic pressure of CR-1018 steel.

4.4 The Formation of Adiabatic Shear Bands

Although the simplified maximum shear stress criterion can be used successfully in dealing with the problem occurrence of adiabatic shear bands, the information provided by this criterion is restrictive due to many reasons. Firstly, a number of assumptions are imposed such as adiabatic deformation and strain rate independent deformation. Secondly, adiabatic shear bands can only be dealt with using continuum mechanics. Therefore, the temporal and special variations can only be described adequately using field equations of continuum mechanics.

It is necessary to justify any empirical criterion proposed using continuum mechanics.

Here the governing differential equations will be presented and the homogeneous solutions and instability analysis related to the occurrence of adiabatic shear banding will be described. For simplicity, discussion will be confined to one-dimensional simple shear.

As a starting point, some fundamental physical laws need to be stated:

1. Adiabatic shear banding can be described using continuum mechanics and fundamental equations concerning conservation of mass, momentum, and energy as well as the constitutive equations are used. These equations are expressed as follows:

$$v_{i,i} = 0 \tag{4.29}$$

$$\rho \dot{v}_i = \sigma_{ij,j} \tag{4.30}$$

$$\rho c \dot{T} + \dot{e} = h_{i,i} + q + \sigma_{ij}\sigma_{i,j} \tag{4.31}$$

   where v_i is the particle velocity, i is the coordinate index with the value 1,2, or 3. The comma is the partial derivative with respect to the spatial coordinates. σ_{ij} is the Cauchy stress tensor, e is the latent energy, h_i is the heat flux vector, and q is the external heat source.
2. Hear conduction is governed by Fourier's law:

$$h_i = -\lambda T_{,i} \tag{4.32}$$

   where λ is the thermal conductivity, which for simplicity is taken to be a constant.
3. The fraction of the plastic work converted into heat is a constant and for simplicity this constant is assumed to be unity.

Usually, in the discussion of adiabatic shear bands the following assumptions are adopted:

1. Elastic deformations are ignored when compared to the large plastic deformations, that is $\varepsilon_{ij} = \varepsilon_{ij}^{p}$
2. The material exhibits no strain rate history effects, is plastically incompressible and isotropic. Hence, the following constitutive law applies:

$$\sigma_{eq} = f\left(\varepsilon_{eq}, \dot{\varepsilon}_{eq}, T\right) \tag{4.33}$$

In addition, the external heat source in not taken into account, i.e. $q = 0$. The basic equations concerning the thermoplastic shearing are:

$$\rho \dot{v}_i = \sigma_{ij,j} \tag{4.34}$$

and

$$\rho c \dot{T} = \lambda T_{i,i} + \beta \sigma_{ij} v_{i,j} \tag{4.35}$$

where $(1-\beta)\sigma_{ij}v_{i,j} = \dot{e}$, according to Taylor and Quinney (1934). Consider a one dimensional simple shear deformation $u(y)$, then the unique component of the shear strain is $\gamma = \partial u/\partial y$. This mode of deformation only affects the (x, y) plane. Furthermore, the stress component σ_z should be zero due to the incompressibility and the absence of any axial strains. The one dimensional assumption also leads to a further simplification, i.e., the gradient in the x-direction is much less than that in the y-direction $(\partial/\partial x \ll \partial/\partial y)$ or simply $\partial/\partial x \approx 0$. Other variables, such as the other normal stresses, σ_x and σ_y, do not appear in the model. This is an analogue of a boundary layer in fluid mechanics with a thin layer undergoing a large gradient perpendicular to it. The final governing equations become:

$$\rho \frac{\partial^2 \gamma}{\partial t^2} = \frac{\partial^2 \tau}{\partial y^2} \tag{4.36}$$

$$\beta \tau \frac{\partial \gamma}{\partial t} = \rho c \frac{\partial T}{\partial t} - \lambda \frac{\partial^2 T}{\partial y^2} \tag{4.37}$$

$$\tau = B_1 \gamma^{n_1} - B_2 \gamma^{n_2} \tag{4.38}$$

Generally speaking, the system of equations can be solved under prescribed initial and boundary conditions. Usually, the initial condition can be set as the shear stress and strain are zero, and the temperature is homogeneous, i.e. the natural state. In the case of defect analysis, inhomogeneities of temperature or geometrical imperfection can be introduced. In addition, the mechanical boundary conditions can be stress, velocity, or displacement controlled. The thermal boundary conditions can be idealized as adiabatic or isothermal.

Following the occurrence of inhomogeneous deformations due to instability somewhere in the gauge length, there will be a heat diffusion governed regime of shear localization. To obtain a complete and exact analytical solution to the problem of banding seems impossible because of the nonlinear thermomechanical coupling of the governing equations and the nonlinearity of the used constitutive equations. Even in the case of simplified quasi-static model the problem is still complicated. Moreover, the transient and localized nature of the deformation requires a self consistent description. Therefore, the best approach to tackle the problem is to combine experimental, analytical and

numerical techniques. Experimentally, the adiabatic shear process has been described in details by many researchers, such as Huang (1987), Marchand and Duffy (1988), and Giovanola (1988a, and 1988b), using different techniques and instruments. Numerical analysis will be discussed thoroughly in Chapter 6. In this section a simple analytical approach is introduced to describe the evolution of the adiabatic shear bands.

As observed by Marchand and Duffy (1988) and Huang (1987), when shear localization occurs, the material outside the localized shear zones appears to undergo no further plastic deformation. Therefore, it is reasonable to assume the material is rigid outside the shear bands. Correspondingly, the shear strain rate at the boundary of the shear zone should be zero. Therefore, in accordance with the definition of shear strain rate, the boundary velocity v in simple shear can be formulated as:

$$v = \int_0^{\delta} \dot{\gamma} dy \tag{4.39}$$

where the y-axis origin is at the center of the shear zone and δ is the half width of the band. Substituting the constitutive equation (equation (4.38)) into the boundary condition gives:

$$v = \int_0^{\delta} \frac{\sigma - \left[(a_1 + a_2 T)\varepsilon^{(a_5 + a_6 T)} - (a_7 + a_8 T)\varepsilon^{(a_{11} + a_{12} T)}\right]}{\left[(a_3 + a_4 T)\varepsilon^{(a_5 + a_6 T)} - (a_9 + a_{10} T)\varepsilon^{(a_{11} + a_{12} T)}\right]} dy \tag{4.40}$$

Considering the representative case of a constant boundary velocity, $v = 0$, one can write:

$$\frac{\partial v}{\partial t} = \frac{\partial v}{\partial \gamma}\frac{\partial \gamma}{\partial t}\Big|_{\delta} + \frac{\partial v}{\partial T}\frac{\partial T}{\partial t}\Big|_{\delta} = 0 \tag{4.41}$$

where

$$\frac{dT}{dt}\Big|_{\delta} = \frac{d}{dt}T\big(t, \delta(t)\big) = \frac{\partial T}{\partial t}\Big|_{\delta} + \frac{\partial T}{\partial y}\Big|_{\delta}\frac{\partial \delta}{\partial t} \tag{4.42}$$

Hence, from equations (4.41) and (4.42) the evolution equation of the shear band width can be expressed as follows:

$$\frac{\partial \delta}{\partial t} = \frac{\frac{\partial v}{\partial \gamma}\frac{\partial \gamma}{\partial t}\Big|_{\delta}}{\frac{\partial v}{\partial T}\frac{\partial T}{\partial y}\Big|_{\delta}} + \frac{\frac{dT}{dt}\Big|_{\delta}}{\frac{\partial T}{\partial y}\Big|_{\delta}} \tag{4.43}$$

where the denominator of the first term of the right hand side represents $\frac{\partial v}{\partial t}\Big|_{\delta}$ which is the strain rate at the boundary of the band. Noting that:

$$\frac{\partial v}{\partial \gamma} = \frac{\partial v}{\partial y}\frac{\partial y}{\partial \gamma} \tag{4.44}$$

then Equation (4.43) can be rewritten as follows:

$$\frac{\partial \delta}{\partial t} = \frac{\frac{\partial \gamma}{\partial t}\Big|_{\delta}}{\frac{\partial \gamma}{\partial y}\Big|_{\delta}} + \frac{\frac{dT}{dt}\Big|_{\delta}}{\frac{\partial T}{\partial y}\Big|_{\delta}} \tag{4.45}$$

The previous equation shows that the evolution of the adiabatic shear band width can be additively decomposed into two parts; the strain and strain rate part, and the thermal part. If the strain and temperature distribution across the band is known during the evolution, the change in the shear band width can then be expressed explicitly. The first term on the right hand side of the equation represents the rate of the plastic work which is always positive when plastic work occurs. This part will attempt to widen the width of the shear band. On the other hand the term $\frac{\partial T}{\partial y}\Big|_{\delta}$ in the second denominator represents the temperature gradient at the boundary of the band δ, and it is always negative because the band acts as a heat source to the surroundings and is coupled to the other terms according to Equation (4.37). This term at the band boundary provides a tendency for the deformed zone to shrink.

Although it can be seen that from these two opposing mechanisms adiabatic shear bands can form, the influence of individual material parameters on the details of the process need to be further investigated. Due to the complications in obtaining the different needed material parameters on the scales on which the adiabatic shearing occurs, it is hard to find experimental results in the literature that can be used for theoretical verification. One way to overcome this dilemma is to use the finite element method. The next chapter will focus on the regularization of the finite element solutions, and Chapter 6 will illustrate the finite element scheme used in analyzing the adiabatic shear banding.

CHAPTER 5: DYNAMIC BASED MATERIAL LENGTH SCALE*

5.1 Introduction

In general, the accuracy of the finite element analysis method can be improved by refining the mesh in the model using more elements and nodes. The density of the mesh depends upon the accuracy requirement of the analysis and the computational resources available. Generally, a finer mesh will yield results that are more accurate, but on the other hand will increase the computational cost. One way to handle this issue is to have a non uniform mesh, where finer meshes are used at the areas with the high displacement gradients or where the accuracy is critical to the analysis.

The focus in this dissertation is on the possibility of investigating shear band instabilities, representing ill posedness of the incremental problem. This gives rise to well-known difficulties in finite element simulations. In incremental nonlinear iterative inelastic analysis the finite element analysis usually suffers mesh dependency and mesh sensitivity. Hence, many regularization approaches have been proposed to numerically regularize this mesh dependency beyond the elliptic range. In particular, two main categories of regularization techniques can be recognized. The first class of approaches relies on modifying the constitutive models to include an intrinsic characteristic length. Non-local models (e.g. Pijaudier-Cabot and Bazant, 1987; and de Borst and Mühlhaus, 1992); strain-gradient models (e.g. Aifantis, 1992; Zbib and Aifantis, 1992; Bammann et al., 1999; Voyiadjis and Deliktas, 2000; Voyiadjis et al., 2001; Voyiadjis and Dorgan, 2001; Fleck and Hutchinson, 1997, 2001, and Wang et al., 2003); viscoplastic models (e.g. Perzyna, 1966, 1986, 1995; Needleman, 1988; Dornowski and Perzyna, 2000; Glema et al., 2000; Voyiadjis and Abed, 2005a, 2005b, 2006a, 2006b, and 2007; and Abed and Voyiadjis, 2007a and 2007b); thermal dissipation models (e.g. LeMonds and Needleman, 1986a, 1986b); and Cosserat continua models (e.g. de Borst and Sluys, 1991; and Voyiadjis et al., 2005) fall within this class. In another class of approaches, numerical regularization is pursued by introducing some special interpolating functions at the element level or by embedding strong discontinuities (e.g. Boria, 2002). All the above-mentioned approaches are based on finite element techniques, while the only analysis with the boundary element method is quite recent (Benallal et al., 2002).

The purpose of this chapter is to demonstrate a numerical technique to be used for finite element regularization, namely, the gradient approach. An experimental procedure is described to obtain a material length scale that will be implemented in the gradient formulation, and a dynamic evolution of the length scale is suggested. Finally, the algorithm of gradient implementation is illustrated in details.

---

*Portions of this chapter are reprinted by permission of Journal of Engineering Materials and Technology.

5.2 Higher Order Gradient Theory

The use of classical rate-independent plasticity theory or local theory to solve both static and dynamic problems does not possess an intrinsic length-scale, and usually leads to numerical stability problems, such as mesh size and mesh alignment sensitivities (e.g. Bammann et al., 1999; Glema et. al., 2000; and Li et. al., 2002), particularly, in problems exhibiting strain localization phenomena. Recently, this has been a great motivation for introducing the non-local or gradient theory.

In addition, experiments on torsion of fine copper wires (Fleck et al., 1994) and bending of thin nickel sheets (Stolken and Evans, 1998) reveal large strength elevations for wire radii and sheet thicknesses in the range from microns to tens of microns. These kinds of micron scale deformations involve too many dislocations to allow for reliable predictions of behavior based on current formulations of dislocation mechanics. Moreover, deformation behavior in the size range from sub-micron to tens of microns merges smoothly with predictions from conventional “large-scale” plasticity. Thus, there is a compelling motivation for extension of conventional plasticity that include strain gradient effects. A wide range of micron scale applications has already been investigated within the framework of continuum strain gradient plasticity (Fleck and Hutchinson, 1997). One drawback of higher-order formulations of strain gradient plasticity is the inherent difficulty associated with their finite element implementation for numerical analysis.

Many researchers have tried to address this size dependency problem through a number of gradient enhanced theories that incorporate an intrinsic length scale in the constitutive equations which are originally based on the classical continuum approach. Gradient approaches typically retain terms in the constitutive equations of higher-order gradients with coefficients that represent length-scale measures of the deformation microstructure associated with the non-local continuum. Aifantis (1984) was one of the first to study the gradient regularization in solid mechanics. The gradient methods suggested by Lasry and Belytschko (1988) and Mühlhaus and Aifantis (1991) provide a good approach to the non-local integral equations. A possible implementation of the gradient terms in plasticity models are introduced through the yield function (e.g. Mühlhaus and Aifantis, 1991; Fleck and Hutchinson, 2001; Chen and Wang, 2002; and Voyiadjis et al., 2001). A fairly complete review of this type of modeling has been given by Bammann et al. (1999).

Gao et al. (1999a, 1999b) and others demonstrated the increase in the material strength with indentation depth. Voyiadjis and Abu Al-Rub (2005) showed the need of a variable length scale that decreases with increase of plastic strains and increases with increase of the strain rate and decrease of the temperature. For example, the plastic zone ahead of the crack tip will decrease with increasing yield stress, which for small scale yielding is of the order of

microns. Therefore, the consideration of strain-rate effect and temperature variation on gradient plasticity, particularly in dynamic localization problems, becomes more necessary.

A typical gradient theory includes higher order derivative terms in the constitutive equation along with coefficients that represent length scale measures of the deformed material in the microscopic level. Gradients are introduced in the constitutive relationships to account for the microstructural interaction where the material behavior at any point is assumed to depend not only on the state of that point but also on the state of its neighboring region. This can be represented by a non local tensor $\overline{\mathbf{A}}$ that can be expressed as the weighted average of its local counterpart $\mathbf{A}$ over a surrounding volume V at a small distance $|\zeta| \leq a$ from a position x such that:

$$\overline{\mathbf{A}} = \frac{1}{V}\int_V \mathbf{h}(z)\mathbf{A}(x+z)dV \tag{5.1}$$

where a is a function of the intrinsic length scale and $\mathbf{h}(\zeta)$ is the weight function that decays smoothly away from point x. Here, $\mathbf{h}(\zeta)$ will be equal $\mathbf{I}h(\zeta)$ where $\mathbf{I}$ is an identity tensor which yields an isotropic weight function. For anisotropic weight function the identity tensor can be replaced with any other suitable tensor. Using a Taylor expansion at $\zeta = 0$ for $\mathbf{A}(x+z)$ one obtains:

$$\mathbf{A}(x+z) = \mathbf{A}(x) + \nabla\mathbf{A}(x)z + \frac{1}{2!}\nabla^2\mathbf{A}(x)z^2 + \frac{1}{3!}\nabla^3\mathbf{A}(x)z^3 + \ldots \tag{5.2}$$

where ∇ denotes the gradient operator. If an isotropic behavior of the averaging is assumed, then the integral in eq. (5.1) will only retain the terms with even gradient operators. For simplicity, only the first two terms will be used to express the non local tensor $\overline{\mathbf{A}}$ such that:

$$\overline{\mathbf{A}} = \frac{1}{V}\int_V \mathbf{h}(z)\mathbf{A}(x)dV + \frac{1}{2!V}\int_V \mathbf{h}(z)\nabla^2\mathbf{A}(x)z^2dV \tag{5.3}$$

which simplifies to:

$$\overline{\mathbf{A}} = \mathbf{A} + a\nabla^2\mathbf{A} \tag{5.4}$$

and $\frac{1}{V}\int_V \mathbf{h}(z)dV = 1$. In Eq. (5.4), $a = k(\ell^*)^2$ is a function related to the square of material length scale and weights all components of the gradient equally, where ℓ^* is the length scale parameter and k is a constant. The gradient form in Eq. (5.4) can be applied for example to strain, strain rate, hardening or temperature. One way to obtain such a length scale is through the experimental results of instrumented indentation. The indentation tests are used to measure one of the basic material characteristics, the hardness of metals. These tests can be described simply as forcing a hard indenter into a relatively softer material and the load on the indenter is measured versus the indentation depth. Micro- and

nano-indentation tests have shown that the material hardness increases with decreasing indentation size in the micro and nano scale (McElhaney et al., 1998; Lim and Chaudhri, 1999; Elmustafa and Stone, 2003; Abu Al-Rub and Voyiadjis, 2004; and Voyiadjis and Abu Al-Rub, 2002). The gradient plasticity theories have shown good agreement with this material size dependence that was observed in instrumented hardness experiments (Nix and Gao, 1998; and Huang et al., 2000).

Different experiments (Stelmashenko et al., 1993; and Ma and Clarke, 1995) have documented a strong size dependence of indentation hardness for micron-size indents that cannot be accounted for by conventional plasticity. Indentation size effect has been one of the motivations underlying the development of a plasticity theory for the micron scale. Conical or pyramidal indents whose widths exceed tens of microns generally produce size-independent hardness values in most metals and can be considered as “large” indents. Smaller indents in the range from sub-micron to about 10 μm in single crystals or fine-grained polycrystals often display a significant size effect. The hardness inferred from pyramidal indents on the order of 1 μm in width can be two or three times the hardness obtained from an indent that is 10 μm across. A clear understanding of the size effect and its connection between material strength is especially important in modern applications involving thin films and multilayers since nano- and micro-indentation are frequently the only means of measuring strength.

It has been reported in the literature that the Vickers microhardness of different materials is independent of load (e.g. Ascheron et al., 1989), increases with load (e.g. Vengatesan et al., 1986), decreases with load (e.g. Sridhar and Yovanovich, 1996; and Tickoo et al., 2003) or shows complex variation with changes in load (e.g. Guille and Sieskind, 1991). At low loads, the effect of the surface layers with different material properties is more pronounced. As the depth of penetration increases the effect of bulk becomes more dominant and eventually there will be no change in the value of hardness with changing the load. In general, this load dependence of microhardness is known as the indentation size effect (ISE). This phenomenon has been associated with various causes such as work hardening, roughness, piling up, singing in and shape of indenter, surface energy, varying composition and crystal anisotropy which are all discussed extensively in the literature. One of the recent theories that is devoted to explaining this behavior is through the strain gradient plasticity (Nix and Gao, 1998).

In recent years, new explanations for the ISE have emerged. The study of Nix and Gao (1998) have introduced the concept of strain gradient plasticity based on dislocation theory. Nix and Gao (1998) have shown that ISE behavior for crystalline materials can be accurately modeled using the concept of geometrically necessary dislocations. Nix and Gao (1998) based their reasoning

on the experimental law needed to advance a mechanism based theory of strain gradient plasticity. Their model can be expressed as:

$$\left(\frac{H}{H_o}\right) = \left(1 + \frac{\ell^*}{h}\right)^{1/2} \tag{5.5}$$

where H is the microhardness, H_o the macrohardness, and h is the indentation depth. For a glassy polymer, Chong and Lam (1999) describe the variation of the hardness using strain gradient plasticity theory, which differs from that of Nix and Gao (1998) in the manner of separation of the permanent deformation process. The model relates microhardness to indentation depth as follows:

$$\left(\frac{H}{H_o}\right) = 1 + \left(\frac{\ell^*}{h}\right)^{1/2} \tag{5.6}$$

Voyiadjis and Abu Al-Rub (2002) and Abu Al-Rub and Voyiadjis (2004) developed a new method to determine a material length scale using microhardness results from conical or pyramidal indenters. The relation between the microhardness H, the macrohardness H_o, and the length scale parameter ℓ^* is as follows:

$$\left(\frac{H}{H_o}\right)^{\beta} = 1 + \left(\frac{\ell^*}{h}\right)^{\beta/2} \tag{5.7}$$

where β is a constant. In fact by using β equals to two, one recovers Nix and Gao (1998) relation. By setting β equals to one, the size dependent hardness proposed by Chong and Lam (1999) is obtained. Hence, it seems that the exponent β should vary between one and two, capturing, in principle, material behavior ranging from crystalline to polymeric.

The aforementioned three strain gradient models of hardness will be used to obtain length scale values of two steel alloys that can be implemented in strain gradient plasticity models for regularization purposes.

5.3 Materials and Experiments

In this experiment, two materials are tested for nano indentation in order to obtain their length scale. The first material is low carbon cold rolled (CR) 1018 mild steel which is among the most commonly available grades in the world. The mechanical properties and chemical composition of CR-1018 steel are listed in Table 5.1. The second material is low carbon hot rolled (HR) A36 mild steel that complies with ASTM A36/A36M-05 standard. The mechanical properties and chemical composition of HR-A36 steel are listed in Table 5.2.

The nano indentation experiments were performed on an MTS Nano Indenter XP system (Figure 5.1) in order to investigate the mechanical properties of these materials. The indenter has a pyramidal Berkovich shaped diamond tip

(E = 1141 GPa) that is capable of indenting materials to depths of 100 to 1000 nm. Meanwhile the force-displacement response is measured during indentation. Through the very high data-sampling rates, NANO Indenter XP systems produce very accurate data of any instrumented nano indentation where each recorded data point is an average of 1000 separate measurements. In addition, when applying the Continuous Stiffness Measurement (CSM) technique which will be presented later, the system records stiffness data along with load and displacement data dynamically, allowing hardness and Young's modulus to be calculated at every data point acquired during the indentation experiment.

Major components inside of the MTS Nano Indenter XP are illustrated in Figure 5.2. This indenter sits on a mechanical vibration isolation table and its container has sound dampening materials inside. The load frame is essentially the gantry of the indenter and should be as stiff as possible, so as not to contribute significantly to the displacement of the load train. The load frame stiffness can be calibrated by an iterative procedure in which a number of deep indents are made in a standard material (i.e. fused silica).

In addition to the MTS Nano indenter XP machine, Brinell hardness machine (Figure 5.3) is used to obtain hardness values on the macro scale. It uses a spherical indenter with loads in kg. The macro-indentations are shown in Figure 5.4.

Table 5.1: Mechanical properties and Chemical composition of CR-1018 Mild (low-carbon) steel

Minimum Properties	Ultimate Tensile Strength, psi	63,800
	Yield Strength, psi	53,700
	Elongation	15.0%
	Rockwell Hardness	B71
Chemistry	Iron (Fe)	98.81 - 99.26%
	Carbon (C)	0.18%
	Manganese (Mn)	0.6 - 0.9%
	Phosphorus (P)	0.04% max
	Sulfur (S)	0.05% max

Table 5.2: Mechanical properties and Chemical composition of HR-A36 Mild (low-carbon) steel

Minimum Properties	Ultimate Tensile Strength, psi	58,000 - 79,800
	Yield Strength, psi	36,300
	Elongation	20.0%
Chemistry	Iron (Fe)	Balance
	Carbon (C)	0.26%
	Manganese (Mn)	0.75%
	Copper (Cu)	0.2%
	Phosphorus (P)	0.04% max
	Sulfur (S)	0.05% max

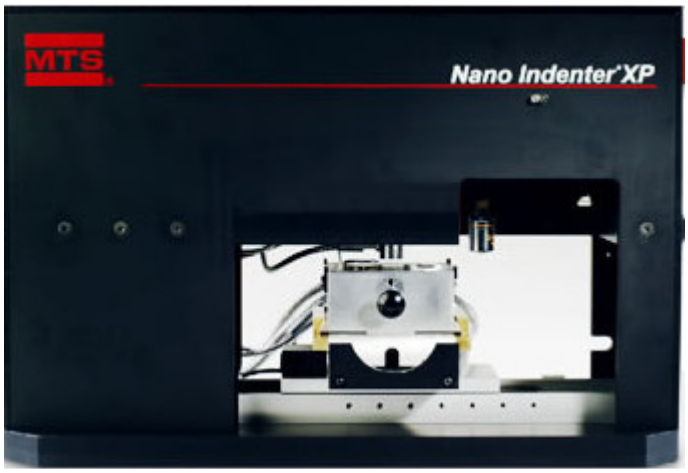

Figure 5.1: MTS Nano Indenter XP machine.

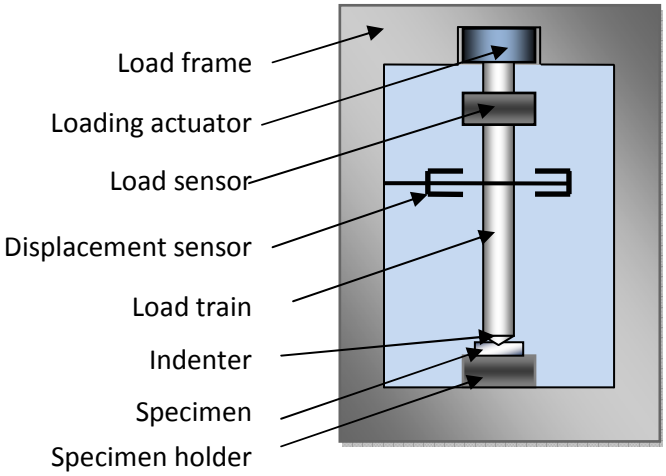

Figure 5.2: Major components in the MTS Nano indenter XP system.

Figure 5.3: Brinell hardness machine.

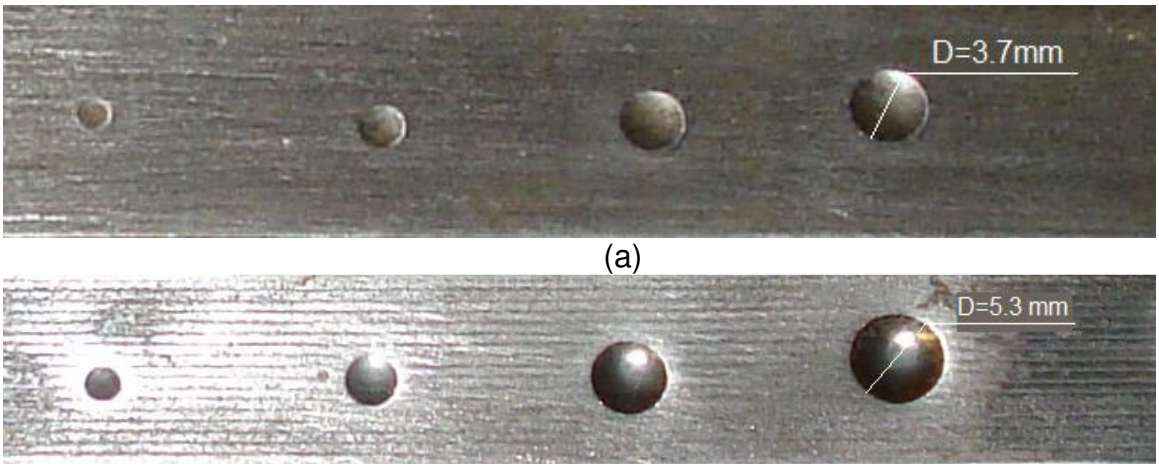

(a)

(b)

Figure 5.4: Brinell macro-indentation of (a) CR-1018 steel, and (b) HR-A36 steel specimen.

Different indentation experiments are conducted on CR-1018 steel with loads of 10, 20, 40, 80, 160, 320, 500, and 640 mN, where the maximum load that can be reached by the machine is 640 mN. At each one of these loads, the result is calculated from the average of nine indentations in order to obtain representative readings. Sometimes one or more of the nine readings are excluded from the average when it is either too high or too low. For HR-A36 steel, loads of 1.25, 2.5, and 5 mN are used in addition to those loads used for CR-1018 steel. For Brinell tests, loads of 3000, 2000, 1000, and 500 kg are used.

5.4 Calculations of Hardness

First, it is recognized that the total compliance is:

$$C_t = C_s + C_m \tag{5.8}$$

where C_s is the indenter/specimen contact compliance and C_m is the machine compliance. Because compliance values are the inverse of stiffness, the relation:

$$C_t = \frac{\sqrt{\pi}}{2\beta E_r \sqrt{A}} + C_m \tag{5.9}$$

can be used to determine machine stiffness. The intercept of the plot of C_t versus $A^{-\frac{1}{2}}$ will give the machine stiffness directly, provided that E_r and A are well known, which is why a reference material and deep indents are used for this procedure. Scanning electron microscopy (SEM) or atomic force microscopy (AFM) can also be used to experimentally find A by imaging residual impressions in highly plastic materials, such as aluminum. However, in this study the load frame stiffness is calibrated by the manufacturer using an iterative procedure in which a number of deep indents are made in fused silica as a standard material that has well known properties.

For the Nano Indenter XP, the load head can apply forces up to about 640 mN. It also has the ability to operate the head over a range of displacements up to 15 mm of allowed travel total. Such a range allows sufficiently sensitive measurements to be made even at relatively far plate separation distances.

Currently, the most common method for extracting the hardness and modulus values from an indentation curve is known as the “Oliver and Pharr” method (Oliver and Pharr, 1992; and Hay and Pharr, 2000). This is the method MTS nanoindenter uses to determine hardness and modulus. While their method requires no imaging of the indentations, it is based on contact mechanics solutions developed for a solid of revolution indenting a half space by Sneddon (1965). This method applies to both sharp and spherical indentation. The Oliver and Pharr method begins by assuming a flat, smooth, isotropic and orthogonal contact between the tool and the material. Elastic deflections of the material are taken into account as illustrated in Figure 5.5. This consideration allows for more precise measurement of hardness and modulus properties, as well as more accurate determination of phase transformation pressures when combined with other contact mechanics relations.

It is widely known that the contact area at a particular depth of indentation depends not only on the shape of the indenter (diamond) but also on the elastic-plastic response of the material being indented. In some cases the volume of material displaced by the indentation pushes out to the sides of the indenter and forms a pile-up of material, making the projected contact area larger than the cross-sectional area of the indenter at that depth. For other materials, the displaced volume is accommodated mainly by far-field elastic displacements, producing what is called a sink-in effect. In this case the contact area is less than the cross-sectional area of the indenter at that depth. Although the pile-up and sink-in effects are widely known, they are not explicitly considered in the current method for determining contact areas from indentation loads and displacements.

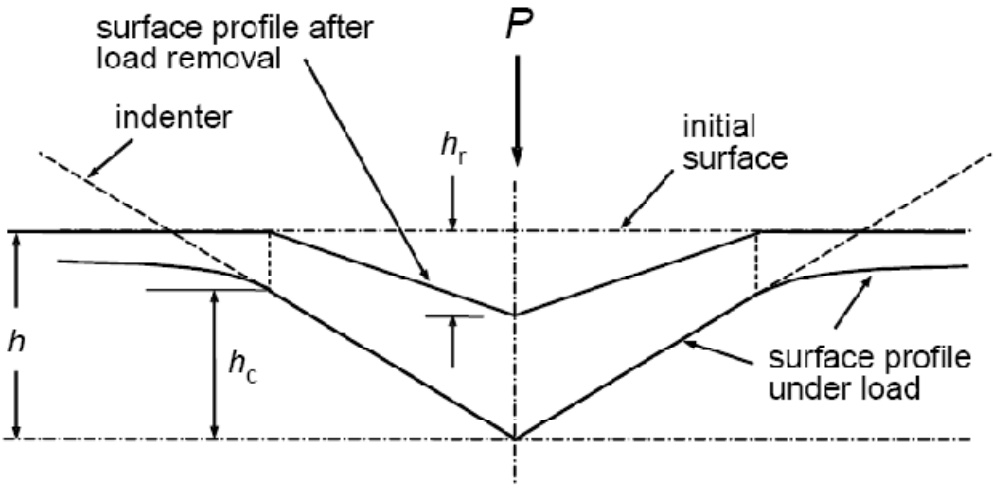

Figure 5.5: Typical indentation profile

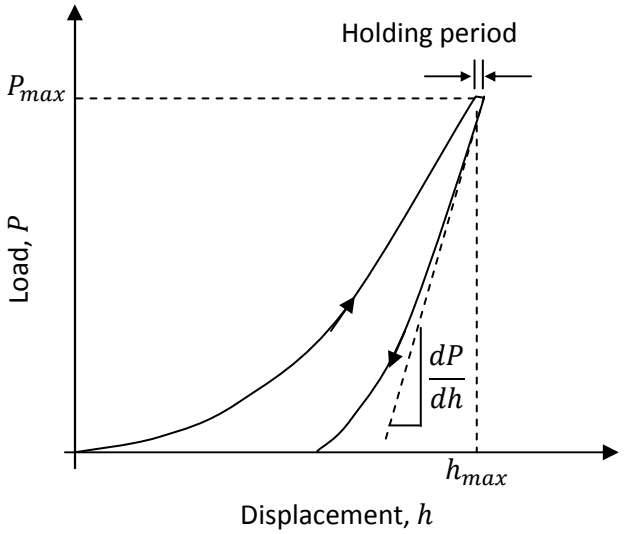

Figure 5.6: Schematic of load-displacement curve for an instrumented nanoindentaion test.

From the generated load-displacement curve (Figure 5.6), the three most important pieces of information that are used to calculate hardness and modulus are the maximum applied load, P_{max}, the displacement into the surface at maximum load, h_{max}, and the slope at the beginning of the unloading curve which is unloading contact stiffness, S. As described by Oliver and Pharr (1992), this unloading curve is fit to the function:

$$P = C(h - h_r)^m \tag{5.10}$$

where P is the applied load at a point in the unloading curve, $C, m,$ and residual depth h_r are empirically fit constants, and h is depth into the surface corresponding to a load P. The value of m is taken to be between about 1 and 2. In order to find the stiffness this fit equation is differentiated with respect to the depth of indentation as follows:

$$S = \left(\frac{dP}{dh}\right)\Big|_{h=h_{max}} \tag{5.11}$$

while h_r can be found experimentally for complete unloading, for this analysis it remains a fit constant. To find material hardness, the relation:

$$H = \frac{P_{max}}{A} \tag{5.12}$$

is used, where A is the area of contact between the indenter and material at load P. Although different hardness definitions exist, this is the definition used in depth-sensing indentation. This is similar to the way hardness is found for the Vickers, Brinell, and Knoop methods, except that in this case the elastic

deflection of the surrounding material is taken into consideration which is not the case here. Hardness is typically evaluated at P_{max}, but this relation can be used to describe contact pressure at any point in the loading curve as well, provided the tip geometry is known. To calculate the modulus, one first finds the reduced modulus derived as:

$$E_r = \frac{S\sqrt{\pi}}{2\beta\sqrt{A}} \tag{5.13}$$

where β is a constant close to 1 that varies depending on the indenter geometry (Hendrix, 1995). This relation was originally derived from purely elastic theory for unloading between a conical indenter and surface, but also holds true for the Berkovich and spherical indenters. The reduced modulus is related to the material modulus E by the relation:

$$\frac{1}{E_r} = \frac{(1-\nu^2)}{E} + \frac{(1-\nu_i^2)}{E_i} \tag{5.14}$$

where ν is Poisson's ratio of the material and the subscript i refers to those properties of the indenter. An inherent weakness of this method is that ν of the tested material must be known or closely estimated beforehand. However, using a rough assumption for ν does not affect the results very much.

Until now, little attention has been paid to the determination of the contact area between the indenter and sample, A. For any indenter shape, A is a function of contact depth h_c, where:

$$h_c = h_{max} - k\frac{P_{max}}{S} \tag{5.15}$$

and k is a constant (usually 0.75) that depends on the indenter's geometry. To find the relation between A and h_c, one should run a series of indentations of various depths into reference material (fused silica in this case) or other well-characterized material. The area, A, is found at various values of h_c using the "Basic Tip Cal" method, by knowing all the other variables in the above Oliver-Pharr equations. The function $A(h_c)$ is found by describing the indenter geometry as:

$$A(h_c) = Bh_c^2 + \sum_{n=0}^{\infty} C_n h_c^{\frac{1}{2^n}} \tag{5.16}$$

where B is a constant which is a strong function of regular indenter geometry for sharp tips, and C_n are constants that describe the imperfections of the tip from ideal geometry. For the area function which describes a spherical tip, B will be equal to $-\pi$ and C_0 equal to $2\pi r$, where r is the effective radius of the indenter tip. For the Berkovich indenter, the ideal geometry is with $B = 24.56$ and the other coefficients are 0. For the ideal cube corner indenter one have $B = 2.5981$.

With respect to the macro hardness, Brinell test is conducted by pressing a tungsten carbide sphere 10mm in diameter into the test surface for 10 seconds with loads of 3000, 2000, 1000, and 500 kg, then measuring the diameter of the resulting depression. The Brinell Hardness Number (BHN) is calculated according to the following formula:

$$BHN = \frac{F}{\frac{\pi}{2}D\left(D-\sqrt{D^2-D_i^2}\right)} \tag{5.17}$$

where F is the imposed load in kg, D is the diameter of the spherical indenter in mm, and D_i is the diameter of the resulting indenter impression in mm. The value of the BHN can then be converted to equivalent diamond pyramid hardness number using any hardness conversion table. This hardness number can then be converted to MPa by multiplying by 9.807 to be compared with nano hardness.

5.5 Results and Discussion

The obtained load-displacement curves for CR-1018 steel are shown in Figure 5.7 at loads starting from 10 mN to 640 mN. On these curves the high initial unloading slope and small recovery depth suggest their high contact stiffness and elastic modulus. Each one of the graphs in Figure 5.7 represents one value for hardness at a specific load and displacement, and they are plotted together with macro hardness results in Figure 5.8. The experimental results show that the hardness value decreases with increasing indentation depth, which indicates that CR-1018 steel possesses indentation size effect. The nano hardness decreases from around 9.7 GPa at 270 nm to the macro hardness of 1.31 GPa at 0.5 mm. One possible explanation for the indentation size effect in ductile materials is the different plastic deformation regimes associated to the size scale of the indent. The flow stress on a small volume of material is higher than that on a larger volume, possibly because of the restriction for nucleation and/or movement of dislocations in a small volume. To obtain the length scale, the three models of Eq. (5.5), Eq. (5.6), and Eq. (5.7) are fitted to these data. The length scale is 15.8 μm according to Eq. (5.5), 10.8 μm according to Eq. (5.6), and 13 μm according to Eq. (5.7) with $\beta = 1.2$. The length scale calculated using Eq. (5.7) (Voyiadjis and Abu Al-Rub, 2002; and Abu Al-Rub and Voyiadjis, 2004) is between the two values obtained using the other two models, which is expected since β is 1 for the model by Nix and Gao (1998) and 2 for the model by Chong and Lam (1999). As a measure of goodness of fit for the regression, coefficient of determination is found for the model suggested by Voyiadjis and Abu Al-Rub (2002) and Abu Al-Rub and Voyiadjis (2004) to be 0.975 compared with 0.972 for the model presented by Chong and Lam (1999) and 0.951 for that by Nix and Gao (1998). Hence, the value of 13 μm will be considered for analysis in this work.

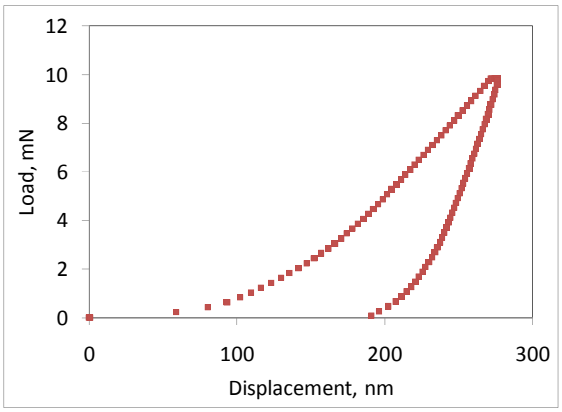

(a)

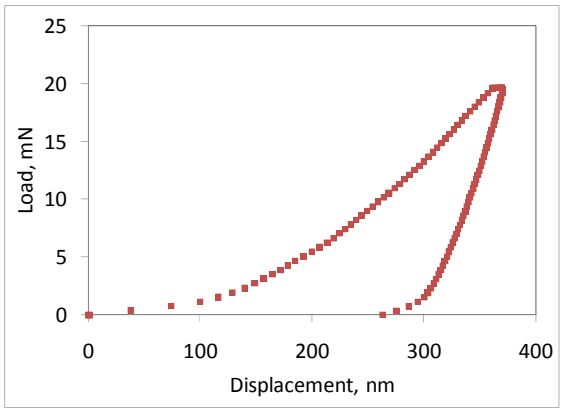

(b)

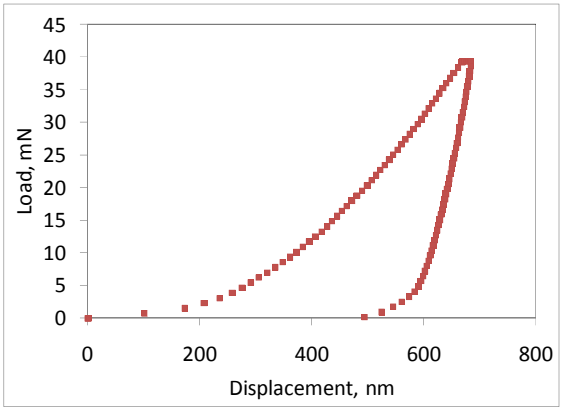

(c)

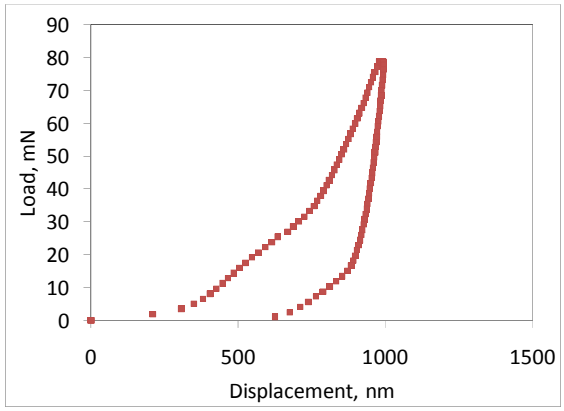

(d)

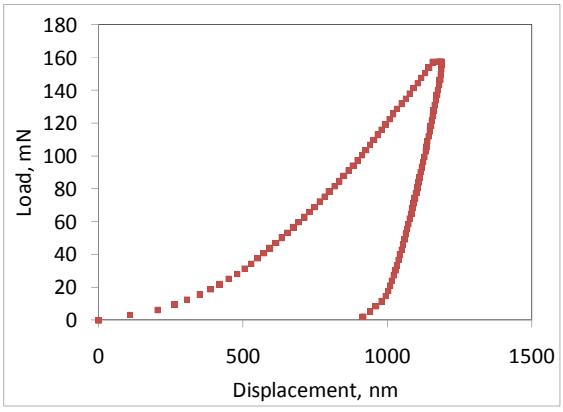

(e)

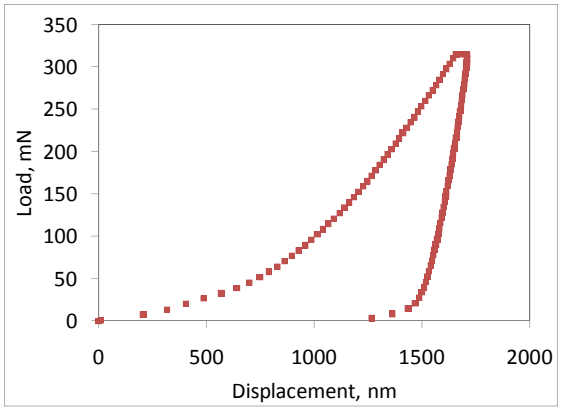

(f)

Figure 5.7: Load-displacement curve of nano indentations of CR-1018 steel at (a) 10 mN, (b) 20 mN, (c) 40 mN, (d) 80 mN, (e) 160 mN, (f) 320 mN, (g) 500 mN, and (h) 640 mN. (Figure continued)

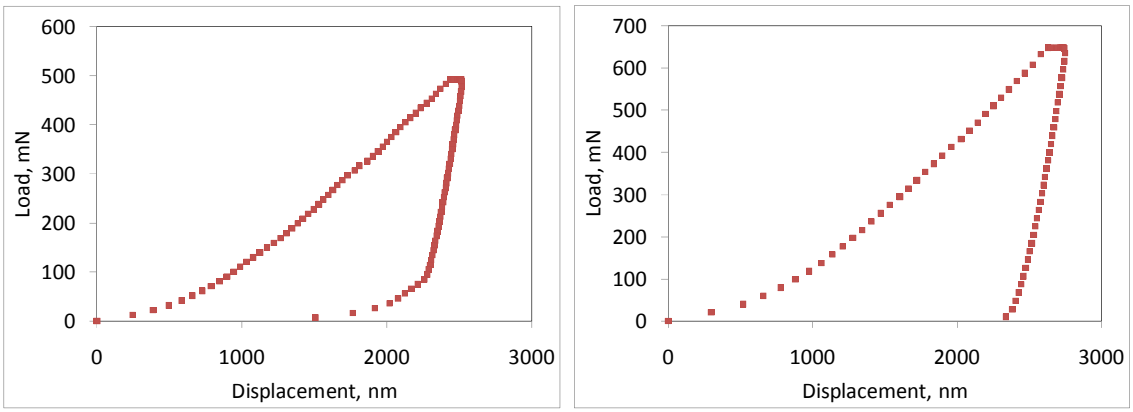

(g) (h)

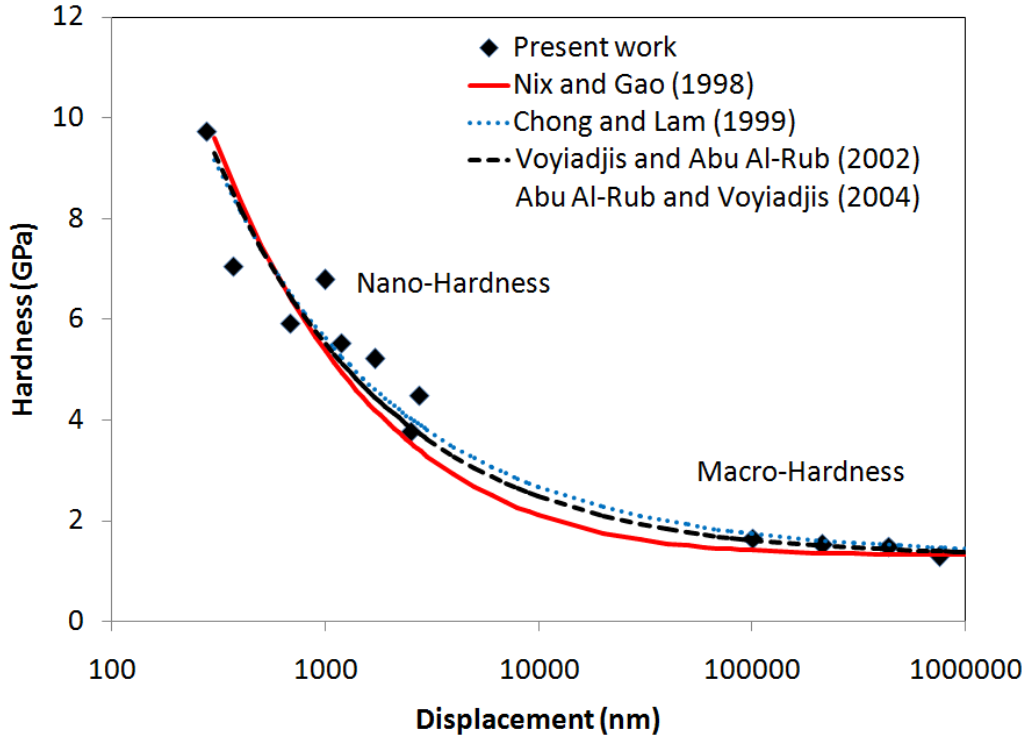

Figure 5.8: Experimental hardness versus indentation displacement with data fitting of different models for CR-1018 steel

Figure 5.9 shows the load-displacement curves for HR-A36 steel at loads starting from 1.25 mN to 640 mN. As in the case of CR-1018 steel, HR-A36 steel have high contact stiffness and elastic modulus that is obvious in the high initial unloading slope and small recovery depth. Hardness versus the indentation depth is plotted in Figure 5.10. Although the general behavior of HR-A36 is similar to CR-1018 steel in the way that the hardness decreases with increasing indentation depth, HR-A36 is less sensitive to the size effect where hardness decreases from around 6 GPa at 200 nm to 3.1 GPa (macro hardness) at 0.5 mm. Eq (5.5) , Eq (5.6), and Eq (5.7) are fitted to the data and the length is found

to be 470 nm according to Eq (5.5), 150 nm according to Eq (5.6), and 220 nm according to Eq (5.7) with $\beta = 1.2$. The model parameter β in Voyiadjis and Abu Al-Rub (2002) and Abu Al-Rub and Voyiadjis (2004) is seen to be the same for both CR-1018 and HR-A36 steel since it is a material constant (Columbus and Grujicic, 2002). It is also seen that HR-A36 steel has a much smaller length scale, which can be justified by the fact that hot rolling causes large grains to elongate, and then the elongated grains recrystallize to form smaller grains. Since length scale is a material parameter related to the microstructure of material it would be expected generally that material with smaller grains will have smaller length scale. On the other hand, impression in materials with smaller grains will cover more grains than that in large grain materials, and hence indentation in small grain material will behave more like bulk material compared to large grain material which justifies the need for smaller loads and smaller indentations for HR-A36 steel to capture the size effect compared to CR-1018 steel. In addition, this behavior points out the role of elastic recovery on the material hardness, since the elastic recovery is smaller in hot rolled steel.

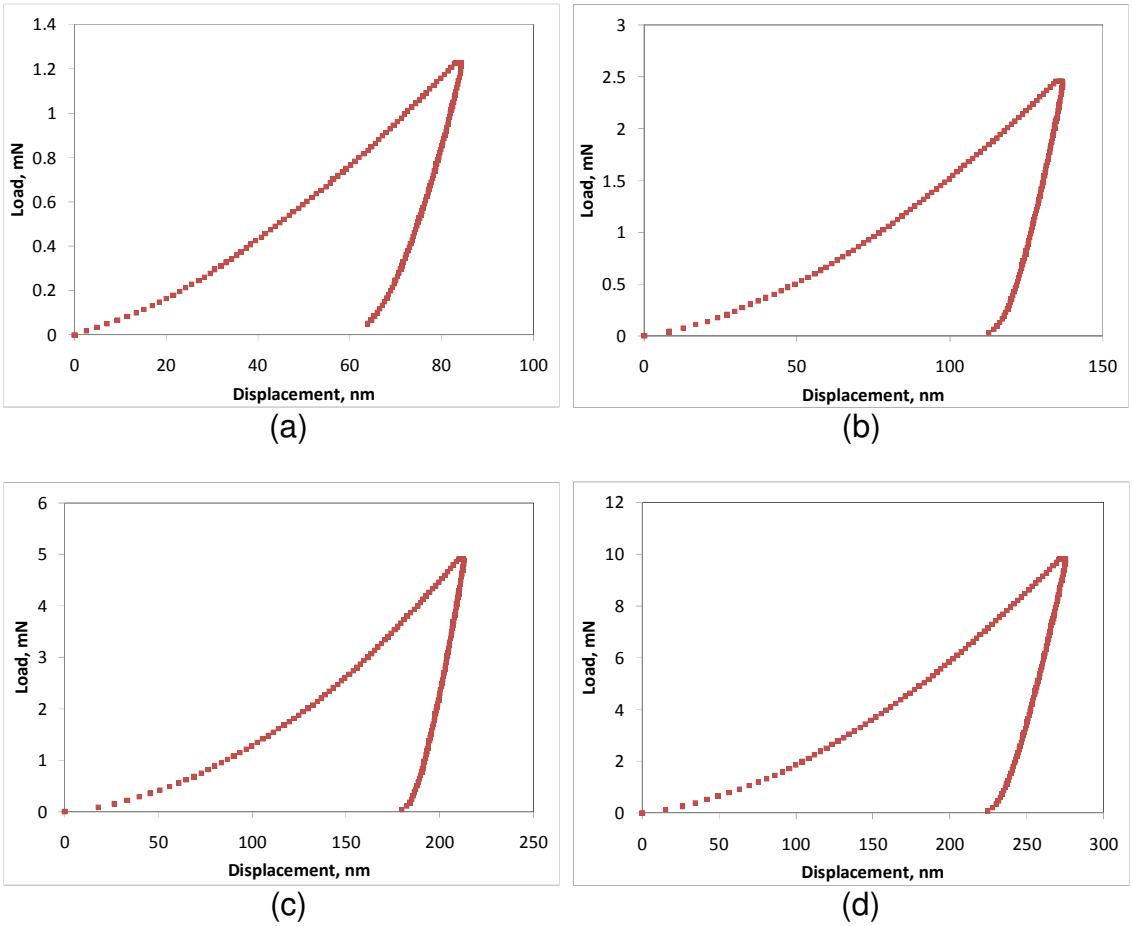

Figure 5.9: Load-displacement curve of nano indentations HR-A36 steel at (a) 1.25 mN, (b) 2.5 mN, (c) 5 mN, (d) 10 mN, (e) 20 mN, (f) 40 mN, (g) 80 mN, (h) 160 mN, (i) 320 mN, (j) 500 mN, and (k) 640 mN. (Figure continued)

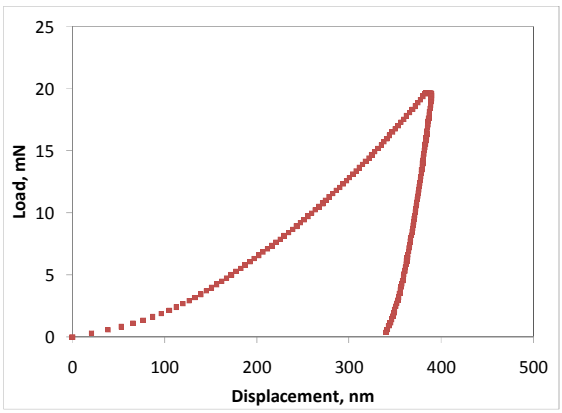

(e)

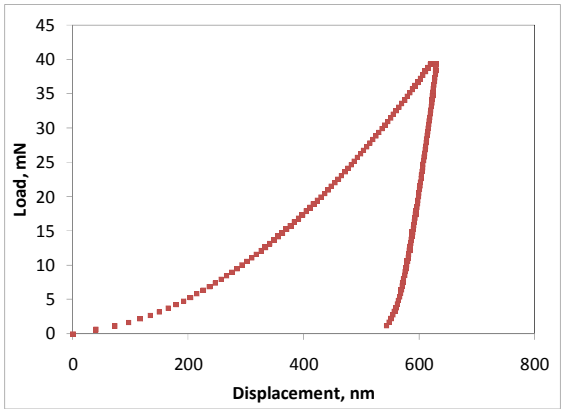

(f)

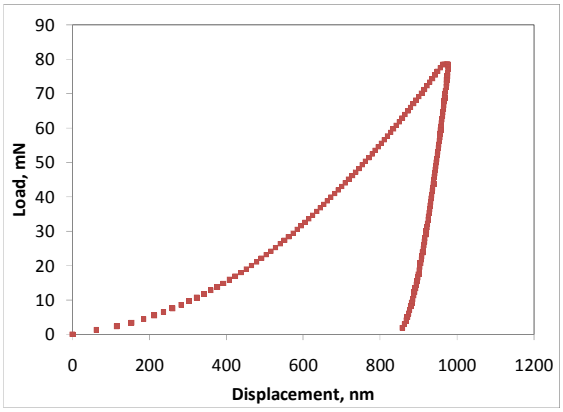

(g)

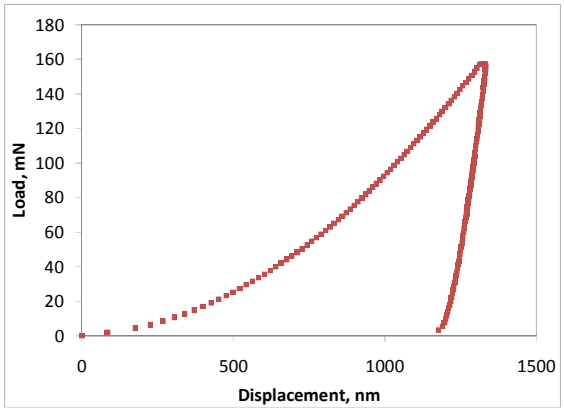

(h)

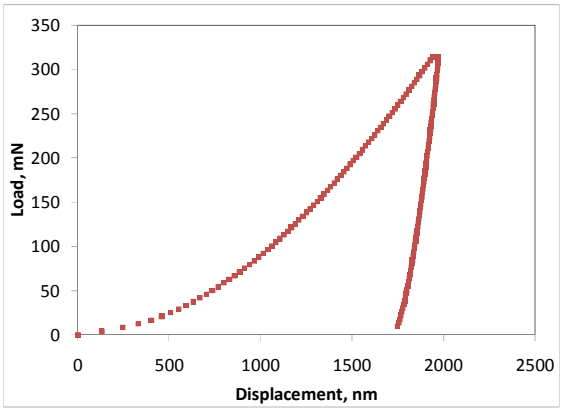

(i)

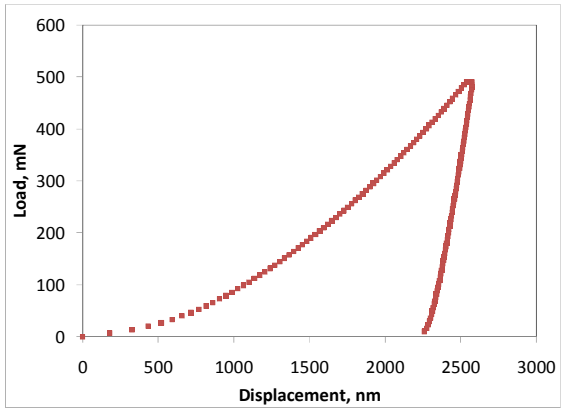

(j)

(Figure continued)

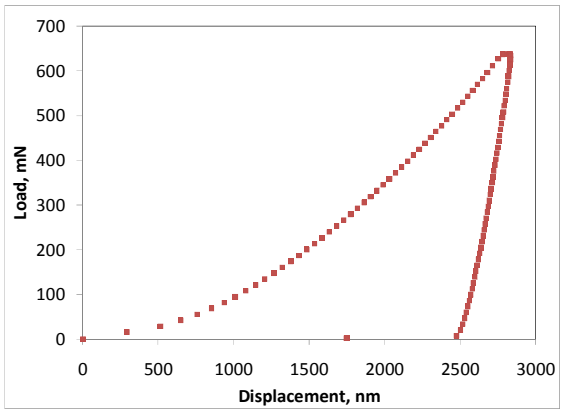

(k)

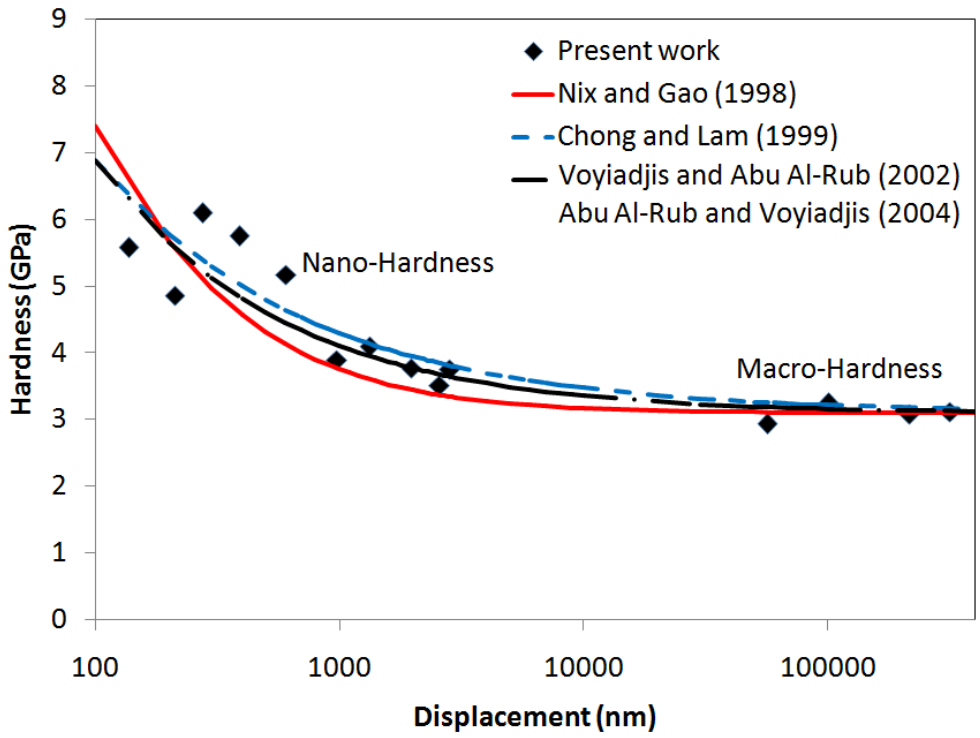

Figure 5.10: Experimental hardness versus indentation displacement with data fitting of different models for HR-A36 steel.

5.6 Dynamic Hardness

Hardness obtained through low rates of loading, termed static hardness in this work, has been studied extensively both experimentally and theoretically through different theories and approaches. However, less work has been carried out studying the hardness behavior for strain dependent material under high strain rate of loading. Tabor (1951) defined the dynamic hardness as the resistance of the metal to local indentation when the indentation is produced by a rapidly moving indenter. He discussed dynamic hardness mainly due to falling

indenter under gravity on the metal surface and defined the dynamic hardness number as the energy of impact over the volume of indentation. Researchers found that the volume of indentation is directly proportional to the kinetic energy of the indenter which implies that the metal offers an average pressure of resistance to the indenter. In a different approach the energy of rebound was taken as a measure of dynamic hardness. Regardless of the method used to measure the dynamic hardness, it was found that dynamic hardness is always higher than static or quasi-static hardness, or in other words hardness value increases with increasing applied load rate and generally with increasing strain rate of loading.

Due to damage in structures subjected to blasts and impact loads there has been considerable recent interest by researchers in determining the dynamic hardness in materials and the effect of strain rate on it. Koeppel and Subhash (1999) used an experimental setup that utilizes the elastic stress wave propagation phenomena in a slender rod to determine the dynamic Vickers indentation hardness in metals. The results were verified by obtaining the constitutive response of materials at similar strain rates and then correlating the yield stress with the corresponding hardness. The characteristics of the induced plastic zone under static and dynamic indentations were investigated by contouring microindentation hardness measurements of the indented regions. The results showed that the size of the plastic zone highly depends on yield stress under static and dynamic conditions. Anton and Subhash (2000) performed static and dynamic Vickers indentations on six different brittle materials to study the rate effects in hardness and fracture toughness. The dynamic indentations were performed on the same aforementioned hardness tester that is based on elastic stress wave propagation phenomena. Under dynamic indentations, an increase in hardness was observed in all the brittle materials compared to their static hardness measurements.

Lu et al. (2003) developed a dynamic indentation technique to measure time-resolved depth and load responses during the process of indentation. A Moiré interferometry-based displacement measurement technique was utilized to measure the depth of indentation and a quartz load transducer was used to measure the load. They introduced a new methodology to deduce the dynamic rate sensitivity of materials using the measured data. Andrews et al. (2002) investigated the impact of a sharp indenter at low impact velocities for elastoplastic materials. They developed a one-dimensional model based on the assumption that under dynamic conditions, as well as under static conditions, the variation of indentation load is a parabolic function of the depth (Kick's Law). The motion of the indenter as it indents and rebounds from the target was investigated. For rate-independent materials agreement with the model was good provided the impact velocity did not exceed certain critical values. For rate dependent materials the relationship between load and depth in the impact problem is no longer parabolic and the model predictions cannot be applied to this case. It was suggested that the rate-dependent case can be solved by

incorporating the relationship between the motion of the indenter and the dynamic flow properties of the material into the equation of motion for the indenter. Initially Voyiadjis and Buckner (1983) and Voyiadjis et al. (1986) studied the axi-symmetric contact problem for the elasto-plastic behavior of materials subjected to spherical static indentation using the finite element method with mixed boundary conditions. Vasauskas (2002) divided the complete dynamic indentation cycle into the three phases: starting phase, indentation phase and rebound phase. He found that the value for several engineering metals obtained by dynamic hardness in various phases of indentation was 1.12 – 1.40 higher than the static hardness. Sundararajan and Tirupataiah (2006a, 2006b) compared the response of four metallic materials indented under both static and dynamic indentation conditions using spherical balls. They investigated the hardness-average strain behavior, the shape and extent of lip formation around the indentation and the size of the plastic zone formed around the indentation. The results showed an evidence for enhanced lip formation under dynamic indentation conditions, indicating to some form of localization of plastic flow underneath the impacting ball unlike in the case of static indentation. It was demonstrated that the decrease in H_d beyond the critical strain (ε_c) is the result of the onset of localization of plastic flow in the material being indented, and that such a localization is triggered by the decrease in flow stress due to the temperature rise in the plastic zone due to the adiabatic nature of deformation. However, this can be explained only if it is additionally postulated that the plastic zone itself shrinks in size with increasing strain. A composite expression has been derived for hardness under dynamic indentation conditions.

On the microscale level, strain rate was known to be related to the dislocation density and average dislocation velocity through Orowan equation. In addition, flow stress can be related to dislocation density using Taylor hardening law. Staker and Holt (1972) developed a dislocation cell structure in polycrystalline Oxygen-Free High-Conductivity (OFHC) copper by deforming tensile specimens by 10 per cent. They found that the flow stress is related to the square root of the dislocation density. Experimental tests on the effect of strain rate and strain rate history during plastic deformation of metals were done by Senseny et al. (1978). The results showed that the flow stress can be affected not only by the strain rate, but also by the strain rate history. The mechanical behavior of OFHC copper at a wide range of strain rates $(10^{-3} - 10^{3}/s)$ was investigated by Kumar and Kumble (1969) based on the dislocation mechanism. The strain rate behavior can be divided into two regions: below $10/s$ where the dislocation motion is thermally activated over forest dislocation barriers, and above $10^{3}/s$ where viscous damping mechanism is dominating. During the viscous damping it was found that the relationship between stress and strain rate is linear, and the mobile dislocation density is independent of both strain and strain rate, noting that in this region the mobile dislocation density is only a small fraction (10^{-6}) of the total dislocation density.

In the present work two models are used to predict strain rate dependency in hardness. The first model is a power law expression that is based on the dependence of the yield stress on the strain rate. This model is relatively simple in implementation and is quite easy to determine its parameters from simple uniaxial experiments. The second model is a micromechanical based model using Taylor's hardening law. It utilizes the behavior of dislocation densities at high strain rates in metals in order to relate dynamic hardness to strain rates. The later model also accounts for any changes in temperature that could exist.

5.6.1 Proposed Power Law Material Model

In indentation tests, the yield stress for work hardened materials was found to vary around the indenter. Using the slip line plasticity theory for indentation of a rigid sphere in a work hardened material it has been stated early by many researchers such as Prandtl (1920) and Tabor (1951) that the mean yield pressure P_m of plastic indentation is related directly to a representative static flow stress σ_{fo} at a specific value of plastic strain as follows:

$$P_m = c\sigma_{fo} \tag{5.18}$$

where c is nearly a constant and has a value of 3. This suggests that for fully work hardened materials the yield pressure is essentially independent of the load and the size of the indentation.

Noting that the static hardness H_o is defined as the total load applied on the indenter divided by the projected area of the indentation, or equivalently the mean pressure the material will support. Accordingly, Eq. (5.18) gives:

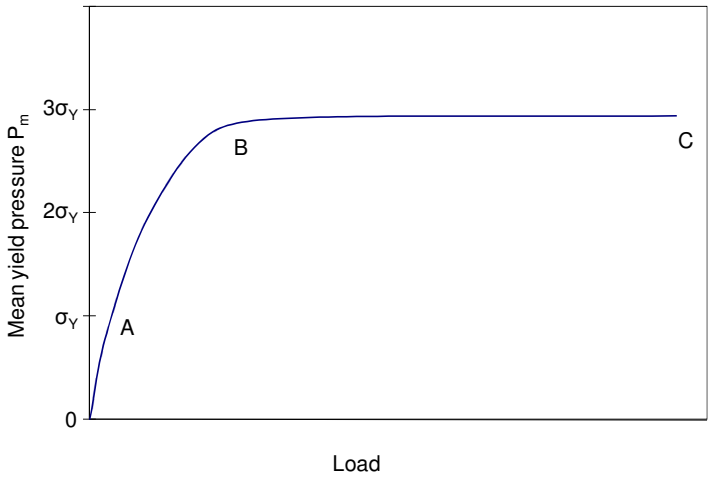

Figure 5.11: Theoretical pressure-load characteristic of an ideally plastic metal deformed by a spherical indenter: OA: elastic deformation region, AB: Transitional region, BC: fully plastic region.

$$H_o = c\sigma_{fo} \tag{5.19}$$

Tabor (1951), based on the mapping of the hardness-indentation depth curve ($H_o - h$ curve) to the tensile stress-plastic strain curve ($\sigma - \varepsilon^p$), assumed that c is always constant regardless of the work hardening degree of the material and approximately equals to 3. The pressure-load curve of a spherical indenter forced into ideal plastic material is illustrated in Figure 5.11, which shows the different deformation stages during an indentation process. The first region in the curve OA represents the initial elastic deformation when the indenter starts to penetrate the material up to the point where plastic deformation starts at a mean pressure of $1.1\sigma_{yo}$, where σ_{yo} is the static yield stress (point A). As the flow stress increases a transitional region exists and is represented by the AB part. Region BC represents the condition of full plasticity that is stated mathematically in Eq. (5.18). It is worthwhile to mention that the assumption that c is a universal constant was doubted by some researchers where they found that the flow stress around spherical indentation of different radii did not show any systematic correlation with the flow stress values at the indentation edge because the plastic strains around the indentation is widely distributed. It is therefore necessary to emphasize at this stage the conditions under which Eq. (5.19) is valid. Firstly, the target solid material is assumed to be isotropic, which implies that, in practice, the metal must be polycrystalline without any preferred orientation. Secondly, it is assumed that it is fully work-hardened and has a constant yield stress σ_{yo} under static loading, i.e. there is no difference between yield stress and flow stress. In practice this means that if the material work-hardens appreciably or shows an upper yield point, some other approach must be used. Lastly, it is assumed that elastic deformation is unimportant.

It is also important to note that for a material that tends to work-harden the indentation process itself will harden the material under the indenter which produces an increase in the flow stress. With the Vickers pyramidal indenter the plastic strains produced will vary from point to point under the indentation and hence the flow stress will also vary from point to point. A detailed analytical solution of the problem is not possible but one may provide a very simple analysis in the following way (Tabor, 1951). It can be assumed that there is a representative value of the flow stress which is related to the observed Vickers hardness by the relation given in Eq. (5.19), where c again has the value of about 3. Using an empirical method it is found that the indentation produces a representative strain (also can be looked at as an average strain) ε_r equivalent to an 8% tensile strain. Hence, if for a given tensile stress-strain curve of the metal one determines the flow stress for an additional 8% strain (i.e. $\sigma_{0.08}$), the Vickers hardness value will be three times this value (Tabor, 1951). It turned out that this additional strain is the same regardless of the size of the indentation as long as it is macro indentation (not micro- or nano-indentation), which is because of the principle of geometric similarity. It was also observed that the additional strain is roughly constant and independent of the initial state of work-hardening in the

specimen. The most common value of this representative strain is about 8%, although Atkins and Tabor (1965) showed that this representative strain is a function of the cone angle for the indentations conducted using the Vicker's indenter. They also found that this value of the effective strain for the 136^o Vicker indenter can be taken as 11%. More recently, Dao et al. (2001) proposed a systematic methodology for extracting various material parameters and as well as the representative strain from sharp indentation experiments. They suggested the representative strain to be 3.3% rather than 8% as has been proposed in the past literature. However, the value 8% obtained by Tabor is still widely used in this field.

Actually, the aforementioned assumption that the elastic deformation is unimportant is not always valid. This is generally true for most metals except for very hard steels; it becomes increasingly inaccurate for materials for which $\sigma_{0.08}/E$ (where E is Young's modulus of elasticity) becomes more than about 0.01. In this case the elastic yielding of the material imposes less constraint on the plastic zone and c is less than 3. This was also observed experimentally in some other materials like glass, bearing steel and soft lead alloy that did not follow a constant c (see for example Marsh, 1964). One explanation for this deficiency in the simple indentation hardness theory was that it might be related to the large elastic strains involved in the indentation process. This explanation was verified by investigating H_o and $\sigma_{0.08}$ for different materials with different modulii of elasticity which reflects the elastic behavior of the material. Also it was clear that the solution provided by the simple indentation theory does not apply to all cases of indentation and hence another mode of deformation was suggested. Based on the work of Samuels and Mulhearn (1957), the deformation during indentation process in some highly elastic materials was seen to be analogous to the expansion of a spherical cavity by internal pressure rather than moving towards the surface as in slip line theory. The slip line theory can be considered successful in explaining the deformation during an indentation process where piling up at the edge of the imprint is observed, but when sinking in around the edge of indentation is seen the spherical cavity approach seems to be more feasible. The spherical cavity solution was physically reasonable to simulate the radial flow mode of deformation for high $\sigma_{0.08}/E$ materials which is less rigid and more susceptible to radial flow. Besides, it provides a lower $H_o/\sigma_{0.08}$ value for highly elastic materials. Assuming in plasticity that the Poisson ratio $\nu = 0.5$, Marsh (1964) utilized the spherical cavity approach to obtain the following expression for the hardness:

$$H_o/\sigma_{0.08} = k + m \ln \frac{2\sigma_{0.08}}{3E} \tag{5.20}$$

where k and m are constants to be calculated from experimental data fitting. Eq. (5.20) was applied to a diversity of materials that included lead, aluminum, copper, mild steel, different types of carbon steel and even some kinds of polymers, and the constants k and m were found by data curve fitting to be 0.28 and 0.60, respectively (Samuels, 1957). This data fitting showed a wide validity

over the experimental results of the different materials. Eq. (5.20) for the static case, is plotted along with Tabor equation in Figure 5.12, where the crossing point between the two equations can be found numerically to be about $\sigma_{0.08}/E = 0.008$ for a strain rate of $10^{-3}/s$. For values of $\sigma_{0.08}/E$ less than 0.008 Tabor equation is the governing relation which means that the slip line deformation is the dominant mode of deformation under indentation. For the case when $\sigma_{0.08}/E$ is larger than 0.008, the spherical cavity mode of deformation becomes the dominant mode where the constraint factor deceases logarithmically, and at very high $\sigma_{0.08}/E$ values the constraint factor approaches the value of unity. The left hand side in Eq. (5.20) (and hence the right hand side also) equals to the static constraint factor. Assuming a steady state indentation, the difference between static and dynamic expressions of cavity expansion was shown by Hopkins (1960) to be $\frac{3}{2}\rho V^2/\sigma_{0.08}$, where ρ is material density and V is the contact velocity. Hence the dynamic constraint factor c_d can be expressed as:

$$c_d = k + m \ln \frac{2\sigma_{0.08}}{3E} + \frac{3}{2}\frac{\rho V^2}{\sigma_{0.08}} \tag{5.21}$$

In rate dependent materials the yield stress is sensitive to changes in the strain rate. However, since the constraint factor in not totally independent of the yield stress this would raise the option that the constraint factor can be actually affected by the changes in strain rates. One simple way to include the strain rate effect is to use the power law:

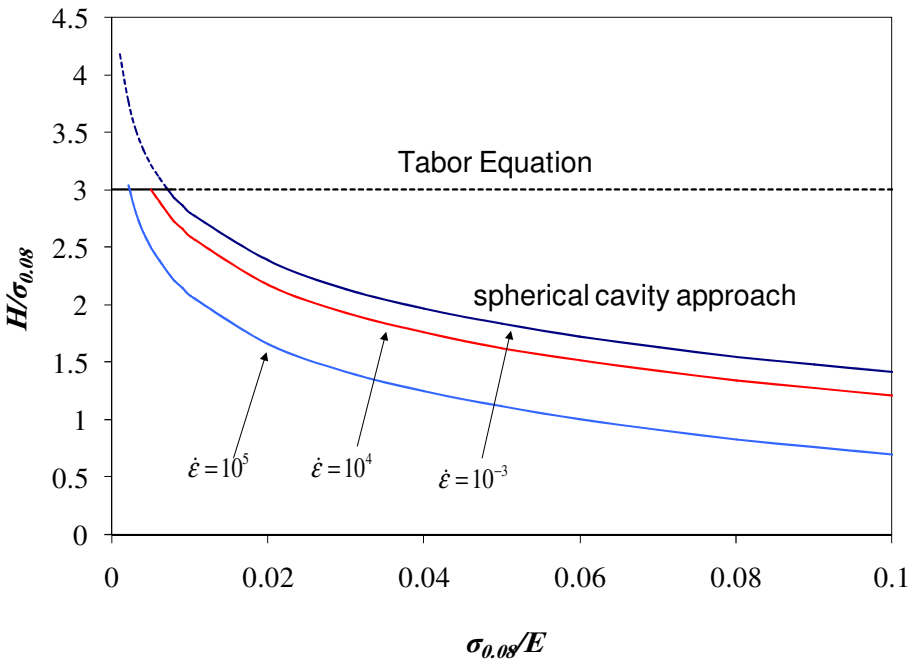

Figure 5.12: Constraint factor versus $\sigma_{0.08}/E$ obtained for different strain rates with typical values of $n = 0.5$ and $\dot{\varepsilon}_r = 10000$.

$$\sigma_{0.08,d}(\varepsilon,\dot{\varepsilon}) = \sigma_{0.08}\left(1+\left(\frac{\dot{\varepsilon}}{\dot{\varepsilon}_r}\right)^n\right) \tag{5.22}$$

where $\sigma_{0.08,d}$ is the dynamic flow stress at 8% strain, $\dot{\varepsilon}$ is the strain rate, and n and $\dot{\varepsilon}_r$ are material constants that can be determined by curve fitting of uniaxial experimental results from yield stresses for different strain rates. Substituting Eq. (5.22) in (5.21) one can obtain the following relation for the dynamic constraint factor:

$$c_d = \begin{cases} c & \frac{\sigma_{0.08}}{E} < \frac{0.008}{1+(\dot{\varepsilon}/\dot{\varepsilon}_r)^n} \\ k + m\ln\frac{2\sigma_{0.08}}{3E}\left(1+\left(\frac{\dot{\varepsilon}}{\dot{\varepsilon}_r}\right)^n\right) + \frac{3}{2}\frac{\rho V^2}{\sigma_{0.08}(1+(\dot{\varepsilon}/\dot{\varepsilon}_r)^n)} & \frac{\sigma_{0.08}}{E} \geq \frac{0.008}{1+(\dot{\varepsilon}/\dot{\varepsilon}_r)^n} \end{cases} \tag{5.23}$$

It can be seen from Eq. (5.23) that the limits are not constant for a specific material $\sigma_{0.08}/E$, but rather depend on the strain rate sensitivity of that material. However, this strain rate sensitivity is not high as it is illustrated in Figure 5.12 for $\dot{\varepsilon} = 10^4/s$ and $\dot{\varepsilon} = 10^5/s$. Typical values of $n = 0.5$, $\rho = 7800Kg/m^3$, $V = 10m/s$, $\sigma_{0.08} = 300 \times 10^6 Pa$ and $\dot{\varepsilon}_r = 10^4/s$ are used for illustration purposes only. Except for very high velocity impact like explosions, the velocity term that is responsible for dynamic cavity expansion is very small and can be neglected. The main effect of dynamic loading arises from the change in $\sigma_{0.08}$ due to the strain rate effect. At high strain rates, $\dot{\varepsilon} = 10^5/s$, the limit between the different indentation mechanisms decreases down to 0.002 instead of 0.008. Also, the equation shows that the constraint factor decreases with increasing strain rate for highly elastic materials in which the spherical cavity mode of deformation dominates.

Koeppel and Subhash (1999) showed experimentally that Eq. (5.19) can be applied to dynamic hardness with the same constant c used for the static case. This means that the increase in the yield stress due to the application of a higher rate of strain is accompanied by an increase of the same order in the hardness:

$$H_d = c\sigma_{0.08,d} \tag{5.24}$$

where H_d is the dynamic hardness. Substituting Eq. (5.19) and (5.24) in (5.22) yields the following relation:

$$H_d = H\left(1+\left(\frac{\dot{\varepsilon}}{\dot{\varepsilon}_r}\right)^n\right) \tag{5.25}$$

As it will be seen later in the examples, $\dot{\varepsilon}_r$ is very high and typically falls in the range of $10^4 - 10^6/s$. For the static case, the strain rate is in the order of $10^{-5} - 10^{-3}/s$, and therefore the inner parenthesis will be very small compared to unity with the resulting hardness being equal to the static one. The advantage of this

relation is that the effect of strain rate in dynamic hardness is accounted for in a simple and easy way to be implemented in any analysis.

5.6.2 Proposed Physically Based Material Model

Physically based material models are those models where knowledge about the physical processes, such as dislocation processes, is used to formulate the constitutive equations. On the other hand, engineering or empirical models, such as the one proposed earlier, are determined by using parametrical curve fitting for experimental data without considering the physical processes causing the observed behavior. These empirical models are also named engineering models as they are more common in engineering applications than the physically based material models. Otherwise, both types of models can be considered “engineering”.

The second model presented here is based on the dislocation mechanism. The strain rate behavior in metals can be divided into four regions. The first region is the one at the lowest stress and strain rate where deformation is dominated by diffusion creep mechanism. Subdivisions of this creep region can be made based on the type of the diffusion of the metal, and will not be discussed here. With increasing strain rate, the material enters a region where the flow stress is almost independent of temperature variation in the material. At this level the free energy of the intrinsic barriers is very large compared to the thermal energy so that the glide dislocations are held up at long range barriers in a way that random thermal fluctuation is unable to capture dislocation motion. The third stage, as described by Meyers (1994), starts when this thermal energy overcomes the energy barriers. Increasing strain rate in this region will increase the thermal energy of atoms which in turn increases their amplitude of vibration. As a result more dislocation will be able to move over short-range barriers. Hence this region is dominated by thermal activation mechanism in which can be expressed in its simplest way in the form of the Arrhenius equation as follows:

$$\dot{\gamma} = \dot{\gamma}_o e^{-\frac{U(\tau)}{kT}} \tag{5.26}$$

where $\dot{\gamma}$ is the shear strain rate, k is Boltzmann’s constant, T is the absolute temperature, $\dot{\gamma}_o$ is a constant, and $U(\tau)$ is the activation energy. Meyers (1994) expressed the activation energy as the difference between the activation energy at 0ºK and the energy of which a dislocation needs to overcome an obstacle. For simplicity this also can be expressed as a function of the applied stress τ as follows:

$$U(\tau) = (\tau_A - \tau)V \tag{5.27}$$

where τ_A is the athermal part of the stress that represents the barriers strength, and V is the activation volume. It is worth mentioning that the activation volume is

larger for fcc metals such as copper and aluminum than for bcc metals and alloys, and that is why the fcc metals are less sensitive to strain rate effects. If the stress exceeds τ_A, the dislocations will no longer be trapped by the barriers and will follow a viscous damping mechanism which is the fourth stage that happens at very high strain rates. Material behavior in this region can be considered as a viscous behavior and solid materials can be approximated as Newtonian viscous materials. Under an external applied stress, the dislocation will accelerate until it reaches a steady-state velocity where the intrinsic drag force on the moving dislocations will be given by:

$$\tau_D b = Bv \tag{5.28}$$

where v is the dislocation velocity, b is the Burgers vector, B is the dislocation drag or damping coefficient, and τ_D is the stress attributed to viscous damping. Furthermore, the dislocation velocity is related to the shear strain rate through:

$$\dot{\gamma} = b\rho v \tag{5.29}$$

where ρ is the density of the mobile dislocations moving with an average velocity v. Kumar and Kumble (1969) represented the flow stress by the equation:

$$\tau = \tau_A + \tau_T + \tau_D \tag{5.30}$$

where τ_T is the thermally activated component of the stress. Based on Eq. (5.26) through (5.30), an equation for the shear strain rate is obtained as follows:

$$\dot{\gamma} = \frac{Nl^2 b}{t_t + t_v} = \frac{Nl^2 b}{\delta^{-1} e^{\frac{U_o - lb^2\tau_f}{kT}} + \frac{lB}{\tau_f b}} \tag{5.31}$$

where N is the number of the moving segments per unit volume, l is the distance between the forest dislocations, or $l^2 b$ represents the shear strain increment due to one jump motion of a segment, t_t is the waiting time in the thermally assisted cutting, t_v is the time required by one jump motion under the control of the viscous drag, U_o is the energy required to form a jog and approximately equals to $\frac{1}{2}Gb^3$, $\tau_f = \tau - \tau_B$ where τ_B is the long range back stress, δ is the frequency factor, k is the Boltzmann's constant, and T is the absolute temperature. The term Nl also represents the density of the moving dislocations (the total length of the moving segments per unit volume). At low stresses the thermally assisted cutting behavior is dominating over the viscous drag one (i.e. $t_t \gg t_v$), and hence t_v can be neglected in this case. In the case of high stresses it becomes $t_t \ll t_v$ and t_t can now be neglected. Therefore, Eq. (5.31) can be approximated by:

$$\dot{\gamma} = \begin{cases} \delta N l^2 b e^{\left(\frac{-U_o + lb^2\tau_f}{kT}\right)} & \frac{\tau_f b}{\delta l B} e^{\left(\frac{U_o - lb^2\tau_f}{kT}\right)} \gg 1 \\ \\ \frac{N l b^2 \tau_f}{B} & \frac{\tau_f b}{\delta l B} e^{\left(\frac{U_o - lb^2\tau_f}{kT}\right)} \ll 1 \end{cases} \tag{5.32}$$

The flow stress in the first part of Eq. (5.32) depends linearly upon the logarithm of the strain rate, while in the second part the flow stress depends linearly upon the strain rate itself.

The tensile flow stress σ_f is related to the shear flow strength τ_f through the Taylor factor Z such that:

$$\sigma_f = Z\tau_f \tag{5.33}$$

The Taylor factor works as an isotropic interpretation of the crystalline anisotropy at the continuum level. This factor can vary from 1 (pure shear) to about 3.67 for single crystals. The average value obtained by Taylor for polycrystals metals was about 3.06 and has been verified later by other researchers. This value of 3.06 is almost the upper limit for the ratio of uniaxial yield strength to resolved shear stress (Taylor, 1938). However, Taylor indicated that this value is in good agreement with experimental data. With respect to strains, the shear strain rate is related to the total strain rate by the Schmid factor M:

$$\dot{\varepsilon} = M\dot{\gamma} \tag{5.34}$$

where the Schmid factor has a maximum value of 0.5. Substituting Eq. (5.19), (5.31) and (5.33) in (5.34) and rearranging the equation yields:

$$H = \begin{cases} \frac{cZ}{lb^2}\left(U_o + kTln\left(\frac{\dot{\varepsilon}}{MNlb^2\delta}\right)\right) & \frac{Hb}{\delta cZlB} e^{\left(\frac{U_o}{kT} - \frac{lb^2 H}{cZkT}\right)} \gg 1 \\ \\ \frac{cZB}{MNlb^2}\dot{\varepsilon} & \frac{Hb}{\delta cZlB} e^{\left(\frac{U_o}{kT} - \frac{lb^2 H}{cZkT}\right)} \ll 1 \end{cases} \tag{5.35}$$

According to this equation the hardness at low strain rates will be linear on a logarithmic scale of strain rates, and will be nonlinearly increasing with increasing the strain rate at high rates. In addition, the slope of the line at low strain rates is related linearly to temperature. Usually the natural logarithm term of the first part of the equation has a negative value at low strain rates, which is the reason that lower strain rates give higher negative values of the logarithm and in turn lower hardness values. This also justifies the fact that higher temperatures will give higher negative terms that yield lower hardness. Here temperature represents part of the slope of the line which will be shown in the next section.

Finite element analysis is carried out and compared to the two proposed models as well as some experimental results. Eight node brick element is used in the commercial finite element program ABAQUS/Explicit (2003). The indentation process is simulated with a plate subject to impact by a Vicker's indenter moving at a specific speed. More details on the finite element modeling will be given in the next sections.

5.6.3 Application to OFHC Copper

The Oxygen Free High Conductivity (OFHC) copper is a very important fcc metal that is widely used in industry due to its attractive properties such as high thermal and electrical conductivity and high ductility along with low volatility which makes this material indispensable in the electronics industry. OFHC copper is used here as an example for the purpose of verification of the proposed models to show the strain rate effect on dynamic hardness measurements. Experimental data of strain rate dependence of the flow stress for work hardened OFHC copper are taken from Rittel et al. (2002) and Senseny et al. (1978). The original results obtained from Rittel et al. (2002) are in terms of true stress and were transformed to engineering stress. The flow stress is normalized with respect to quasi-static yield stress of the OFHC copper ($\sigma_{yo} = 120Mpa$). Experimental results and its curve fitting using Eq. (5.22) are shown in Figure 5.13 with $n = 0.35$ and $\dot{\varepsilon}_r = 2.5 \times 10^4/s$. It can been seen that the flow stress is almost unchanged up to strain rates of $10^2/s$. After that it starts to increase rapidly and reaches around four times the quasi-static value ($\approx 500MPa$) at a strain rate of the order $10^6/s$. The calculated constants $n = 0.35$ and $\dot{\varepsilon}_r = 2.5 \times 10^4/s$ are entered into Eq. (5.25) in order to simulate the behavior of the dynamic hardness of OFHC copper, which is illustrated in Figure 5.14 with a static hardness $H_o = 940MPa$ (Koeppel and Subhash, 1999). It is known that the strain rate is not constant during an indentation process, and hence an average strain rate is generally used as in Koeppel and Subhash (1999). They expressed the average strain rate as:

$$\text{Average strain rate} = \frac{\text{velocity of the indenter}}{\text{size of indentation}} \tag{5.36}$$

where the size of indentation can be taken as either the depth, h, or the diagonal of indentation, d. The order of the strain rate will not vary significantly whether the depth or diagonal of indentation is used. However, since the strain rate results of Koeppel and Subhash (1999) are based on the diagonal of indentation, the same choice will be used in the results obtained by Lu et al. (2003). The results from both papers are shown in Figure 5.14 in addition to the power law results. The power law shows a good agreement with the experimental results at high strain rates as well as at low rates. Hardness of OFHC copper increases very slightly with increasing the strain rate until about $10^2/s$ where after that the rate increase in hardness is higher and it reaches about 2.5GPa at a strain rate $10^5/s$.

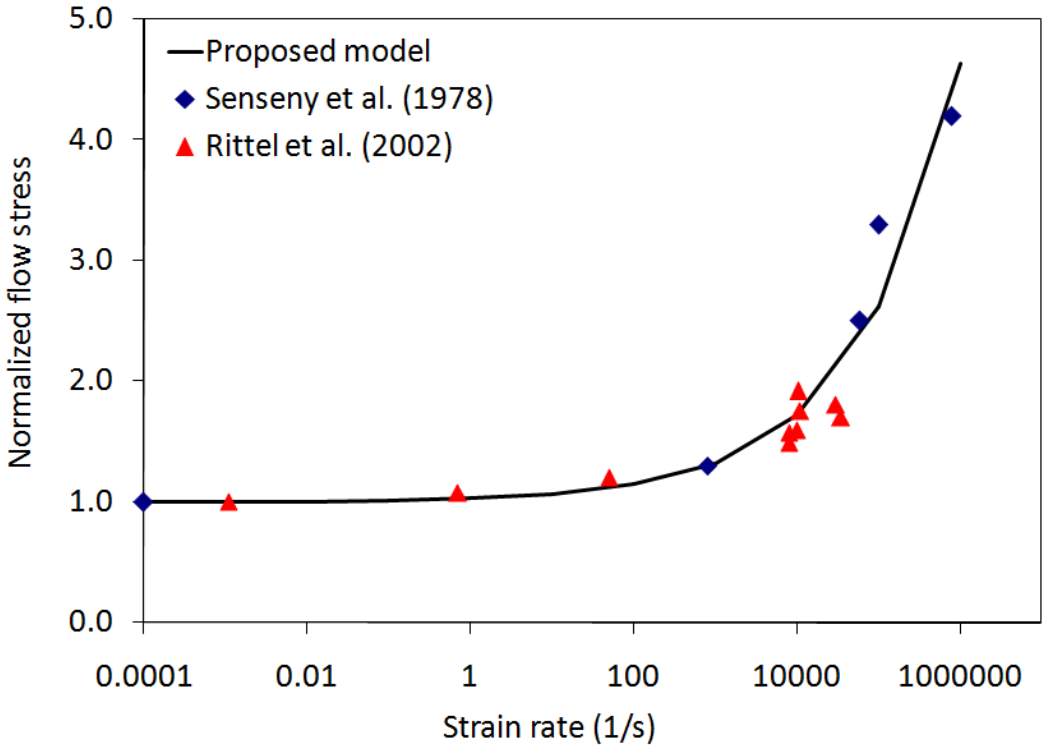

Figure 5.13: Normalized flow stress versus strain rate of OFHC copper.

Eq. (5.35) is also plotted in Figure 5.14 for OFHC copper using the following parameters: $M = 0.5$, $N = 5 \times 10^{17} m^{-3}$, $l = 2.3 \times 10^{-8}\text{m}$, $b = 2.5 \times 10^{-10} m$, $\delta = 1.0 \times 10^{13}$, $T = 293K$, $U_o = 3.75 \times 10^{-19}\text{N.m}$, $k = 1.38 \times 10^{-23} m^2.kg.sec^{-2}.K^{-1}$, $c = 3.0$, $Z = \sqrt{3}$, and $B = 7.0 \times 10^{-4}\text{N.sec.}m^{-2}$. The plot shows a very good agreement between this model and both the first model and the experimental results at low strain rates where the dislocation movement is obstructed at the barriers and the thermally activated behavior is dominating. At higher strain rates the dislocations spent less time at the barrier waiting for thermal fluctuation, and hence a higher external applied load is needed for the dislocations to overcome the barriers. The external load is related directly to the hardness of the material, which means increasing the strain rate will necessarily increase the hardness of the material. The rate of increase in the hardness with the increase in strain rate is very slow at low strain rates (in the thermally activated region) until the strain rate reaches a critical value of $5 \times 10^3/s$ in which case the rate of increase in hardness becomes very high after that point. This is attributed to the viscous damping behavior where dislocations travel between barriers in a viscous medium. In fact, the lack of existence of experimental data for Hardness of OFHC copper over a wide range of strain rates is a limiting factor in the full verification of both proposed models. The reason for that is the huge number of materials that have been tested and available in the literature. Even if results of the same metal were found in the literature, their properties would vary significantly because of the production method. For example, many results in

hardness tests of OFHC copper can be found in the literature, but for different kinds of copper (i.e. Annealed, quenched, work hardened, etc), not to mention the copper alloys. It will be very beneficial to conduct several experimental hardness tests on a wide range of strain rates like those for the yield stress that can be found in scientific references.

To overcome this shortage of experimental data, a finite element simulation is carried out using ABAQUS/Explicit (2003). A projectile Vicker's indenter of 136º is modeled as a rigid body with a mass of 0.025 kg as given by Lu et al. (2003). The bottom of the specimen is fixed. Bilinear stress strain curve is assumed with yield stress of $320MPa$ and ultimate stress of $402MPa$ at a plastic strain of 100%. Velocities of 5 to 30 m/s with 5 m/s increments are used for the indenter as those used by Lu et al. (2003). The average pressure under the indenter is used as a definition for the hardness according to Eqs. (5.18) and (5.19). The results are kind of lower than the experimental results, however, they show a good agreement with both the theoretical models in that strain rate range of $10^3 - 10^4/s$.

This method of impacting an indenter to the target material to obtain the dynamic hardness is seen to be inaccurate. This is because there is a critical impacting velocity at which below it there will be no plastic deformation and no hardness. This means that decreasing the impacting velocity will not give eventually the static hardness, but instead zero hardness. The proposed two models overcome this flaw and approach the static hardness at low strain rates. A typical pressure distribution under an impacting indenter moving with a velocity of 10 m/s is shown in Figure 5.15.

The temperature effect on the hardness of OFHC copper with increasing strain rate can be seen in Figure 5.16 for the physically based model. When the strain rate is low, the thermally activated mechanism will control the deformation behavior of moving dislocations which will encounter periodic barriers of different spacing and different lengths. Here in this strain rate region increasing temperature plays an important role in increasing the thermal energy of the dislocations at the barriers which in turn help them to overpass the barriers with lower stress (or in other words lower applied load which means lower hardness). Also at high temperatures, dislocations will have higher thermal energy which makes it easier for strain rates to cause higher flow stresses than for the case of low temperatures. This sensitivity can be referred mathematically as the slope of the hardness with respect to the strain rate, and it is clear that the curve slope is higher (higher sensitivity) at higher temperatures.

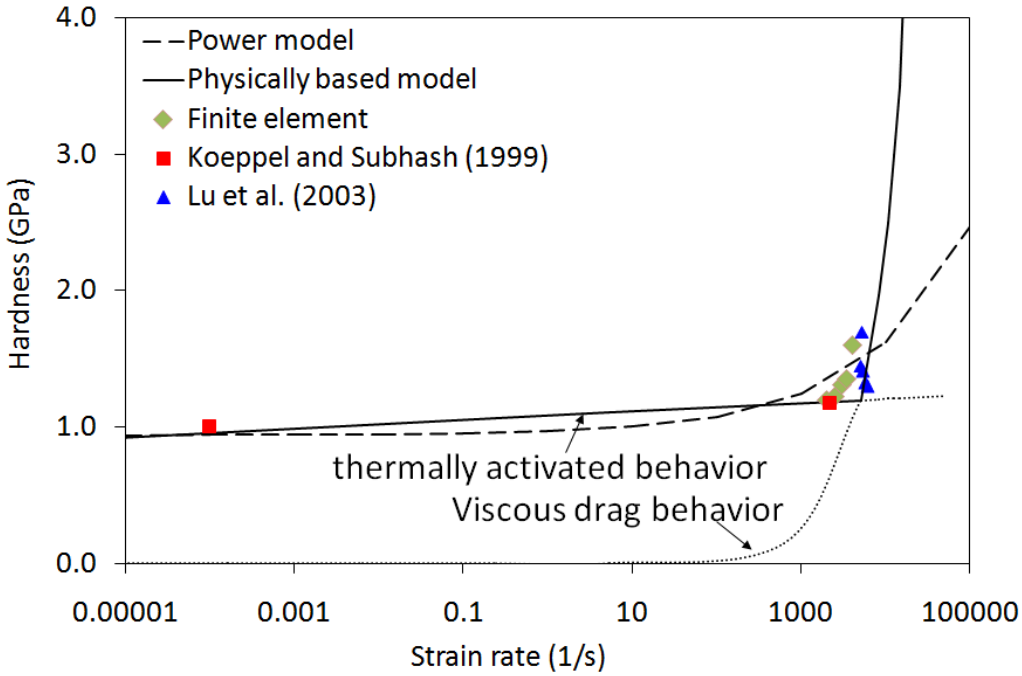

Figure 5.14: Hardness versus strain rate of OFHC copper

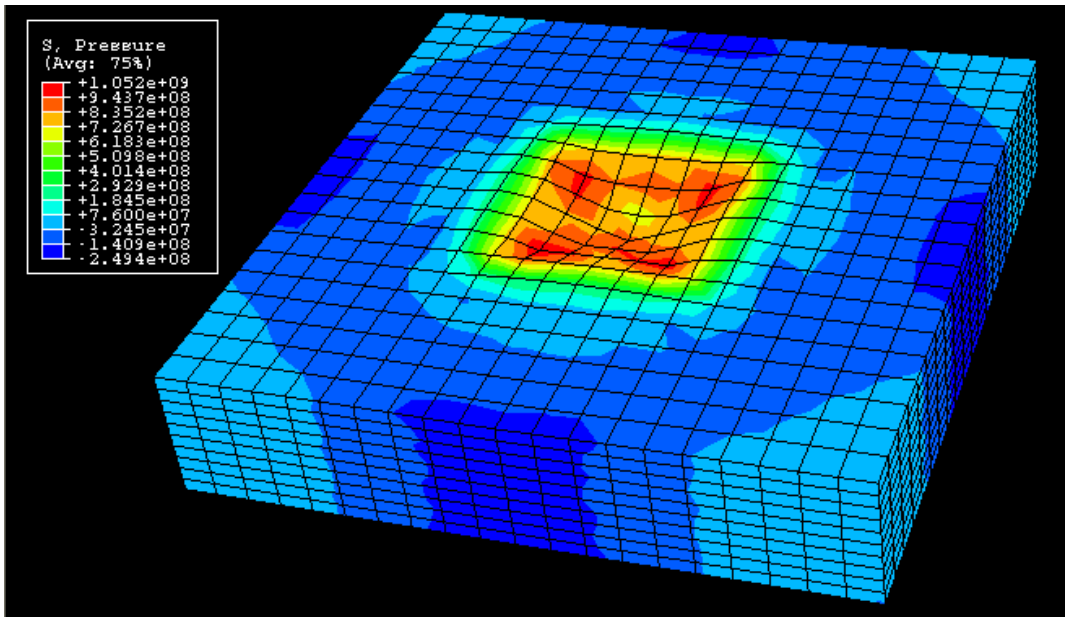

Figure 5.15: Pressure distribution under the indenter impacting target at a velocity of 10 m/s. (stresses are in Pa)

When a higher energy is provided to overcome the obstacles, the hardness appears to become independent of temperature at high strain rates where the viscous behavior is the controlling process. This agrees with the results for different fcc metals obtained by Voyiadjis and Abed (2005) which show that the stress dependency on temperature starts to disappear with increasing

strain rates. The reason for that is because at the high strain rates (of the order $10^4/s$) the dislocations movement in the viscous medium is independent of the thermal energy of the material, in contrast to the low strain rate range.

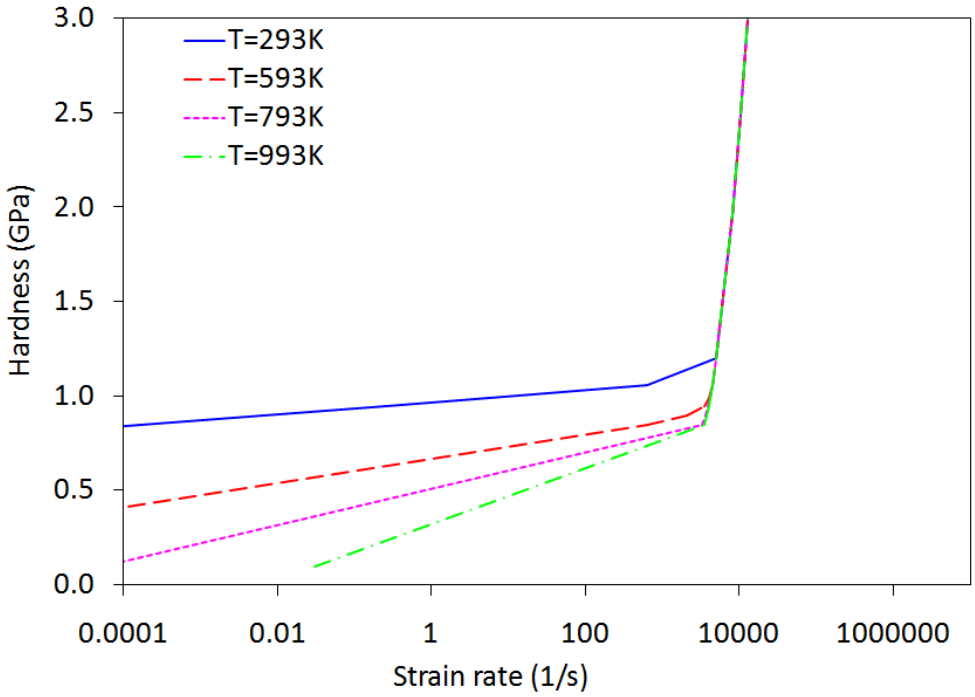

Figure 5.16: Effect of temperature change on Hardness behavior versus strain rate of OFHC copper.

5.6.4 Application to Cold Rolled 1018 Steel

Cold rolled low carbon (1018) steel is one of the most common grades of steel currently available. CR-1018 steel is valued because it can be easily formed, machined, welded, and fabricated. Its chips are continuous and rigid which result in a fine finish. CR-1018 steel is often utilized in high volume screw machine part applications commonly found in shafts, spindles, pins, rods, and more. Experimental data of strain rate dependence of the flow stress of CR-1018 Steel are taken from Costin et al. (1980), Shawki and Clifton (1989) and Steidel and Makerov (1960) and shown in Figure 5.17 normalized with respect to the initial yield stress of 470 *MPa*. Eq. (5.22) is also plotted in the figure with $n = 0.2$ and $\dot{\varepsilon}_r = 1.25 \times 10^6/s$. The rate of increase of the normalized flow stress in CR-1018 steel can be seen to be lower than that of OFHC copper. For example the increase in the flow stress of CR-1018 steel is about 60% at a strain rate of $10^5/s$ compared to about 450% increase for OFHC copper at the same strain rate. The constants n and $\dot{\varepsilon}_r$ are used to plot Eq. (5.25) for the dynamic hardness of CR-1018 steel in Figure 5.18. The proposed model is compared to the experimental results from Clough et al. (2003) and Ramanathan and Foley (2001) and shows a generally good agreement with the results. The results obtained by Clough et al. (2003) have a highly varying hardness values over a very narrow range of strain

rates $5 \times 10^3/s$ to $1 \times 10^4/s$, which do not coincide with the power law model, but rather coincide more with the physically based model. The following constants are used for characterizing CR-1018 steel through the physically based model: $M = 0.5$, $N = 1 \times 10^{17} m^{-3}$, $l = 3.5 \times 10^{-8}\text{m}$, $b = 2.23 \times 10^{-10} m$, $\delta = 2.0 \times 10^{13}$, $U_o = 4.88 \times 10^{-19}\text{N.m}$, $k = 1.38 \times 10^{-23} m^2.kg.sec^{-2}.K^{-1}$, $T = 293K$, $c = 3.0$, $Z = \sqrt{3}$, and $B = 7.0 \times 10^{-5}\text{N.sec.}m^{-2}$.

One of these points at strain rates of $5 \times 10^3/s$ corresponds to a hardness value of 1.1 GPa which is lower than that of the quasi-static value of 1.31 GPa at very low strain rates and should not be compared to the model. At low strain rates where the behavior follows the thermally activated behavior, the physically based model tends to underestimate the dynamic hardness compared to the power model with about 8-10% strain. When the controlling behavior is the viscous drag phenomenon at high strain rates the physically based model coincides better with the experimental data than the power law model. According to the physically based model the rate of increase in the hardness is very high when the viscous drag behavior is reached which is not the case for the power model. Despite that, as in the case of the OFHC copper, more experiments over the whole range of the strain rates are needed to verify the effectiveness of both models.

For the finite element simulation, the indenter is modeled as a rigid body with a mass of 1.210 kg as given by Clough et al. (2003). The CR-1018 steel is assumed to have a bilinear stress strain curve with a yield stress of 520 MPa and an ultimate stress of 560 MPa at a plastic strain of 10%. Four velocities of the indenter are used: 1.40, 1.92, 2.82, and 4.17 m/s that are equivalent to the dropped balls velocity by Clough et al. (2003). Again the results are lower than the experimental ones but show a reasonable accuracy. Both the finite element and the experimental results appear to follow the viscous drag mechanism of the physically based model more than the thermally activated mechanism or the power law model. However, impacting indenters at very low velocities predict a hardness lower than the static one and that needs to be investigated in the future.

Figure 5.19 illustrates the temperature effect on dynamic hardness for CR-1018 steel with increase in the strain rate. The thermally activated behavior controls the hardness decrease with the increase in temperature at low strain rates. In addition, the slope or the sensitivity in change in the hardness with increase in the strain rate does not change significantly with that of the increase in the temperature. In other words, unlike the case of OFHC copper, the change in temperature will decrease the hardness of the steel, but has only low effect on its strain rate sensitivity. Although this may be attributed somehow to the different alloy structure behavior of CR-1018 steel, the thermal activation concept still can describe this mechanism in a robust way. At a critical value of strain rate of about $7 \times 10^3/s$ the viscous damping mechanism becomes the dominating behavior of deformation at which the temperature sensitivity of flow stress

disappears. In this region the strain rates curves obtained at different temperatures coincide with each other because the dislocation movement in this range is independent of the thermal energy of the material.

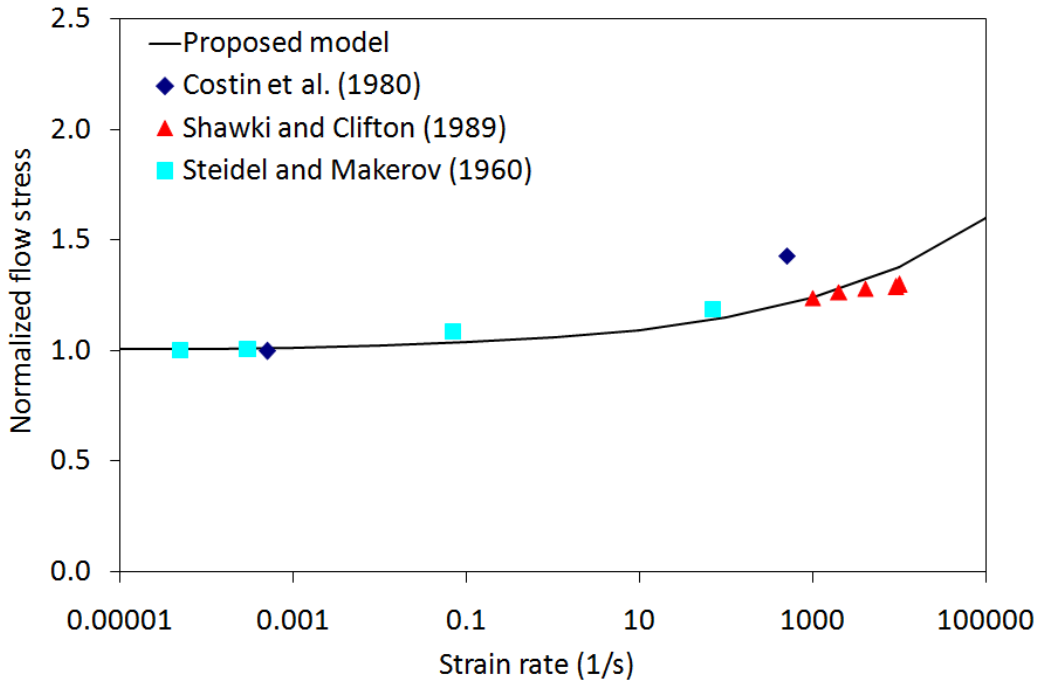

Figure 5.17: Normalized flow stress versus strain rate for CR-1018 steel.

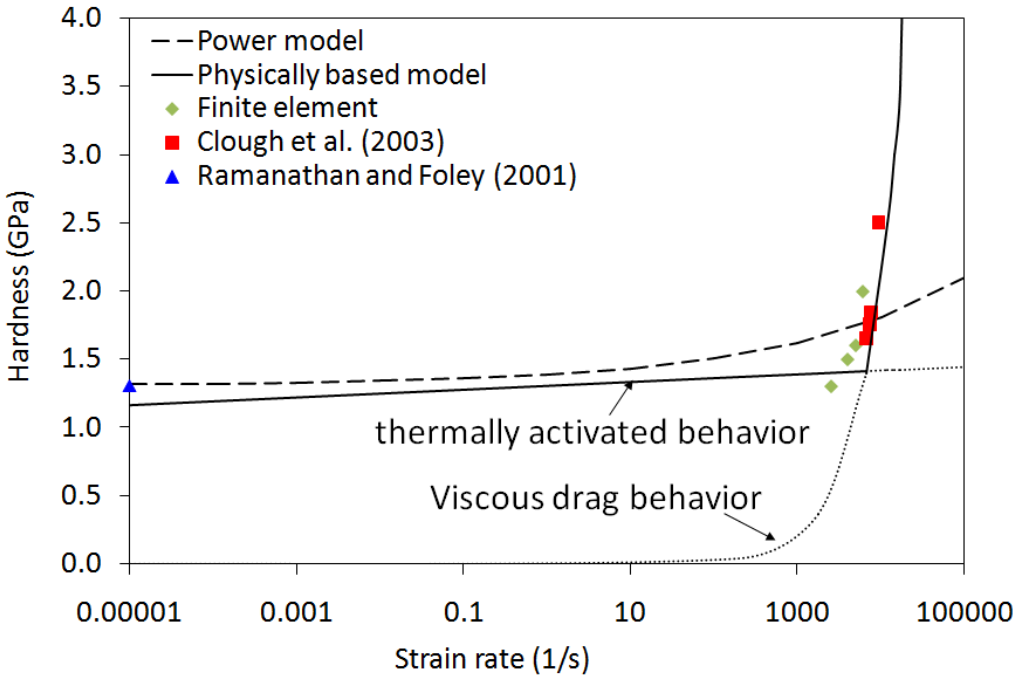

Figure 5.18: Hardness versus strain rate for CR-1018 steel.

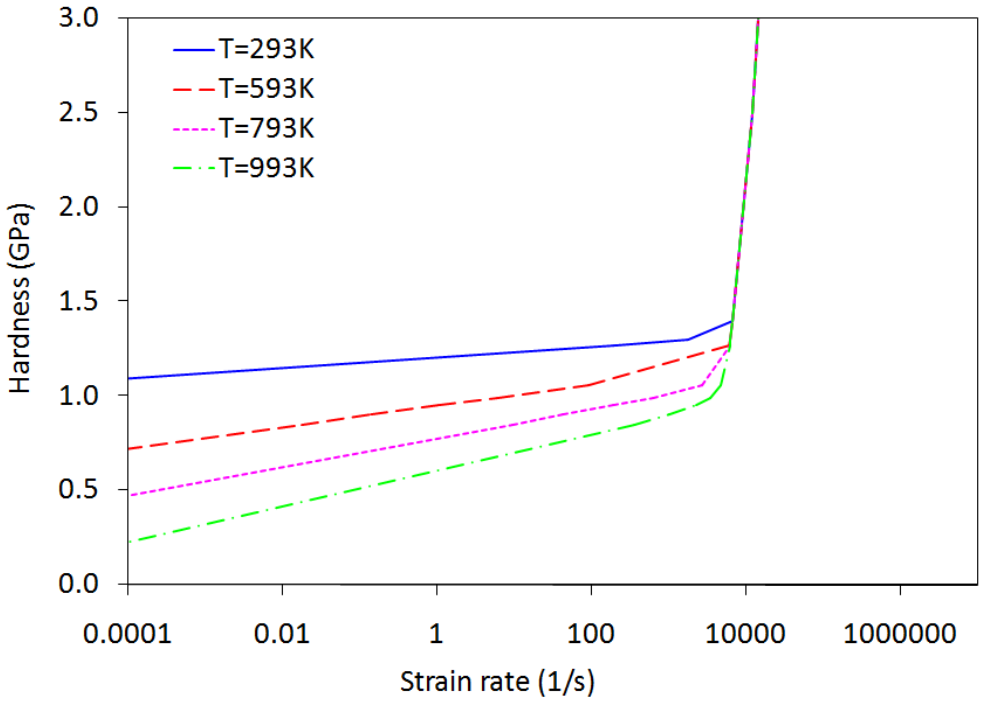

Figure 5.19: Effect of temperature change on the Hardness behavior versus strain rate for CR-1018 steel.

5.7 Dynamic Length Scale

Many researchers have questioned the assumption of fixed length scale (Voyiadjis and Abu Al-Rub, 2005). Berthier et al. (2005) studied the viscosity of glass formation. They tested an old idea that the dynamics becomes sluggish as the glass transition approaches, because increasingly larger regions of the material have to move simultaneously to allow flow. New multipoint dynamical susceptibilities were introduced to estimate quantitatively the size of these regions and provide direct experimental evidence that the glass formation of molecular liquids and colloidal suspensions is accompanied by growing dynamic correlation length scales. In addition to solids, this has been noticed also in liquids. Liquid can sustain shear waves up to a minimum wave number, indicating solid-like behavior over short length scales. With the increase of density this critical wave number decreases, indicating a growth of a dynamic length scale. Das (2000) investigated the growth of this dynamic length scale in the supercooled regime the transverse correlation function and by computing the feedback effects of dynamic correlation in an extended mode-coupling model where the structure factor of the liquid is used as an input.

Voyiadjis and Abu Al-Rub (2005) showed that the length scale depends on the microstructure of the material, and that the current gradient plasticity theories do not give sound interpretations of the size effects in micro-tests if a definite and fixed length scale parameter is used. They suggested that a fixed value of the

material length-scale is not always realistic and that different problems could require different values. The experimental results from size effect tests (micro/nano indentation, micro-torsion of thin wires, micro-bending of thin beams) showed that the intrinsic material length-scale ℓ is not fixed but evolves with the course of deformation. A semi-empirical evolution law for ℓ in terms of the grain size, the specimen size, the equivalent strain, and the hardening level has been proposed.

The equivalent plastic strain and the hardening level in dynamic problems are known to depend on the loading rate. Since length scale also depends on these factors, it is expected that the material length scale will depend also on the strain rate. For dynamic indentation, the dynamic hardness is usually higher than static hardness for the same load, and the indentation area (or depth) is less than the static one. Assuming the same load P_{max} is applied at higher rate, Eq. (5.12) can be written for dynamic conditions as follows:

$$H_d = \frac{P_{max}}{A_d} \tag{5.37}$$

where A_d is the area of the indentation under dynamic loading. Substituting Eq. (5.12), (5.25), (5.7) and the first term in Eq. (5.16) in Eq. (5.37) and rearranging one obtains:

$$\ell_d^* = \ell^* \left(1 + \frac{\dot{\varepsilon}}{\dot{\varepsilon}_r}\right)^{-n/2} \tag{5.38}$$

where ℓ_d^* is the dynamic length scale. This relationship predicts a decrease in the length scale with increasing the loading rate as shown in Figure 5.20 for CR-1018 steel. That is caused by the minus sign in the exponent. Experimental results were found to agree with this in the way that deformations at high rates are usually more localized in smaller area of material, and the deformation at those areas are less affected by the surrounding material. However, it is clear from the exponent that the sensitivity of the length scale toward the change in the strain rate is half the sensitivity of the hardness or the flow stress in general. The advantages of this relationship are that it is easy to obtain its constants and easy to be implemented in any analysis method such as the finite element subroutines. The previous relation will be used later in a finite element procedure in order to calculate the value of the dynamic length scale at each material point.

In this chapter an experimental procedure has been illustrated and nano-indentation tests were carried out on two types of steel; HR-A36 and CR-1018 steel, in order to obtain values for the material intrinsic length scale. In addition two models are proposed to capture the rate sensitivity in material hardness. The first is a power law model that uses material constants that can be obtained experimentally though simple axial tests. The second model is a physically based model that is based on the dislocation behavior. Both models show good agreement with the experimental results for both OFHC copper and CR-1018

steel. In fact, due to the lack of experimental results available in the literature several experiments on different materials are needed in order to gain more understanding about the behavior of dynamic hardness on a wide range of strain rates. It should be mentioned that using an impacting indenter to obtain the dynamic hardness has a major flaw at low impacting velocities, where it would predict hardness values that are less than the static one. Hence, this issue should be taken into consideration when such a procedure is implemented. However, the power law model is used here to obtain an expression for the material dynamic length scale that can be used in the gradient theory formulation to help regularize finite element meshes.

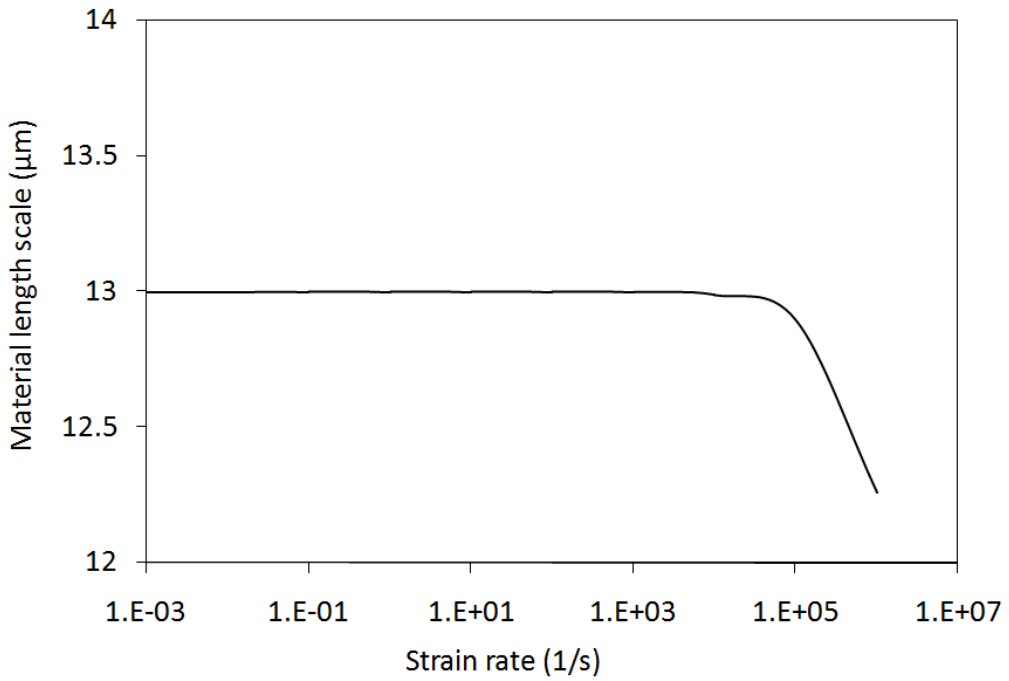

Figrue 5.20: Change in material length scale of CR-1018 steel versus strain rate.

CHAPTER 6: FINITE ELEMENT ANALYSIS

6.1 Introduction

Adiabatic shear bands have been investigated analytically in Chapter 4, where mechanisms of initiation and evolution of shear bands were discussed. While it has revealed some of the fundamentals behind the banding process, the results and conclusions remain mostly qualitative. This is mainly attributed to the oversimplified assumptions made in theoretical formulation, which were necessary to obtain a solution. In addition, it becomes almost impossible analytically to take into account the different mechanisms present during any shear band deformation, such as heat diffusion, wave trapping, viscous dissipation, and effects attributed to geometry, disturbances, imperfections, etc. The short time duration of such a problem adds another challenge to the experimental verification, since this makes the process of obtaining any analytical model parameters highly dependable on the experimental setup.

Numerical techniques can be a very helpful tool in unveiling and simulating the detailed process of shear banding. If the numerical simulation is carefully chosen and well designed, the modeling may be able to simulate several mechanisms during the different stages of shear banding, and to obtain a fairly good prediction of initiation and propagation of adiabatic shear bands. However, there are some special problems that are usually encountered while conducting these numerical simulations. The three main issues that have been noticed are: the unknown position of the shear localization; instability in the calculations; and the scale of localization. All these three problems rise from the abrupt changes in the different variables in an extremely narrow area. This suggests that the three problems are fairly related and coupled.

Computational instabilities can sometimes take place in calculations associated with strain localization, especially in the region where strain softening is clear. In early work on the simulation of banding, computational instability was not reported. It was not reported even in some relatively new works such as these by Costin and coworkers (1980). This might be the case because these calculations did not extend to the fully developed shear band accompanied by a sharp drop in shear stress where the softening behavior is noticeable. Nevertheless, Wright and Batra (1985) did experience instability in their analysis. The computations in their finite element algorithm became unstable as soon as the abrupt drop in the shear stress occurred. Thus the validity of the results of a fully developed adiabatic shear band remained in doubt. It is therefore clear that a stable algorithm is required throughout all stages of the process especially for the late stage, which shows rapid drop in stress and rapid increases in strain rate and temperature.

The position of the localized shear zone highly depends on the geometry of the problem under consideration. It may be located near the loading boundary

or near the supporting boundary. Any inhomogeneity can play an important role in determining the location of the adiabatic shear bands. A further possibility is that the localized shear zone with its localization may drift between the boundaries position and the inhomogeneities position. In fact, this is somehow easy to be adjusted in the numerical simulation.

To analyze the adiabatic shear localization, the finite element package ABAQUS/Explicit will be used in this work. The selected explicit finite element scheme is explained thoroughly in this chapter. Also, the implementation of the gradient formulation in a VUMAT user subroutine that can be connected to the finite element program is also presented.

6.2 Finite Element: Explicit Dynamic Analysis

The explicit dynamics analysis procedure in Abaqus/Explicit is based on the implementation of an explicit integration rule together with the use of diagonal or "lumped" element mass matrices. This kind of analysis is computationally efficient for the analysis of large models with relatively short dynamic response times and for the analysis of extremely discontinuous events or processes. In addition, it includes general automatic contact capability that facilitates the definition of complex contact conditions for the case of impact between different bodies. Explicit dynamic scheme is particularly helpful for analysis of adiabatic shear banding where inelastic dissipation is expected to generate heat in the material. Furthermore, a consistent large deformation theory is used to simulate large rotations and large deformations.

The equations of motion for the body under analysis are integrated using the explicit central difference integration rule:

$$u^{(i+1)} = u^{(i)} + \Delta t^{(i+1)} V^{(i+1/2)} \tag{6.1}$$

$$V^{(i+1/2)} = V^{(i-1/2)} + \left[\left(\Delta t^{(i+1)} + \Delta t^{(i)}\right)/2\right] a^{(i)} \tag{6.2}$$

where u is the degree of freedom (displacement or rotation), V is the velocity, and a is the acceleration. The superscript (i) referes to the increment number and $(i-1/2)$ and $(i+1/2)$ refer to mid increment values in an explicit dynamic step. The central difference integration operator is explicit in a way that the kinematic state can be advanced using known values of $V^{(i-1/2)}$ and $a^{(i)}$ from the previous increment. The explicit integration rule is quite simple but by itself does not provide the computational efficiency associated with the explicit dynamics procedure. The key to the computational efficiency of the explicit procedure is the use of diagonal element mass matrices because the accelerations at the beginning of the increment are computed by:

$$a^{(i)} = M^{-1} \Delta F \tag{6.3}$$

where

$$\Delta F = \left(P^{(i)} - I^{(i)}\right) \tag{6.4}$$

where M is the diagonal lumped mass matrix, P is the applied force vector, and I is the internal force vector. A lumped mass matrix is used because its inverse is simple to compute and because the vector multiplication of the mass inverse by the inertial force requires only n operations, where n is the number of degrees of freedom in the structure. The explicit procedure requires no iterations and no tangent stiffness matrix which reduces the calculation cost significantly for large models. The internal force vector, I, is assembled from contributions from the individual elements such that a global stiffness matrix need not be formed.

The explicit integration scheme in Abaqus/Explicit requires nodal mass or inertia to exist at all activated degrees of freedom unless constraints are applied using boundary conditions. More precisely, a nonzero nodal mass must exist unless all activated translational degrees of freedom are constrained and nonzero rotary inertia must exist unless all activated rotational degrees of freedom are constrained. Nodes that are part of a rigid body do not require mass, but the entire rigid body must possess mass and inertia unless constraints are used.

The explicit procedure integrates through time by using many small time increments. The central-difference operator is conditionally stable, and the stability limit for the time increment Δt_{cr} (with no damping) is given as:

$$\Delta t_{cr} \leq \frac{2}{\omega_{max}} \tag{6.5}$$

where ω_{max} is the highest frequency of the finite element assemblage. With damping, the stable time increment is given by:

$$\Delta t_{cr} \leq \frac{2}{\omega_{max}}\left(\sqrt{1+\xi_{max}^2} - \xi_{max}\right) \tag{6.6}$$

Where ξ_{max} is the fraction of critical damping in the mode with the highest frequency. Contrary to our usual engineering intuition, introducing damping to the solution reduces the stable time increment. In Abaqus/Explicit a small amount of damping is introduced in the form of bulk viscosity, which was described in Chapter 2, to control high frequency oscillations. Physical forms of damping, such as dashpots or material damping can also be introduced in the model.

An approximation to the stability limit is often written as the smallest transit time of a dilatational wave across any of the elements in the mesh as follows:

$$\Delta t_{cr} \approx L_{min}/c_d \tag{6.7}$$

where L_{min} is the smallest element dimension in the mesh and c_d is the dilatational wave speed in terms of Lame's constants (λ and μ) defined below. All integration schemes that require the use of a time step Δt smaller than a critical time step Δt_{cr}, such as the central difference method, are considered to be conditionally stable. If a time step larger than Δt_{cr} is used the integration is unstable. It means that any errors resulting from the numerical integration or round off in the computer grow and makes the response calculations worthless in most cases. Also when the solution becomes unstable, the time history response of solution variables such as displacements will usually oscillate with increasing amplitudes. The total energy balance will also change significantly. If the model contains only one material type, the initial time increment is directly proportional to the size of the smallest element in the mesh. The use of small increments (dictated by the stability limit) is advantageous because it allows the solution to proceed without iterations and without requiring tangent stiffness matrices to be formed. It also simplifies the treatment of contact which is helpful for analysis of body impact problems. The explicit dynamics procedure is ideally suited in analyzing high-speed dynamic events, but many of the advantages of the explicit procedure also apply to the analysis of slower (quasi-static) processes as well.

The results in an explicit dynamics analysis are not automatically checked for accuracy as they are in Abaqus/Standard (Abaqus/Standard uses the half-step residual). In most cases this is not of concern because the stability condition imposes a small time increment such that the solution changes only slightly in any one time increment, which simplifies the incremental calculations. While the analysis may take an extremely large number of increments, each increment is relatively inexpensive, often resulting in an economical solution. The method is, therefore, computationally attractive for problems where the total dynamic response time that must be modeled is only a few orders of magnitude longer than the stability limit; such as the wave propagation studies.

The dilatational wave speed, c_d, is determined in Abaqus/Explicit by calculating the effective hypoelastic material moduli from the material's constitutive response. Effective Lamé's constants for isotropic material are determined as follows:

$$\lambda = \frac{E\nu}{(1+\nu)(1-2\nu)} \tag{6.8}$$

$$\mu = \frac{E}{2(1+\nu)} \tag{6.9}$$

These effective moduli represent the element stiffness and determine the current dilatational wave speed in the element as:

$$c_d = \sqrt{\frac{\lambda+2\mu}{\rho}} \tag{6.10}$$

where ρ is the density of the material. It should be noted that generally when the ratio of deformation speed to dilatational wave speed is greater than 0.3, the purely mechanical material constitutive relationship is no longer valid and that a thermo-mechanical equation of state is required. However, hypervelocity impact problems are beyond the scope of this work and hence no need for any equation of state.

In some problems, such as adiabatic shear banding, stress analysis is known to be dependent on the temperature distribution, and the temperature distribution itself depends on stress solution. In these cases, fully coupled thermal-stress analysis is needed For example, metalworking problems may include significant heating due to inelastic deformation of the material which, in turn, changes the material properties. In addition, contact conditions exist in some problems where the heat conducted between surfaces may depend strongly on the separation of the surfaces or the pressure transmitted across the surfaces. This is also seen in rapid shear localization where the rate of heat generated due to plastic deformation is higher than the dissipated heat. For such cases the thermal and mechanical solutions must be obtained simultaneously rather than sequentially. Coupled temperature-displacement elements are available for this purpose in Abaqus/Explicit.

The heat transfer equations are integrated using the explicit forward-difference time integration rule:

$$T^{(i+1)} = T^{(i)} + \Delta t^{(i+1)} \dot{T}^{(i)} \tag{6.11}$$

where T is the nodal temperature, the subscript i refers to the increment number in an explicit dynamic step, and $\dot{T}$ is the temperature change. The forward-difference integration is explicit in the sense that no equations need to be solved when a lumped capacitance matrix is used. The current temperatures are obtained using known values of $\dot{T}$ from the previous increment. The values of $\dot{T}$ are computed at the beginning of the increment by:

$$\dot{T}^{(i)} = C^{-1}\left(P^{(i)} - F^{(i)}\right) \tag{6.12}$$

where C is the lumped capacitance matrix, P is the applied nodal source vector, and F is the internal flux vector. The mechanical solution response is obtained using the explicit central-difference integration rule with a lumped mass matrix as described before. Since both the forward-difference and central-difference integrations are explicit, the heat transfer and mechanical solutions are obtained simultaneously by an explicit coupling. Therefore, no iterations or tangent stiffness matrices are required. In this case, the approximate stability limit for the forward-difference operator in the thermal solution response is given by:

$$\Delta t_{cr} \approx L_{min}^2 / 2\alpha \tag{6.13}$$

where α is the thermal diffusivity and is given by $\alpha = k/\rho c$. The parameters k and c represent the material thermal conductivity and specific heat, respectively. In most applications of explicit analysis the mechanical response will govern the stability limit.

During the finite element analysis, the quadratic bulk viscosity pressure described in Equations (2.46) and (2.47) will smear a shock front across several elements and is introduced to prevent elements from collapsing under extremely high velocity gradients. Consider a simple one element problem in which the nodes on one side of the element are fixed and the nodes on the other side have an initial velocity in the direction of the fixed nodes. If the initial velocity is equal to the dilatational wave speed of the material, the element—without the quadratic bulk viscosity—would collapse to zero volume in one time increment (because the stable time increment size is precisely the transit time of a dilatational wave across the element). The quadratic bulk viscosity pressure will introduce a resisting pressure that will prevent the element from collapsing.

With respect to contact analysis in the Abaqus/Explicit code, two different contact algorithms are available: the kinematic and the penalty. In the case of kinematic enforcement of contact conditions, in each increment of the analysis the solver first advances the kinematic state of the model into a predicted configuration without considering the contact conditions. The solver then determines which slave nodes in the predicted configuration penetrate the master surfaces. The depth of each slave node penetration, the mass associated with it, and the time increment are used to calculate the resisting force required to oppose the penetration. The penalty contact algorithm, instead, results in less stringent enforcement of contact constraints than the kinematic contact algorithm. In this case, the algorithm searches for slave node penetrations in the current configuration. Contact forces that are a function of the penetration distance are applied to the slave nodes to oppose the penetration, while equal and opposite forces act on the nodes of master faces being penetrated. The “spring” stiffness that relates the contact force to the penetration distance is chosen automatically for the hard penalty contact, such that the effect on the time increment is minimal yet the allowed penetration is not significant in most analysis.

Having the ability to incorporate the most applicable material model for the problem at hand is of great benefit to an analyst. The user-defined material subroutine (VUMAT) capability in Abaqus/Explicit provides this functionality. Full details about the implementation methodology via VUMAT material user subroutine can be found in Abaqus manual (2003). The material model along with the gradient formulation is implemented numerically in a user-defined subroutine to be run in parallel with Abaqus/Explicit. The gradient formulation is discussed next.

6.3 Implementation of Gradient Formulation

Next, it will be shown how to compute the nonlocal terms of the plastic multiplier $\|\nabla d\lambda\|$ and $\nabla^2 d\lambda$ using a simple and easy approach. Usually, in the classical plasticity theory as in Chapter 2, the consistency condition of the yield function is used to determine the current value of the plastic multiplier $d\lambda$. The plastic multipliers are not considered here as independent global variables but as local internal variables. This simplifies the problem in the sense that it does not require to introduce shape functions for the interpolation of the plastic multipliers in the finite element.

In classical plasticity, the plastic multiplier is calculated by restoring the consistency condition iteratively. However, for the nonlocal formulation, it is not possible because it depends on the strain gradient. To evaluate the gradients $\|\nabla d\lambda\|$ and $\nabla^2 d\lambda$ at any integration point, m, the values of $d\lambda$ at that point as well as the values at the neighboring points (nonlocality) are required. The gradient at each integration point m is evaluated from the derivatives of a polynomial function that interpolates the values of plastic multiplier at the neighboring points. Therefore, the gradient terms $\|\nabla d\lambda\|$ and $\nabla^2 d\lambda$ can be expressed in terms of $d\lambda_n$ with $n \in \{1, \ldots, NIP\}$, where NIP is the number of Gaussian integration points in the nonlocal area, using the following relation:

$$\|\nabla d\lambda\|_m = \sum_{n=1}^{NIP} (g_{mn} d\lambda_n) \tag{6.14}$$

$$\nabla^2 d\lambda_m = \sum_{n=1}^{NIP} (\bar{g}_{mn} d\lambda_n) \tag{6.15}$$

where g_{mn} and $\bar{g}_{mn}$ are coefficient matrices that will be calculated next. Voyiadjis and Dorgan (2004), Voyiadjis and Abu Al-Rub (2006) and Abu Al-Rub and Voyiadjis (2006) proposed different simplified numerical procedures to evaluate the gradients for two dimensional analyses at the integration points.

Figure 6.1 shows a schematic illustration for the computation of the gradient terms from a regular finite element mesh, where the local terms are needed at the integration point of each element. This approach can be applied for two or three dimensional meshes. As an example, the three dimensional mesh with eight nodded element and eight integration points (full integration) is assumed. To calculate the gradient terms for any integration point, the distance between the point and its neighbor points is calculated using point coordinates. If the distance from the center point to the other point is greater than the length scale ℓ^*, then the point is excluded from the calculations. If the distance is less than the length scale, the point is taken into account to calculate the gradient terms. This scheme is valid for any element with any number of integration points. Despite that this procedure is applied here for regular finite element mesh, it can be extended to non regular mesh discretization. However, more elaborate studies are needed to generalize this approach to non-regular mesh discretization.

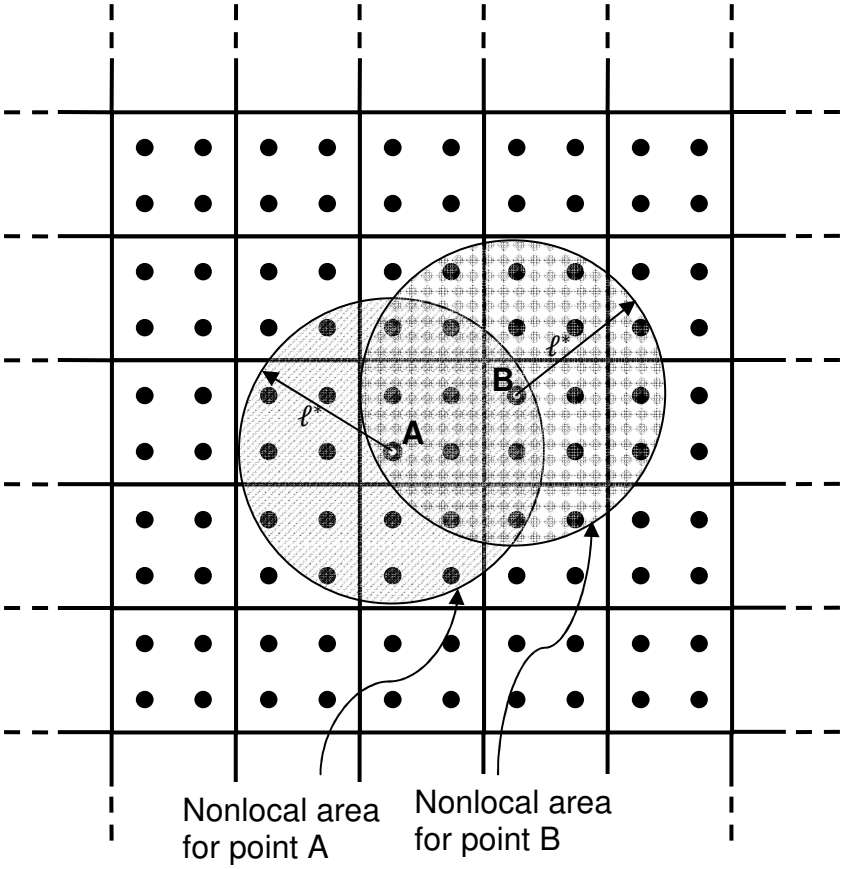

Figure 6.1: Illustration for the nonlocal concept of a four nodded element with four integration points.

In order to determine the coefficients g_{mn} and $\bar{g}_{mn}$, a complete second order polynomial function is used to evaluate the plastic multipliers around point m, such that:

$$d\lambda = a^T v \tag{6.16}$$

where a is the coefficient vector, and $\boldsymbol{v}$ is the variables vector. For example for two dimensional problems, $a^T = [a_1 \quad a_2 \quad a_3 \quad a_4]$ and $v^T = [1 \quad x \quad y \quad xy]$, while for three dimensional problems, $a^T = [a_1 \quad a_2 \quad a_3 \quad a_4 \quad a_5 \quad a_6 \quad a_7]$ and $v^T = [1 \quad x \quad y \quad z \quad xy \quad yz \quad zx]$. To obtain the coefficients vector a, a minimization method by least squares is used. Moreover, the interpolation is made in the global coordinate system (x, y) or (x, y, z) of the generated mesh with NIP integration points. The coefficients vector $\boldsymbol{a}$ can be expressed in the following form:

$$\Lambda = M^T a \tag{6.17}$$

where $\Lambda = [d\lambda_1 \quad d\lambda_2 \quad \dots \quad d\lambda_{NIP}]^T$, and the mesh matrix, M, for two and three dimensional problems are, respectively:

$$M = \begin{bmatrix} 1 & 1 & \dots & 1 \\ x_1 & x_2 & \dots & x_{NIP} \\ y_1 & y_2 & \dots & y_{NIP} \\ x_1y_1 & x_2y_2 & \dots & x_{NIP}y_{NIP} \end{bmatrix} \tag{6.18}$$

$$M = \begin{bmatrix} 1 & 1 & \dots & 1 \\ x_1 & x_2 & \dots & x_{NIP} \\ y_1 & y_2 & \dots & y_{NIP} \\ z_1 & z_2 & \dots & z_{NIP} \\ x_1y_1 & x_2y_2 & \dots & x_{NIP}y_{NIP} \\ y_1z_1 & y_2z_2 & \dots & y_{NIP}z_{NIP} \\ z_1x_1 & z_2x_2 & \dots & z_{NIP}x_{NIP} \end{bmatrix} \tag{6.19}$$

Multiplying both sides of Eq. (6.17) by M, one obtains:

$$M\Lambda = Ha \tag{6.20}$$

where $H = MM^T$ is a symmetrical square matrix which has the following form for two and three dimensional cases, respectively:

$$H = \sum_{i=1}^{NIP} \begin{bmatrix} 1 & x_i & y_i & x_iy_i \\ x_i & x_i^2 & x_iy_i & x_i^2y_i \\ y_i & x_iy_i & y_i^2 & x_iy_i^2 \\ x_iy_i & x_i^2y_i & x_iy_i^2 & x_i^2y_i^2 \end{bmatrix} \tag{6.21}$$

$$H = \sum_{i=1}^{NIP} \begin{bmatrix} 1 & x_i & y_i & z_i & x_iy_i & y_iz_i & z_ix_i \\ x_i & x_i^2 & y_ix_i & z_ix_i & x_i^2y_i & y_iz_ix_i & z_ix_i^2 \\ y_i & x_iy_i & y_i^2 & z_iy_i & x_iy_i^2 & y_i^2z_i & z_ix_iy_i \\ z_i & x_iz_i & y_iz_i & z_i^2 & x_iy_iz_i & y_iz_i^2 & z_i^2x_i \\ x_iy_i & x_i^2y_i & x_iy_i^2 & z_ix_iy_i & x_i^2y_i^2 & x_iy_i^2z_i & x_i^2y_iz_i \\ y_iz_i & x_iy_iz_i & y_i^2z_i & y_iz_i^2 & x_iy_i^2z_i & y_i^2z_i^2 & x_iy_iz_i^2 \\ z_ix_i & z_ix_i^2 & y_iz_ix_i & z_i^2x_i & x_i^2y_iz_i & x_iy_iz_i^2 & z_i^2x_i^2 \end{bmatrix} \tag{6.22}$$

For small deformations, changes in coordinates of nodal integration points are assumed to be small. Hence, H can be considered constant and needs to be calculated only at the beginning of the analysis. However, for large deformations, the changes in coordinates become significant and the matrix H will need to be obtained and updated at each time increment step.

Equation (6.20) can be rewritten as:

$$M\Lambda = \bar{v} \tag{6.23}$$

where for two dimensions case:

$$\bar{v} = \begin{Bmatrix} \sum_{i=1}^{NIP} d\lambda_i \\ \sum_{i=1}^{NIP} d\lambda_i x_i \\ \sum_{i=1}^{NIP} d\lambda_i y_i \\ \sum_{i=1}^{NIP} d\lambda_i x_i y_i \end{Bmatrix} \tag{6.24}$$

and for three dimensions case:

$$\bar{v} = \begin{Bmatrix} \sum_{i=1}^{NIP} d\lambda_i \\ \sum_{i=1}^{NIP} d\lambda_i x_i \\ \sum_{i=1}^{NIP} d\lambda_i y_i \\ \sum_{i=1}^{NIP} d\lambda_i z_i \\ \sum_{i=1}^{NIP} d\lambda_i x_i y_i \\ \sum_{i=1}^{NIP} d\lambda_i y_i z_i \\ \sum_{i=1}^{NIP} d\lambda_i z_i x_i \end{Bmatrix} \tag{6.25}$$

Using Eq. (6.20) and (6.23) in (6.16) one obtains:

$$d\lambda = (H^{-1}\bar{v})^T v \tag{6.26}$$

and the constants vector becomes:

$$a = H^{-1}\bar{v} \tag{6.27}$$

One can then compute the plastic multiplier gradients as follows:

$$\nabla d\lambda = \begin{cases} (a^T v)_{,x} i + (a^T v)_{,y} j & For\ 2D \\ (a^T v)_{,x} i + (a^T v)_{,y} j + (a^T v)_{,z} k & For\ 3D \end{cases} \tag{6.28}$$

$$\|\nabla d\lambda\| = \begin{cases} \sqrt{\left[(a^T v)_{,x}\right]^2 + \left[(a^T v)_{,y}\right]^2} & For\ 2D \\ \sqrt{\left[(a^T v)_{,x}\right]^2 + \left[(a^T v)_{,y}\right]^2 + \left[(a^T v)_{,z}\right]^2} & For\ 3D \end{cases} \tag{6.29}$$

$$\nabla^2 d\lambda = \begin{cases} (a^T v)_{,xx} + (a^T v)_{,yy} & For\ 2D \\ (a^T v)_{,xx} + (a^T v)_{,yy} + (a^T v)_{,zz} & For\ 3D \end{cases} \tag{6.30}$$

where the subscript "," represents the partial derivative in the specified direction.

It is clear that the gradients depend on the coordinates of the Gaussian integration points as well as their plastic multipliers. This is a simple, easy and robust procedure that will be used in the next chapter to analyze different two

and three dimensional problems of deformation localization, including adiabatic shear banding.

CHAPTER 7: NUMERICAL ANALYSIS AND DISCUSSION

Although the physical phenomenon of adiabatic shear bands may have been known for at least three decades or more, the precise observation and measurement of such physical process had not been obtained until late 1980's. However, many of the theoretical analyses as well as numerical simulations failed to predict the experimental outcome of such deformation, and in general dynamic shear band propagation has remained to be elusive to numerical simulations. Different published simulation results such as Batra and Gummalla (2000) and Needleman and Tvergaard (2000) have not been able to capture the physical process of dynamic shear band propagation.

Batra and Kim (1990) used Marchand and Duffy's (1988) test data on the torsion of a HY-100 steel thin-walled tube deformed at a nominal strain-rate of 3300/s to calibrate five viscoplastic relations, namely the Litonski (1977), Wright and Batra (1985), Bodner and Partom (1975), Johnson and Cook (1983) and the power law (e.g. see Klopp et al., 1985). They determined the values of material parameters by solving an initial boundary-value problem simulating simple-shearing deformations of homogeneous and isotropic thermo-viscoplastic body. These five constitutive relations were used to analyze the initiation and development of a shear band in a block of the same material deformed in simple shear at a nominal strain-rate of 1600/s. They found that the five constitutive relations gave essentially similar time-histories of the evolution of the shear stress, shear strain, temperature and strain-rate till the initiation of a shear band. However, the post localization response predicted by these constitutive relations was quite different; these and results of other numerical investigations are summarized in Batra (1998). For steady-state deformations, Wright (1987) showed that these constitutive relations predict virtually the same response. Batra and Chen (2001) investigated thermomechanical deformations of a steel block deformed in simple shear and modeled the thermoviscoplastic response of the material by four different relations, where the dependence upon the nominal strain-rate of the critical strain, the average strain at which a shear band initiates, the nominal strain corresponding to the shear band spacing and the width of a shear band formed in a HY-100 steel block which is deformed in simple shear were addressed. The models are by Wright–Batra, Johnson–Cook, Bodner–Partom and a power law relation. It is found that the qualitative responses predicted by all the models were the same except for the Bodner–Partom relation. This indicates that the qualitative results of any simulation highly depend on the selection of the model used in the analysis.

Li et al. (2002) carried out two and three dimensional mesh free Galerkin simulation of adiabatic shear bands in pre-notched plate under impact load. They were able to capture the details of the adiabatic shear band to a point where the periodic temperature profile inside shear band at the microscale can clearly be seen. The simulation also showed an intense high strain rate region in front of the shear band tip, which they believe is caused by wave trapping at the shear

band tip. They suggested that this might be the main reason of damage and stress collapse inside the shear band and provides a key link for self-sustained instability. Baucom and Zikry (1999) conducted a perturbation analysis on material instabilities and adiabatic shear bands under high strain rate load conditions. They were able to characterize the material instabilities beyond the initial instability point, and then it was possible to monitor the strength of this material instability throughout the deformation history to distinguish between material instabilities and shear strain localization. Zhu and Batra (1990) studied the problem of plain strain thermomechanical deformations in viscoplastic body that contains a rigid ellipsoidal inclusion at the center, subjected to high strain rate. The rigid inclusion can act as a second phase particle such as oxides or carbides in steel, and can act as a nucleus for the shear band. The results showed that the shear band initiates near the tip of the inclusion and propagates along a line inclined 45º with respect to the horizontal axis. The effective stress near the inclusion tip drops noticeably near the tip of the inclusion and as the band propagates along the 45° direction the shear stress drops also. This was followed somewhat later by a sharp increase in the maximum principal logarithmic strain at the same point. Brun et al. (2003) utilized the boundary element method to analyze the incremental elastic deformations resulting from a given homogeneous strain. Shear bands are analyzed as special case of bifurcations of elastic structures. This special case where shear bands may occur as the first possible bifurcation is the so-called "van Hove condition", in which the solid is subjected to prescribed displacements over the entire boundary and the current state (deformation and stress) is homogeneous. Batra and Wang (1994) studied the finite dynamic plane strain thermomechanical deformations of a thermally softening viscoplastic body of square cross-section subjected to combined compression and shear at high strain-rate. Different ratios of the compressive to shear loadings were applied. A material thermal defect in the body was entered into the analysis by adding a temperature bump centered at the centroid of the cross-section, while the rest of the body is under uniform initial temperature distribution. This higher temperature at the centroid softens the material there and causes more deformation at that area. These higher deformations around the centroid of the cross-section heat it up more and the temperature there rises faster than the rest of the body, and eventually instability initiates at the centroid and propagates to one edge in the direction of maximum shearing.

Kim and Batra (1992) also investigated thermomechanical deformations of a thermally softening viscoplastic block undergoing overall adiabatic simple shearing deformations. The analysis accounted for the dependence of the specific heat, thermal conductivity and shear modulus of the material on the temperature. To ensure the formation of an ASB, a geometric defect in the form of smoothly variable thickness was suggested. It was found that due to a higher initial temperature in the specimen, a delay in the initiation of the shear bands occurred, and the width of the bands was wider. Another numerical approach for studying thermo-visco-plastic deformation was developed by Zhou et al. (2006).

They were able to simulate fully localized plastic flow with high resolution and good efficiency. This was applied to ASBs where the interactions between a single shear band and its surroundings and between shear bands themselves was taken into account. The study showed that a shear band may grow intermittently because of the interactions with other bands. They suggest that this method is specifically adequate for investigating the self-organized multiple ASBs. Edwards et al. (2005) developed a model for quantifying shear band propagation in bulk metallic glasses. The stress, temperature, and band propagation speed were implemented in the model. The model quantifies the shear-band length, width, and speed, as well as the direction of propagation and the magnitude of displacement across the band. Feng and Bassim (1999) modeled the formation of ASB in AISI 4340 steel using the finite element method. Both strain hardening and thermal softening were considered in the modeling during initialization and growth of the shear band. The obtained results show that the ASB could initialize at material defects. The stress evolution for the ASB was roughly divided into three stages. In the first stage, the stress resistance stays constant which indicates the absence of any plastic deformation. It then increases to some extent due to strain hardening effect. Finally a significant decrease occurs where thermal softening dominates. The growth of the ASB was affected by the strain hardening, thermal softening and thermal conduction. They state that "without thermal conduction, it appears impossible to increase the width of the ASB."

Localization is not always due to material inhomogeneities. For example, in a homogeneous material, localization may occur due to deformation gradients. In this work, explicit finite element analysis will be used to solve different problems of adiabatic shear banding. These examples include adiabatic shear bands due to material inhomogeneities as well as due to deformation gradients. The constitutive model proposed in Chapter 3 is implemented along with the gradient formulation described in Chapters 5 and 6 in a FORTRAN user subroutine. Abaqus/Explicit 6.4 is used for this purpose. The problems are: shear localization in two dimensional plate subjected to velocity boundary conditions, penetration of steel circular plate, and impact of steel beam by a rigid solid block. Each model is independent of the others and specific parameters will be studied as will be described next.

7.1 Two Dimensional Plate Subjected to Velocity Boundary Conditions

This example is introduced to show the potential of the gradient theory in regularizing the finite element results. A two dimensional plate is subjected to velocity boundary conditions at the upper edge as shown in Figure 7.1, while the bottom one is fixed. The forces per unit area at both sides of the specimen are set to zero. Their horizontal displacements are assumed to be small and neglected all along the boundaries. To initiate a shear band in the mesh, an area in the bottom left-hand corner of the sample is assigned 10% lower yield strength

than the rest of the mesh. This imperfect area is normalized to be 1/10 of the base length, so it is the same for each mesh.

Three meshes with 15×30, 30×60, and 45×90 four-noded elements with 2×2 integration points (full integration) are analyzed. The dimensions of the plates are $H = 0.6\,m$, $W = 0.3\,m$, and the material properties are Young's modulus $E = 200\,GPa$, and the Poisson's ratio $\nu = 0.35$. Material parameters are also taken from Chapter 3 while the gradient parameters are taken from Chapter 5.

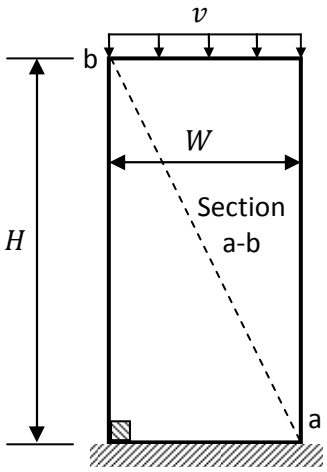

Figure 7.1: Finite element configuration for two dimensional plate under velocity boundary conditions.

The deformed shapes of the different meshes are plotted in Figure 7.2. The local mesh-dependent analysis that does not include the gradient theory shows high mesh sensitivity in Figure 7.2-(a). The deformation is noticed to increase where the plate is more compressed and the shear band is more localized when the mesh is refined. This localization is highly concentrated near the inhomogeneity which indicates high mesh sensitivity. However, this sensitivity is eliminated in the nonlocal gradient theory analysis as shown in Figure 7.2-(b). The deformation shape and magnitude are almost the same in the three meshes. Also the shear band width is similar in the meshes, indicating that the gradient formulation is successful in reducing any mesh dependency.

In addition to the deformed shape, the equivalent plastic strain contours is illustrated in Figure 7.3 for the local analysis and in Figure 7.4 for the nonlocal analysis. The contour of equivalent plastic strain for the local analysis is mesh-dependent which is expected since deformation is seen to be mesh-dependent. For the nonlocal analysis, the shear band width seems to be independent of the element size and has a unique width. A profile of the equivalent plastic strain across section a-b (see Figure 7.1) is shown in Figure 7.5. The equivalent plastic strain for local analysis is increased with refining of the mesh which means more

strain localization occurs. On the other hand, the difference between the results of nonlocal equivalent plastic strain in the three meshes is much less than that of the local one, due to the regularizing effect of the gradient theory.

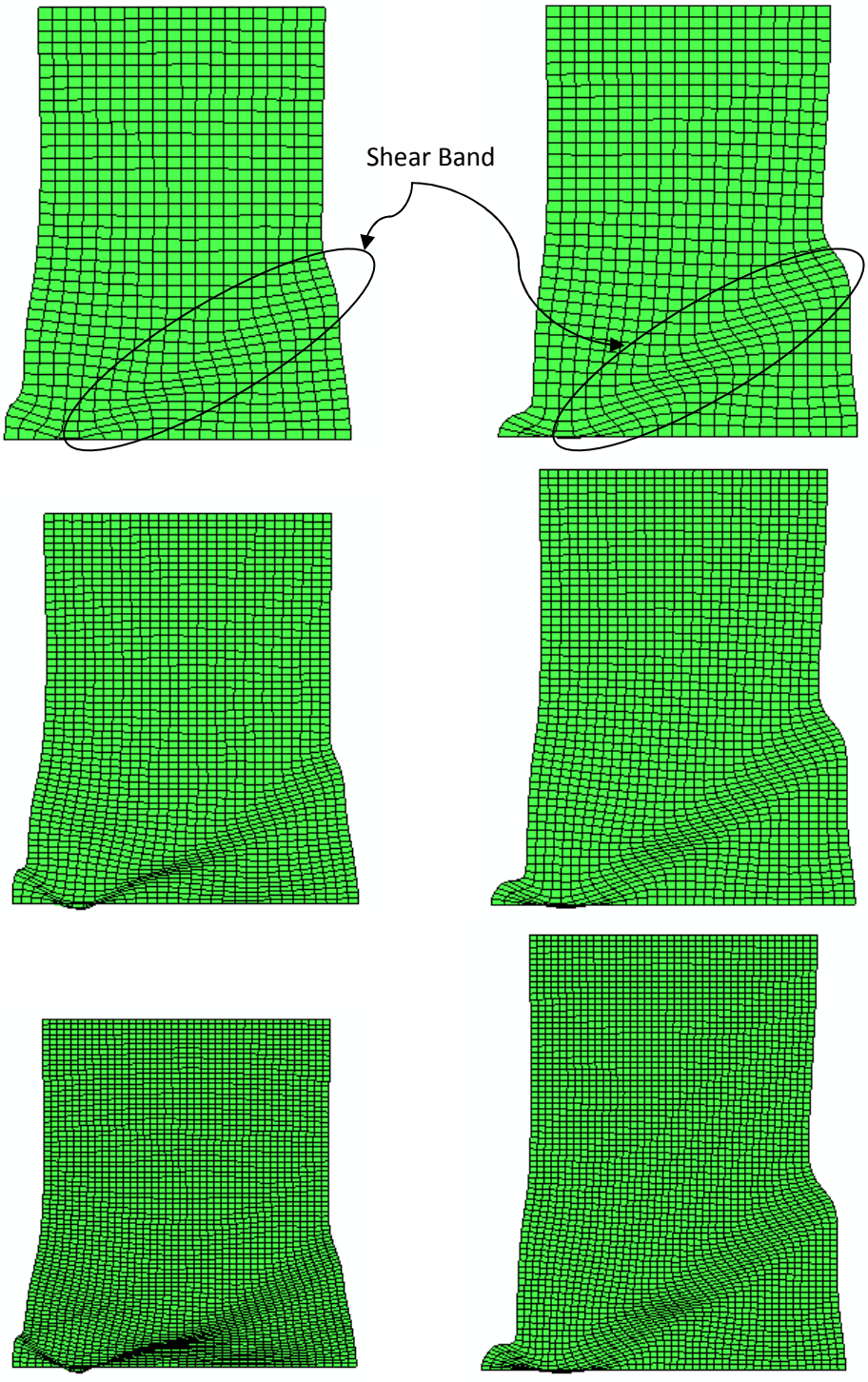

Figure 7.2: Deformed shape of steel plate with consecutively refined mesh using (a) local mesh-dependent analysis and (b) nonlocal mesh-independent analysis.

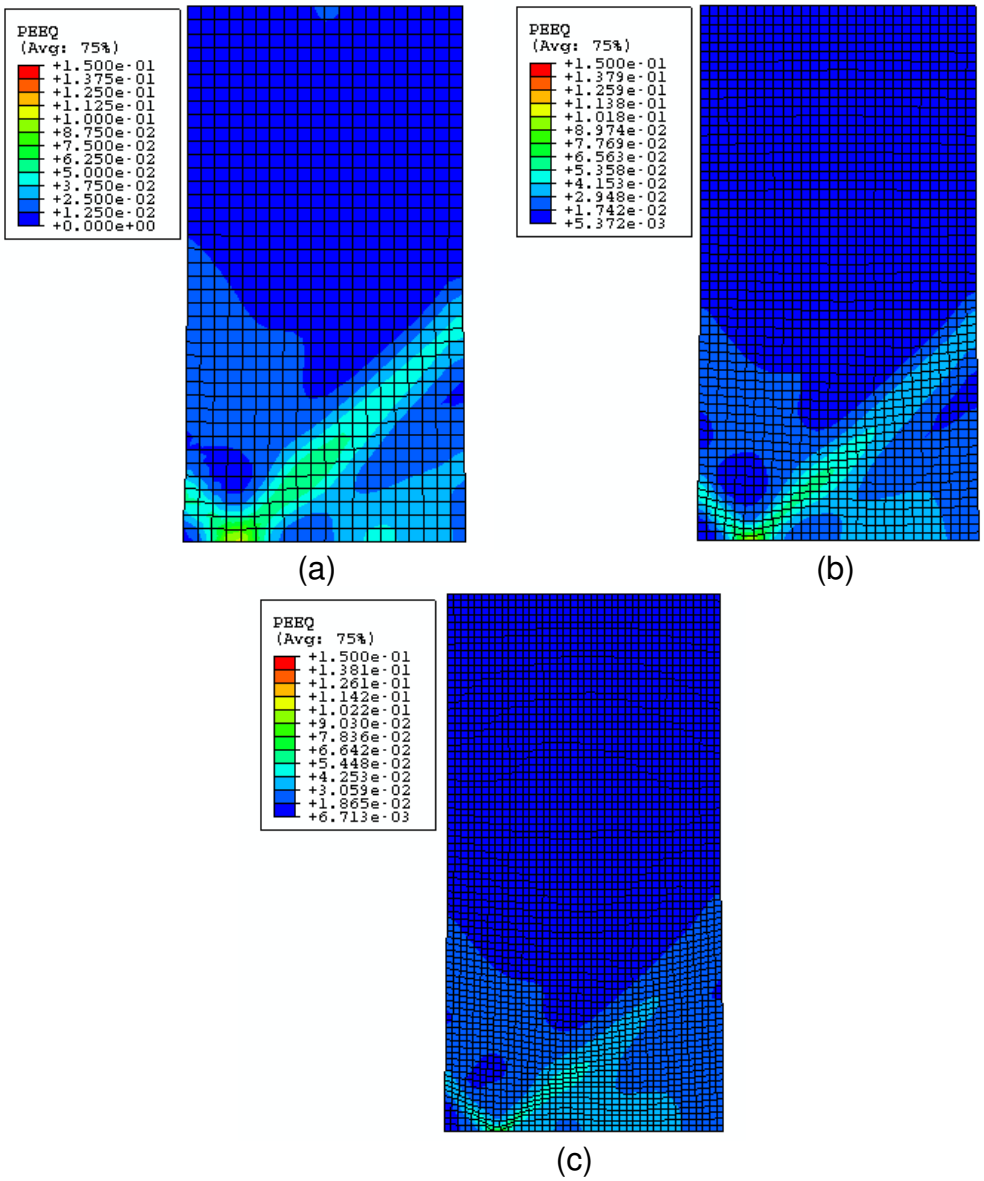

Figure 7.3: Equivalent plastic strain contours under local mesh-dependent analysis for (a) course, (b) medium, and (c) fine meshes.

This example and its associated results prove the applicability of the gradient theory and the ability of this approach to reduce and even eliminate mesh dependencies. Therefore, one does not need a very fine mesh to simulate deformation localization problem, and a reasonably fine finite element mesh can be used instead as will be shown in the next example.

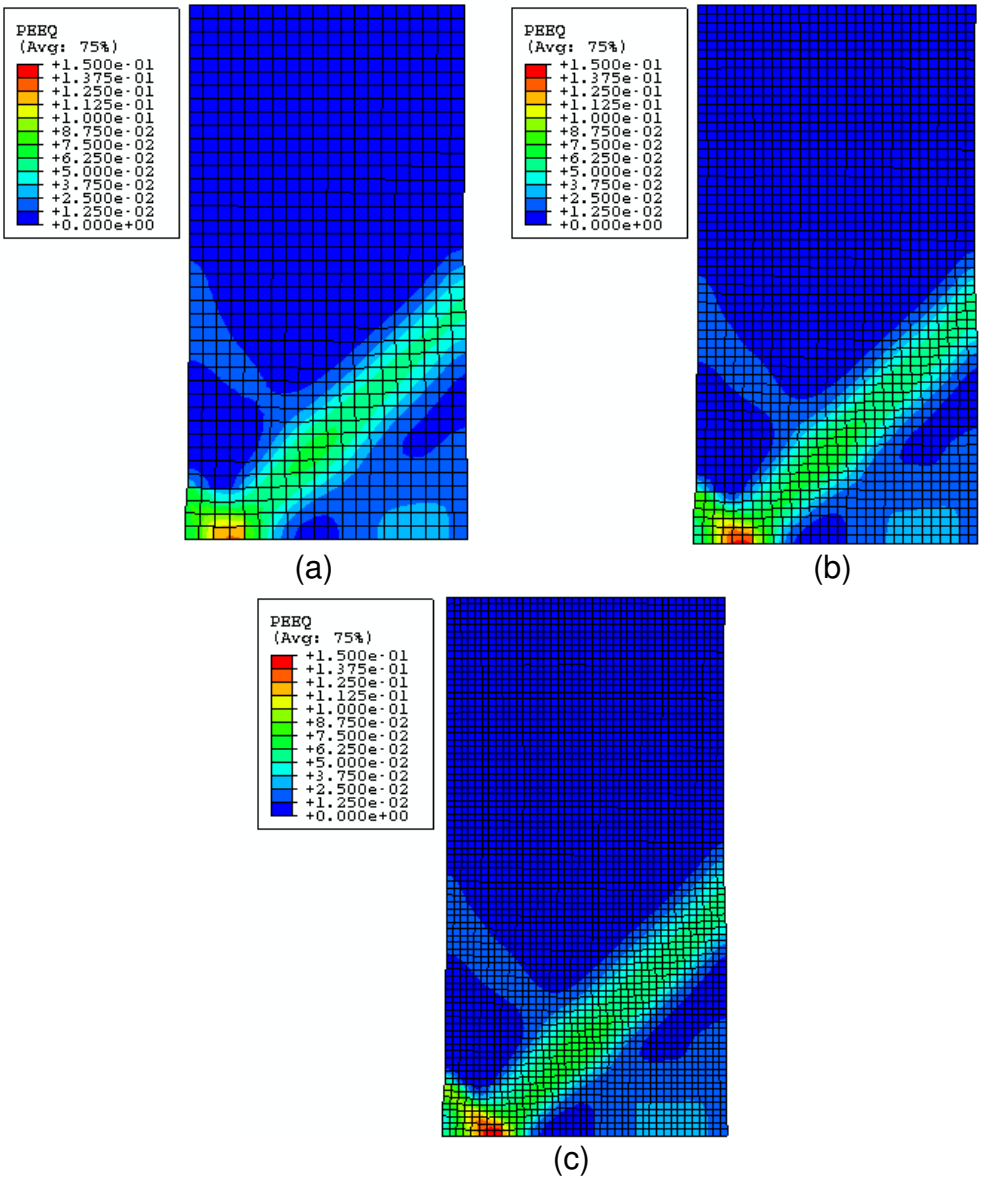

Figure 7.4: Equivalent plastic strain contours under nonlocal mesh-independent analysis for (a) course, (b) medium, and (c) fine meshes.

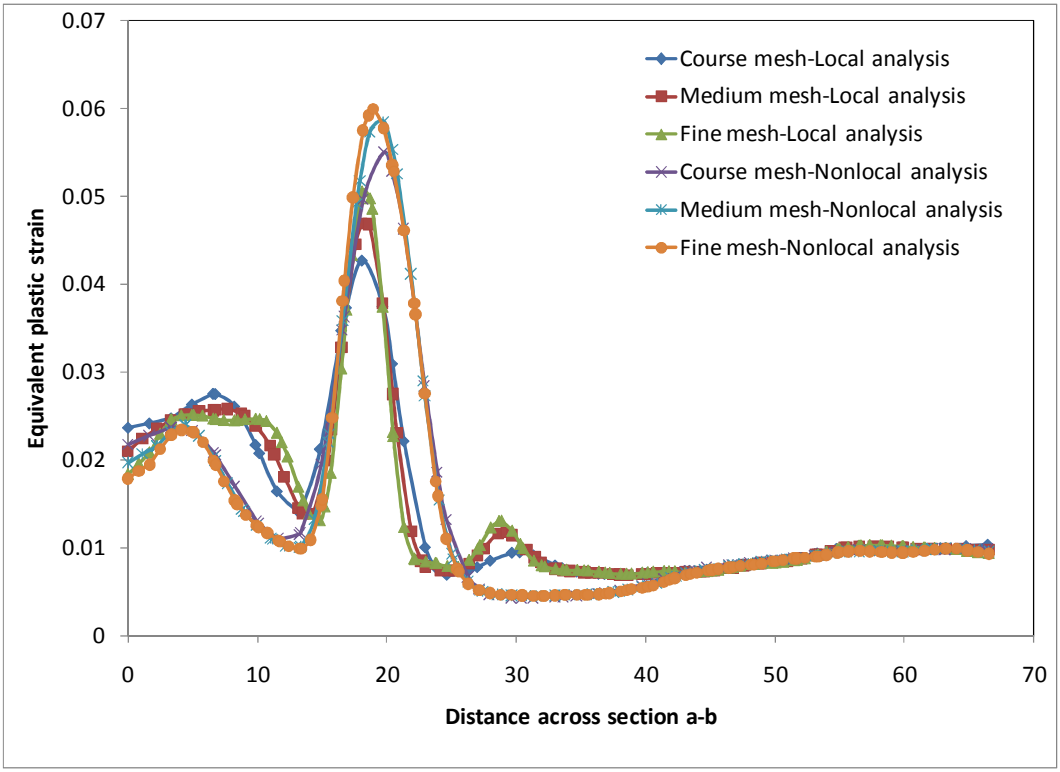

Figure 7.5: Equivalent plastic strain profile across section a-b in the CR-1018 steel plate.

7.2 Plate Punch Problem

Failure in a punch test is often a mixture of shear localization and macrocracking (Bai and Dodd, 1992). Thus, the process is not easy to analyze. Furthermore, no visual records of the deformation and failure during the test can be taken experimentally since fracture occurs on internal, hidden surfaces. Therefore, finite element modeling of the punch test is carried out in conjunction with the experimental tests to allow for greater understanding of the internal deformation. The occurrence of adiabatic shear localization in punching operations as well as the effects of shear localization on punching load and energy are discussed in terms of experimental evidence and numerical models.

Many experimental studies have been reported on punching and blanking operations mainly due to simplicity of the procedure and its importance in the manufacturing industry. Slater and Johnson (1967) conducted punch tests on copper and mild steel and examined the energy required to punch through the two metals. Johnson and Travis (1965) performed similar tests on copper discs using an industrial stud driver. Punch energy measurements have also been reported by Davies and Dhawan (1965), Daneshi and Harding (1974), and Dowling et al. (1970) on a variety of ferrous and non-ferrous metals. Zurek (1994) conducted punch impact experiments on 4340 pearlitic steel to examine the plastic instabilities that can occur.

Among these authors, there seems to be some disagreement on the amount of energy needed to produce a plug as punch speed increases. Many tests show the energy increases with loading rate, while others show the exact opposite behavior. This inconsistency was noted and explained by Rogers (1979). In his review, he references work done by Stock and Wingrove (1971) who found that for low carbon steels energy absorption increased, but for higher carbon steels, punching energy reached a maximum at 10 m/s punch speed and then dropped below quasistatic levels at 14 m/s. A change in failure from a tensile fracture mode to a shear dominated one was present. This failure mode transition is presumably responsible for the drop in punching energy in these tests. However, few investigations have attempted to clearly verify this conclusion experimentally. Furthermore, few, if any, numerical analyses of shear localization in punching and blanking operations have appeared. Much understanding of the role of shear localization in this economically important process is to be gained from such complementary experimental and numerical studies.

Roessig and Mason (1999a) conducted an experimental investigation which examines the failure modes of 1018 steel, 6061-T6 aluminum alloy, and titanium 6%Al±4%V alloy (Ti6Al4V) in a series of punch tests with varying punch/die clearances at average strain rates ranging from 10^{-3} to $10^{4}/sec$, using a servo-hydraulic compression machine, a mechanical press, and a Hopkinson bar apparatus. These materials were chosen because of their widespread use in industry and the wide variety in material properties. Roessig and Mason (1999b) also examined the failure in the punch test using numerical modeling. Both experimental and numerical results are used here to verify the model proposed earlier in Chapter 3 for CR-1018 steel.

Three separate testing methods are used to determine load displacement curves at a range of nominal average strain rates from 10^{-3} to $10^{4}/sec$. Though the average strain rates do not seem very high, concentrations within the specimen can lead to very high strain rates locally. The specimens in each test are the same. Square plates 3mm thick are made from CR-1018 Steel Alloy. However, the insert (see Figure 7.6) is circular in cross section, and hence the finite element model will be a circular plate. The mild steel was tested in the mill annealed condition. The punch/die configuration in the Hopkinson bar apparatus is shown simplified in Figure 7.6. The bar is made of 4340 steel hardened to HRC 45. The bar was ground to a diameter of 30mm and straightened to within 0.1mm using a centerless grinding technique. The clearance in the system is defined as the difference between the inner diameter of the insert and the outer diameter of the punch. By placing different inserts with different inner diameters in the die, different clearances between the punch and insert can be used. The clearances could be varied from 1.6 to 50 mm, but only the 1.6 and 3.2mm cases are reported here as they are found to be the most interesting in terms of failure by shear localization. Velocities of the bar were limited to those that would keep stresses at impact below the yield strength of the bar. Through elastodynamics

the maximum allowable velocity can be calculated to be 30 m/s allowing for a small margin of safety. For the competition between bending and shear failures to occur, higher clearance to thickness ratios, $w = h$, are required. From the geometrical data written above, $w = h$ values for the two clearances are ½ and 1.0, respectively. The die and cover plate were made of mild steel, while the punch and inserts were made of 4340 steel hardened to 45 on the Rockwell C scale. Tests were performed quasistatically, at low velocity of 1m/sec and high velocity of 14m/s.

Average strain rates in the specimen can be in terms of the punch velocity, V_P, and radial clearance, w (Zurek, 1994). The definition of shear strain in the specimen is:

$$\varepsilon_{rz} = \frac{1}{2}\left(\frac{\partial u}{\partial z} + \frac{\partial v}{\partial r}\right) \tag{7.1}$$

where u and v are displacements in the in the r and z directions, respectively. In the punch test, $\partial v/\partial r = u/w$ and $\partial u/\partial z = 0$, therefore:

$$\varepsilon_{rz} = \frac{1}{2}\frac{\Delta u}{w} \tag{7.2}$$

and the average shear strain rate becomes:

$$\dot{\varepsilon}_{rz} = \frac{1}{2}\frac{V_P}{w} \tag{7.3}$$

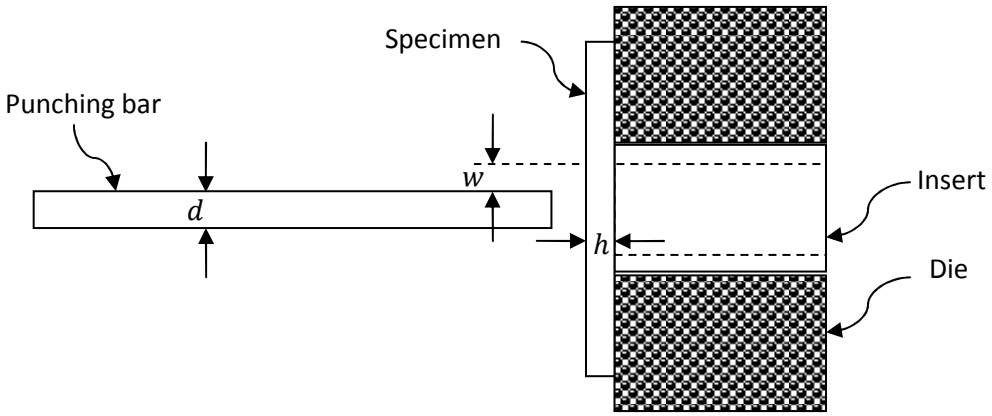

Figure 7.6: Schematic drawing of the punch loading Hopkinson bar apparatus.

Due to the symmetry of the problem, the plate is modeled through half plate finite element model with appropriate boundary conditions as shown in Figure 7.7. Infinite elements (gray elements in Figure 7.7) are used to represent the extension of the plate in that direction. The punching bar mass is 4.2 kg, represented as a rigid body cylinder and assumed not to suffer any deformation.

It is worth mentioning that the rigid body cylinder is not perfectly symmetric, where it is slightly skewed in order to simulate realistic experimental results. This will cause very small asymmetry in the results as will be shown later. The deformation of the 3.2 mm thick plate at punching velocity of 14.25 m/s at different time frames is illustrated in Figure 7.8. The punching bar penetrates the plate totally at around t = 180μs. The infinite elements allow more realistic simulation of the plate where it permits the sides of the plate to rotate with deformation.

Figures 7.9 and 7.10 show the equivalent plastic strain at the shear band area of 3.2 mm and 1.6 mm thick plate, respectively, at a punching velocity of 14.25 m/s. The shear band become clear at about t = 80 μs for the 3.2 mm plate, while it is delayed to about t = 120 μs for the 1.6 mm one. This means that the shear strain concentrates earlier in thicker plates. For the thick plate (3.2 mm), stress concentration takes place at two positions: at the upper surface of the plate under the punch and at the lower surface of the plate above the support. The values of the two concentrations are close to each other. These two points of strain localization will try to propagate toward each other at about t = 120μs. However, a new stress concentration area appears at the lower surface of the plate exactly under the punch. This new concentration point will connect to the one at the upper surface of the plate forming a fully developed shear band as shown in Figure 7.9c at approximately t = 160μs, until the total failure occurs at t = 180μs. In the case of 1.6 mm plate, the stress concentration at the support is relatively small compared to the one under the punch. The main reason for that is the relatively high ratio of the clearance between the punch and the support to the plate thickness. A full vertical shear band forms directly below the punch at about t = 120μs, which is earlier than in the case of the 3.2 mm plate. The total failure happens at almost the same time for the thick plate at approximately t = 180μs. it is noticed that the bending effect is large in the 1.6 mm plate where the elements above the support are largely rotated compared to the elements in the 3.2 mm plate. This is again due to the high clearance to thickness ratio in the thin plate.

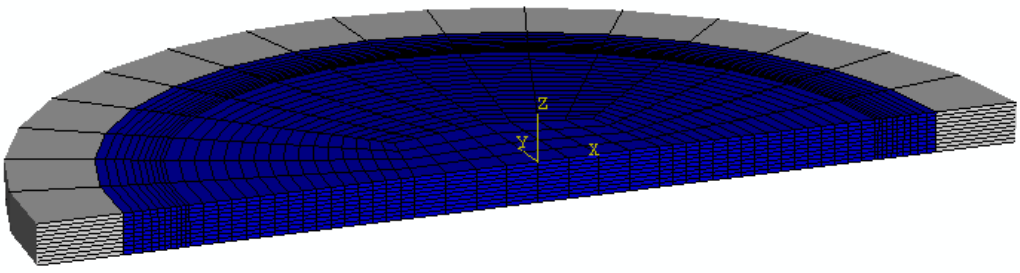

Figure 7.7: Typical finite element mesh of half plate.

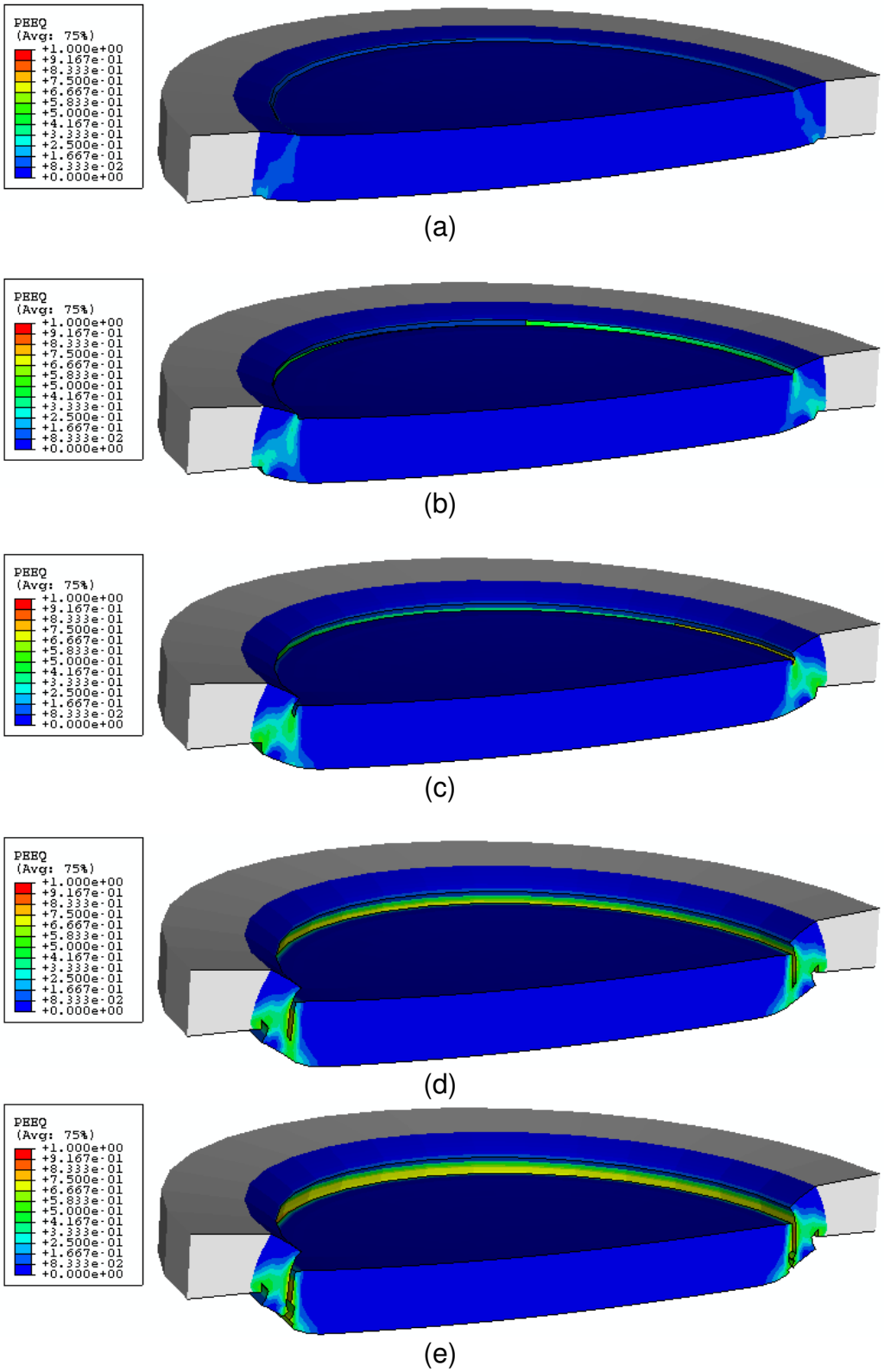

Figure 7.8: Deformed 3.2 mm thick plate due to an impact velocity of 14.25 m/s at (a) t = 40μs (b) t = 80μs (c) t = 120μs (d) t = 160μs (e) t = 180μs

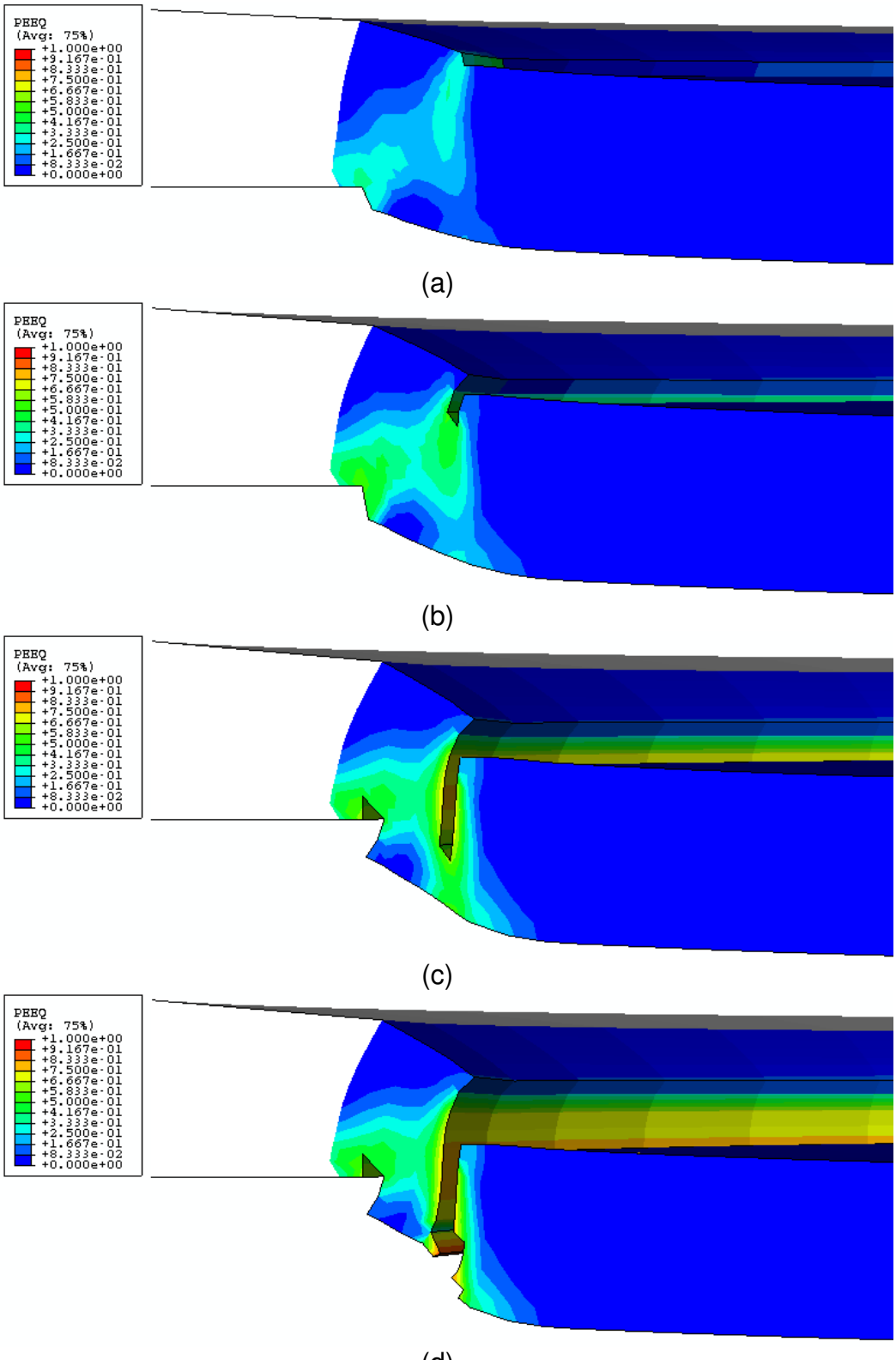

Figure 7.9: Equivalent plastic strain of 3.2 mm thick plate due to an impact velocity of 14.25 m/s at (a) t = 80μs (b) t = 120μs (c) t = 160μs (d) t = 180μs

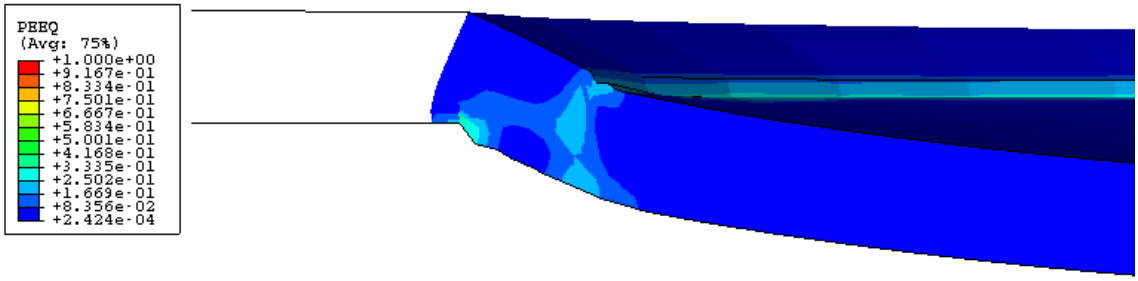

(a)

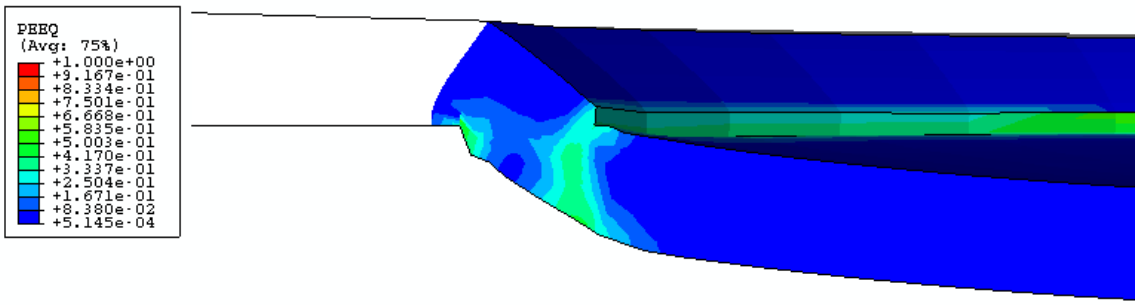

(b)

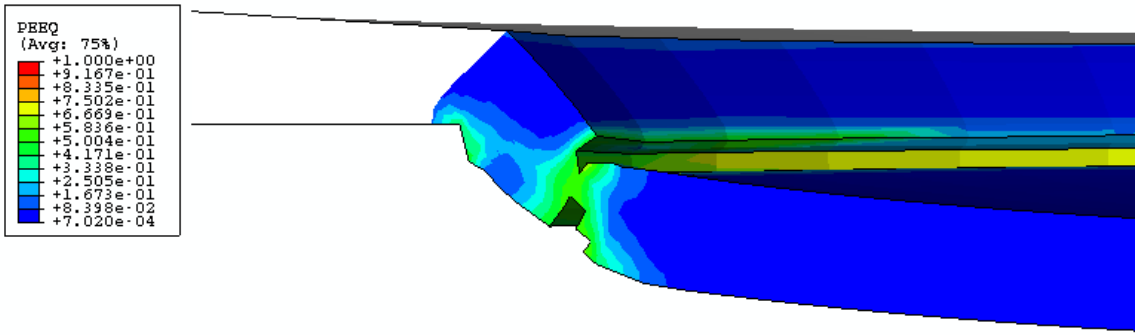

(c)

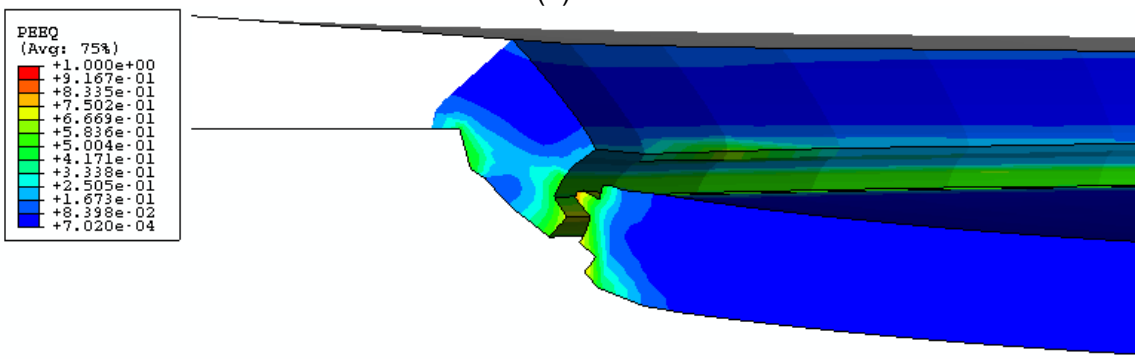

(d)

Figure 7.10: Equivalent plastic strain of 1.6 mm thick plate due to an impact velocity of 14.25 m/s at (a) t = 80μs (b) t = 120μs (c) t = 160μs (d) t = 180μs

Figure 7.11 and 7.12 show the von Mises stress for the 3.2 mm and 1.6 mm thick plates, respectively, under impact velocity of 14.25 m/s. For both thicknesses, the stresses distribution away from the shear band area shows domination for bending stresses, where the upper and lower surfaces of the plate possess higher stresses than at the neutral axis of the plate, although the neutral axis for the 1.6 mm plate is shifted to the top of the plate as can be seen in Figure 7.12a. In the thick plate, the propagation of the shear band from the top surface to the bottom surface causes stress release at the top surface of the plate as shown in Figure 7.11c. On the other hand, in the thin plate the shear band initiates and propagates from both surfaces of the plate and causes stresses to stay at both sides of the plate. This behavior is absent at the shear band area since shear stresses are the dominant one, where shear stresses, roughly, are in the order of 500 MPa compared to bending stresses that are in the order of 400 MPa for both plates.

The load versus displacement of the steel plates along with experimental results by Roessig and Mason (1999a) are plotted in Figure 7.13. The load is obtained from the pressure distribution at the top surface of the steel plate, and the displacement is taken at the center of the bottom surface. Numerical analysis prediction of the 3.2 mm plate stiffness coincides with the experimental results. However, the hardening behavior is not captured very well. Even the numerical analysis by Roessig and Mason (1999b) was unable to capture the same hardening behavior. The reason behind this could be the insufficient information about CR-1018 steel used in the experiments such as stress-strain diagrams at different temperatures and strain rates. The slope (stiffness) of the load-displacement curve for the 1.6 mm plate is seen to be approximately half the one for the 3.2 mm plate. This indicates that, unlike in the case of bending problems, the stiffness of the plate is related linearly to the plate thickness when deformation is of the shear localization type. Although the failure load of the two thicknesses are close (105 MPa for the 1.6 mm plate and 110 MPa for the 3.2 mm plate), failure displacements were not that close, with a value of approximately 2.4 mm and 1.5 mm for the 1.6 mm and 3.2 mm plates, respectively.

Kinetic energy of the punching bar is shown in Figure 7.14. For the 4.2 kg punching bar moving at a velocity of 14.25 m/s, the initial kinetic energy is 426 N.m. This energy decreases and transforms to strain energy and viscous dissipated energy which are shown in Figures 7.15 and 7.16, respectively. The decrease in kinetic energy for the 1.6 mm plate is about 45 N.m, while it is about 83 N.m for the 3.2 mm plate. Hence, doubling the thickness, roughly, will double the decrease in the kinetic energy in the case of shear band deformation. This is also true for the strain energy density stored in the body as can be seen in Figure 7.15, where it reaches to a maximum value of 0.8 MPa for the 3.2 mm plate compared to 0.4 MPa for the 1.6 mm plate. However, the viscous dissipation energy does not behave in a similar way. It increases from around 9 N.m for the

1.6 mm plate to about 11 N.m for the 3.2 mm, which means that the viscous dissipation is not linearly related to the shear band length.

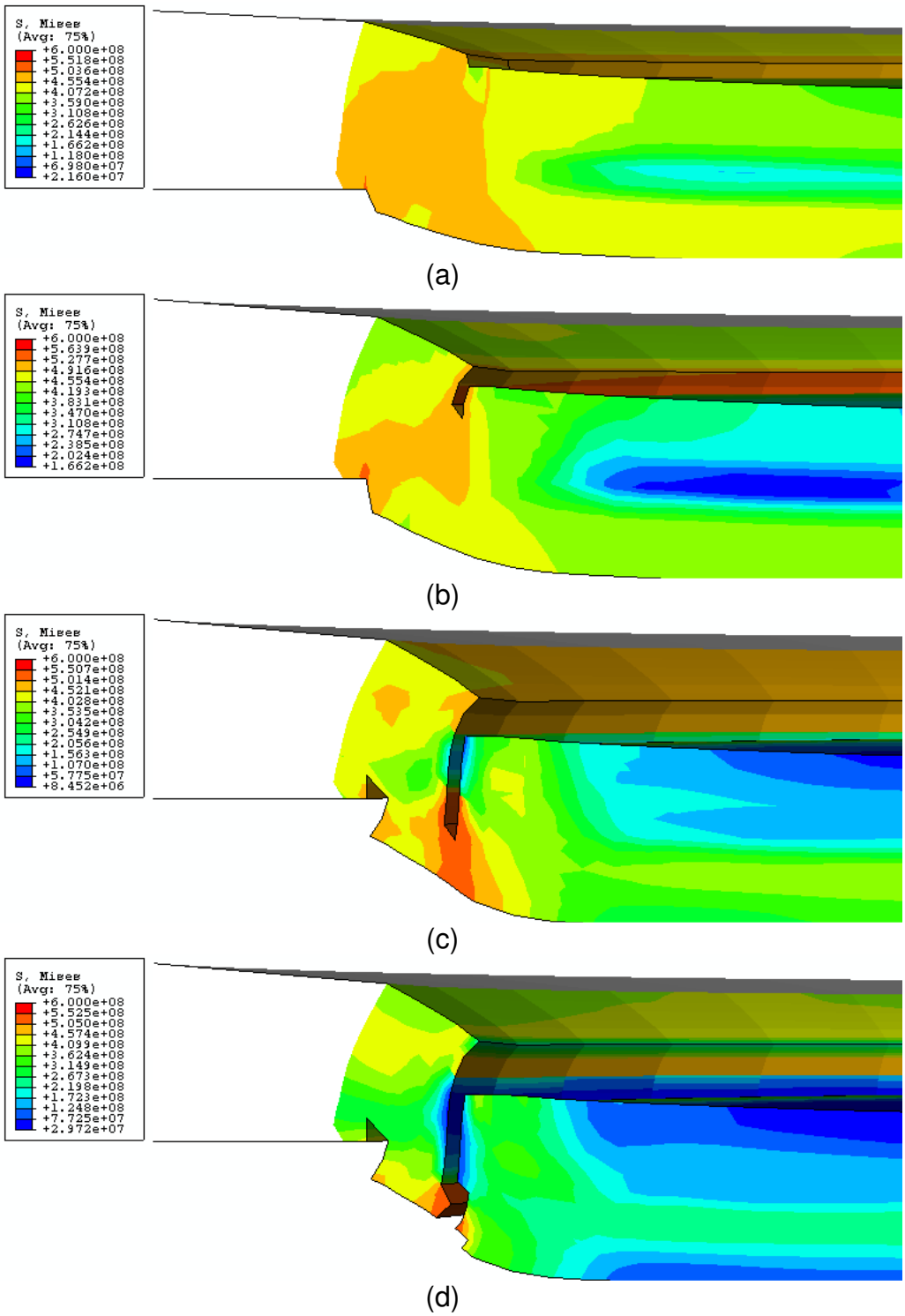

Figure 7.11: Von Mises stress of 3.2 mm thick plate due to an impact velocity of 14.25 m/s at (a) t = 80μs (b) t = 120μs (c) t = 160μs (d) t = 180μs

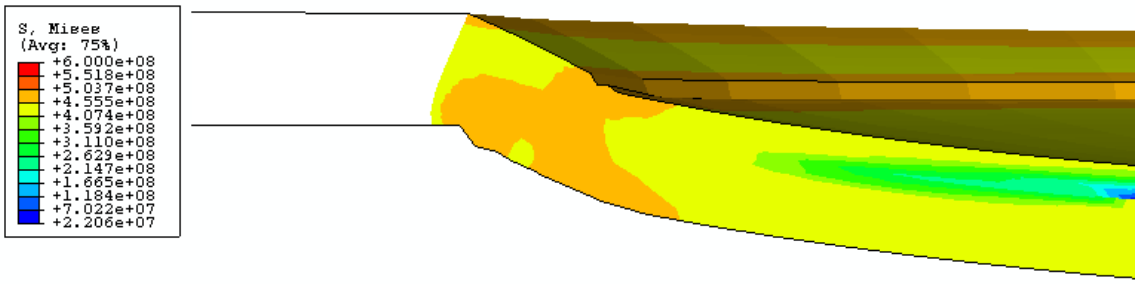

(a)

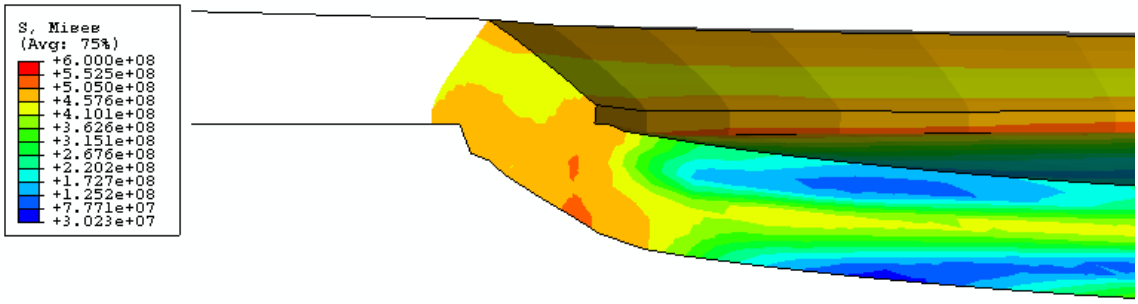

(b)

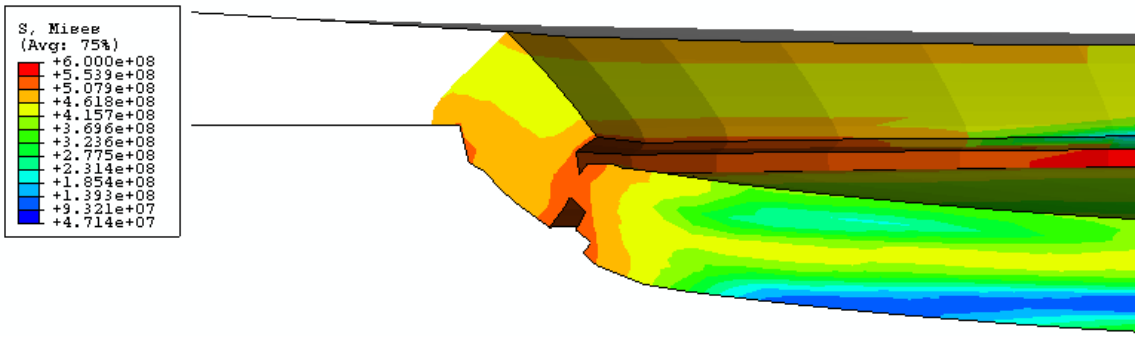

(c)

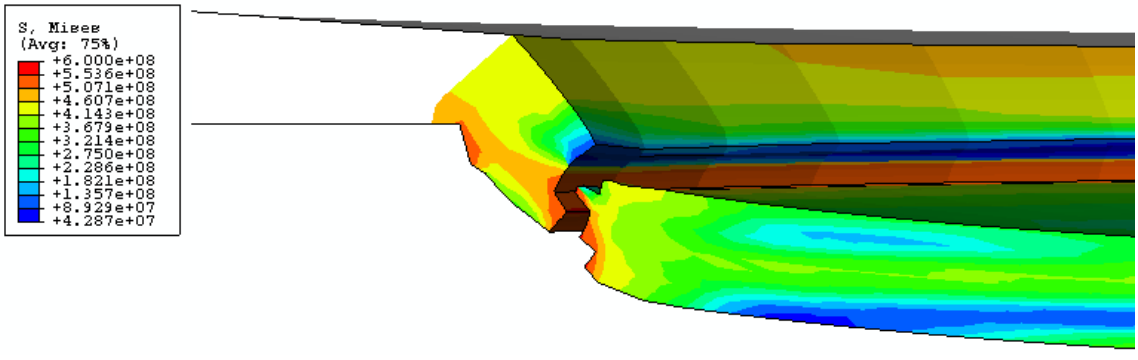

(d)

Figure 7.12: Von Mises stress of 1.6 mm thick plate due to an impact velocity of 14.25 m/s at (a) t = 80μs (b) t = 120μs (c) t = 160μs (d) t = 180μs

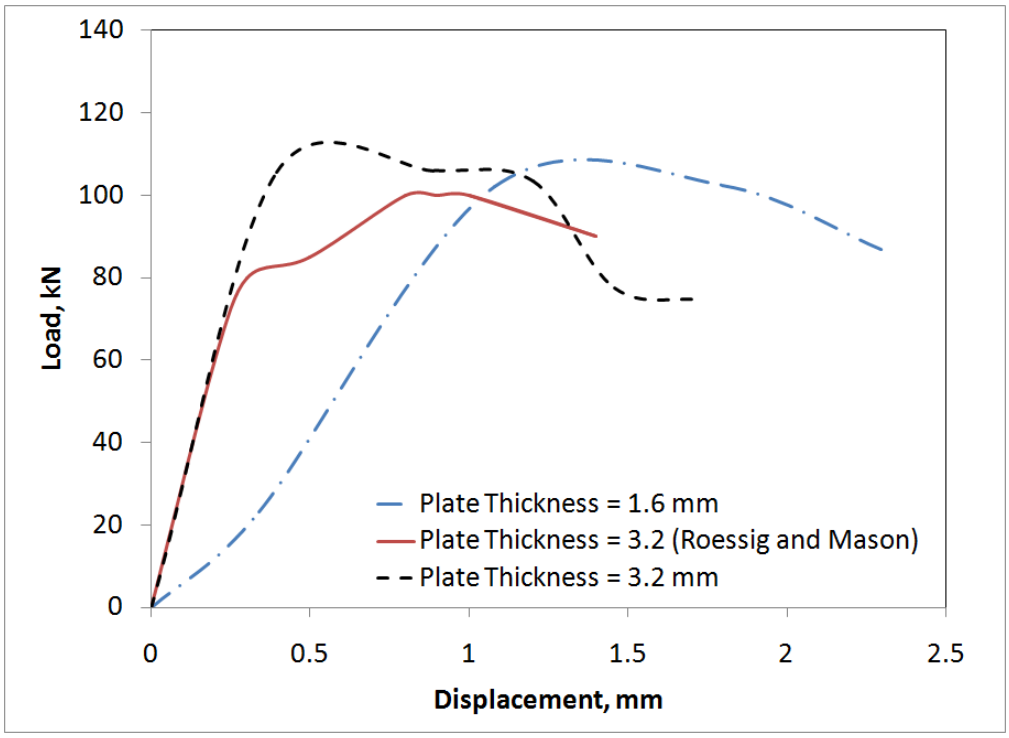

Figure 7.13: Load versus displacement of CR-1018 steel plate due to an impact velocity of 14.25 m/s.

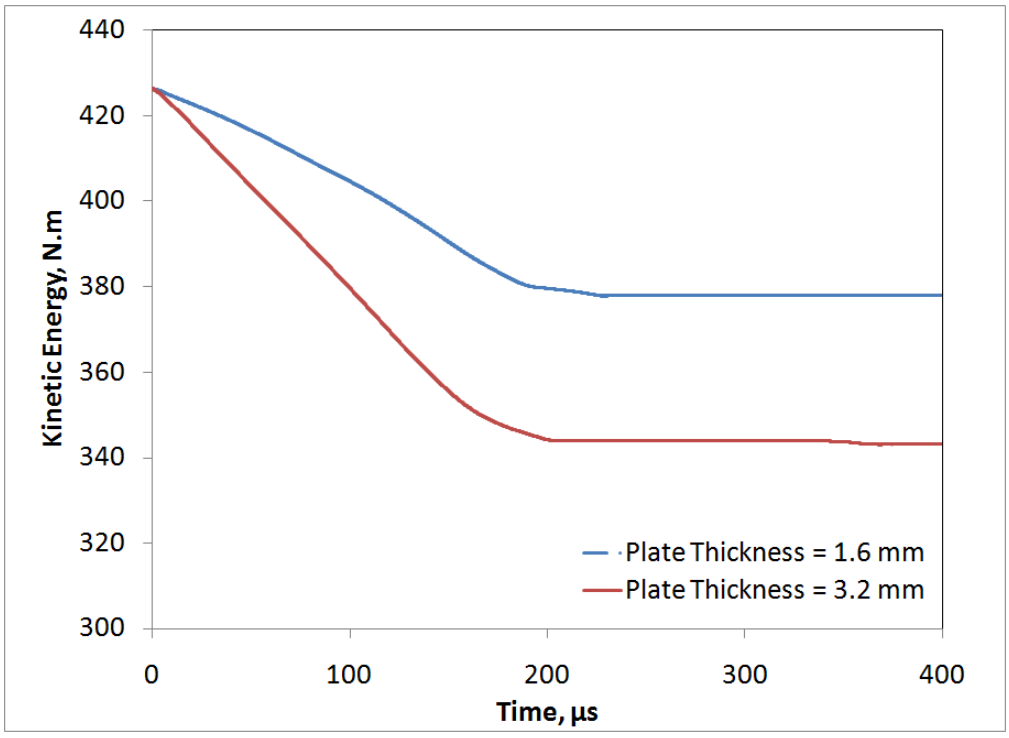

Figure 7.14: Kinetic energy of CR-1018 steel plate due to an impact velocity of 14.25 m/s.

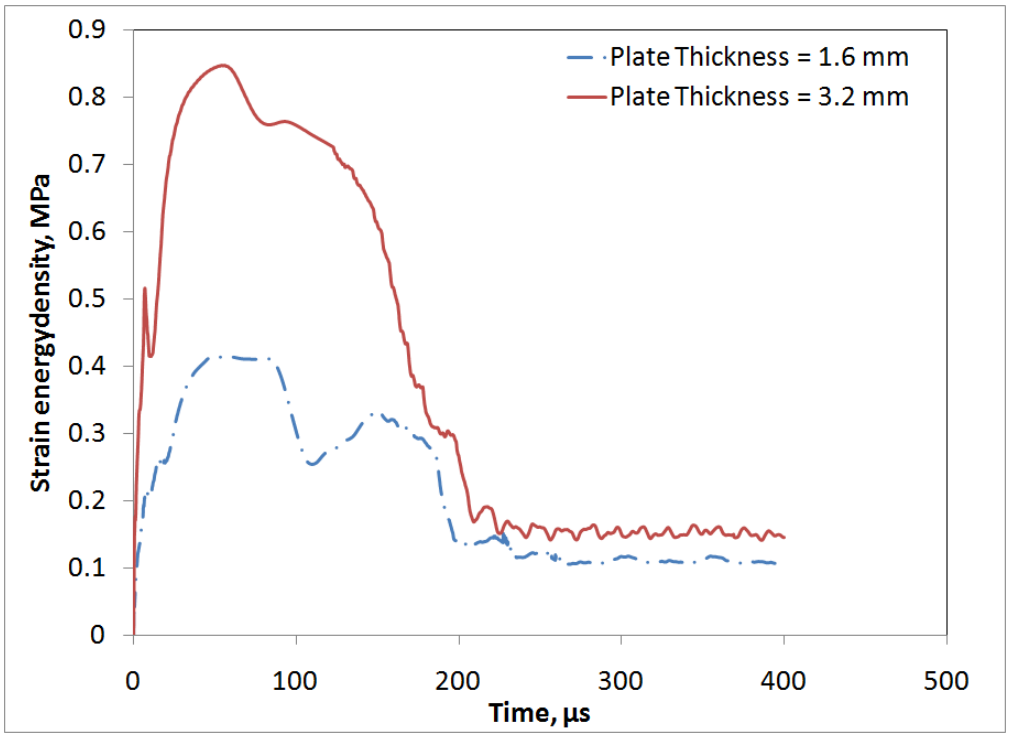

Figure 7.15: Strain energy density of CR-1018 steel plate due to an impact velocity of 14.25 m/s.

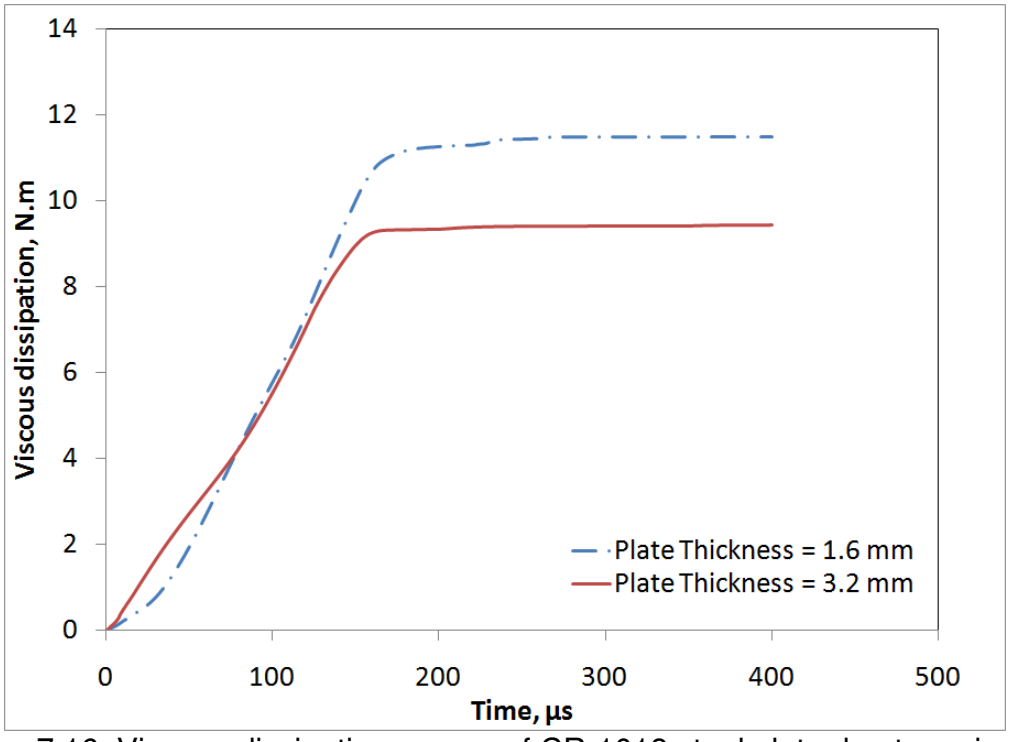

Figure 7.16: Viscous dissipation energy of CR-1018 steel plate due to an impact velocity of 14.25 m/s.

The equivalent plastic strain and von Mises stress are plotted versus time in Figures 7.17 and 7.18, respectively, for two elements; the first is at the support and the other is directly under the punching bar. The failure equivalent plastic strains of elements under the punch (which is 1) is higher than those for elements at the support (which is 0.8 for 1.6 mm plate, and 0.9 for 3.2 mm plate). This is because of the higher ductility of elements under the punch due to higher rise in temperature resulting from plastic deformation. In addition, the equivalent plastic strain in the 3.2 mm plate is higher than that for the 1.6 mm plate, since temperature is more released and less contained in the thinner plate. The hardening characteristic for the von Mises stress is almost the same for all elements. Nevertheless, it differs in the failure time where elements under the punch failed before elements at the support, which agrees with the equivalent plastic strain results.

The same problem is analyzed under a 1 m/s impact velocity to investigate the change in deformation behaviors. Figures 7.19 and 7.20 show the equivalent plastic strain for the 3.2 mm and 1.6 mm plates, respectively, under an impact velocity of 1 m/s. The shear band for the 3.2 mm plate is much wider than the one caused by the 14.25 m/s impact. Moreover, the deformation for the 1.6 mm plate is dominated by the bending mode more than the shear band mode. This is illustrated clearer through the von Mises stress contours in Figures 7.21 and 7.22.

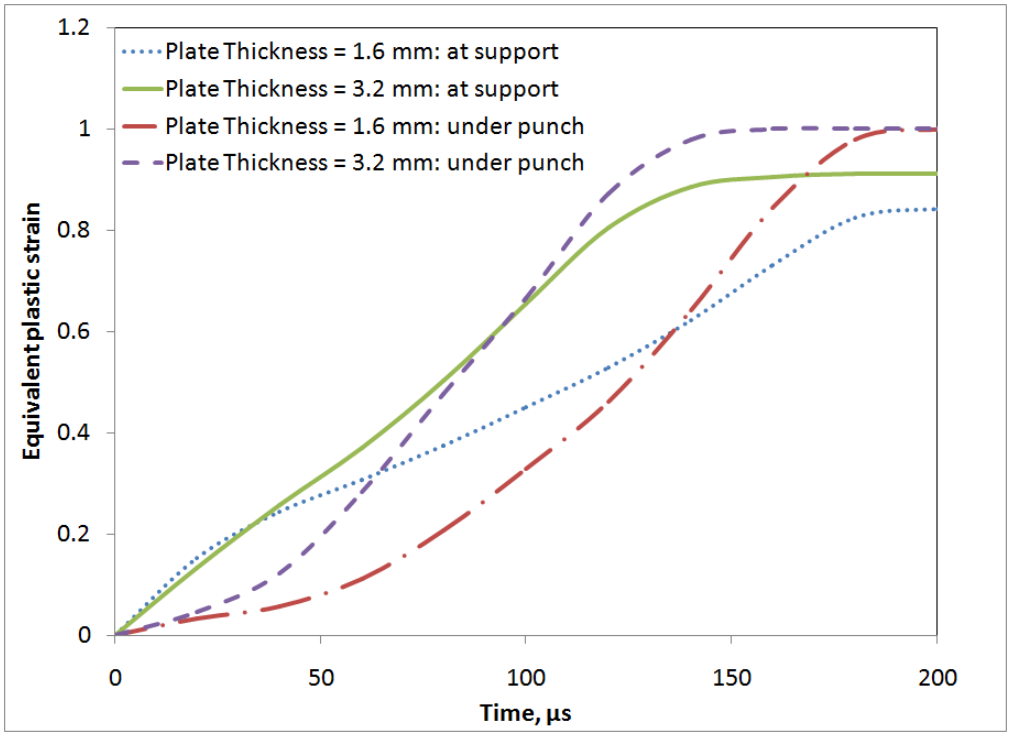

Figure 7.17: Equivalent plastic strain of CR-1018 steel plate due to an impact velocity of 14.25 m/s.

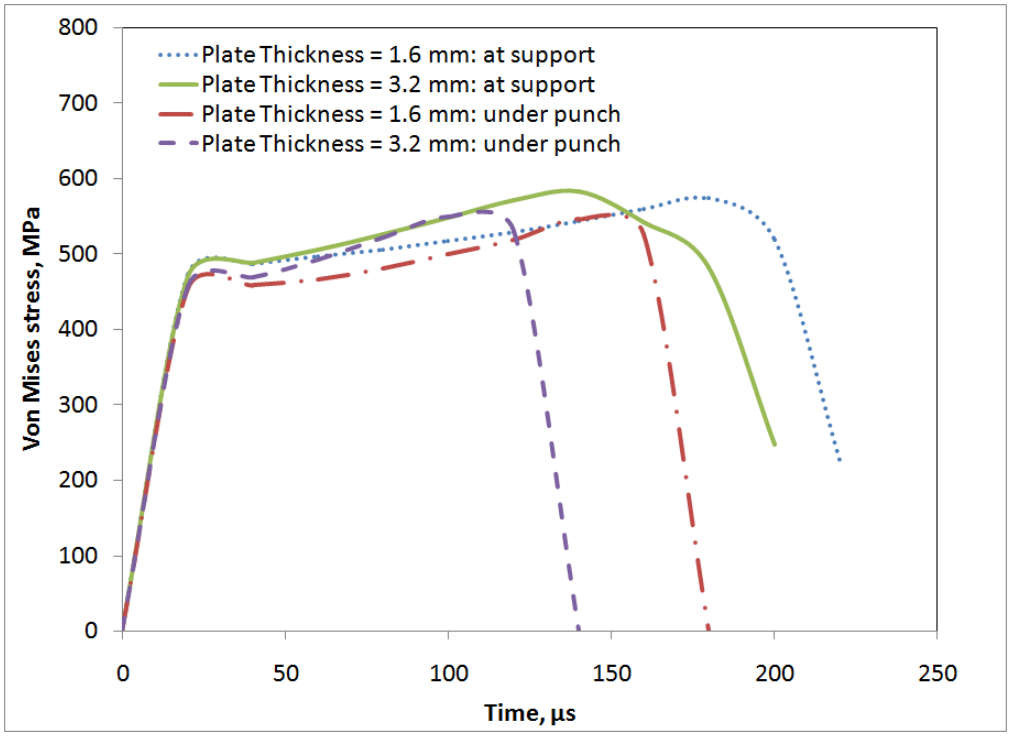

Figure 7.18: Von Mises stress of CR-1018 steel plate due to an impact velocity of 14.25 m/s.

Figure 7.23 shows the load-displacement curve of the 3.2 mm and 1.6 mm plates with experimental results of the 3.2 mm plate obtained by Roessig and Mason (1999a) and the numerical simulation by Roessig and Mason (1999b). The numerical simulation by Roessig and Mason (1999b) under-predicts the hardening behavior significantly. On the other hand, the current numerical analysis is in very good agreement with the experimental results compared to the numerical analysis by Roessig and Mason for both aspects; the stiffness and the hardening. The proposed constitutive model shows excellent capability in predicting plate stiffness represented by the slope of the load-displacement curve as well as relatively good simulation of the plate hardening behavior except at the early hardening stages, where it slightly over-predicts the strain hardening.

The strain energy density of CR-1018 steel plate under an impact velocity of 1 m/s is illustrated in Figure 7.24, where almost the same maximum values are obtained as those for the impact velocity of 14.25 m/s. However, the retained strain energy density after failure is about 0.3 MPa which is higher than about 0.15 MPa for the case of 14.25 m/s impact. This can be justified by the fact that a slower impact velocity will allow material to absorb and store more energy during impact from one side, and that the deformation and failure modes differ which also change the energy absorption of the material. Viscous dissipation energy is also higher here for low velocity impact (1 m/s) compared with high velocity impact (14.25 m/s) as shown in Figure 7.25, since the material will flow more viscously at lower impact velocities.

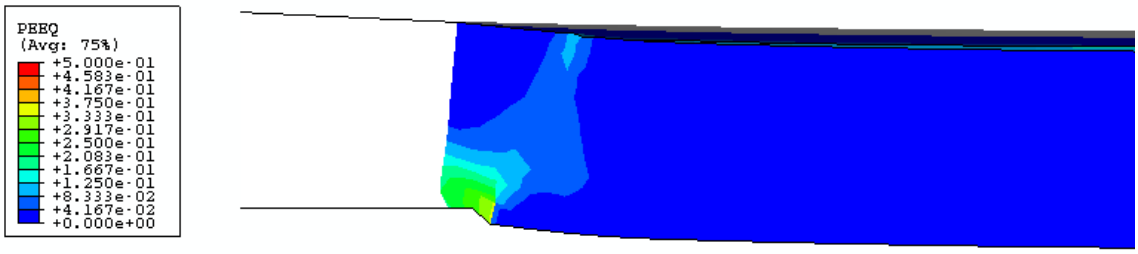

(a)

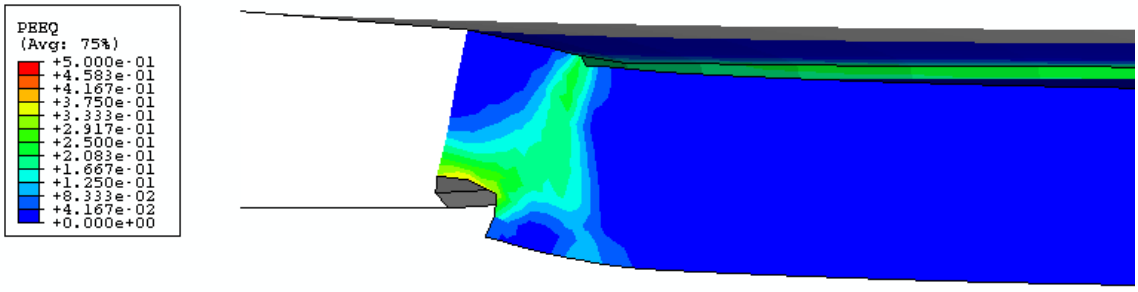

(b)

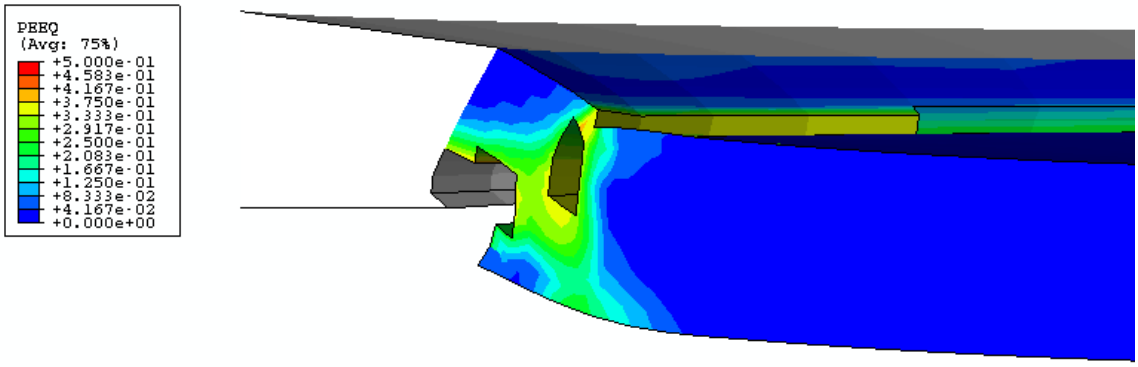

(c)

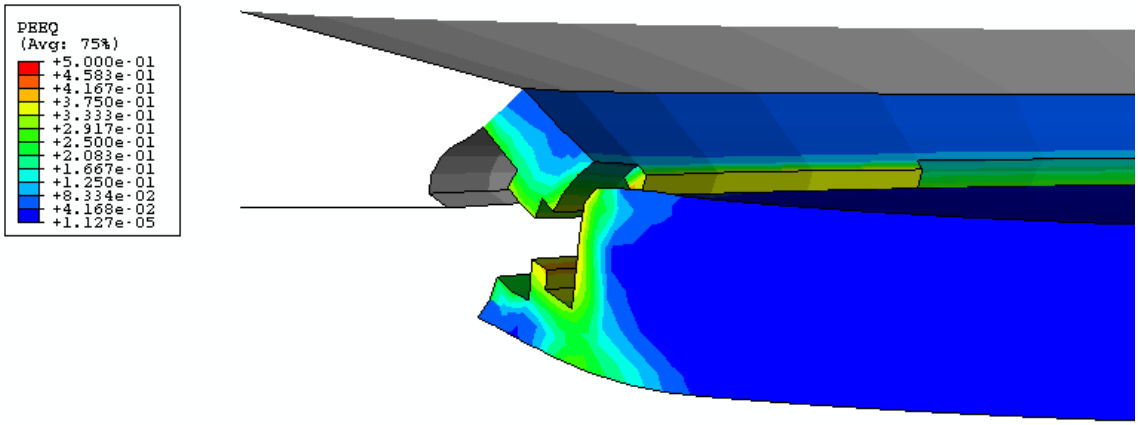

(d)

Figure 7.19: Equivalent plastic strain of 3.2 mm thick plate due to an impact velocity of 1 m/s at (a) t = 100μs (b) t = 200μs (c) t = 400μs (d) t = 600μs

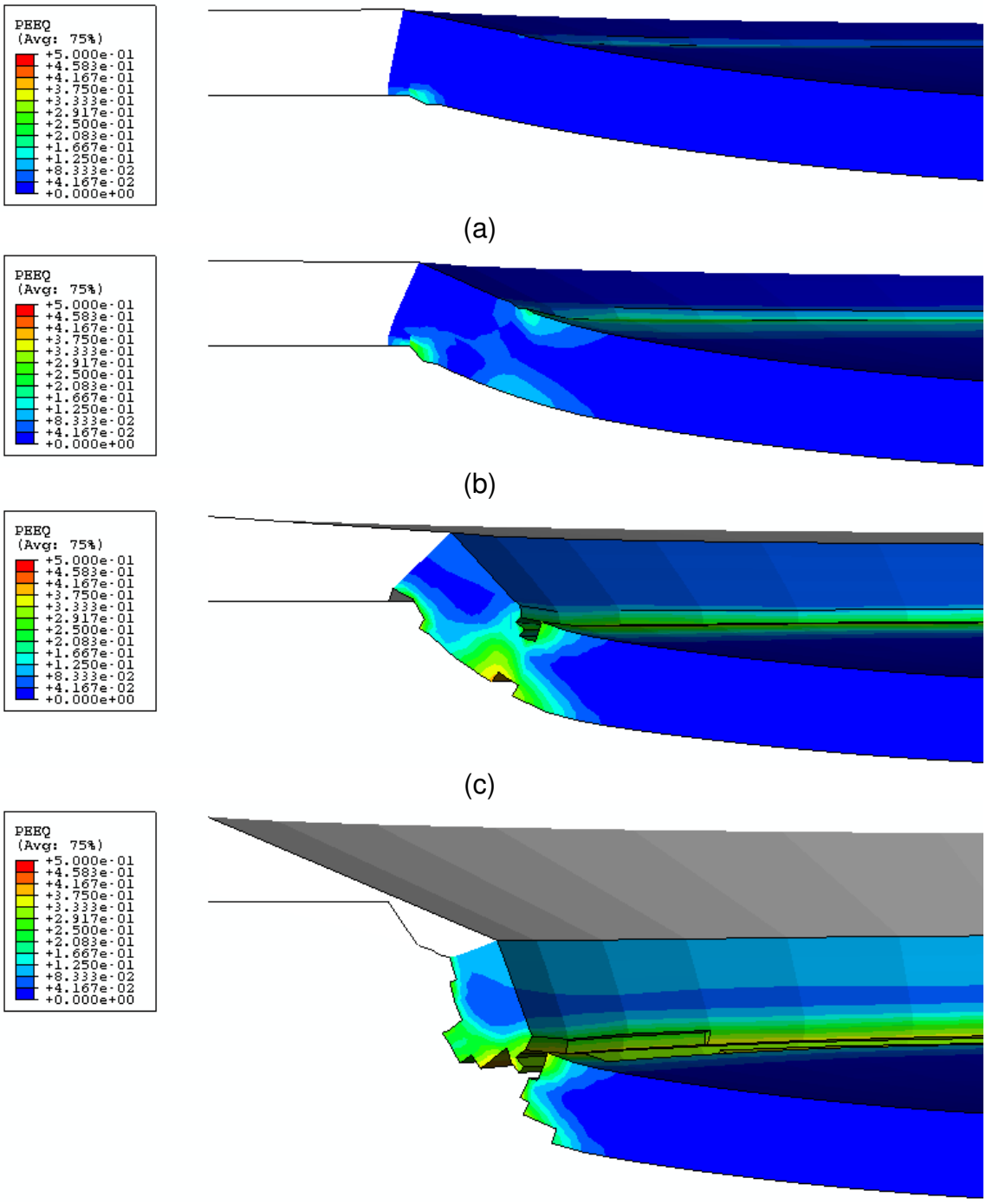

Figure 7.20: Equivalent plastic strain of 1.6 mm thick plate due to an impact velocity of 1 m/s at (a) t = 100μs (b) t = 200μs (c) t = 400μs (d) t = 900μs

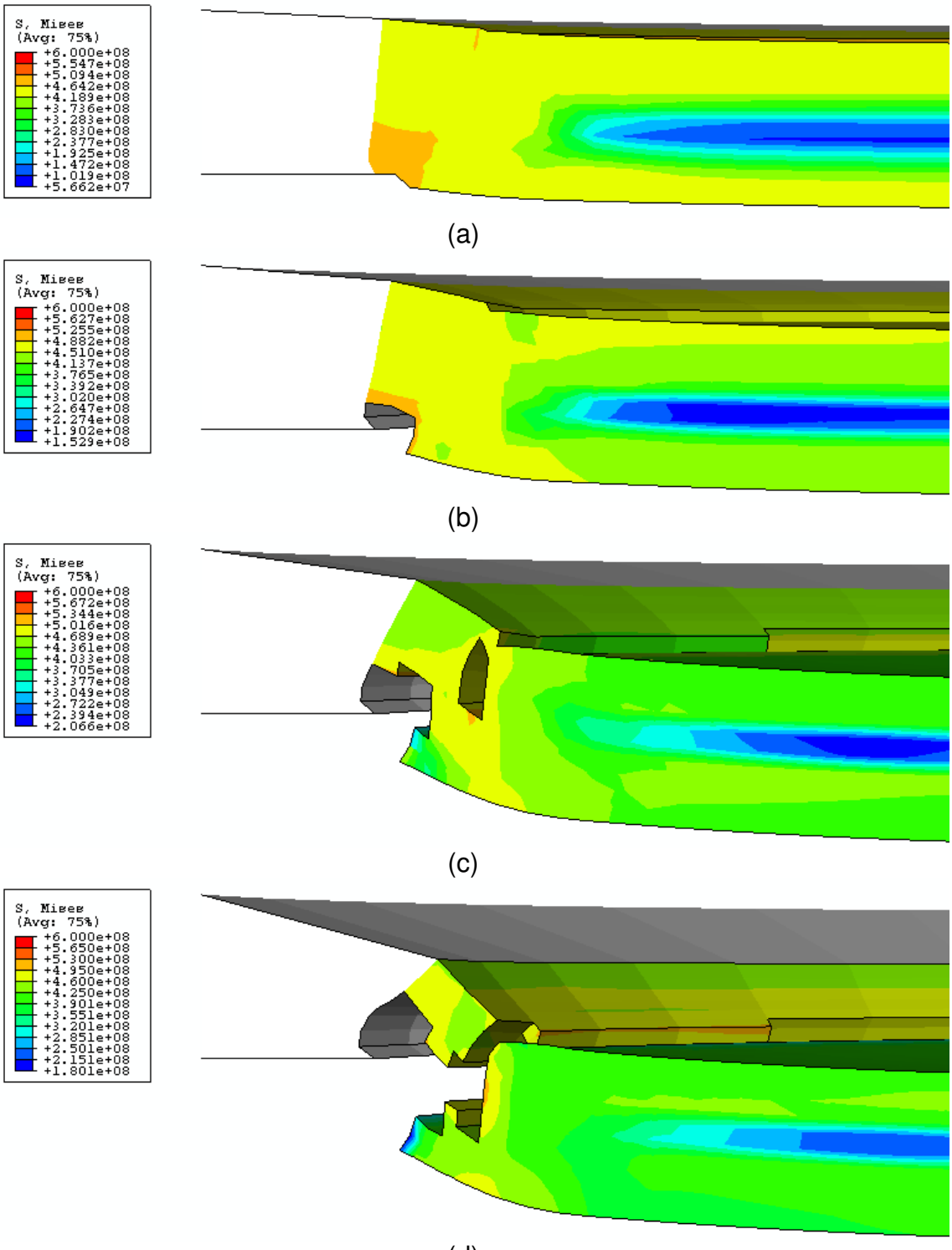

Figure 7.21: Von Mises stress of 3.2 mm thick plate due to an impact velocity of 1 m/s at (a) t = 100μs (b) t = 200μs (c) t = 400μs (d) t = 600μs

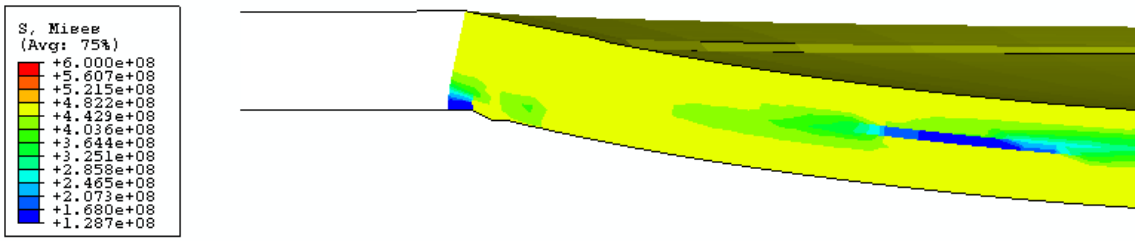

(a)

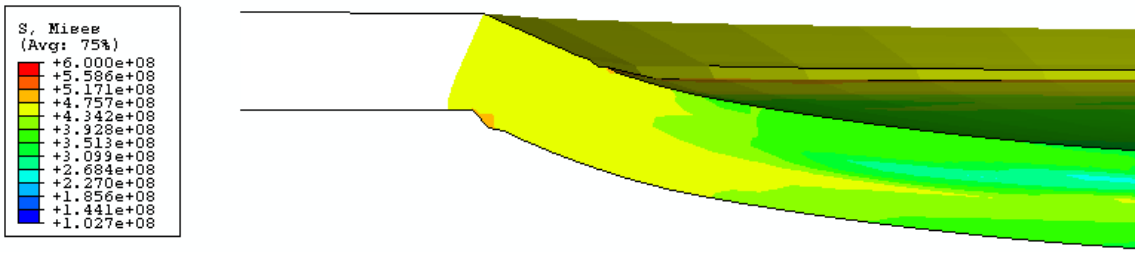

(b)

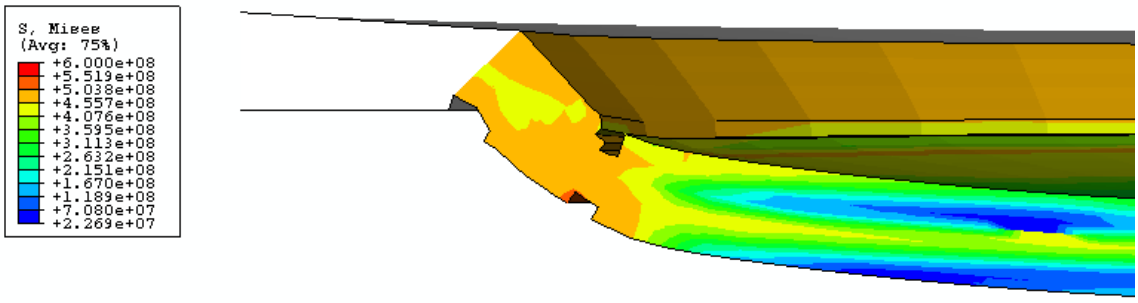

(c)

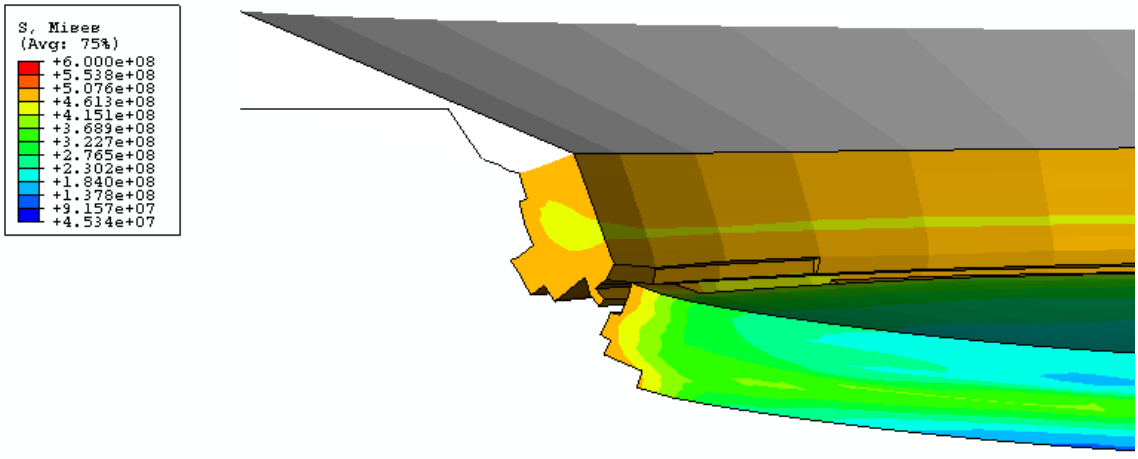

(d)

Figure 7.22: Von Mises stress of 1.6 mm thick plate due to an impact velocity of 1 m/s at (a) t = 100μs (b) t = 200μs (c) t = 400μs (d) t = 900μs

Equivalent plastic strains and the von Mises stress is plotted in Figures 7.26 and 7.27, respectively. Both the equivalent plastic strain and the von Mises stress under 1 m/s impact velocity behave almost the same as in the case of

14.25 m/s expect that the strains are lower. This happens because, as it is well known, higher velocity impact usually results in the higher shear strains.

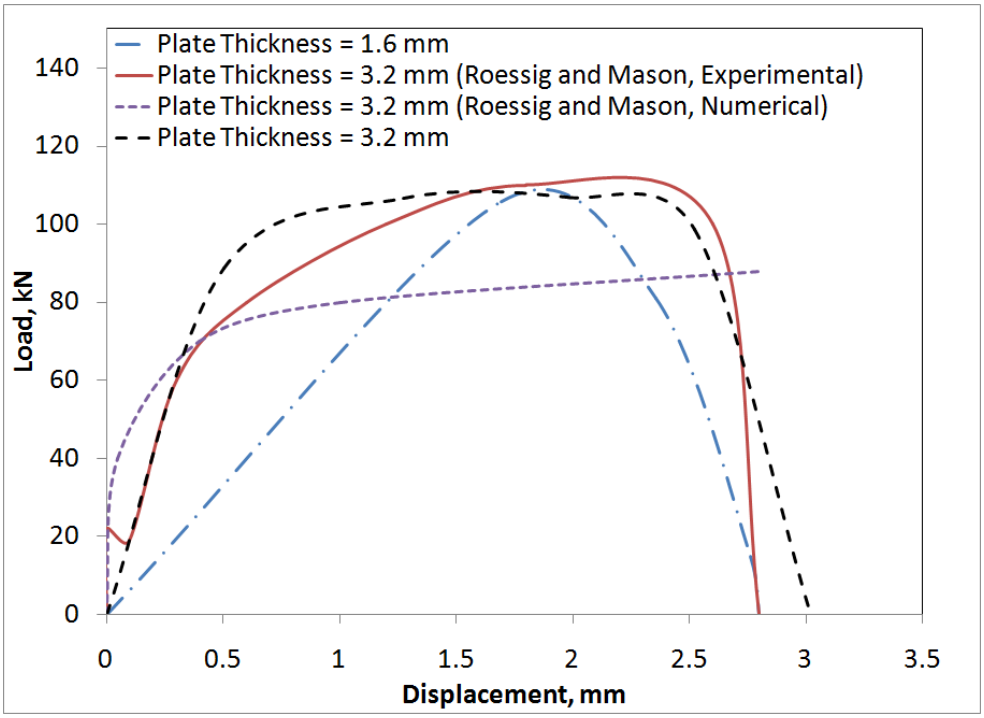

Figure 7.23: Load versus displacement of CR-1018 steel plate due to an impact velocity of 1 m/s.

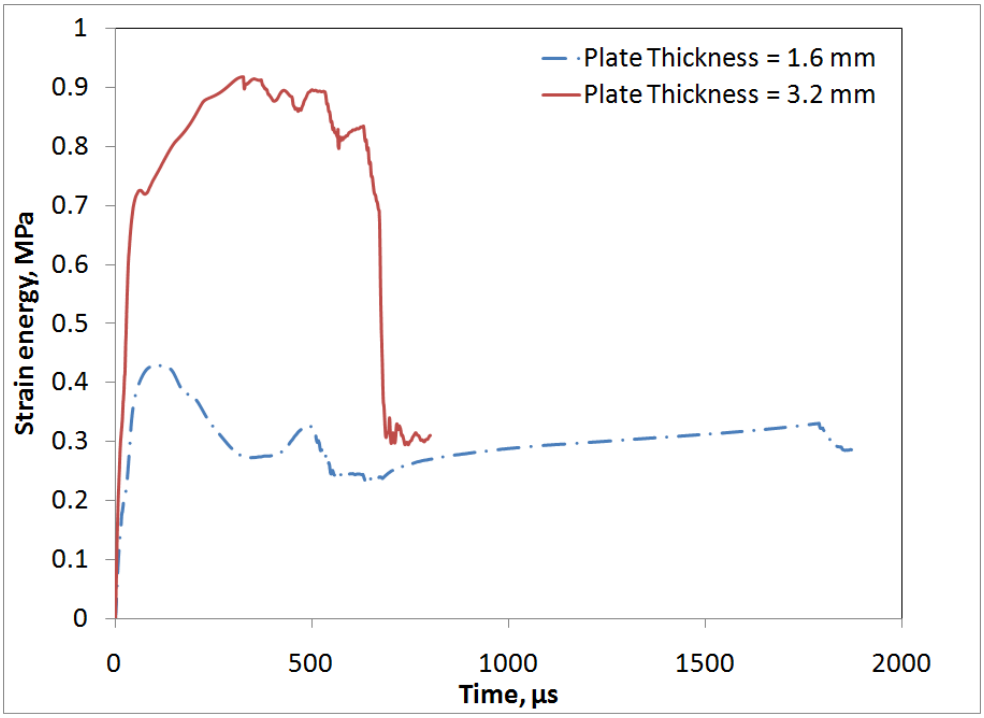

Figure 7.24: Strain energy density of CR-1018 steel plate due to an impact velocity of 1 m/s.

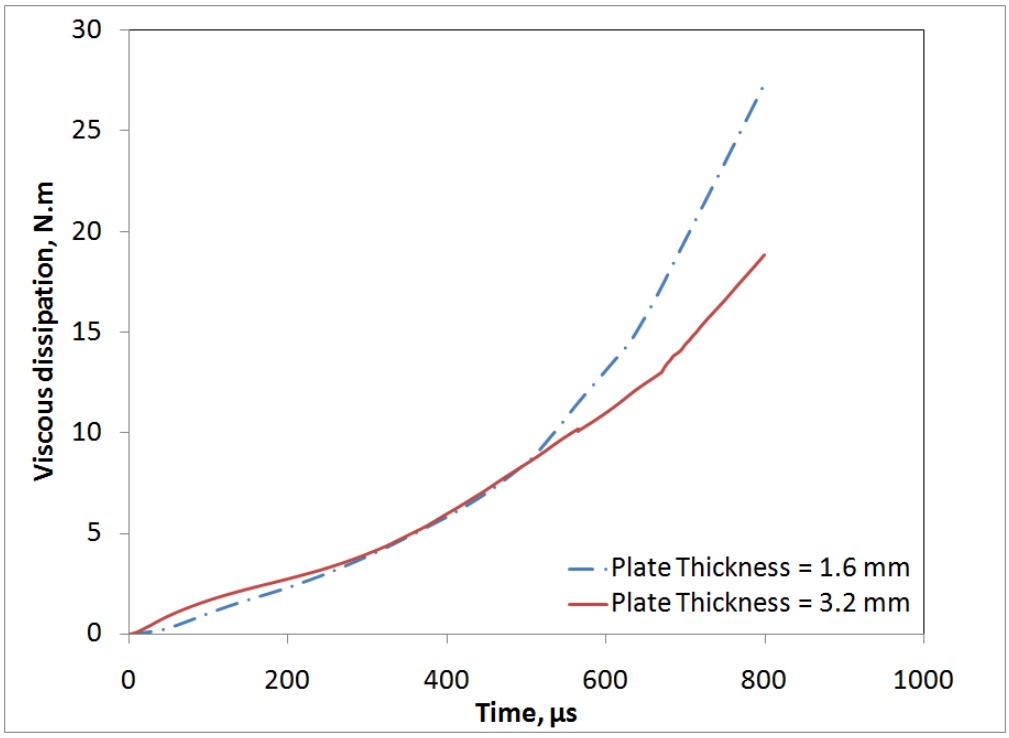

Figure 7.25: Viscous dissipation energy of CR-1018 steel plate due to an impact velocity of 1 m/s.

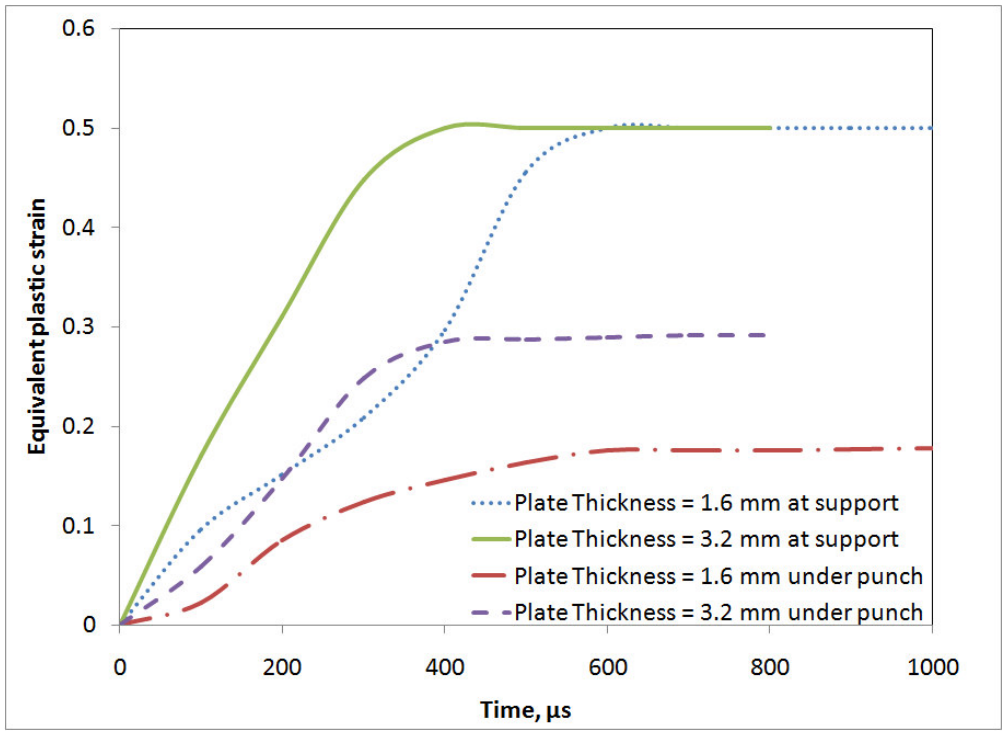

Figure 7.26: Equivalent plastic strain of CR-1018 steel plate due to an impact velocity of 1 m/s.

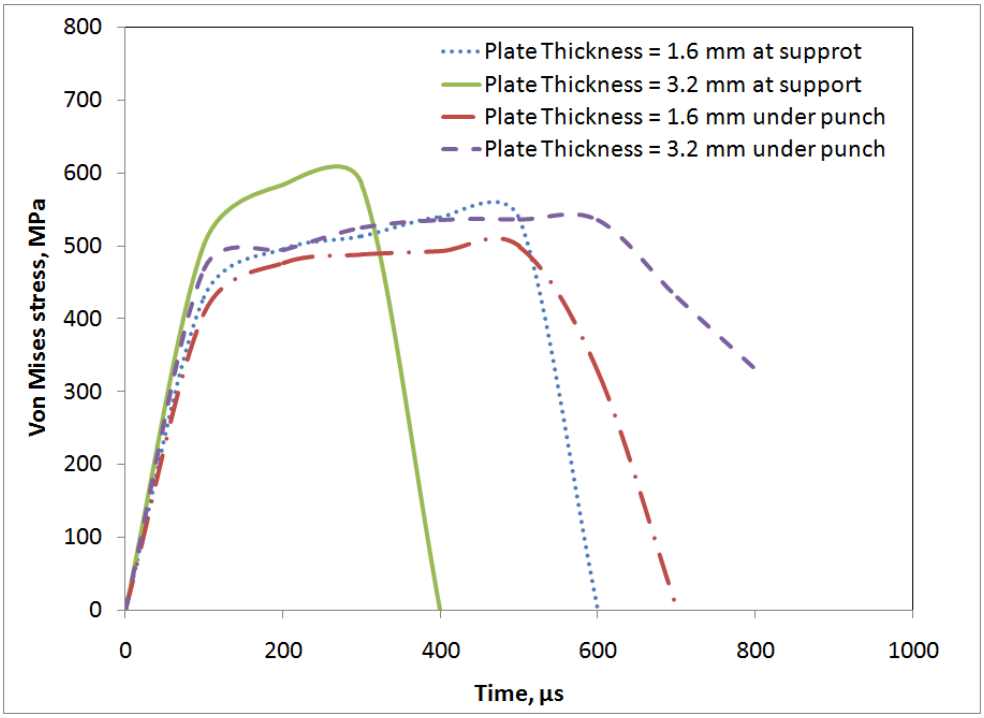

Figure 7.27: Von Mises stress of CR-1018 steel plate due to an impact velocity of 1 m/s.

7.3 Impact of Steel Beam Plate

The last example in this chapter is the impact of CR-1018 steel beam. The beam's dimensions are 3 m (length) X 0.3 m (width) X 0.03 m (depth), and it is fully fixed from both sides (Figure 7.28). Like the previous example, a very small skewness is added to the beam to simulate more realistic experimental conditions. The impact block is a cube with edge length of 0.3 m, and it is assumed to be a rigid body. The impact block has different initial velocities of 200 m/s, 400 m/s and 600 m/s to show how deformation changes. The main purpose of this example is to illustrate the interaction between the bending deformation mode and the shear banding mode.

The shear strain contours in the steel beam under impact velocities of 200 m/s, 400 m/s, and 600 m/s are shown in Figures 7.29, 7.30, and 7.31, respectively. It can be noticed that the bending deformation is significant and overcomes the shear banding deformation at relatively low velocity of impact (200 m/s). With increasing temperature, the dominated deformation mode becomes the shear banding as seen in Figure 7.31b, where full shear failure occurs with almost no bending deformation. However, as illustrated in Figure 7.31c, the deformation wave propagation will cause some bending deformation after the total shear band failure. The shear banding failure occurs only at one side of the impact area for impact velocities of 200 m/s and 400 m/s due to the small asymmetry of the beam, where this banding failure takes place at both

sides of impact area for the 600 m/s impact because the deformation is more localized and less affected by the little asymmetry of the beam.

Axial stress contours are plotted in Figures 7.32, 7.33, and 7.34 for impact velocities of 200 m/s, 400 m/s, and 600 m/s, respectively. At 200 m/s and 400 m/s impact velocity, the stresses in the beam are mainly tensile stresses (represented by red color) with minor compressive waves (represented by blue color). On the other hand, at an impact velocity of 600 m/s there are more noticeable and distinctive compressive waves as can be seen in Figure 7.34c.

Figures 7.35, 7.36, and 7.37 show the temperature distributions in the steel beam for impact velocities of 200 m/s, 400 m/s, and 600 m/s, respectively. There is a slight increase in the temperature in almost the whole beam under 200 m/s impact due to the bending deformation, where the beams under 400 m/s and 600 m/s suffer temperature increase only in the local shear banding area since there is almost no bending deformation at these impact velocities. Temperature rise localizes more at higher velocity impact as shown in Figure 7.37c. The increase in temperature in a finite element located directly under the edge of the impact block (which is where shear band occurs) is plotted in Figure 7.38. Under 600 m/s impact, the temperature reaches about 700°K compared to 425°K for 400 m/s impact. In fact, temperature of 425°K is not enough to cause the strain to soften in CR-1018 steel as was shown in Chapter 3, which justifies the use of softening term in the constitutive model as shown in Eq. (3.43). In addition, it is clear that the relationship between increasing temperature with increasing impact velocity is not linear.

This example shows mainly how bending deformation can affect shear band localization, and how increasing impact velocity can change the dominating deformation mode from bending to shear banding.

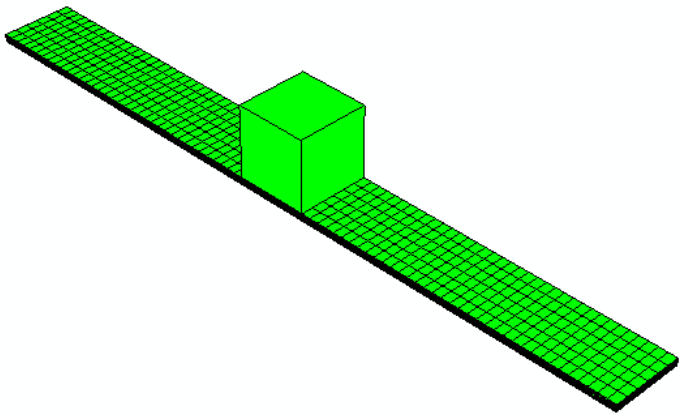

Figure 7.28: CR-1018 steel beam under impact loading.

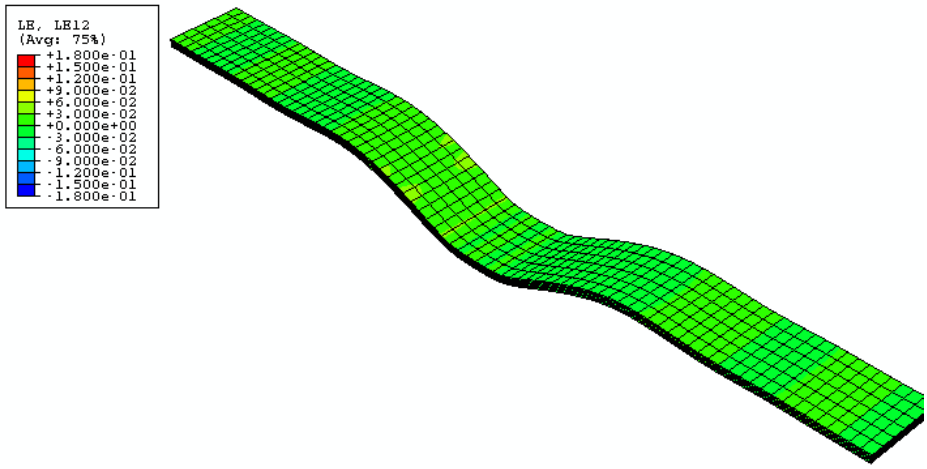

(a)

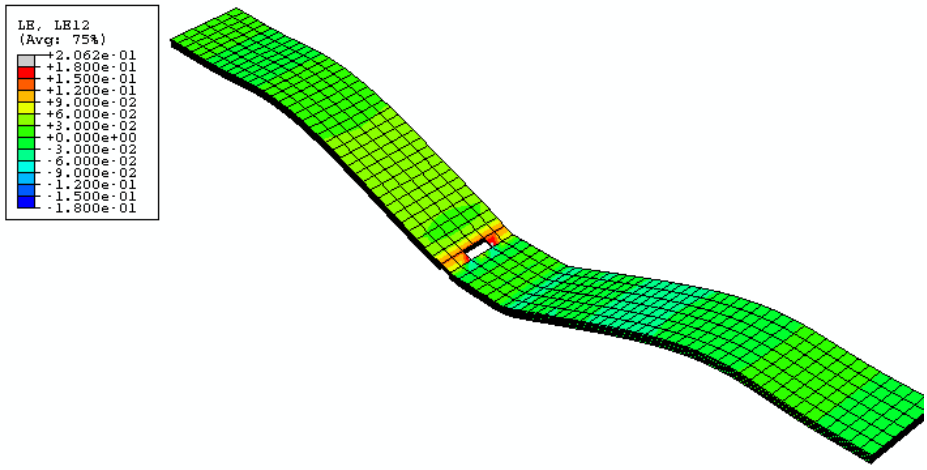

(b)

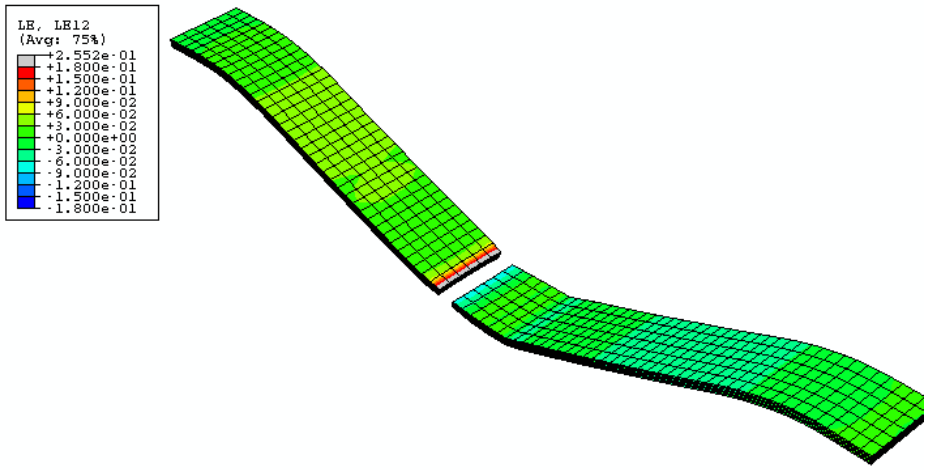

(c)

Figure 7.29: Shear strain in CR-1018 steel beam due to an impact velocity of 200 m/s at (a) t = 800 μs, (b) t = 1440 μs (c) t = 2080 μs

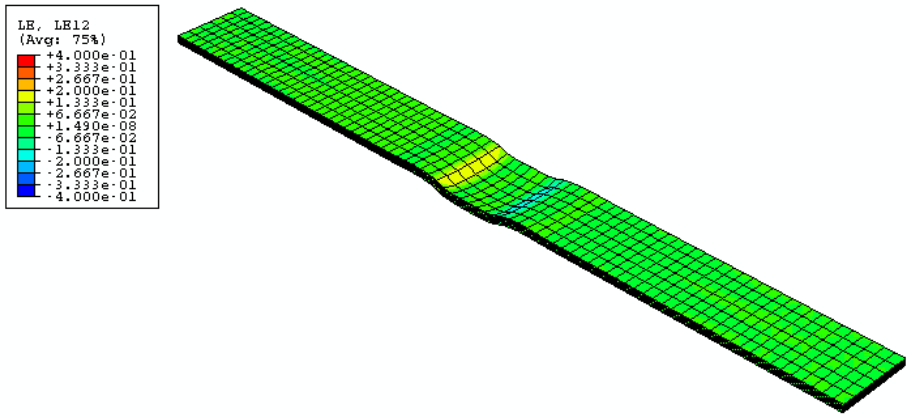

(a)

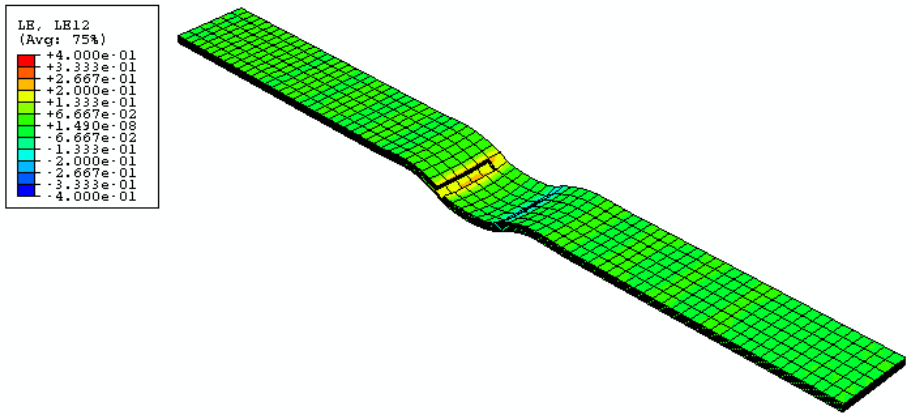

(b)

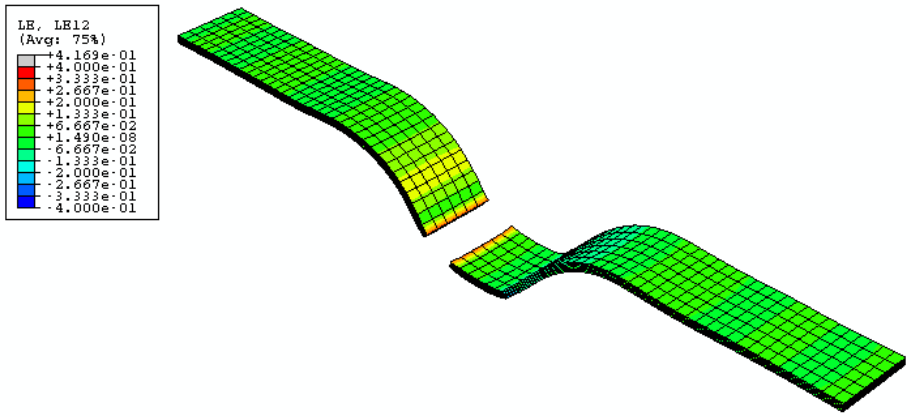

(c)

Figure 7.30: Shear strain in CR-1018 steel beam due to an impact velocity of 400 m/s at (a) t = 80 μs, (b) t = 160 μs (c) t = 800 μs

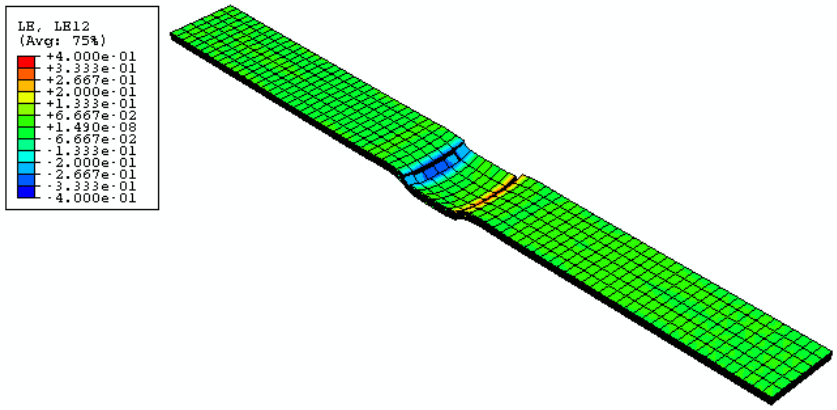

(a)

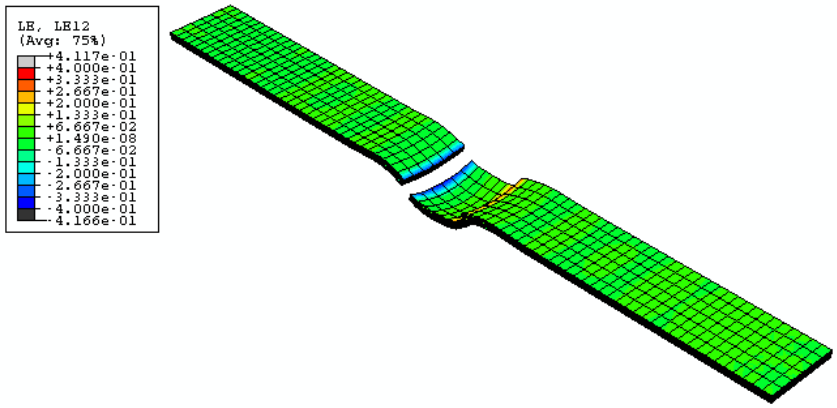

(b)

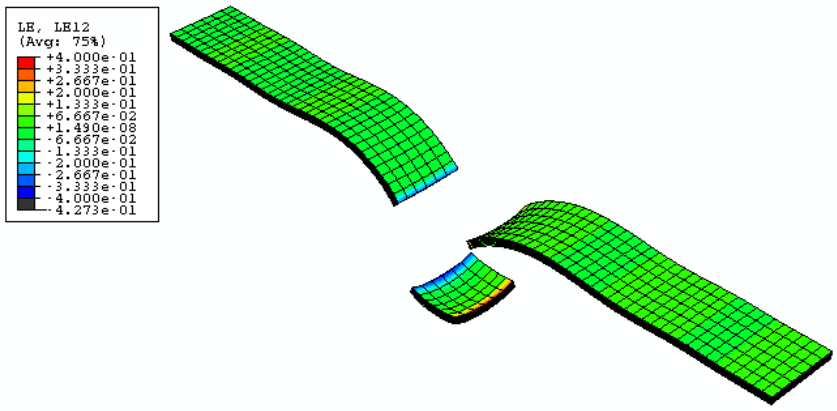

(c)

Figure 7.31: Shear strain in CR-1018 steel beam due to an impact velocity of 600 m/s at (a) t = 80 μs, (b) t = 160 μs (c) t = 800 μs

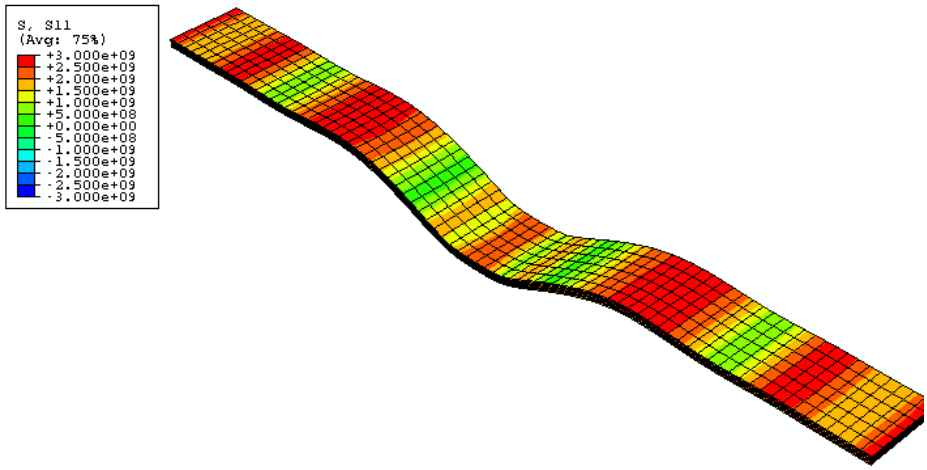

(a)

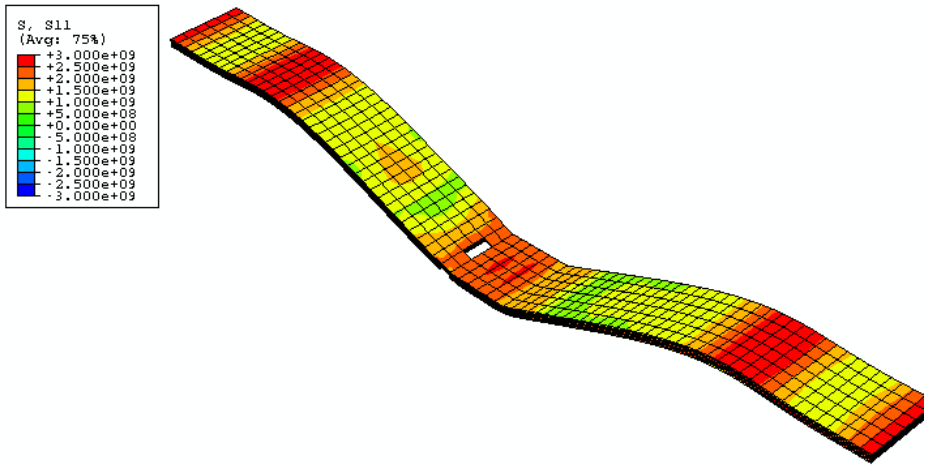

(b)

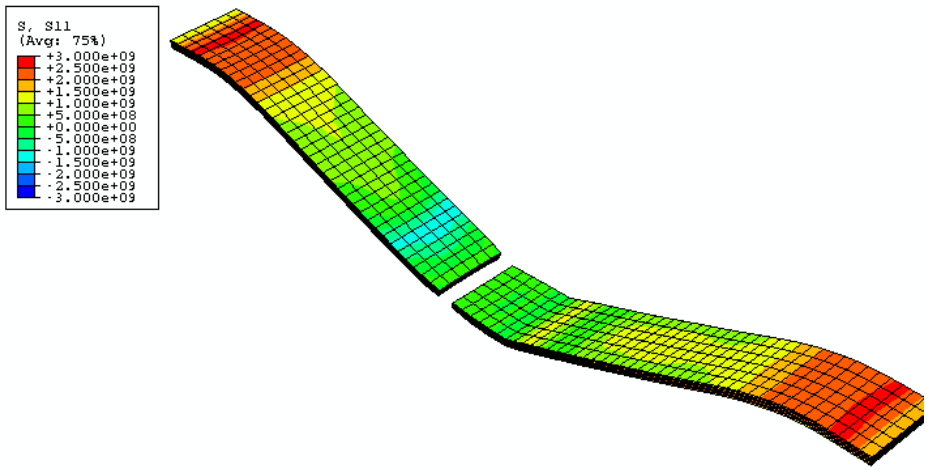

(c)

Figure 7.32: Axial stress in CR-1018 steel beam due to an impact velocity of 200 m/s at (a) t = 800 μs, (b) t = 1440 μs (c) t = 2080 μs

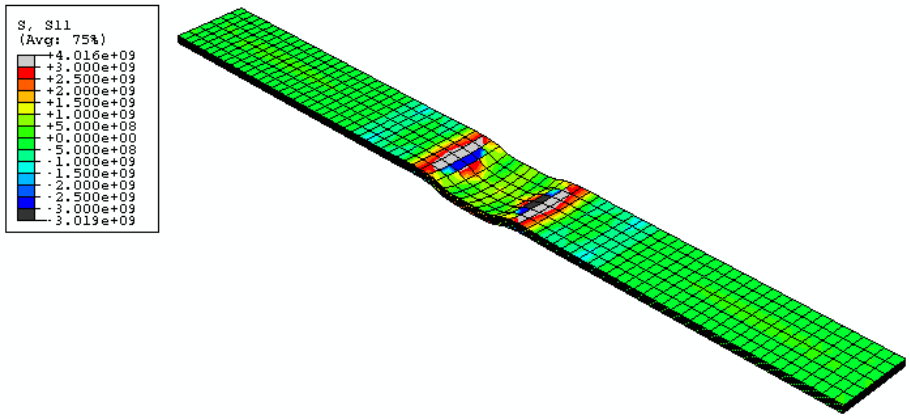

(a)

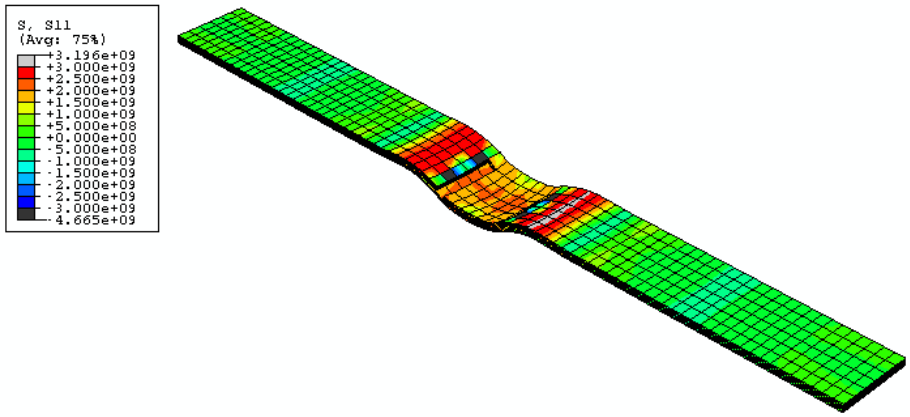

(b)

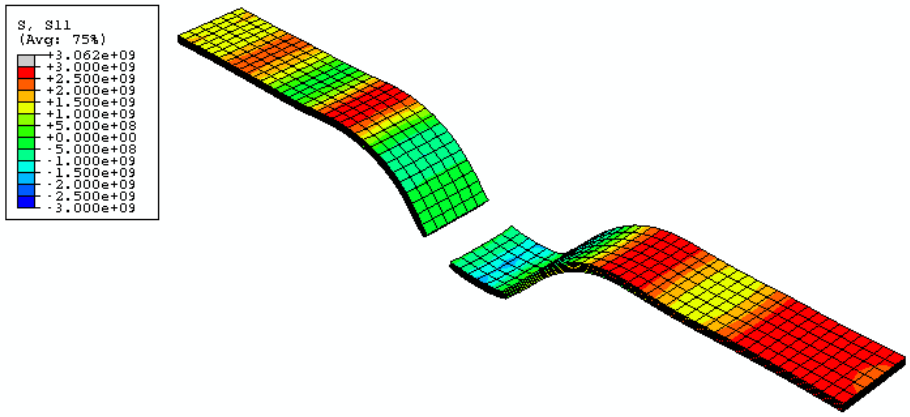

(c)

Figure 7.33: Axial stress in CR-1018 steel beam due to an impact velocity of 400 m/s at (a) t = 80 μs, (b) t = 160 μs (c) t = 800 μs

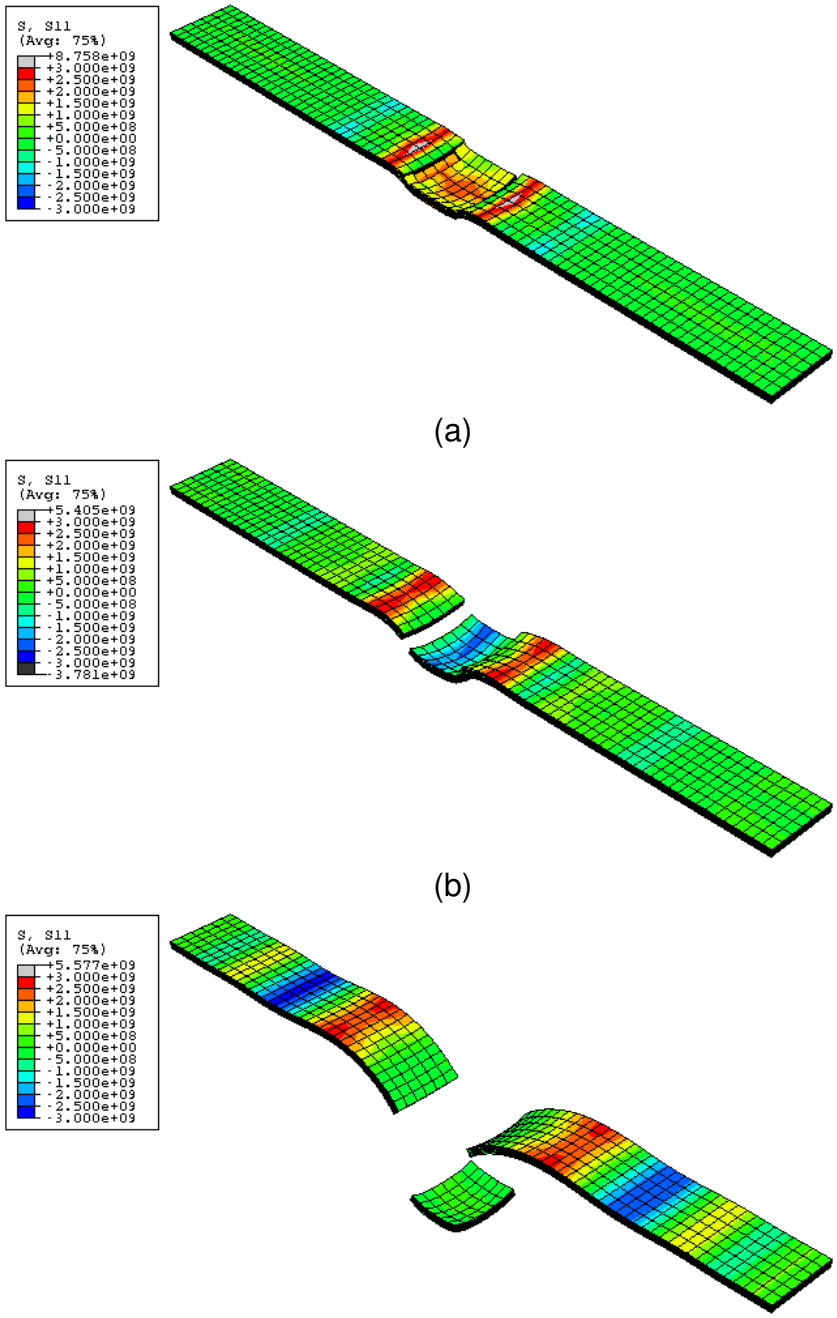

Figure 7.34: Axial stress in CR-1018 steel beam due to an impact velocity of 600 m/s at (a) t = 80 μs, (b) t = 160 μs (c) t = 800 μs

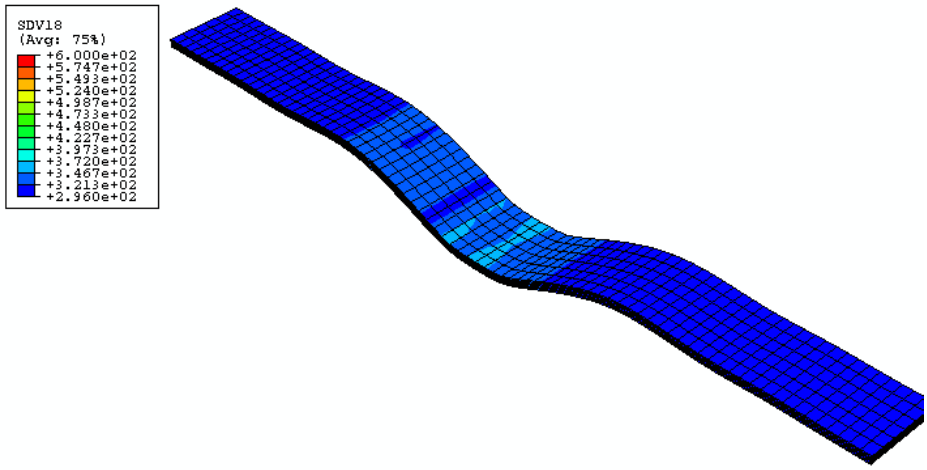

(a)

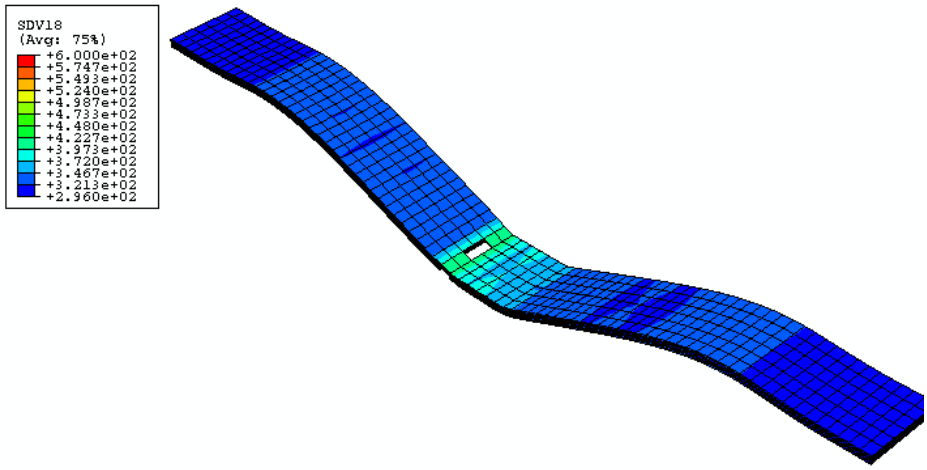

(b)

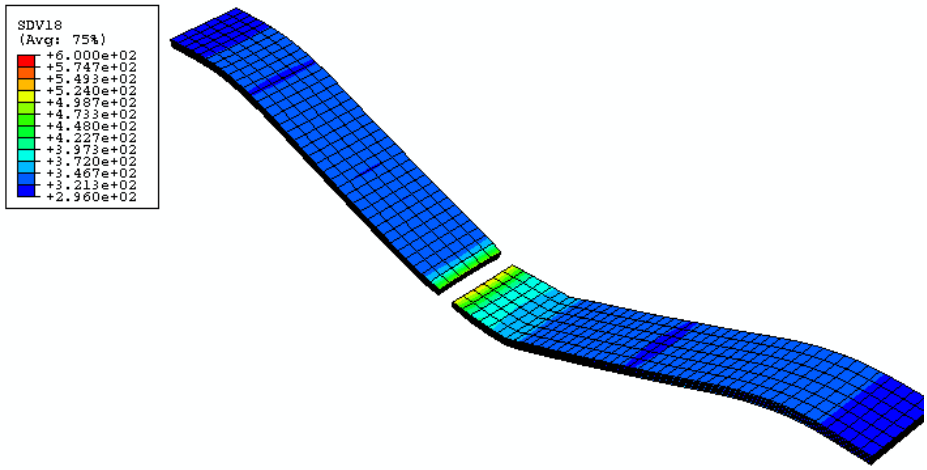

(c)

Figure 7.35: Temperature distribution in CR-1018 steel beam due to an impact velocity of 200 m/s at (a) t = 800 μs, (b) t = 1440 μs (c) t = 2080 μs

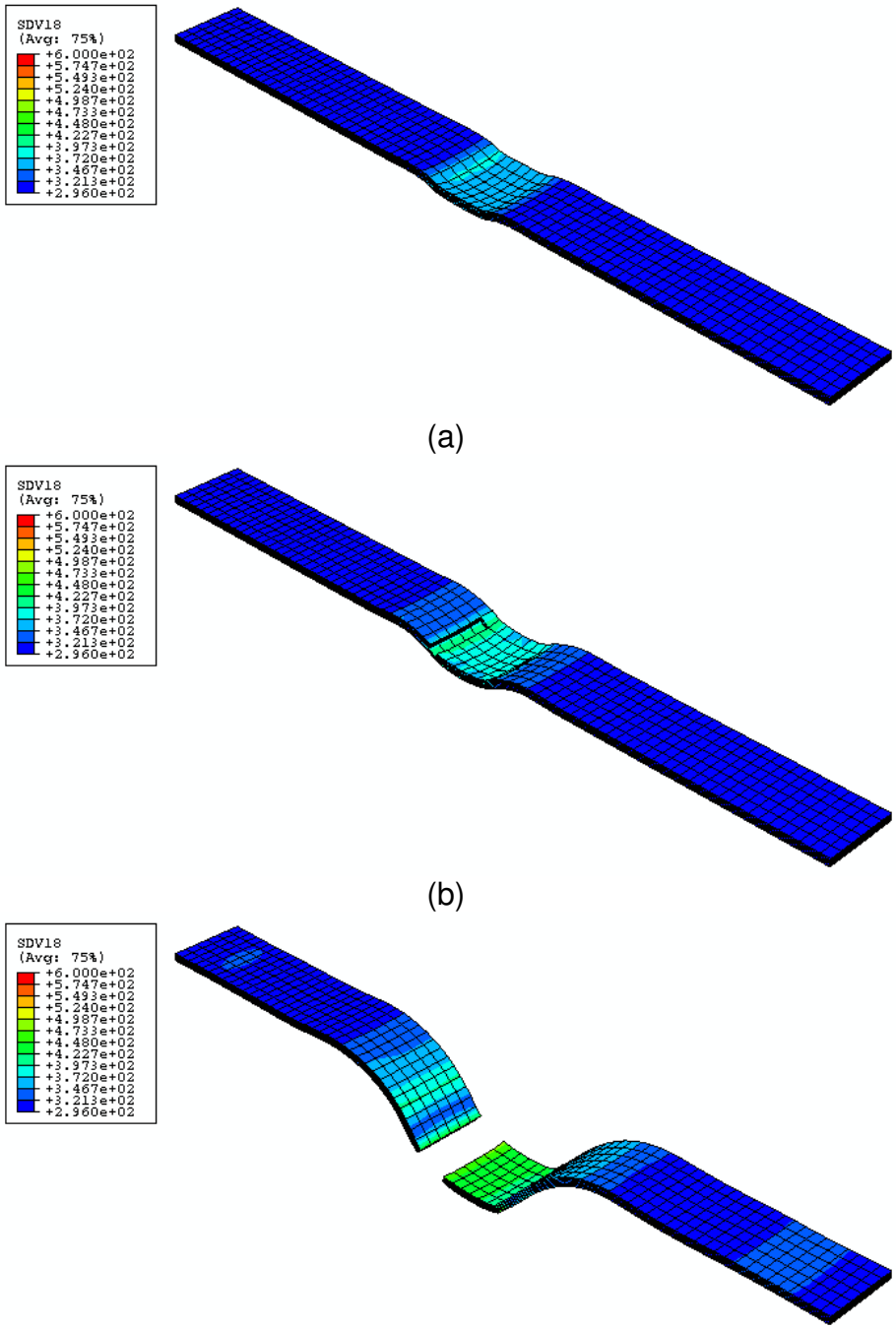

Figure 7.36: Temperature distribution in CR-1018 steel beam due to an impact velocity of 400 m/s at (a) t = 80 μs, (b) t = 160 μs (c) t = 800 μs

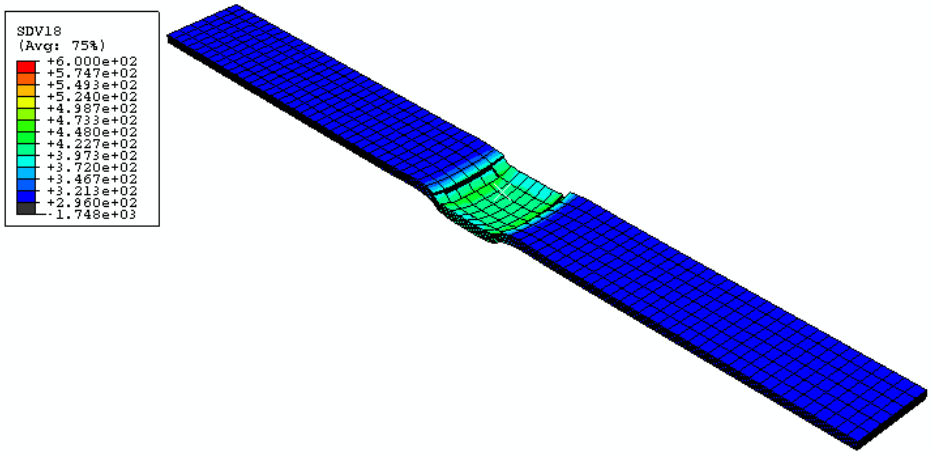

(a)

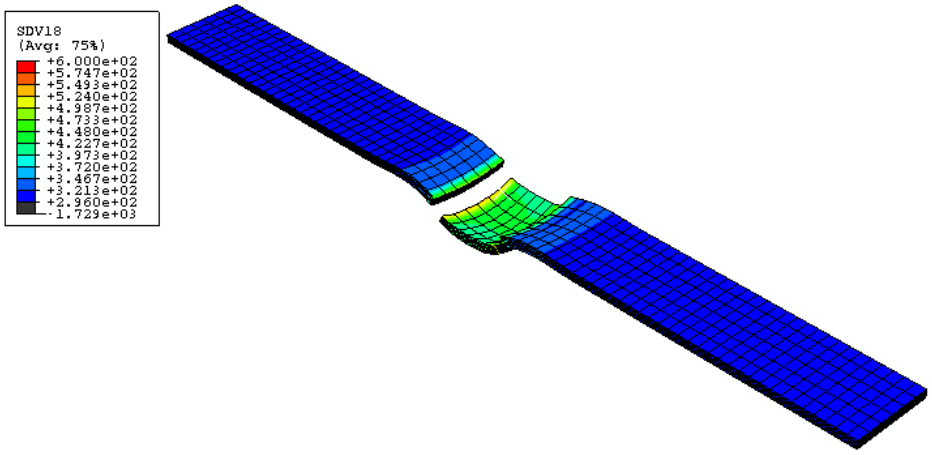

(b)

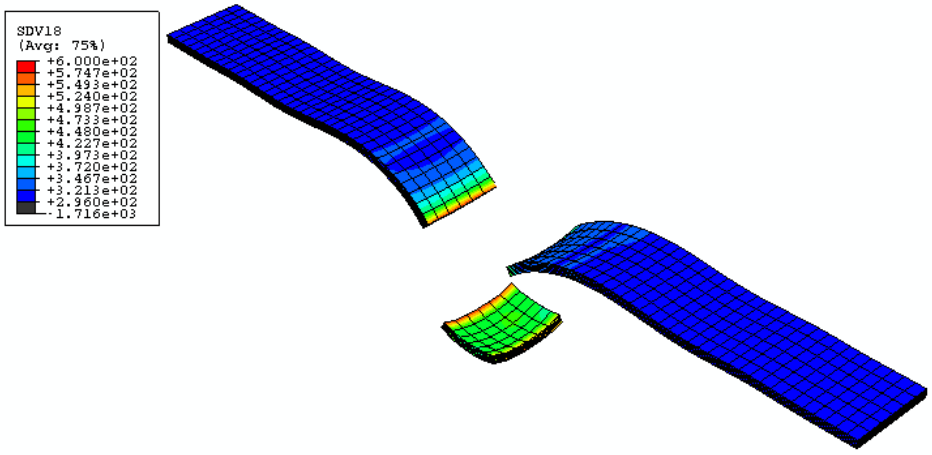

(c)

Figure 7.37: Temperature distribution in CR-1018 steel beam due to an impact velocity of 600 m/s at (a) t = 80 μs, (b) t = 160 μs (c) t = 800 μs

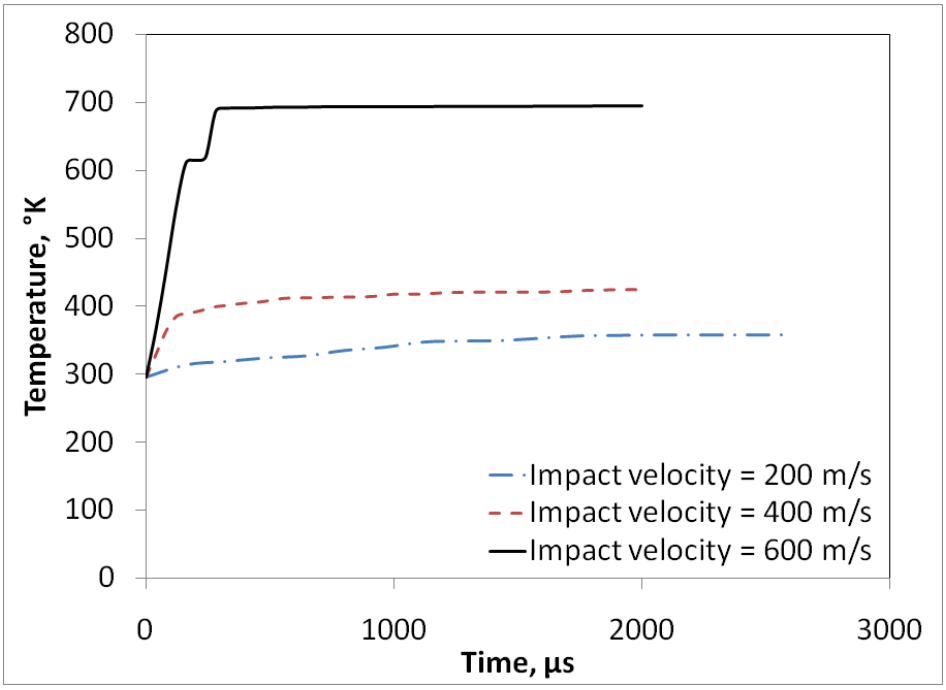

Figure 7.38: Increase in temperature in CR-1018 steel beam under impact loading.

CHAPTER 8: SUMMARY, CONCLUSIONS, AND FUTURE RECOMMENDATIONS

8.1 Summary

This dissertation sheds some light on the analysis and numerical simulation of shear banding as a deformation mode in metals. The work can be divided into three correlated parts: (1) constitutive modeling through capturing the stress-strain behavior of faced centered cubic (fcc) metals, body centered cubic (bcc) metals, and metal alloys under different conditions of strain rates and temperatures; (2) conducting experimental tests to obtain a basic material property, namely the intrinsic material length scale, to be used in conjunction with the regularization of the numerical analysis; and (3) utilizing the finite element method to simulate the shear localization process in metals.

Initially, two constitutive models were developed in this work to describe the mechanical behavior of (fcc) and (bcc) metals under a wide range of strain rates and temperatures. The models are based on macromechanical state variables such as stress, strain and material constants that include threshold and transition temperature as well as micromechanical terms such as mobile dislocation density and Burgers vector. The principle of the activation energy and its dependence on temperature, strain rate, and stress is the key point in these proposed models. The models were used to simulate the experimental behavior of OFHC copper as an fcc metal, and pure iron as a bcc metal at various temperatures and strain rates in order to obtain the different model parameters. The models showed good capability in capturing the coupling between strain rate and temperature, plastic strain and strain rate, and plastic strain and temperature. The models were then used to characterize the hardness of material at low and high strain rates for a representative strain of 8%. These models were utilized to characterize the constitutive behavior of metals such as steel alloys, but were unsuccessful because they were unable to capture any softening behavior that usually appear in different kinds of steel. Hence, a simple power law model with strain rate and temperature dependencies with softening term was proposed to address the problem. The power model in this case was effective in capturing the softening behavior in metals at high strain rates, which is used in simulating the shear band process.

In chapter 3, the adiabatic shear banding was studied using the power law model proposed, since analysis of these localizations highly depends on the selection of the constitutive model itself. Instability strain, localization strain, as well as evolution of shear localization were investigated at different temperatures and strain rates.

In order to determine the intrinsic material length scale and use it as one of the basic material properties, nano-indentation as well as the regular Brinell hardness tests were conducted on two types of steel alloys; CR-1018 steel and

HR-A36 steel. Three theoretical models (Nix and Gao, 1998; Chong and Lam, 1999; Abu Al-Rub and Voyiadjis, 2004; and Voyiadjis and Abu Al-Rub, 2002) were used to find a value for the material length scale. The results of hardness for these steel alloys were obtained at very low and high loads which helped in determining the length scale for each material. However, the available testing equipment can run only at static loads, and hence the obtained length scales were static ones. In order to find a dynamic length scale, a model was required to take the strain rate effect into account. For this reason dynamic hardness model was suggested to measure hardness at high strain rates. This model was implemented in the length scale expression in order to get an equation for the dynamic length scale. To use this expression, a simple nonlocal gradient theory was illustrated, which will help regularizing strain localization problems.

Finally, the proposed power law constitutive model along with the nonlocal gradient theory with dynamic length scale is implemented in a user subroutine attached to Abaqus/Explicit finite element package. Finite element with fully coupled thermal-stress analysis was used where plastic deformation transforms into heat is considered. Three different examples of shear bands are simulated; (1) shear band in two dimensional plate under velocity boundary condition; (2) penetration of circular steel plate at low velocities; and (3) impact of steel beams at high velocities.

8.2 Concluding Remarks

Two constitutive models for fcc and bcc metals was proposed to characterize the material behavior for a wide range of temperatures and strain rates based on the concept of energy activation of the material. The use of a power law instead of an exponential expression to relate the dislocation glide velocity to the stress proved to have a very good capability in capturing the strain rate sensitivity of metals. Proposed models are capable of capturing both strain rate and temperature dependency for the flow stress as well as the interaction between the temperature and strain rate behavior. The effectiveness of the model is attributed to the dependence of the flow stress on temperature and strain rate in a coupled form, which represents a more realistic behavior for bcc metals. The developed constitutive models were also used to predict the static and dynamic hardness of bcc and fcc metals through the use of Tabor's relationship (Tabor, 1951). The models generally gives excellent predictions of the hardness at both low and high strain rates at the representative strain of 8% as suggested by Tabor (Tabor, 1951). However, the models diverge from experimental results at high strains, which are attributed to some localization mechanism that occurs under indentation tests at large strains. This localization behavior is not accounted for in the models and is beyond the scope of this work. These models were unable to capture any softening behavior in stress-strain diagrams of metals alloys. Nevertheless, the proposed power law constitutive model was able to capture this softening characteristic through an extra term that

is a function of strain rate and temperature. The model was able to simulate softening of CR-1018 steel at high strain rates.

This power law constitutive model was utilized to investigate the adiabatic shear banding process in Chapter 4. It is suggested that the thermal softening caused by the rise in temperature due to the plastic deformation is not enough to overcome strain hardening for CR-1018 steel. Hence, a strain softening term was necessary to the constitutive model to simulate real softening behavior. Furthermore, the model was used to predict the instability strain, localization strain and evolution of shear localization. Instability strain was seen to decrease with increasing strain rate and temperature, while localization strain decreases only with increasing strain rate, and increases with increasing temperature. Evolution of shear band width is shown to be additively decomposed into two parts; a strain and strain rate part, and a thermal part. Finally, the hydrostatic pressure seems to have noticeable effect in increasing and delaying the instability strain and hence delaying the whole banding process.

With respect to the experimental nano indentation results, the tests were very helpful in obtaining a value for the material length scale through three size effect models. The three models predicted very close results for the length scale to be around 13 μm for CR-1018 steel but more scattered for HR-A36 steel with an average value of 280 nm. The reason why HR-A36 steel has a much smaller length scale is believed to be because hot rolling causes large grains to elongate, and then the elongated grains recrystallize to form smaller grains. Since length scale is a material parameter related to the microstructure of material it would be expected generally that material with smaller grains will have smaller length scale. On the other hand, impression in materials with smaller grains will cover more grains than that in large grain materials, and hence indentation in small grain material will behave more like bulk material compared to large grain material which justifies the need for smaller loads and smaller indentations for HR-A36 steel to capture the size effect compared to CR-1018 steel.

Two models were suggested for dynamic hardness; one is a simple power law and one is a dislocation based equation. The two models were able to capture the increase in hardness of CR-1018 steel due to high strain rates. However, for its simplicity, the power law equation was used along with the dynamic hardness definition to find a simple expression for the dynamic length scale. It was found that the length scale decreases with increasing strain rate which agrees with the experimental observations in the way that deformations at high rates are usually more localized in smaller areas of the material and the deformation at those areas are less affected by the surrounding material. It was also noticed that the sensitivity of the length scale toward the change in the strain rate is half the sensitivity of the hardness or the flow stress in general.

Different numerical examples were run using the finite element method to simulate shear localization in two and three dimensional problems. The two

dimensional steel plate problems under velocity boundary condition showed a very good potential of the gradient theory in regularizing the finite element results. The second example which is the plate punching problem tested the shear band initiation and propagation successfully. It was noticed that the kinetic energy and strain energy stored in the body are both related linearly to the shear band length (i.e. plate thickness), while viscous dissipation is not. The proposed model was able to successfully simulate the load-displacement curves at the early stages of the analysis, but slightly deviated from experimental results at the hardening stage because the material used to obtain the constitutive model parameters might be slightly different than the one used in shear band tests. Also the failure displacements were predicted with good accuracy especially at the lower impact velocities. The last example, where a rigid block impacts a steel beam at high velocities, has shown how deformation mode changes from bending one to shear localization one with increasing impact velocity. When shear banding is the dominating deformation mode, axial deformation waves were seen to initiate and propagate in the beam. As it is expected, the temperature rise is more localized in the beam under high impact velocity, and it is related to the impact velocity in an exponential relation rather than a linear one.

Generally speaking, the proposed constitutive material model used in the finite element with the nonlocal gradient theory associated with the dynamic length scale have shown to be a very promising tool in analyzing and simulating adiabatic shear localization and banding problems. This approach may be used in solving very complex problems where finite element method is becoming the best and more reliable method in engineering applications.

8.3 Future Recommendations

The following issues and ideas are recommended for future research and for conducting more investigations in helping address a better understanding of this subject:

- The physically based nature of strain softening behavior in metals generally and alloys specifically needs to be investigated and studied extensively to understand the physical concepts behind it.
- It will be helpful to have a parametric study for the different parameters of the physically based material models since they are related to the microstructural physical quantities, in order to show the significance of each parameter.
- Experimental tests of dynamic nano indentations are needed to form a better understanding about material length scale at high strain rates.
- Adaptive meshing technique can be used in the future to improve finite element simulation of strain localizations.
- The procedure described in this dissertation can be extended to be applied for cyclic shear banding by conducting experiments and incorporating kinetic hardening to the viscoplasticity formulations.

- Applications can be extended in the future to high impact velocities. However, an equation of state connecting together the pressure, volume, and temperature will be necessary in the formulations.

BIBLIOGRAPHY

ABAQUS (2003) User Manual, Version 6.4, Habbitt, Karlsson and Sorensen, Inc: Providence, RI.

Abed, F.H., and Voyiadjis, G.Z., (2005) "Plastic deformation modeling of AL-6XN stainless steel at low and high strain rates and temperatures using a combination of bcc and fcc mechanisms of metals," International Journal of Plasticity, 21: 1618-1639.

Abed, F.H., and Voyiadjis, G.Z., (2007a) "Adiabatic Shear Band Localizations in BCC Metals at High Strain Rates and Various Initial Temperatures," International Journal for Multiscale Computational Engineering, 5(3-4): 325-349.

Abed, F.H., and Voyiadjis, G.Z., (2007b) "Thermodynamic Consistent Formulations of Viscoplastic Deformations in FCC Metals," Journal of Engineering Mechanics, ASCE, 133(1): 76-86.

Abu Al-Rub, R.K., and Voyiadjis, G.Z., (2004) "Analytical and experimental determination of the material intrinsic length scale of strain gradient plasticity theory from micro- and nano-indentation experiments," International Journal of Plasticity, 20(6): 1139-1182.

Abu Al-Rub, R.K., and Voyiadjis, G.Z., (2006) "A Finite Strain Plastic-Damage Model for High Velocity Impact Using Combined Viscosity and Gradient Localization Limiters: I. Theoretical Formulation," International Journal of Damage Mechanics, 15(4): 293-334.

Abu-Farsakh, G.A., and Almasri, A.H., (2004) "Effect Of Material Nonlinearity On Failure Of Laminated Fibrous Composite Shells Using Finite Element," Proceedings of the 7th International Conference On Concrete Technology in developing countries (ICCT 2004), Kuala Lumpur, Malaysia, 63-75.

Aifantis, E.C., (1984) "On the Microstructural Origin of Certain Inelastic Models," Journal of Engineering Materials and Technology, 106: 326-330.

Aifantis, E.C., (1992) "On the Role of Gradients in the Localization of Deformation and Fracture," International Journal of Engineering Science, 30: 1279-1299.

Almasri, A.H., and Voyiadjis, G.Z., (2006) "Damage Variable and Damage Evolution through Fabric Tensors," Proceedings of the 43rd Annual Technical Meeting of Society of Engineering Science, Pennsylvania USA.

Almasri, A.H., and Voyiadjis, G.Z., (2006) "Fabric Tensors to Quantify Micro-Cracks in Metal Matrix Composite Materials," Proceedings of the 43rd Annual Technical Meeting of Society of Engineering Science, Pennsylvania USA.

Almasri, A.H., and Voyiadjis, G.Z., (2007) “Constitutive Modeling of BCC metals: Application to Ingot Iron,” Proceedings of McMat2007 conference, University of Texas at Austin, Texas, USA.

Almasri, A.H., and Voyiadjis, G.Z., (2007) “Regularizing Shear Bands Using Dynamic Length Scale,” Proceedings of the 44th Annual Technical Meeting of the Society of Engineering Science, College Station, Texas, USA.

Almasri, A.H., and Voyiadjis, G.Z., (2007) “The Effect of Strain Rate on The Dynamic Hardness in Metals,” Journal of Engineering Materials and Technology, 129(4): 505-512.

Almasri, A.H., and Voyiadjis, G.Z., (2008) “A Physically Based Constitutive model for BCC metals with Applications to Iron,” Journal of Engineering Mechanics, in press.

Andrews, E.W., Giannakopoulos, A.E., Plisson, E., and Suresh, S., (2002) “Analysis of the Impact of a Sharp Indenter,” International Journal of Solids and Structures, 39(15): 281-295.

Anton, R.J., and Subhash, G., (2000) “Dynamic Vickers Indentation of Brittle Materials,” Wear, 239(1): 27-35.

Ascheron, C., Huse, C., Kuhn, G., and Neumann, H., (1989) “Microhardness of Sn-doped In P,” Crystal Research and Technology, 24(2): 33-35.

Ashby, M.F., and Frost, H.J., (1975) Constitutive Relations in Plasticity. A. Argon. MIT Press.

Atkins, A.G., and Tabor, D., (1965) “Plastic Indentation in Metals with Cones,” Journal of Mechanics and Physics of Solids, 13(3): 149-164.

Backman, M.E., and Finnegan, S.A., (1973) “The propagation of adiabatic shear,” Metallurgical effects at high strain rates, by Rhode, R.W., Butcher, B.M., Holland, J.R., and Karnes, C.H., (Eds.), Plenum press, New York, 531-543.

Bai, Y., and Dodd., B., (1992) Adiabatic Shear Localization: Occurrence, Theories and Applications. Pergamon Press, New York.

Bammann, D.J., (2001) “A model of crystal plasticity containing a natural length scale.” Materials Science and Engineering A, 309-310: 406-410.

Bammann, D.J., and Aifantis, E.C., (1982) “On a proposal for a continuum with microstrueture.” Acta Mechanica, 45: 91-121.

Bammann, D.J., Mosher, D., Hughes, D.A., Moody, N.R., and Dawson, P.R., (1999) “Using Spatial Gradients to Model Localization Phenomena,” Sandia

National Laboratories Report, SAND99- 8588, Albuquerque, New Mexico 87185 and Livermore, CA.

Batra, R.C., (1987) “The initiation and growth of, and the interaction among, adiabatic shear bands in simple and dipolar materials,” International Journal of Plasticity, 3: 75-89.

Batra, R.C., (1998) “Numerical solution of initial-boundary value problems with shear localization,” Localization and Fracture Phenomenon in Inelastic Solids, by Perzyna, P., (Ed.), Springer, Wien, NY, 301-389.

Batra, R.C., and Chen, L., (2001) “Effect of viscoplastic relations on the instability strain, shear band initiation strain, the strain corresponding to the minimum shear band spacing, and the band width in a thermoviscoplastic material,” International Journal of Plasticity, 17: 1465-1489.

Batra, R.C., and Gummalla, R.R., (2000) “Effect of Material and Geometric Parameters on Deformations Near The Notch-Tip of a Dynamically Loaded Pre-notched Plate,” Internationl Journal of Fracture, 101: 99-140.

Batra, R.C., and Kim, C.H., (1990) “Effect of viscoplastic flow rules on the initiation and growth of shear bands at high strain rates,” Journal of the Mechanics and Physics of Solids, 38: 859-874.

Batra, R.C., and Wang, L., (1994) “Analysis of dynamic shear bands under combined loading,” International Journal For Engineering Analysis And Design, 1: 79-90.

Batra, R.C., and Wei, Z.G., (2007) “Instability strain and shear band spacing in simple tensile/compressive deformations of thermoviscoplastic materials,” International Journal of Impact Engineering, 34: 448-463.

Baucom, J.N., and Zikry, M.A., (1999) “Perturbation analysis of high strain-rate shear localization in B.C.C. crystalline materials,” Acta Mechanica, 137: 109-129.

Bazant, Z.P., and Pijaudier-Cabot, G., (1988) “Nonlocal continuum damage, localization instability and convergence,” Journal of Applied Mechanics, 55: 287-293.

Bazant, Z.P., Belytschko, T., and Chang, T.P., (1984) “Continuum theory for strain-softening,” ASCE Journal of Engineering Mechanics, 110: 1666-1691.

Benallal, A., Fudoli, C.A., and Venturini, W.S., (2002) “An implicit BEM formulation for gradient plasticity and localization phenomena,” International Journal for Numerical Methods in Engineering, 53: 1853-1869.

Berthier, L., Biroli, G., Bouchaud, J.P., Cipelletti, L., El Masri, D., L'Hote, D., Ladieu, F., and Pierno, M., (2005) "Direct Experimental Evidence of a Growing Length Scale Accompanying the Glass Transition," Science, 310(5755): 1797-1800.

Bodner, S.R. and Partom, Y., (1975) "Constitutive equations for elastic–viscoplastic strain-hardening materials," Journal of Applied Mechanics, 42: 385-389.

Boria, R.I., (2002) "Finite element simulation of strain localization with large deformation: capturing strong discontinuity using a Petrov-Galerkin multiscale formulation," Computer Methods in Applied Mechanics and Engineering, 191: 2949-2978.

Bourne, B., Jones, P.N., and Markham, J.A., (1984) "Microstructural features of sock-loaded metals," Machanical Properties at High Rates of Strain, by Harding, J., (Ed.), Conference Series Number 70, The Institute of Physics, Bristol and London.

Bronkhorst, C.A., Cerreta, E.K., Xue, Q., Maudlin, P.J., Mason, T.A., and Gray III, G.T., (2006) "An experimental and numerical study of the localization behavior of tantalum and stainless steel," International Journal of Plasticity, 22: 1304-1335.

Brun, M., Bigoni, D., and Capuani, D., (2003) "Bifurcations and shear bands by the boundary element method," 16th AIMETA Congress of Theoretical and Applied Mechanics, Ferrara.

Burns, T.J., and Davies, M.A., (2002) "On repeated adiabatic shear band formation during high-speed machining," International Journal of Plasticity, 18: 487-506.

Cabot, T.G.P., and Bazant, Z.P., (1987) "Nonlocal damage theory," ASCE Journal of Engineering Mechanics, 113: 1512-1533.

Chen, S.H., and Wang, T.C., (2002) "A New Deformation Theory with Strain Gradient Effects," International Journal of Plasticity, 18: 971-995.

Chong, A.C.M., and Lam, D.C.C., (1999) "Strain gradient plasticity effect in indentation hardness of polymers," Journal of Materials Research, 14(10): 4103-4110.

Christian, J.W., (1983) "Some surprising features of the plastic deformation of body centered cubic metals and alloys." Metallurgical and Materials Transactions A, 14A: 1237-1256.

Clough, R.B., Webb, S.C., and Armstrong, R.W., (2003) “Dynamic Hardness Measurements Using a Dropped Ball: with Application to 1018 Steel,” Materials Science and Engineering A, 360(1-2): 396-407.

Columbus, D., and Grujicic, M., (2002) “A Comparative Discrete-Dislocation/ Nonlocal Crystal-Plasticity Analysis of Plane-Strain Mode I Fracture,” Materials Science and Engineering A, 323: 386-402.

Considère, A.G., (1885) “Memoire sur l’Emploi du Fer et de l’Acier dans les Constructions,” Annales des Ponts et Chausses, 6(9): 574-775.

Costin, L.S., Crisman, E.E., Hawley, R.H., and Duffy, J., (1980) “On the Localization of Plastic Flow in Mild Steel Tubes Under Dynamic Torsional Loading,” in Mechanical Properties of High Rates of Strain, Conf. Ser. No. 47, Harding, J., (Ed.), Institute of Physics, London, 90-100.

Daneshi, G.H., and Harding, J., (1974) “The high speed punching of a quenched and tempered 11/2% Cr Mo steel,” Proceedings on Mechanical Properties at High Rates of Strain. Conference Series no. 21, 404-416.

Dao, M., Chollacoop, N., Van Vliet, K.J., Venkatesh, T.A., and Suresh, S., (2001) “Computational Modeling of the Forward and Reverse Problems in Instrumented Sharp Indentation,” Acta Materialia, 49(19): 3899-3918.

Das, S.P., (2000) “Dynamic length scales and feedback from long-time structural relaxation in a simple liquid,” Journal of Physics: Condensed Matter, 12: 6423-6430.

Davies, R., and Dhawan, S.M., (1965) “A preliminary investigation of high-speed blanking and piercing of metals,” Proceedings of the Institution of Mechanical Engineers 180, 182-196.

de Borst, R., and Mühlhaus, H.B., (1992) “Gradient-Dependent Plasticity Formulation and Algorithmic Aspects,” International Journal of Numerical Methods Engineering, 35: 521-539.

De Borst, R., and Pamin, J., (1996) “Some novel developments in finite element procedures for gradient-dependent plasticity,” International Journal for Numerical Methods in Engineering, 39: 2477-2505.

de Borst, R., Sluys, L.J., (1991) “Localization in a Cosserat continuum under static and dynamic loading conditions,” Computer Methods in Applied Mechanics and Engineering, 90: 805-827.

de Saint-Venant, B., (1870) “Memoire sur l’establissement des equations differentielles des mouvements interieurs operes dans les corps solides ductiles au dela des limites ou l’ elasticite pourrait les ramener a leur premier etat.”

Comptes Rendus hebdomadaire s des Seances de l'A cademie de s Sciences, 70: 473-480.

Dornowski, W., and Perzyna, P., (2000) "Localization Phenomena in Thermo-Viscoplastic Flow Processes Under Cyclic Dynamic Loadings," Computer Assisted Mechanics and Engineering Sciences, 7: 117-160.

Dowling, A.R., Harding, J., and Campbell, J.D., (1970) "The dynamic punching of metals," Journal of Institute of Metals, 98: 215-224.

Drucker, D.C. (1951). "A more fundamental approach to plastic stress-strain relations," ASME, Proc. First US National Congress of Applied Mechanics, 487-491.

Duan, C.Z., and Wang, M.J., (2005) "Characteristics of adiabatic shear bands in the orthogonal cutting of 30CrNi3MoV steel," Journal of Materials Processing Technology, 168: 102-106.

Duan, Z.Q., Li, S.X., and Huang, D.W., (2003) "Microstructures and adiabatic shear bands formed by ballistic impact in steels and tungsten alloy," Fatigue and Fracture of Engineering Materials and Structures, 26(12): 1119-1126.

Duesbery, M.S., and Vitek, V., (1998) "Plastic anisotropy in b.c.c. transition metals." Acta Materialia, 46(5): 1481-1492.

Edwards, B.J., Feigl, K., Morrison, M.L., Yang, B., Liaw, P.K., and Buchanan, R.A., (2005) "Modeling the Dynamic Propagation of Shear Bands in Bulk Metallic Glasses," Scripta Materialia, 53(7): 881-885.

Elmustafa, A.A., and Stone, D.S., (2003) "Nanoindentation and the Indentation Size Effect: Kinetics of Deformation and Strain Gradient Plasticity," Journal of the Mechanics and Physics of Solids, 51: 357-381.

Farren, W.S., and Taylor, G.I., (1925) "The heat developed during plastic extension of metals," Proceedings of the Royal Society of London, Series A, 107(743): 422-451.

Feng, H., and Bassim, M.N., (1999) "Finite element modeling of the formation of adiabatic shear bands in AISI 4340 steel," Materials Science and Engineering, 266: 255-260.

Fleck, N.A., and Hutchinson, J.W., (1997) "Strain Gradient Plasticity," Advances in Applied Mechanics, 33: 295-361.

Fleck, N.A., and Hutchinson, J.W., (2001) "A Reformulation of Strain Gradient Plasticity," Journal of the Mechanics and Physics of Solids, 49: 2245-2271.

Fleck, N.A., Muller, G.M., Ashby, M.F., and Hutchinson, J.W., (1994) “Strain gradient plasticity: theory and experiment,” Acta Metallurgica et Materialia, 42: 475-487.

Follansbee, P.S., Regazzoni, G., and Kocks, U.F., (1984) “The Transition to Drag-Controlled Deformation in Copper at High Strain Rates,” Proceedings of the Third Conference on the Mechanical Properties of materials at High Rates of Strain, Oxford, by Harding, J., (Ed.), 71-80.

Freed, A.D., Raj, S.V., and Walker, K.P., (1991) “Stress versus temperature dependent activation energies in creep.” [microform] Prepared for the 3rd International Conference on Constitutive Laws or Engineering Materials, Tucson, Arizona.

Gao, H., Huang, Y., and Nix, W.D., (1999) “Modeling Plasticity at the Micrometer Scale,” Naturwissenschaften, 86: 507-515.

Gao, H., Huang, Y., Nix, W.D., Hutchinson, J.W., (1999) “Mechanism-Based Strain Gradient Plasticity - I. Theory,” Journal of the Mechanics and Physics of Solids, 47(6): 1239-1263.

Geil, G.W., and Carwile, N.L., (1950) “Tensile properties of ingot iron at low temperatures.” Journal of Research of the National Bureau of Standards, 45(2): 129-147.

Gillis, P.P., and Gilman, J.J., (1965) “Dynamical dislocation theory of crystal plasticity.” Journal of Applied Physics, 86: 3370-3380.

Giovanola, J.H., (1988a) “Adiabatic shear banding under pure shear loading. Part1: Direct observation of strain localization and energy dissipation measurement,” Mechanics of Materials, 7: 59-71.

Giovanola, J.H., (1988b) “Adiabatic shear banding under pure shear loading. Part II: Fragtographic and metallorgraphic observations,” Mechanics of Materials, 7: 73-87.

Glema, A., Lodygowski, T., and Perzyna, P., (2000) “Interaction of Deformation Waves and Localization Phenomena in Inelastic Solids,” Computer Methods in Applied Mechanics and Engineering, 183: 123-140.

Gourdin, W.H., and Lassila, D.H., (1996) “Multiple mechanisms in the thermally activated plastic flow of tantalum.” Proceedings of the American Physical Society Topical Conference: Shock Wave in Condensed Matter, Seattle, WA, 370, 519-522.

Grebe, H.A., Pak, H., and Meyers, M.A., (1985) “Adiabatic shear localization in titanium an Ti-6 Pct Al-4 Pct V alloy,” Metallurgical Transactions, 16: 761-775.

Guduru, P.R., Rosakis, A.J., and Ravichandran, G., (2001) “Dynamic shear bands: an investigation using high speed optical and infrared diagnostics,” Mechanics of Materials, 33: 371-402.

Guille, J., and Sieskind, M., (1991) “Microindentation studies on BaFCl single crystals,” Journal of Materials Science, 26(4): 899-903.

Gurson, A.L., (1977) “Continuum Theory of Ductile Rupture by Void Nucleation and Growth. Part I: Yield Criteria and Flow Rules for Porous Ductile Media,” Journal of Engineering Materials and Technology, 99(2): 2-15.

Hancock, E.L., (1908) “Results of tests on materials subjected to combined stresses,” Philosophical Magazine, 11: 276.

Hay, J.L., and Pharr, G.M., (2000) “Instrumented indentation testing,” ASM Handbook, Volume 8: Mechanical Testing and Evaluation, Materials Park OH, by Kuhn, H., Medlin, D., (Eds.): 232-243.

Hendrix, B.C., (1995) “The use of shape correction factors for elastic indentation measurements,” Journal of Materials Research, 10(2): 255-257.

Hoge, K.G, and Mukherjee, A.K., (1977) “The temperature and strain rate dependence of the flow stress of tantalum,” Journal of Materials Science, 12: 1666-1672.

Hollomon, J.H., (1944) “The effect of heat treatment and carbon content on the work hardening characteristics of several steels.” Transactions of the American Society of Metals, 32: 123-131.

Hopkins, H.G., (1960) “Dynamic Expansion of Spherical Cavities in Metal,” Progress in Solid Mechanics 1, by Sneddon, I.N., and Hill, R., (Eds.), North Holland, Amsterdam.

Huang, X.L., (1987) Deformed Shear Bands and Ductile Fracture. Master Thesis, Institute of Mechanics, Beijing.

Huang, Y., Xue, Z., Gao, H., and Xia, Z.C., (2000) “A Study of Micro-Indentation Hardness Tests by Mechanism-Based Strain Gradient Plasticity,” Journal of Material Research, 15: 1786-1796.

Jia, D, Rames, K.T., and Ma, E., (2003) “Effects of nanocrystalline and ultrafine grain sizes on constitutive behavior and shear bands in iron.” Acta Materialia, 51: 3495-3509.

Johnson, G., and Holmquist, T., (1988) “Evaluation of cylinder impact test data for constitutive model constants.” Journal of Applied Physics, 64: 3901-3910.

Johnson, G.R., and Cook, W.H., (1983) “A constitutive model and data for metals subjected to large strains, high strain rates, and high temperatures,” Proceedings of the 7th International Symposium on Ballistics, the Hague, the Netherlands, The Netherlands, 541-547.

Johnson, W., and Travis, F.W., (1965) “High speed blanking of copper,” Proceedings of the Institution of Mechanical Engineers, 180: 197-204.

Kalthoff, J.F., (2000) “Modes of dynamic shear failure in solids,” International Journal of Fracture, 101: 1-31.

Kelly, J.M., and Gillis, P.P., (1974) “The influence of a limiting dislocation flux on the mechanical response of polycrystalline metals.” International Journal of Solids and Structures, 10: 45-59.

Kim, C.H., and Batra, R.C., (1992) “Effect of initial temperature on the initiation and growth of shear bands in a plain carbon steel,” International Journal of Non-Linear Mechanics, 27(2): 279-291.

Klepaczko, J.R., (1987) “Modelling of structural evolution at medium and high strain rates, FCC and BCC metals.” Impact: Effects of fast transient loading, A.A. Balkema, Rotterdam-Brookfield, Denmark, 3-35.

Klepaczko, J.R., (1988) “Constitutive modelling in dynamic plasticity based on physical state variables: A review,” International Proceedings on Mechanical and Physical Behaviour of Materials under Dynamic Loading, Les editions de physique, Les Ulis., C3/49, 553-560.

Klopp, R.W., Clifton, R.J., and Shawki, T.G., (1985) “Pressure-Shear Impact and the Dynamic Viscoplastic Response of Metals,” Mechanics of Materials, 4(3-4): 375-385.

Kocks, U.F., Argon, A.S., and Ashby, M.F., (1975) “Thermodynamics and Kinetics of Slip,” Progress in Materials Science, by Chalmers, B., Christian, J.W., and Massalski, T.B., (Eds.), Pergamon Press, Oxford, 19: 1-129

Koeppel, B.J., and Subhash, G., (1999) “Characteristics of Residual Plastic Zone under Static and Dynamic Vickers Indentations,” Wear, 224(12): 56-67.

Kubin, L.P., and Estrin, Y., (1990) “Evolution for dislocation densities and the critical conditions for the portevin-le chatelier effect.” Acta Metallurgia et Materialia, 38: 697-708.

Kumar, A., and Kumble, R.G., (1969) “Viscous Drag Dislocation at High Strain Rates in Copper,” Journal of Applied Physics, 40(9): 3475-3480.

Lasry, D., and Belytschko, T., (1988) “Localization Limiters in Trasient Problems,” International Journal of Solids and Structures, 24: 581-597.

Le Monds, J., and Needleman, A., (1986b) “An Analysis of Shear Band Development Incorporating Heat Conduction,” Mechanics of Materials, 5: 363-373.

Lee, C.G., Park, W.J., Lee, S., and Shin, K.S., (1998) “Microstructural development of adiabatic shear bands formed by ballistic impact in a WELDALITE 049 Alloy,” Metallurgical and Materials Transactions A, 29: 477-483.

Lee, W., Lin, C., Liu, C., and Tzeng, F., (2004) “Impact properties of 304L stainless steel GTAW joints elevated by high strain rate of compression tests,” Journal of Nuclear Materials, 335: 335-344.

LeMonds, J., and Needleman, A., (1986a) “Finite Element Analysis of Shear Localization in Rate and Temperature Dependent Solids,” Mechanics of Materials, 5: 339-361.

Lennon, A.M., and Ramesh, K.T., (2004) “The influence of crystal structure on the dynamic behavior of materials at high temperatures,” International Journal of Plasticity, 20: 269-290.

Li, S., Liu, W.K., Rosakis, A.J., Belystchko, T., and Hao, W., (2002) “Mesh-Free Galerkin Simulations of Dynamic Shear Band Propagation and Failure Mode Transition,” International Journal of Solids and Structures, 39: 1213-1240.

Lim, Y.Y., and Chaudhri, Y.Y., (1999) “The Effect of the Indenter Load on the Nanohardness of Ductile Metals: An Experimental Study of Polycrystalline Work-Hardened and Annealed Oxygen-Free Copper,” Philosophical Magazine A, 79(12): 2979-3000.

Littonski, J., (1977) “Plastic Flow of a Tube Under Adiabatic Torsion,” Bulletin of the Polish Academy of Sciences, 25: 7-14.

Lu, J., Suresh, S., and Ravichandran, G., (2003) “Dynamic Indentation for Determining the Strain Rate Sensitivity of Metals,” Journal of the Mechanics and Physics of Solids, 51(11-12): 1923-1938.

Ludwik, P. (1908) “Die kegeldruckprobe, ein neues verfahren zur hartebestimmung von materialien,” Springer, Berlin.

Ludwik, P., (1909) Elemente der Technologischen Mechanik. Springer-Verlag, Berlin.

Ma, Q., and Clarke, D.R., (1995) “Size dependent hardness of silver single crystals,” Journal of Materials Research, 10: 853-863.

MacGregor, C.W., (1944a) “The true stress-strain tension test—its role in modern materials testing: Part I.” Journal of the Franklin Institute, 238(2): 111-135.

MacGregor, C.W., (1944b) “The true stress-strain tension test—its role in modern materials testing: Part II.” Journal of the Franklin Institute. 238(3): 159-176.

Marchand, A., and Duffy, J., (1988) “An experimental study of the formation process of adiabatic shear bands in a structural steel,” Journal of the Mechanics and Physics of Solids, 36: 251-283.

Marsh, D.M., (1964) “Plastic Flow in Glass,” Proceedings of the Royal Society of London. Series A, Mathematical and Physical Sciences, 279(1378): 420-435.

Mason, C., and Worswick, M.J., (2001) “Adiabatic shear in annealed and shock-hardened iron and in quenched and tempered 4340 steel,” International Journal of Fracture, 111: 29-51.

Massey, H.F., (1928) “The flow of metal during forging,” Proceedings Manchester Association of Engineers, 21-26.

McElhaney, K.W., Valssak, J.J., and Nix, W.D., (1998) “Determination of Indenter Tip Geometry and Indentation Contact Area for Depth Sensing Indentation Experiments,” Journal of Materials Research, 13: 1300-1306.

Meyers, M.A., (1994) Dynamic Behavior of Materials. Wiley, New York.

Miller, A., (1976) “An inelastic constitutive model for monotonic, cyclic, and creep deformation: Part I-Equations development and analytical procedures.” Journal of Engineering Materials Technology, 98: 97-105.

Molinari, A. and Clifton, R.J., (1987) “Analytical characterization of shear localization in thermoviscoplastic solids,” Journal of Applied Mechanics ASME, 54: 806-812.

Mühlhaus, H.B., and Aifantis, E.C., (1991) “A Variational Principle for Gradient Plasticity,” International Journal of Solids and Structures, 28: 845-857.

Naka, T., Torikai, G., Hino, R., and Yoshida, F., (2001) “The effects of temperature and forming speed on the forming limit diagram for type 5083 aluminum-magnesium alloy sheet,” Journal of Materials Processing Technology, 113: 648-653.

Needleman, A., (1988) “Material Rate Dependent and Mesh Sensitivity in Localization Problems,” Computer Methods in Applied Mechanics and Engineering, 67: 68-85.

Needleman, A., (1989) “Dynamic shear band development in plane strain,” Journal of Applied Mechanics, 56: 1-9.

Needleman, A., and Tvergaard, V., (2000) “Numerical Modeling of The Ductile-Brittle transition,” International Journal of Fracture, 101: 73-97.

Nemat-Nasser, S., and Li, Y., (1998) “Flow Stress of F.C.C. Polycrystals with Application to OFHC Cu,” Acta Materialia, 46(2): 565-577.

Nix, W.D., and Gao, H., (1998) “Indentation Size Effects in Crystalline Materials: A Law for Strain Gradient Plasticity,” Journal of the Mechanics and Physics of Solids, 46 (3): 411-425.

Odeshi, A.G., Bassim, M.N., Al-Ameeri, S., and Li, Q., (2005) “Dynamic shear band propagation and failure in AISI 4340 steel,” Journal of Materials Processing Technology, 169: 150-155.

Oliver, J., (1989) “A consistent characteristic length for smeared cracking problem,” International Journal for Numerical Methods in Engineering, 28: 461-474.

Oliver, W.C., and Pharr, G.M., (1992) “An improved technique for determining hardness and elastic modulus using load and displacement sensing indentation experiments,” Journal of Materials Research, 7(6): 1564-1583.

Perzyna, P., (1966) “Fundamental Problems Visco-plasticity,” In: Kuerti, H. (Ed.), Advances in Applied Mechaics, Academic Press, 9: 243-377.

Perzyna, P., (1986) “Internal State Variable Description of Dynamic Fracture of Ductile Solids,” International Journal of Solids and Structures, 22: 797-818.

Perzyna, P., (1995) “Interactions of Elastic-Viscoplastic Waves and Localization Phenomena in Solids,” In: Wegner, J.L., Norwood, F.R. (Eds.) Proc. ASME Book AMR, 137: 114-121.

Pijaudier-Cabot, T.G.P., and Bazant, Z.P., (1987) “Nonlocal Damage Theory,” ASCE Journal of Engineering Mechanics, 113: 1512-1533.

Pollack, H.W., Materials Science and Metallurgy, 4th edition, Prentice-Hall, 1988.

Prandtl, L., (1920) “Uber die Härte plastischer Körper,” (The Hardness of Plastic Bodies), Nachr. D. Gesellschaft d. Wissensch. Zu gottingen, Mathematisch-physikalische Klasse, 74-85.

Prasad, Y.V.R.K., and Rao, K.P., (2004) “Kinetics of high-temperature deformation of polycrystalline OFHC copper and the role of dislocation core diffusion,” Philosophical Magazine, 84(28): 3039-3050.

Raftenberg, M.N., and Krause, C.D., (1999) “Metallographic observations of armor steel specimens from plates perforated by shaped charge jets,” International Journal of Impact Engineering, 23: 757-770.

Ramanathan, R., and Foley, R.P., (2001) “Effect of Prior Microstructure on Austenite Decomposition and Associated Distortion,” MMAE Department, Illinois Institute of Technology.

Ratner, S.I., (1949) Strength and Plasticity. National Defense Press, Moscow.

Regazzoni, C., and Montheillet, F., (1984) “Influence of Strain Rate on the Flow Stress and Ductility of Copper and Tantalum at Room Temperature,” Proceedings of the Third Conference on the Mechanical Properties of materials at High Rates of Strain, Oxford, by Harding, J., (Ed.), 63-70.

Rice, J.R., and Tracey, D.M., (1969) “On The Ductile Enlargement Of Voids In Triaxial Stress Fields,” Journal of the Mechanics and Physics of Solids, 17: 201-217.

Rittel, D., Ravichandran, G., and Lee, S., (2002) “Large Strain Constitutive Behavior of OFHC Copper Over a Wide Range of Strain Rates Using the Shear Compression Specimen,” Mechanics of Materials, 34(16): 627-642.

Rittel, D., Ravichandran, G., and Venkert, A., (2006) “The mechanical response of pure iron at high strain rates under dominant shear.” Materials Science and Engineering A, 432: 191–201.

Roessig, K.M., and Mason, J.J., (1999a) “Adiabatic shear localization in the dynamic punch test, part I: experimental investigation,” International Journal of Plasticity, 15: 241-262.

Roessig, K.M., and Mason, J.J., (1999b) “Adiabatic shear localization in the dynamic punch test, part II: numerical simulations,” International Journal of Plasticity, 15: 263-283.

Rogers, H.C., (1979) “Adiabatic plastic deformation,” Annual Review of Materials Science, 9: 283-311.

Rogers, H.C., and Shastry, C.V., (1981) “Material factors in adiabatic shearing in steels,” Shock Wave and High Strain Rate Phenomena in Metals, by Meyers, M.A., and Murr, L.E., (Eds.), Plenum Press, New York, 285-298.

Samuels, L.E., and Mulhearn, T.O., (1957) “An Experimental Investigation of the Deformed Zone Associated with Indentation Hardness Impressions,” Journal of Mechanics and Physics of Solids, 5(2): 125-134.

Senseny, P.E., Duffy, J., and Hawley, R.H., (1978) “Experiments on Strain Rate History and Temperature Effects During the Plastic Deformation of Close-Packed Metals,” Journal of Applied Mechanics, 45(1): 60-66.

Shawki, T.G., and Clifton, R.J., (1989) “Shear Band Formation in Thermal Viscoplastic Materials,” Mechanics of Materials, 8(1): 13-43.

Shockey, D.A., (1986) “Materials aspects of adiabatic shear phenomenon,” Metallurgical Applications of Shock-Wave and High-strain-Rate Phenomena, by Murr, L.E, Staudhammer, K.P., and Meyers, M.A., (Eds.), Marcel Dekker Press, New York, 633-656

Shu, J.Y., and Fleck, N.A., (1998) “The prediction of a size effect in micro-indentation,” International Journal of Solids and Structure, 35: 1363-1383.

Slater, R.A.C., and Johnson, W., (1967) “The effect of temperature, speed, and strain rate on the force and energy required in blanking,” International Journal of Mechanical Sciences, 9(5): 271.

Smith. C.A., (1909) “Some experiments on solid steel bars under combined stress,” Engineering, 20: 238-243.

Sneddon, I.N., (1965) “The relation between load and penetration in the axisymmetric Boussinesq problem for a punch of arbitrary profile,” International Journal of Engineering Science, 3:47-57.

Sridhar, M.R., and Yovanovich, M.M., (1996) “Empirical methods to predict Vickers microhardness ,” Wear, 193(1): 91-98.

Staker, M.R., and Holt, D.L., (1972) “The Dislocation Cell Size and Dislocation Density in Copper Deformed at Temperatures between 25 and 700ºC,” Acta Metallurgica, 20(4): 569-579.

Steidel, R.F., and Makerov, C.E., (1960) “The Tensile Properties of Some Engineering Materials at Moderate Rates of Strain,” ASTM bulletin, Philadelphia, No. 247: 57-64.

Stein, D.L., and Low, J.R., (1960) “Mobility of edge dislocations in silicon-iron crystals,” Journal of Applied Physics, 31: 362-369.

Stelmashenko, N.A., Walls, M.G., Brown, L.M., and Milman, Y.V., (1993) “Microindentations on W and Mo oriented single crystals: an STM study,” Acta Metallurgica et Materialia, 41: 2855-2865.

Stock, T.A.C., and Wingrove, A.L., (1971) “The energy required for high speed shearing of steel,” Journal of Mechanical Engineering Science, 13: 110-115.

Stolken, J.S., Evans, A.G., (1998) “A microbend test method for measuring the plasticity length scale,” Acta Materialia, 46(14): 5109–5115.

Sundararajan, G., and Tirupataiah, Y., (2006a) “The Localization of Plastic Flow under Dynamic Indentation Conditions: I Experimental Results,” Acta Materialia, 54(3): 565-575.

Sundararajan, G., and Tirupataiah, Y., (2006b) “The Localization of Plastic Flow under Dynamic Indentation Conditions: II. Analysis of Results,” Acta Materialia, 54(3): 577-586.

Tabor, D., (1951), The hardness of metals. Oxford: Clarendon Press.

Tanner, A.B., and McDowell, D.L., (1999) “Deformation, temperature and strain rate sequence experiments on OFHC Cu,” International Journal of Plasticity, 15: 375-399.

Taylor, G., (1992) “Thermally-activated deformation of BCC metals and alloys.” Progress in Materials Science, 36: 29-61.

Taylor, G.I. and Quinney, H., (1934) “The latent energy remaining in a metal after cold working,” Proceedings of the Royal Society of London, Series A, 143(849): 307-326.

Taylor, G.I., (1938) “Plastic Strain in Metals,” Journal of the Institute of Metals, 62: 307-324.

Taylor, G.I., and Quinney, H., (1931) “The plastic distortion of metals,” Philosophical Transactions of the Royal Society of London Series A, 230: 323-362.

Tickoo, R., Tandon, R.P., Bamzai, K.K., and Kotru, P.N., (2003) “Microindentation studies on samarium-modified lead titanate ceramics,” Materials Chemistry and Physics, 80(2): 446-451.

Timothy, S.P., and Hutchings, I.M., (1985) “The structure of adiabatic shear bands in a Titanium alloy,” Acta Metallurgica, 33(4): 667-676.

Tresca, H., (1864) “Sur I’e coulement des corps solids soumis a de fortes pression,” Comptes Rendus hebdomadaires des Seances de l’ Academie des Sciences, 59: 754-758.

Tresca, H., (1878) “On further application to the flow of solids,” Proceedings Institute of Mechanical Engineers, 30: 301-345.

Vasauskas, V., (2002) “Dynamic Hardness During Different Phases of Indentation,” VDI BERICHTE: Joint International Conference IMEKO TC3/TC5/TC20, no. 1685: 359-364.

Vengatesan, B., Kanniah, H., and Ramasvamy, P., (1986) “Microhardness and crack patterns of CVT grown CdGa2S4 single crystals,” Journal of Materials Science Letters, 5(10): 987-988.

Voyiadjis, G.Z., (1988) “Degradation of Elastic Modulus in Elasto-Plastic Coupling with Finite Strains,” International Journal of Plasticity, 4: 335-353.

Voyiadjis, G.Z., Alsaleh, M.A., and Alshibli, K.A., (2005) “Evolving Internal Length Scales in Plastic Strain Localization for Granular Materials,” International Journal of Plasticity, 21(10): 2000-2024.

Voyiadjis, G.Z., and Abed, F.H., (2005) “Microstructural Based Models for BCC and FCC Metals with Temperature and Strain Rate Dependency,” Mechanics of Materials, 37(2-3): 355-378.

Voyiadjis, G.Z., and Abed, F.H., (2005b) “Effect of Dislocation Density Evolution on the Thermomechanical Response of Metals with Different Crystal Structures at Low and High Strain rates and Temperatures,” Archives of Mechanics, 57(4): 299-343.

Voyiadjis, G.Z., and Abed, F.H., (2006a) “Implicit Algorithm for Finite Deformation Hypoelastic-Viscoplasticity in FCC Metals,” International Journal for Numerical Methods in Engineering, 67: 933-959.

Voyiadjis, G.Z., and Abed, F.H., (2006b) “A Coupled Temperature and Strain Rate Dependent Yield Function for Dynamic Deformations of BCC Metals,” International Journal of Plasticity, 22(8): 1398-1431.

Voyiadjis, G.Z., and Abed, F.H., (2007) “Transient Localizations in Metals Using Microstructure-Based Yield Surfaces,” Modelling and Simulation in Materials Science and Engineering, 15: S83-S95.

Voyiadjis, G.Z., and Abu Al-Rub R.K., (2002) “Length Scales in Gradient Plasticity,” Proceedings of the IUTAM Symposium on Multiscale Modeling and Characterization of Elastic-Inelastic Behavior of Engineering Materials, by Ahzi, S., Cherkaoui, M., Khaleel, M.A., Zbib, H.M., Zikry, M.A., and LaMatina, B., (Eds.), Morocco, October 2002, Kluwer Academic Publishers, 167-174.

Voyiadjis, G.Z., and Abu Al-Rub, R.K., (2005) “Gradient Plasticity Theory with a Variable Length Scale Parameter,” International Journal of Solids and Structures, 42(14): 3998-4029.

Voyiadjis, G.Z., and Abu Al-Rub, R.K., (2006) “A Finite Strain Plastic-Damage Model for High Velocity Impact Using Combined Viscosity and Gradient Localization Limiters: II. Numerical Aspects and Simulations,” International Journal of Damage Mechanics, 15(4): 335-373.

Voyiadjis, G.Z., and Almasri, A.H., (2005) “Using Fabric Tensors to Quantify Micro-Cracks in Composite Materials,” Proceedings of McMat2005: Joint ASME/ASCE/SES Conference on Mechanics and Materials, Baton Rouge, Louisiana, USA.

Voyiadjis, G.Z., and Almasri, A.H., (2006) “Effect of Strain Rate in Dynamic Hardness for Metals,” Proceedings of the 43rd Annual Technical Meeting of Society of Engineering Science, Pennsylvania USA.

Voyiadjis, G.Z., and Almasri, A.H., (2007) “Effect of Strain Rate in Dynamic Hardness for Metals through Constitutive Modeling,” Proceedings of TMS Annual Meeting & Exhibition, Orlando, Florida, USA.

Voyiadjis, G.Z., and Almasri, A.H., (2007) “Experimental Study and Fabric Tensor Quantification of Micro-Crack Distributions in Composite Materials,” Journal of Composite Materials, 41(6): 713-745.

Voyiadjis, G.Z., and Almasri, A.H., (2008) “A Physically Based Constitutive model for FCC metals with Applications to Dynamic Hardness,” Mechanics of Materials, 2008, doi:10.1016/j.mechmat.2007.11.008.

Voyiadjis, G.Z., and Buckner, N.E., (1983) “Indentation of a Half-Space with a Rigid Indentor,” International Journal for Numerical Methods in Engineering, 19(10): 1555-1578.

Voyiadjis, G.Z., and Deliktas, B., (2000) “Multi-Scale Analysis of Multiple Damage Mechanics Coupled with Inelastic Behavior of Composite Materials,” Mechanics Research Communications, 27(3): 295-300.

Voyiadjis, G.Z., and Dorgan, R.J., (2001) “Gradient Formulation in Coupled Damage-Plasticity,” Archives of Mechanics, 53(4-5): 565-597.

Voyiadjis, G.Z., and Dorgan, R.J., (2004) “Bridging of Length Scales through Gradient Theory and Diffusion Equations of Dislocations,” Computer Methods in Applied Mechanics and Engineering, 193(17-20): 1671-1692.

Voyiadjis, G.Z., Deliktas, B., and Aifantis, E.C., (2001) “Multi-scale Analysis of Multiple Damage Mechanics Coupled with Inelastic Behavior of Composite Materials,” Journal of Engineering Mechanics, 127(7): 636-645.

Voyiadjis, G.Z., Poe, A.A., and Kiousis, P.D., (1986) “Finite-Strain Elasto-Plastic Solution for Contact Problems,” ASCE Journal of Engineering Mechanics, 112(3): 273-292.

Wang, W., Huang, Y., Hsia, K.J., Hu, K.X., and Chandra, A., (2003) “A Study of Microbend Test by Strain Gradient Plasticity,” International Journal of Plasticity, 19: 365-382.

Wingrove, A., (1973) “The influence of projectile geometry on adiabatic shear and target failure,” Metallurgical Transactions, 4: 1829-1833.

Winstone, M.R., (1984) “Influence of prestress on the yield surface of the cast nickel super alloy Mar-M002 at elevated temperature,” Mechanical Behavior of Materials-4 (ICM-4), Carlsson, J., and Ohlson, N.G., (Eds.), Pergamon Press, 1: 199-205.

Winter, R.W., (1975) “Adiabatic shear of titanium and polymethylmethacrylate,” Philosophical magazine, 31: 765-773.

Woodward, R.L., Baxter, B.J., and Scarlett, N.V.Y., (1984) “Mechanics of the adiabatic shear plugging failure in high strength Aluminum and Titanium alloys,” Mechanical Properties at High Rates of Strain, by Harding, J. (Ed.), Conference Series Number 70, The Institute of Physics, Bristol and London.

Wright, T.W., (1987) “Steady shearing in a viscoplastic solid,” Journal of the Mechanics and Physics of Solids, 35: 269-282.

Wright, T.W., and Batra, R.C., (1985) “The initiation and growth of adiabatic shear bands,” International Journal of Plasticity, 1: 205-212.

Xu, Y.B., Zhong, W.L., Chen, Y.J., Shen, L.T., Liu, Q., Bai, Y.L., and Meyers, M.A., (2001) “Shear localization and recrystallization in dynamic deformation of 8090 Al–Li alloy,” Materials Science and Engineering, 299: 287-295.

Zbib, H.M., and Aifantis, E.C., (1992) “On the Gradient-Dependent Theory of Plasticity and Shear Banding,” Acta Mechanica, 92: 209-225.

Zener, C., and Hollomon, J.H., (1944) “Effect of strain rate on plastic flow of steel,” Journal of Applied Physics, 15: 22-32.

Zerilli, F.J., and Armstrong, R.W., (1987) “Dislocation-mechanics-based constitutive relations for material dynamics calculation,” Journal of Appllied Physics, 5: 1816-1825.

Zerilli, F.J., and Armstrong, R.W., (1987) “Dislocation-mechanics-based constitutive relations for material dynamics calculation.” Journal of Applied Physics, 5: 1816-1825.

Zhang, Z., and Clifton, R.J., (2003) “Shear band propagation from a crack tip,” Journal of the Mechanics and Physics of Solids, 51: 1903-1922.

Zhou, F., Wright, T.W., and Ramesh, K.T., (2006) “A numerical methodology for investigating the formation of adiabatic shear bands,” Journal of the Mechanics and Physics of Solids, 54: 904-926.

Zhu, H.T., and Zbib, H.M., (1995) “On the role of strain gradients in adiabatic shear banding,” Acta Mechanica, 111: 111-124.

Zhu, Z.G., and Batra, R.C., (1990) “Dynamic shear band development in plane strain compression of a viscoplastic body containing a rigid inclusion,” Acta Mechanica, 84: 89-107.

Zurek, A.K., (1994) “The study of adiabatic shear band instability in a pearlitic 4340 steel using a dynamic punch test,” Metallurgical and Materials Transactions A, 25(11): 2483-2489.

APPENDIX A: PERMISSION LETTERS

PERMISSION LETTER FOR DISSERTATION

2/27/2008
Amin H. Almasri.
Department of Civil and Environmental Engineering
Louisiana State University, Baton Rouge, LA 70803
USA

Dear Journal of Engineering Mechanics:

I am completing a doctoral dissertation at the Louisiana State University/USA entitled "DYNAMIC SHEAR BANDS IN METALS UNDER HIGH STRAIN RATES." I would like your permission to reprint in my dissertation excerpts from the following:

> Almasri, A.H., and Voyiadjis, G.Z., (2008) "A Physically Based Constitutive model for BCC metals with Applications to Iron," Journal of Engineering Mechanics, in press. Manuscript number EM/2007/024506

The excerpts to be reproduced are the figures. The requested permission extends to any future revisions and editions of my dissertation, including the electronic publication of my dissertation by Louisiana State University. These rights will in no way restrict republication of the material in any other form by you or by others authorized by you. Your signing of this letter will also confirm that you own the copyright to the above-described material.

If these arrangements meet with your approval, please sign this letter where indicated below and return a scanned copy to the attached email. Thank you very much.

Sincerely,

Amin H. Almasri

PERMISSION GRANTED FOR THE USE REQUESTED ABOVE:

Permission is granted for you to reuse "A Physically Based Constitutive model for BCC metals with Applications to Iron," in your doctoral dissertation. Please add a full credit line to the material being reprinted: "In Review" or "In Press" (With permission from ASCE).

Xi Van Fleet
Senior Manager, Information Services
Publication Division
American Society of Civil Engineers
1801 Alexander Bell Drive
Reston, VA 20191
(703) 295-6278-FAX
PERMISSIONS@asce.org

Date: 2/27/08

PERMISSION LETTER FOR DISSERTATION

2/27/2008
Amin H. Almasri.
Department of Civil and Environmental Engineering
Louisiana State University, Baton Rouge, LA 70803
USA

Dear Journal of Engineering Materials and Technology:

I am completing a coctoral dissertation at the Louisiana State University/USA entitled "DYNAMIC SHEAR BANDS IN METALS UNDER HIGH STRAIN RATES." I would like your permission to reprint in my dissertation excerpts from the following:

> Almasri, A.H., and Voyiadjis, G.Z., (2007) "The Effect of Strain Rate on The Dynamic Hardness in Metals," Journal of Engineering Materials and Technology, 129(4): 505-512.

The excerpts to be reproduced are the figures. The requested permission extends to any future revisions and editions of my dissertation, including the electronic publication of my dissertation by Louisiana State University. These rights will in no way restrict republication of the material in any other form by you or by others authorized by you. Your signing of this letter will also confirm that you own the copyright to the above-described material.

If these arrangements meet with your approval, please sign this letter where indicated below and return a scanned copy to the attached email. Thank you very much.

Sincerely,

Amin H. Almasri

PERMISSION GRANTED FOR THE USE REQUESTED ABOVE:

Date: Feb. 27, 2008

As is customary, we request that you ensure proper acknowledgment of the exact sources of this material, the authors, and ASME as original publisher.

VITA

Amin Hisham Almasri was born in Jordan on November 18, 1979. His childhood was spent traveling back and forth between Saudi Arabia and Jordan, where he received his primary and secondary education in various schools in both countries. This led to a better understanding of differences between the cultures. He started his high education attending Jordan University of Science and Technology in 1997. Amin graduated in 2001 with a degree in civil engineering and, after a small break, started pursuing a master's degree also in civil engineering at the same university. Meanwhile, he worked as a teaching assistant, research assistant, and field engineer during the different stages in the graduate study. In 2004, Amin finished his study under the guidance of Professor Ghazi Abu-Farsakh and left Jordan to the United States. Mr. Almasri began his doctoral study immediately at Louisiana State University (LSU) under the supervision of Boyd Professor George Z.. Voyiadjis. Four years later he completed the research presented in this dissertation with a 3.9 GPA. He has been involved in researches in several areas, such as structural dynamics, computational mechanics, mechanics of materials, mechanics of solids and structures, fracture and damage mechanics, and multiscale modeling of steel alloys. He has several publications that have been published in several prestigious journals in the field of structural engineering and engineering mechanics. He has also participated in a number of international and national conferences. Amin is planning on going back to Jordan, settling down, starting a family and building a great career.